CONTENTS

Page

INTENTIONALLY LEFT BLANK

TABLES

Page

TABLES (Continued)

TABLES (Continued)

Page

INTENTIONALLY LEFT BLANK

FIGURES

Page

FIGURES (Continued)

FIGURES (Continued)

FIGURES (Continued)

Page

FIGURES (Continued)

Page

FIGURES (Continued)

Page

2.3.4 Mechanical Degradation of the Engineered Barrier System

[NUREG-1804, Section 2.2.1.3.2.3: AC 1(1) to (5), (7), AC 2, AC 3, AC 4, AC 5; Section 2.2.1.3.3.3: AC 1(3), (4), AC 3(3), (4), AC 4(4), AC 5(3)]

Section 2.3.4 outlines the models and analyses used to evaluate mechanical degradation of the Engineered Barrier System (EBS). This section addresses the requirements of proposed 10 CFR 63.114(a)(1) through (a)(7) and (b) regarding the abstraction of mechanical disruption of the EBS in the performance assessment and specific acceptance criteria of NUREG-1804.

The objective of Section 2.3.4 is to describe and justify the mechanical degradation submodel as a component of the overall total system performance assessment (TSPA). The following material is presented in this section:

- Data from the site and surrounding region, uncertainties and variabilities in parameter values, and alternative conceptual models used in the analyses
- Specific features, events, and processes (FEPs) included in the analyses
- Specific degradation, deterioration, and alteration processes included in the analyses and the technical bases for inclusion of the processes
- Technical bases for models used in the performance assessment.

The categories of information contained in this section and the corresponding proposed 10 CFR Part 63 regulatory requirements and NUREG-1804 acceptance criteria are presented in the following table. NUREG-1804, Section 2.2.1.3.2.3, Acceptance Criterion 1(6) is not referenced below because the impact of transient criticality on the integrity of the engineered barrier features is addressed in Section 2.2.1.4.1. NUREG-1804, Section 2.2.1.3.2.3, Acceptance Criterion 1(7) is referenced in the table because radiation effects on material properties were not included in the current structural response calculations based on a peer review (Section 2.3.4.5.1.3.1; Beavers et al. 2002). This peer review evaluated the technical basis at that time for estimating the performance of waste packages and drip shields. It was performed in accordance with procedures that are consistent with NUREG-1297 (Altman et al. 1988a). With regard to data qualification, this section does not discuss the approach used. However, scientific analyses, model development, and data qualification activities were conducted in accordance with project procedures that comply with Quality Assurance Program requirements. The project procedures governing data qualification are consistent with NUREG-1298 (Altman et al. 1988b) in keeping with Acceptance Criterion 1(7).

The methodology for the identification, classification, and screening of FEPs is described in Sections 2.2.1.1 and 2.2.1.2 of this document. Table 2.2-5 provides a comprehensive list of FEPs having the potential to affect the performance of the repository system, including a description of and the screening decision for each FEP. The detailed screening justifications are documented in *Features, Events, and Processes for the Total System Performance Assessment: Analyses* (SNL 2008a, Section 6).

SAR Section	Information Category	Proposed 10 CFR Part 63 Reference	NUREG-1804 Reference
2.3.4	Mechanical Degradation of the Engineered Barrier System	63.114(a)(1) 63.114(a)(2) 63.114(a)(3) 63.114(a)(4) 63.114(a)(5) 63.114(a)(6) 63.114(a)(7) 63.114(b) 63.342(c)	Section 2.2.1.3.2.3: Acceptance Criterion 1(1) Acceptance Criterion 1(2) Acceptance Criterion 1(3) Acceptance Criterion 1(4) Acceptance Criterion 1(5) Acceptance Criterion 1(7) Acceptance Criterion 2 Acceptance Criterion 3 Acceptance Criterion 4 Acceptance Criterion 5 Section 2.2.1.3.3.3: Acceptance Criterion 1(3) Acceptance Criterion 1(4) Acceptance Criterion 3(3) Acceptance Criterion 3(4) Acceptance Criterion 4(4) Acceptance Criterion 5(3)
2.3.4.1	Summary and Overview	Not applicable	Not applicable
2.3.4.2	System Description and Model Integration	63.114(a)(4) 63.114(a)(5) 63.114(a)(6) 63.114(b) 63.342(c)	Section 2.2.1.3.2.3: Acceptance Criterion 1(1) Acceptance Criterion 1(2) Acceptance Criterion 1(3) Acceptance Criterion 1(5) Section 2.2.1.3.3.3: Acceptance Criterion 1(3) Acceptance Criterion 1(4)
2.3.4.3	Ground Motion and Fault Displacement Analyses	63.114(a)(1) 63.114(a)(2) 63.114(a)(3) 63.114(a)(4) 63.114(a)(5) 63.114(a)(6) 63.114(a)(7) 63.114(b) 63.342(c)	Section 2.2.1.3.2.3: Acceptance Criterion 1(1) Acceptance Criterion 1(2) Acceptance Criterion 1(3) Acceptance Criterion 1(4) Acceptance Criterion 2(Acceptance Criterion 3 Acceptance Criterion 4 Acceptance Criterion 5 Section 2.2.1.3.3.3: Acceptance Criterion 1(3) Acceptance Criterion 1(4) Acceptance Criterion 3(3) Acceptance Criterion 5(3)

SAR Section	Information Category	Proposed 10 CFR Part 63 Reference	NUREG-1804 Reference
2.3.4.4	Rockfall Analysis	63.114(a)(1) 63.114(a)(2) 63.114(a)(3) 63.114(a)(4) 63.114(a)(5) 63.114(a)(6) 63.114(a)(7) 63.114(b) 63.342(c)	Section 2.2.1.3.2.3: Acceptance Criterion 1(1) Acceptance Criterion 1(2) Acceptance Criterion 1(3) Acceptance Criterion 1(4) Acceptance Criterion 2 Acceptance Criterion 3(1) Acceptance Criterion 3(2) Acceptance Criterion 3(3) Acceptance Criterion 4 Acceptance Criterion 5 Section 2.2.1.3.3.3: Acceptance Criterion 1(3) Acceptance Criterion 1(4) Acceptance Criterion 3(3) Acceptance Criterion 3(4) Acceptance Criterion 4(4) Acceptance Criterion 5(3)
2.3.4.5	Structural Response of EBS Features to Mechanical Degradation	63.114(a)(1) 63.114(a)(2) 63.114(a)(3) 63.114(a)(4) 63.114(a)(5) 63.114(a)(6) 63.114(a)(7) 63.114(b) 63.342(c)	Section 2.2.1.3.2.3: Acceptance Criterion 1(1) Acceptance Criterion 1(2) Acceptance Criterion 1(3) Acceptance Criterion 1(4) Acceptance Criterion 1(7) Acceptance Criterion 2 Acceptance Criterion 3(1) Acceptance Criterion 3(2) Acceptance Criterion 3(3) Acceptance Criterion 4 Acceptance Criterion 5(2) Acceptance Criterion 5(3) Section 2.2.1.3.3.3: Acceptance Criterion 1(3) Acceptance Criterion 1(4) Acceptance Criterion 3(3) Acceptance Criterion 3(4) Acceptance Criterion 4(4) Acceptance Criterion 5(3)
2.3.4.6	Computational Algorithm for Seismic Scenario Class	63.114(a)(1) 63.114(a)(2) 63.114(a)(3) 63.114(a)(4) 63.114(b) 63.342(c)	Section 2.2.1.3.2.3: Acceptance Criterion 3(2) Acceptance Criterion 3(3) Acceptance Criterion 5(3)

SAR Section	Information Category	Proposed 10 CFR Part 63 Reference	NUREG-1804 Reference
2.3.4.7	Evaluation of Material Supporting Mechanical Disruption of the EBS	63.114(a)(1) 63.114(a)(2) 63.114(a)(3) 63.114(a)(6)	Section 2.2.1.3.2.3: Acceptance Criterion 1(1) Acceptance Criterion 1(2) Acceptance Criterion 1(3) Acceptance Criterion 1(4) Acceptance Criterion 5 Section 2.2.1.3.3.3: Acceptance Criterion 1(3) Acceptance Criterion 1(4) Acceptance Criterion 5(3)
2.3.4.8	Conclusions	Not applicable	Not applicable

2.3.4.1 Summary and Overview

The capability of the EBS may be compromised by disruptive natural events. Analyses indicate that mechanical disruption of EBS features after repository closure may have a significant effect on repository performance. Mechanical disruption of an EBS feature is defined as partial or total mechanical failure of the feature resulting from external events that immediately or eventually reduce design life and intended performance. The EBS features that contribute to barrier performance are the emplacement drifts, drip shields, waste packages, waste forms, waste package internals, waste package pallets, and the emplacement drift inverts. The EBS features are designed to work together and complement the natural barriers by preventing or substantially reducing the release rate of radionuclides from the waste and preventing or substantially reducing the rate of movement of radionuclides from the repository to the accessible environment. Figure 2.3.4-1 illustrates the features of the EBS in a typical emplacement drift. The design aspects of the EBS are described in detail in Sections 1.3.4 and 1.5.2. The performance aspects of the EBS are described in detail in Sections 2.1, 2.3.5, 2.3.6, and 2.3.7, while the mechanical degradation of the EBS features is described in Section 2.3.4.

Mechanical disruption of the EBS is considered in the seismic scenario class, one of the disruptive events scenario classes of the TSPA, and includes the potential effects associated with seismic events (e.g., vibratory ground motion, rockfall, or fault displacement). The seismic scenario class utilizes ground motion, rockfall, and EBS structural analyses to describe a sequence of events and processes that, if they were to occur, could impact the magnitude and timing of radiological releases to the reasonably maximally exposed individual (RMEI). Section 2.2.2.1 describes the approach to assessment of seismic hazards.

Three seismic-related included FEPs (Table 2.3.4-1) have been determined to be important to the barrier capability of the EBS at Yucca Mountain (Table 2.1-3):

- **Seismic Ground Motion Damages EBS Components**—Seismic activity that causes repeated vibration of the EBS components (drip shield, waste package, pallet, and invert) could result in severe disruption of the drip shields and waste packages through vibration

damage or through contact between EBS components. Such damage mechanisms could lead to degraded performance.

- **Seismic-Induced Drift Collapse Damages EBS Components**—Seismic activity could produce jointed-rock motion and/or changes in rock stress leading to enhanced drift collapse that could impact drip shields, waste packages, or other EBS components. Possible effects include both dynamic and static loading.

- **Seismic-Induced Drift Collapse Alters In-Drift Thermal Hydrology**—Seismic activity could produce jointed-rock motion and/or changes in rock stress leading to enhanced drift collapse and/or rubble infill throughout part or all of the drifts. Drift collapse could impact flow pathways and condensation within the EBS, mechanisms for water contact with EBS components, and thermal properties within the EBS.

The following related FEPs, of potential importance to the mechanical response of EBS components, have been excluded from consideration in the TSPA:

- **Seismic-Induced Rockfall Damages EBS Components**—Seismic activity could produce jointed-rock motion and/or changes in rock stress leading to rockfall that could impact drip shields, waste packages, or other EBS components. As used for FEP 1.2.03.02.0B, rockfall refers to rock blocks that fall from the roof or sides of a drift in the nonlithophysal zones of the repository during a seismic event, rather than complete or partial collapse of the emplacement drift, which may cover the drip shield with rubble and cause a sustained, static loading to the structure (addressed in included FEP 1.2.03.02.0C, Seismic-induced drift collapse damages EBS components). Damage to the drip shields and waste packages as a result of seismic-induced rockfall from jointed-rock motion in nonlithophysal units is excluded from the TSPA model, as documented by the analysis in *Features, Events, and Processes for the Total System Performance Assessment: Analyses* (SNL 2008a, FEP 1.2.03.02.0B, Seismic-induced rockfall damages EBS components). The effects of rockfall on the drip shields have been quantified in terms of damaged areas and the probability of rupture of the drip shield plates (Section 2.3.4.5.2.2). However, damaged area on the drip shields is excluded from the TSPA model because advective flow through stress corrosion cracks in the drip shields is excluded from the TSPA model (see excluded FEP 2.1.03.10.0B, Advection of liquids and solids through cracks in the drip shield, Table 2.2-5), and failure of the drip shield plates is excluded because it has low consequence for the TSPA. Rupture of the axial stiffeners occurs only for an impact by a 28.3 metric ton (MT) rock block and is excluded on the basis of low probability. Finally, damage to the waste packages and waste package internals from seismically induced rockfall in jointed rock in nonlithophysal units is excluded from the TSPA model because the drip shields do not separate and because the drip shields remain intact mechanically and can deflect rockfall away from the waste packages. Based on this analysis, the functionality of EBS features is not compromised, and the effects of seismic-induced rockfall in the nonlithophysal units are excluded from TSPA. Note that the effects of seismic-induced drift collapse in the lithophysal units of the repository are included in TSPA via included FEP 1.2.03.02.0C, Seismic-induced drift collapse damages EBS components, as discussed above.

- **Rockfall**—Rockfall may occur with blocks large enough to mechanically tear or rupture drip shields or waste packages. This excluded FEP deals with rockfall related to nominal (nonseismic) processes such as drift degradation induced by in situ gravitational and excavation-induced stresses as well as thermally induced stresses. Analyses presented in *Drift Degradation Analysis* (BSC 2004a, Section 6.3.1) and summarized in Section 2.3.4.4 indicate that potential rock block sizes generated from nominal processes are not sufficient to tear or rupture the drip shield plates. Potential advective flux through stress corrosion cracks resulting from denting of the drip shield plates by rockfall has been excluded due to low consequence (excluded FEP 2.1.03.10.0B, Advection of liquids and solids through cracks in the drip shield, in Table 2.2-5).

- **Drift Collapse**—Partial or complete collapse of the drifts, as opposed to discrete rockfall, could occur as a result of thermal effects, stresses related to excavation or other mechanisms (nonseismic processes). Drift collapse could affect the stability of the engineered barriers and waste packages and/or result in static loading from rock overburden. Rockfalls of small blocks may produce rubble throughout part or all of the drifts. Analyses presented in *Drift Degradation Analysis* (BSC 2004a, Section 6.3.1 and Appendix S) and summarized in Section 2.3.4.4 demonstrate that drift collapse resulting from excavation and thermal stresses is expected to be relatively minor during the time of the thermal phase in which the drifts heat to maximum temperature and thermal stress condition. Additionally, time-dependent strength degradation of the rock mass over the first 20,000 years after emplacement is expected to result in only partial drift collapse in either lithophysal or nonlithophysal rock masses. Therefore, the impact of drift collapse on the performance of the drip shield, waste package, emplacement pallet, and invert has been excluded on the basis of low consequence.

- **Advection of Liquids and Solids Through Cracks in the Drip Shield**—The presence of one or more cracks or other small openings of sufficient size in a drip shield may provide a pathway for the advective flow of water (e.g., thin films or droplets) or solid material through the drip shield. The resulting flux may affect drip shield performance or subsequent dripping onto the waste packages. Partial or full plugging of the drip shield cracks by chemical or physical reactions after their formation (e.g., healing) could also affect water flow through the drip shield. The process of formation and the physical characteristics of stress corrosion cracks resulting from denting of the drip shield by seismically induced rockfall or drift collapse is summarized in Section 2.3.4.5.2.2. The advection of liquids through seismically induced stress corrosion cracks in the drip shield is excluded from the TSPA based on low consequence as a result of a number of factors, including: (1) the small aperture width (narrow opening and tight cracks) and the presence of capillary forces within the stress corrosion cracks; and (2) the potential for plugging of the cracks due to mineral deposits. In response to stresses induced by rockfall deformations, stress relief via creep mechanisms or stress corrosion cracking of the drip shield may occur. Such cracks in passive alloys, such as Titanium Grade 7 (UNS R52400), are tight (e.g., small crack-opening displacement) and are expected to be plugged by corrosion products and precipitates, as discussed in *Stress Corrosion Cracking of Waste Package Outer Barrier and Drip Shield Materials* (SNL 2007a, Section 6.8.5.2).

Field geologic and seismologic investigations, seismologic monitoring, laboratory and field testing of rock mechanical properties, analogue studies, and reviews of published literature provide the technical basis for the description of past seismic activity in the Yucca Mountain region, and for the development of conceptual, process, and consequence models that represent potential future events. The process models have been used to develop simplified model abstractions that are incorporated within the TSPA model to generate a probabilistic representation of the likelihood and consequences of the seismic scenario class.

The models, analyses, and information used to assess mechanical degradation of the EBS, and their interactions within the seismic scenario class, are illustrated schematically in Figure 2.3.4-2 and described in Section 2.3.4.2. In that section, the relevant FEPs are summarized, the inputs from and outputs to the various component process models are shown, and the seismic consequence abstraction for the seismic scenario class is described.

Section 2.3.4.3 presents the ground motion modeling and analyses used to estimate the likelihood of ground motions that may occur at the repository location. Site-specific ground motions and estimates of fault displacement were determined based on results developed from a probabilistic seismic hazard analysis (PSHA) described in Section 2.2.2.1. Ground motion time histories and fault displacements representing preclosure and postclosure hazard levels were then used as input to models of seismically induced emplacement drift rockfall as well as the dynamic behavior of EBS features for assessing mechanical disruption and damage. The technical basis for the ground motion analysis is presented and illustrates how appropriate data from the site and surrounding region, uncertainties and variabilities in parameter values, and alternative conceptual models have been used to develop site-specific ground motion time histories.

Rockfall modeling and analyses that assess emplacement drift damage as a function of ground motion level and thermal-mechanical stresses and time-dependent rock strength degradation are presented in Section 2.3.4.4. Analyses summarized in this section show that rockfall resulting from thermal-mechanical stresses or time-dependent strength degradation is minor in comparison to that resulting from vibratory motion. Based on these analyses, thermal-mechanical and time-dependent effects on drift degradation have been excluded (FEP 2.1.07.01.0A, Rockfall, and FEP 2.1.07.02.0A, Drift collapse, in Table 2.2-5). Description of the analysis of drift degradation resulting from thermal-mechanical stresses and time-dependency are provided here as a summary of the information that provides the FEP exclusion bases. The potential for mechanical disruption of EBS features due to rockfall associated with vibratory ground motion was assessed using detailed two- and three-dimensional tunnel stability models. Sensitivity studies of the thermal-mechanical and dynamic stability of emplacement drifts in the nonlithophysal and lithophysal tuff rock units that comprise the repository host horizon are presented. Results from the rockfall analysis include distributions of rockfall mass, velocity, drip shield impact timing, location and energy, and total rockfall volume per kilometer of drift as a function of the ground motion level. The accumulated rubble load distribution on the drip shield after seismic events is also estimated to provide input to drip shield structural evaluations. Emplacement drift profiles and the porosity of rubble material in the drift following a seismic event or from long-term degradation are estimated to support evaluation of potential impacts on drift seepage and the in-drift environment. The technical basis for rockfall analysis is presented, including a review of data from the site and surrounding region, uncertainties and variabilities in parameter values, and alternative conceptual models. The technical

basis for the exclusion of drift degradation resulting from the nominal thermal-mechanical stresses and time-dependent rock strength change is also provided.

An analysis of the structural response of EBS features to the long-term evolution of the EBS environment is presented in Section 2.3.4.5. Mechanical effects from multiple seismic events and rockfall are examined to account for degradation of EBS components. The EBS components include the emplacement drift, the invert, the waste package emplacement pallet, the waste package, the waste package internals, the waste form, and the drip shield. The waste package inventory is represented by two general types of waste packages: the TAD-bearing and co-disposal packages.

Throughout this section, the terms "degradation," "damage," and "failure" are often used. The following are definitions:

- "Degradation" refers to the alteration and enlargement of the emplacement drift profile resulting from rockfall or drift collapse. Degradation is the result of rock mass yielding from in situ gravitational, tectonic, and excavation-induced stresses which are increased by transient seismically induced and/or thermally induced stress changes. The natural time-dependent reduction in rock mass strength resulting from stress corrosion processes (termed "static fatigue") may also contribute to degradation.

- "Damage" refers to regions of plastic deformation wherein the residual tensile stress is high enough to initiate stress corrosion crack development in the drip shield plates or the waste package outer corrosion barrier. The plastic deformation of EBS components may be induced by impact denting (e.g., from rock block impact or from impact of EBS components during seismic shaking) or by quasi-static forces from rock rubble loading (which may be amplified by ground acceleration during seismic shaking).

- "Failure" refers to an immediate loss of function of an EBS component, including a tensile rupture, tearing or puncture of the drip shield plates or waste package outer corrosion barrier, or the collapse of the drip shield framework.

Structural calculations assess damage and structural collapse of the drip shield as a result of impact from rockfall and from drift collapse induced by vibratory ground motion. These calculations are based on the use of two- and three-dimensional, dynamic structural analysis models that incorporate the details of the drip shield design, as well as a representation of the rockfall for the lithophysal and nonlithophysal rock units. The static load applied to the drip shield from accumulating rock rubble, and the impact loading from rock blocks are derived from the drift degradation calculations presented in Section 2.3.4.4. Vibratory ground motion frequency and amplitude are derived from the bounded seismic hazard curve that is presented in Section 2.3.4.3. Dynamic analyses of rock block impacts on the drip shield, as well as static loading and dynamic amplification of the load from the accumulated rubble, are modeled to examine surface damage and permanent deformation of the drip shield structure. In addition to the potential for structural damage due to rockfall, the potential for separation of the interlocking drip shields subjected to low-probability seismic events is also examined.

The ultimate failure of the drip shield under the combined static load of accumulated rubble, and the dynamic amplification of that load due to multiple seismic events occurring over long time periods,

is examined and included in abstractions to the TSPA. Included in this analysis is the thinning and weakening of the drip shield surface plates and framework over long time periods resulting from general corrosion as presented in Section 2.3.6. The limiting structural loads for tensile tearing of the drip shield plates, or buckling of the drip shield framework, are determined for various degrees of corrosion thinning. These ultimate plastic load limits are used as criteria for defining the probability of drip shield failure under the static and dynamically amplified rubble loads.

Structural calculations were also used to assess damage to the TAD canister-bearing and representative codisposal waste packages from vibratory ground motion. The structural response for these packages is determined for a range of outer corrosion barrier thicknesses representative of the range of general corrosion thinning expected to occur over the regulatory period. Additionally, the calculations account for the state of the internal structures within the waste package. Two states are considered: an intact state in which internal structures are unaffected, and a degraded state in which internal structures are completely corroded after waste package breach has allowed diffusion of water vapor and fluids into the waste package interior. When the drip shield is intact, the waste package and pallets will be free to translate beneath them in response to vibratory motion. The potential damage to the waste package due to ground motion-induced interactions with other waste packages, the pallet, and the drip shield is examined via parametric studies using three-dimensional finite element kinematic models. The damage or rupture potential resulting from impact parameters (such as impact force, location, and angle), are interpreted using the results of detailed finite element damage models. Surface area damage (based on a residual tensile stress criterion for the Alloy 22 (UNS N06022) waste package outer barrier), as well as tensile rupture of the outer barrier (based on tensile strain limits), are abstracted as a function of the peak ground velocity (PGV) for input to the abstraction of seismic consequence.

Drip shield failure will eventually occur, over very long time periods, as thinning from general corrosion weakens the structure. Failure of the drip shield can occur either by loss of load capacity of the framework that supports the plates, or by tensile rupture or tearing of the plates. The drip shield framework is expected to fail by buckling of the supporting legs under the action of rubble loading, followed (at some later time) by tearing of the drip shield plates. When the drip shield legs buckle, it will then rest upon the waste package outer barrier, transmitting the rubble load directly to the package. Analyses indicate that the drip shield plates will maintain structural integrity after the legs buckle. Since the clearance space between the waste package and drip shield crown is small, the crown and its support bulkheads are expected to come to rest directly on the top of the waste package with little distortion of its shape. Thus, with plates intact, the drip shield is expected to maintain its function in seepage water diversion, even in the collapsed state, for a period of time. Eventually, the drip shield plates will tear, allowing seepage water and rubble to directly contact the waste package. After drip shield plate failure, the static and dynamically amplified load of the rock rubble can damage and potentially breach the waste package. Structural calculations using two- and three-dimensional structural models are used to examine the surface damage and tensile rupture potential of the waste packages when subjected to static and dynamic rock rubble loads.

The waste package pallet will also eventually fail as the stainless steel connector tubes between the Alloy 22 end piers corrode and lose their structural capacity. The end piers may then tilt under the action of vibratory motion with the waste package potentially resting on the end piers, the invert, or some combination of the two. In the structural calculations presented in this section, the pallet is assumed to be intact and supporting the waste package since greater damage to the waste package

outer corrosion barrier results during vibratory motion when the waste package impacts the relatively stiff pallet as opposed to the crushed tuff invert. The three-dimensional structural analysis of the waste package and pallet assumes that the Alloy 22 end piers may yield and deform plastically under the action of external loading. They are also assumed to thin with time due to general corrosion at the same rate as the waste package outer corrosion barrier. The pallet thus becomes structurally weaker and more deformable.

The invert ballast material is crushed tuff. Although this material is, in general, considered to be rigid, analyses have been performed to examine the dynamic shaking effects on the invert and the mechanical response of the waste package, pallet and drip shield. The analyses indicate that these effects are minor.

The structural calculations presented in Section 2.3.4.5 provide the technical basis for seismic consequence abstractions, and illustrate how appropriate data from the site and surrounding region, along with uncertainties and variabilities in parameter values, and alternative conceptual models have been used in the analysis. The calculations also show how specific degradation, deterioration, and alteration processes have been included in the analyses, taking into consideration their effects on annual dose. The calculations also demonstrate the linkage or coupling of these analyses to information derived from other sections in the license application.

An analysis of fault displacement presented in Section 2.3.4.5.5 examines how fault displacement may contribute to mechanical disruption of EBS features. Estimates of low-probability fault displacement are compared with the clearance between EBS components to estimate potential damage. The repository design provides for a minimum 60 m standoff between a Quaternary fault with potential for significant displacement and repository openings (Section 1.3.2.4.3.2). However, there is some potential for distributed faulting on faults or fractures located away from faults undergoing primary displacement. The calculations described in this section assess potential damage to EBS features from such fault displacements with low annual probabilities of exceedence. The fault displacement analysis shows how appropriate data from the site and alternative conceptual models have been considered.

The methodology for abstraction of mechanical disruption of EBS features into the TSPA is presented in Section 2.3.4.6. The outputs from the evaluation of the seismic scenario class to the TSPA are mathematical relationships that describe the damage or failure states of the EBS features. The EBS features consist of: (1) the invert; (2) the emplacement pallet; (3) the waste package; (4) the drip shield; (5) the waste form; (6) the waste package internals; and (7) the emplacement drift. The waste package and drip shield are the primary focus in this section because their response to seismic events has the potential to form new pathways for release of radionuclides from the EBS. The drift invert, emplacement pallet, waste package internals, and waste form are included in the kinematic and structural response calculations for the seismic scenario class, but it is not necessary to develop damage abstractions for these components because they do not form new pathways for transport and release of radionuclides after seismic events or because TSPA is not taking credit for commercial spent nuclear fuel (SNF) cladding as a feature that retards release of radionuclides (SNL 2008b, Section 6.6.1.1.3). Finally, the uneven settlement of the invert ballast from seismic events does not compromise the capability of the drip shield to support static loads, as discussed in excluded FEP 2.1.06.05.0B, Mechanical degradation of the invert (Table 2.2-5).

Damage abstractions are developed for EBS features including the waste emplacement drift, the waste package, and the drip shield. Abstractions are not developed explicitly for the waste package pallet, the waste package internal structures and the emplacement drift invert. However, the effect of these EBS components on damage to or failure of the waste package and drip shield are included implicitly in the waste package and drip shield damage abstractions in that their mechanical effects have been included in the structural calculations described in Sections 2.3.4.5.2, 2.3.4.5.3 and 2.3.4.5.4. The damage states represented in the seismic scenario class are expressed in terms of the magnitude of the horizontal component of PGV, and include the following:

- Accumulation of rubble volume in the emplacement drift, resulting from repetitive seismic events.

- Damage to the waste package (expressed as an area of stress corrosion cracks on the waste package surface), or rupture probability of the waste package outer barrier, as a result of deformation due to vibratory motion while the drip shield is intact and protects the waste package from rockfall.

- Damage to the drip shield plates (expressed as an area of stress corrosion cracks on the drip shield surface) or rupture/puncture probability as a result of accumulated rockfall or impact from rock blocks. The advective flux of liquids through stress corrosion cracks on the drip shield surface has been excluded from the TSPA model based on low consequence (excluded FEP 2.1.03.10.0B, Advection of liquids and solids through cracks in the drip shield, Table 2.2-5). However, the abstraction of damage to the drip shield plates is described in Section 2.3.4.5.2.2 as it was used as input for studies that formed the basis for the low consequence exclusion of FEP 1.2.03.02.0B, Seismic-induced rockfall damages EBS components.

- Probability of failure (fragility) of the drip shield by tensile rupture of its plates or by buckling of the drip shield framework as a result of accumulated rockfall and dynamic load amplification for future states of general corrosion thinning.

- Damage to the waste package (expressed as an area of stress corrosion cracks on the waste package surface), or rupture/puncture probability of the waste package outer barrier, as a result of collapse of the drip shield framework. The drip shield continues to act to prevent seepage from reaching the waste package, but mechanically loads the waste package outer barrier with static and dynamically amplified rubble loads. This accounts for future states of corrosion thinning of the drip shield framework, waste package outer barrier, and degradation of waste package internals.

- Damage to the waste package (expressed as an area of stress corrosion cracks on the waste package surface), or puncture probability of the waste package outer barrier, as a result of drip shield plate tearing failure. The drip shield fails to prevent seepage and rockfall, with subsequent rubble in direct contact with the waste package outer barrier, thus applying static and dynamically amplified rubble loads. This accounts for future states of corrosion thinning of the drip shield plates, waste package outer barrier, and degradation of waste package internals.

The abstractions for damaged area (i.e., the area that exceeds a residual stress threshold (RST)) and rupture/puncture probability to the waste package or drip shield are based on a three-part approach:

- The probability of rupture or puncture occurring is defined as a function of PGV and the effective tensile strain limit of Alloy 22 or Titanium Grade 7.
- The probability of nonzero damage is defined as a function of PGV and the RST damage criteria for stress corrosion cracking for Alloy 22 or Titanium Grade 7.
- When nonzero damaged area occurs, a conditional probability distribution for the magnitude of the conditional damaged area is defined as a function of PGV and the RST. Normal, log-normal, gamma, and Weibull distributions were evaluated as alternate conceptual models to represent the nonzero damaged area.

The EBS features are robust under seismic loads and will help to prevent or substantially reduce the release rate of radionuclides from the waste and the rate of movement of water and radionuclides from the repository to the accessible environment. The most likely failure mechanism from a seismic event is accelerated stress corrosion cracking in the damaged areas that exceed the RST for Alloy 22 (the waste package outer barrier). This damage is the result of two mechanisms: (1) the kinematic motion and impacts of the waste package and pallet while the drip shield is intact, and (2) the stresses from static rockfall load combined with the dynamic amplification from the vibratory ground motions during a seismic event after failure of the drip shield plates. Other failure mechanisms include the potential for rupture or puncture of the outer corrosion barrier of the waste package in response to a high amplitude low probability earthquake after general corrosion has significantly weakened the EBS components. Cladding failure is not considered here because TSPA is not taking credit for the contribution of commercial SNF cladding as a feature that retards the release of radionuclides (SNL 2008b, Section 6.6.1.1.3).

2.3.4.2 System Description and Model Integration

[NUREG-1804, Section 2.2.1.3.2.3: AC 1(1) to (3), (5); Section 2.2.1.3.3.3: AC 1(3), (4)]

This section summarizes the model, describes the relationship and integration of the submodels, and presents a discussion of the seismic scenario class.

2.3.4.2.1 Summary Description of the Model

The following section provides a summary description of the seismic scenario class and explains how it was integrated into the TSPA. Table 2.3.4-1 summarizes the seismic-related FEPs included in the TSPA.

2.3.4.2.1.1 Summary Description of Seismic Scenario Class and Integration into the Total System Performance Assessment

The seismic scenario class evaluates the effects of seismic hazards (vibratory ground motion and fault displacement) on releases of radionuclides through groundwater and the potential effects of an

earthquake if it were to occur near the repository. The seismic hazards result in mechanical disruption of EBS features in response to vibratory ground motion and to the rockfall induced by vibratory ground motion. Rockfall may also occur from emplacement drift instability resulting from in situ and thermally induced stresses as well as time dependent degradation of the rock mass. However, rockfall from this latter mechanism was found to be minor in comparison to that related to vibratory motion (Excluded FEPs 2.1.07.01.0A, Rockfall, and 2.1.07.02.0A, Drift collapse, in Table 2.2-5). The structural analyses consider rock rubble loading resulting from partial or complete collapse of an emplacement drift, and the dynamic amplification of the rubble loading due to subsequent seismic events. The seismic scenario class is composed of two modeling cases: a seismic vibratory ground motion modeling case and a seismic fault displacement modeling case (Section 2.4.1.2.4).

Figure 2.3.4-3 illustrates the transfer of information for the seismic scenario class into the TSPA and provides a visualization of how information flows between principal TSPA model components within the scenario class. The seismic scenario class utilizes many of the same models and parameters as the nominal scenario class, but also utilizes several models that have been revised from the nominal scenario such as the model for Drift Seepage and Drift Wall Condensation as shown in Figure 2.3.4-3.

FEP analyses (Excluded FEPs 1.2.10.01.0A, Hydrologic response to seismic activity; 2.2.06.01.0A, Seismic activity changes porosity and permeability of rock; 2.2.06.02.0A, Seismic activity changes porosity and permeability of faults; 2.2.06.02.0B, Seismic activity changes porosity and permeability of fractures; and 2.2.06.03.0A, Seismic activity alters perched water zone, documented in *Features, Events, and Processes for the Total System Performance Assessment: Analyses* (SNL 2008a, Section 6), indicate that these seismic hazards will not significantly alter the long-term flow of water through the mountain. Thus, groundwater transport away from the damaged packages is calculated using the nominal scenario class models, and doses to humans from contaminated groundwater are determined using nominal biosphere dose conversion factors (SNL 2008b, Section 6.3.11).

The model analyses that comprise the seismic scenario class are initiated with a seismic event that is characterized in the TSPA by its probability and amplitude. Seismic hazards at the repository horizon associated with the seismic event include vibratory ground motion and fault displacement. These seismic hazards may cause mechanical disruption as a result of:

- Effects of ground motion–induced drift collapse on drip shields and waste packages if a drip shield were to fail as an EBS feature
- Effects of direct ground motion–induced shaking on drip shields, waste packages, and pallets
- Effects of fault displacement on drip shields and waste packages
- Effects of ground motion-induced rockfall on the seepage, temperature, and humidity environment for EBS features within the emplacement drift.

Emplacement drift damage from seismic events may also result in impact to the Upper Natural Barrier, due to effects of drift damage and rockfall on seepage due to change in drift size and shape, as well as damage to the rock mass in the periphery of the drift (Section 2.3.3.2.1.4).

The methodology used for the seismic scenario and assessment of mechanical disruption of EBS features included the following sequence of analyses (Figure 2.3.4-2):

Ground Motion and Fault Displacement Analysis—The amplitude and likelihood of a ground motion or fault displacement event was analyzed in the PSHA (Section 2.2.2.1). The PSHA assessed the characteristics of seismic sources, faulting, and ground motion in the Yucca Mountain region, including their uncertainties. Results were expressed as hazard curves that indicate the annual probability that a given level of ground motion or fault displacement will be exceeded (CRWMS M&O 1998). For ground motion, estimates of PGV and corresponding ground motion time histories were developed for the emplacement drifts based on the results of the PSHA and a ground motion site-response model (BSC 2004b, Section 6.3). The time histories, which incorporate an appropriate range of amplitude, frequency content, and duration, serve as input to models of the dynamic behavior of EBS features for assessing mechanical disruption or damage to these features. For fault displacement, results from the PSHA are used directly for examination of potential EBS feature damage. In addition to the seismic inputs developed for rockfall and structural response calculations, an analysis also determined a bound to low-probability horizontal PGV at the emplacement drifts based on the physical limitations of the rock, geologic observations, and ground motion site-response results. The bounded hazard curve is used in TSPA for the seismic scenario class to limit ground motions. Further analyses and modeling using additional data and an alternate approach to characterizing extreme ground motions at Yucca Mountain indicate that the PGV hazard curve used in TSPA overestimates the probability that a given level of PGV will be exceeded (BSC 2008, Section 6.5.3.2).

Seismically Induced Drift Collapse and Structural Analysis—The extent of mechanical disruption of EBS features is based on structural and kinematic analyses leading to estimates of how much damage or failure may be caused by ground motion or fault displacement. The analyses include assessments of damage to the drip shield and waste package.

Assessment of damage to and failure of the drip shield plates and framework in response to the static and dynamic rock rubble forces resulting from seismically induced drift collapse was performed. Damage to the drip shield from the transient impact forces from nominal or seismically induced rockfall onto the drip shield and the advection of liquids through stress corrosion cracks in the drip shield have been excluded from TSPA on the basis of low consequence (excluded FEPs 2.1.07.01.0A, Rockfall; 1.2.03.02.0B, Seismic-induced rockfall damages EBS components; and 2.1.03.10.0B, Advection of liquids and solids through cracks in the drip shield). However, as described in Section 2.3.4.5.2.2, assessment of damage from both the transient rockfall and drift collapse mechanisms has been examined and summarized to provide background for the FEP exclusion basis.

A series of sensitivity studies of rockfall and drift collapse resulting from vibratory ground motion were performed using two- and three-dimensional discontinuum numerical process-level models. These studies examine the impact of the variability of ground motion hazard level and site-specific ground motion time histories, the variability of rock mass mechanical and thermal properties, and

the variability of rock mass geologic structure on resulting rockfall mass and velocity and accumulation of rockfall rubble produced during the drift collapse process. Drift collapse from nominal processes, including thermal-mechanical and excavation-induced stresses and rock strength time dependency, are considered secondary in comparison to drift collapse resulting from seismic shaking and is therefore excluded from consideration of the mechanical effects on EBS features (SNL 2008a, FEP 2.1.07.02.0A, Drift collapse).

Detailed structural analyses were used to assess damage to the drip shield and waste package as a result of the site-specific vibratory ground motion (SNL 2007b, Sections 6.3 to 6.5). These analyses were conducted using three-dimensional finite element, finite difference, and two-dimensional discontinuum process models and incorporated structural descriptions of the waste package and drip shield, as well as site-specific ground motion time histories and multiple seismic events. The structural analyses include assessments of damage to the drip shield resulting from rock block impacts. Analysis of the drip shield failure from framework collapse and plate tensile rupture (tearing) mechanisms was also performed. The effect of long-term thinning of EBS components from corrosion is taken into account in these analyses. Damage to the EBS components is expressed in terms of damaged surface area on the waste package as a function of the PGV, RST, and long-term thinning of the EBS component (SNL 2007c, Sections 6.5 to 6.11). The damage or potential rupture of the waste package takes into account the potential failure of the drip shield structural framework and plates.

In addition to damage to EBS features due to seismic events, rockfall may result in significant change in the emplacement drift profile, as well as broken rock rubble in the drift. The emplacement drift profile change has an effect on seepage of groundwater into the drift as described in Section 2.3.3.2.3.4.2. The broken rock rubble also impacts the in-drift environment (specifically humidity and temperature) and is dependent on the timing of the event with respect to waste emplacement.

Seismic Consequence Abstraction—The representation of mechanical disruption on the performance of the EBS features for TSPA is developed in the seismic consequence abstraction. Within this abstraction, the damage from multiple mechanical disruption events is expressed as a damaged area on the surfaces of the waste package, as well as a potential rupture of the drip shield plates or outer corrosion barrier of the waste package. The damaged areas on the waste package, the rupture/puncture of the waste package, the buckling of the sidewalls of the drip shield, and the rupture of the drip shield plates include the combined effects of vibratory ground motion, fault displacement, and lithophysal drift collapse. The output from the seismic damage abstraction is mathematical relationships of rock rubble volume, waste package damage (expressed as an area of stress corrosion cracks on the waste package surface), probability of drip shield framework or plate failure, and waste package rupture potential to the intensity of the seismic event (expressed in terms of the PGV). The damage is expressed as a conditional probability distribution that reflects uncertainty and variability in the damage level for a given value of PGV. The seismic scenario is then computed within the TSPA using these damage abstractions as input (SNL 2007c, Sections 6.5 to 6.11).

2.3.4.3 Ground Motion and Fault Displacement Analyses

[NUREG-1804, Section 2.2.1.3.2.3: AC 1(1) to (4), AC 2, AC 3, AC 4, AC 5; Section 2.2.1.3.3.3: AC 1(3), (4), AC 3(3), AC 5(3)]

The seismic analysis consists of two parts: vibratory ground motion and fault displacement. These analyses provide input for the levels of ground motion and fault displacement that could be exceeded at Yucca Mountain with different annual probabilities. These inputs are used in subsequent analyses of rockfall, dynamic structural and kinematic response of EBS features, and seismic consequence abstraction.

The vibratory ground motion analyses consist of four elements:

- The PSHA for ground motion
- A model of the ground motion site-response
- An analysis to develop site-specific time histories (seismograms)
- An analysis to establish a bound to extreme, low-probability peak horizontal ground velocities.

The relationship of these analyses is shown schematically in Figure 2.3.4-2.

The PSHA for ground motion used a formal, structured expert elicitation process to determine the annual probability with which various levels of ground motion will be exceeded at Yucca Mountain (Section 2.2.2.1). The results of the PSHA process provided hazard curves for a reference rock outcrop defined to have seismic-wave propagation properties the same as those found at depth inside Yucca Mountain. These results were then modified to account for the effects of the local, site-specific geology of Yucca Mountain on the ground motions. The effects of the site materials (approximately the upper 300 m of rock and soil) on ground motions at the waste emplacement level were calculated using a ground motion site-response model (Section 2.3.4.3.2). The model determined how an earthquake response spectrum or PGV level at the PSHA reference rock outcrop is modified by the overlying site materials. The acceleration response spectrum consists of the maximum response of a single-degree-of-freedom oscillator system (for a given damping ratio) to an input motion (accelerogram) as a function of the natural frequency of the system. The output of the site-response model, location-specific response spectra and PGV values, was used to scale recordings from past earthquakes to produce acceleration and velocity time histories (seismograms) for dynamic analyses supporting postclosure performance assessment (Section 2.3.4.3.2). Finally, when the models developed in the PSHA were applied, low-probability ground motion values were allowed to increase without bound, eventually reaching levels that are inconsistent with the geologic setting for Yucca Mountain (Section 2.3.4.3.3). Therefore, using data, analyses, and modeling results developed after the PSHA, a separate analysis was performed, to determine a reasonable bound to peak horizontal ground velocity at the waste emplacement level. The analysis takes into account geologic observations that indicate the maximum strain levels sustainable by repository rocks have not been experienced at Yucca Mountain. This analysis is described in Section 2.3.4.3.3. Additional work to characterize extreme, low-probability ground motions at Yucca Mountain, carried out after this analysis, is described in Section 1.1.5 and compared to the

earlier results in Section 2.3.4.3.3.5. The emphasis on peak horizontal ground velocity reflects the use of that ground motion measure to parameterize rockfall and damage to EBS features for postclosure analyses.

The fault displacement analysis is derived directly from the PSHA for fault displacement (Section 2.2.2.1). This analysis used a formal, structured expert elicitation process to determine how the annual probability of exceedance for fault displacement at the surface varies as a function of the size of the displacement. The results also apply to the waste emplacement level and are used directly in the seismic consequence abstraction.

2.3.4.3.1 Probabilistic Seismic Hazard Analysis

To assess the seismic hazards of vibratory ground motion and fault displacement at Yucca Mountain, a PSHA was performed (CRWMS M&O 1998). The PSHA was conducted based on the evaluation of a large set of data pertaining to earthquake sources, fault displacement, and ground motion propagation in the Yucca Mountain region. Quantitative hazard results (annual probabilities that various levels of seismic ground motion will be exceeded at Yucca Mountain) are provided in the PSHA to support an assessment of the performance of the repository and to form the basis for developing seismic design criteria. The methodology that the U.S. Department of Energy (DOE) used for the Yucca Mountain PSHA is consistent with guidance in NUREG/CR-6372 (Budnitz et al. 1997). It also generally conforms to U.S. Nuclear Regulatory Commission (NRC) guidance, NUREG-1563, on the use of expert elicitation in the high-level radioactive waste (HLW) program (Kotra et al. 1996). The methodology is documented in *Methodology to Assess Fault Displacement and Vibratory Ground Motion Hazards at Yucca Mountain* (YMP 1997). The major inputs from the PSHA to the analysis of mechanical disruption of the EBS features are ground motion and fault displacement hazard curves. The PSHA is discussed in detail in Sections 2.2.2.1 and 5.4.

2.3.4.3.2 Ground Motion Site-Response Analysis and Development of Time Histories

[NUREG-1804, Section 2.2.1.3.2.3: AC 1(1) to (4), AC 2, AC 3, AC 4, AC 5]

A site-response analysis was performed to develop earthquake ground motion input for postclosure assessment of the repository. The purpose of the ground motion site-response model is to incorporate the effects of the upper rock and soil layers at Yucca Mountain on earthquake ground motions. Incorporation of these effects was decoupled from the PSHA, which provided ground motion for a reference rock outcrop (Figure 2.3.4-4 and Section 2.2.2.1.3.2) (CRWMS M&O 1998, Section 5.3.1.2; BSC 2004b, Section 1). The site-response model determines, for specific locations of interest such as at the depth of the waste emplacement area, how ground motion propagation through the site materials modifies the PSHA results. These results are then used to develop time histories (seismograms) representing ground motion for a given annual probability of exceedance. The time histories provide input to analyses of rockfall and kinematic and structural response of EBS features under seismic loads.

In evaluating potential preclosure and postclosure effects of ground motion, incorporation of site-response effects on ground motion at Yucca Mountain has followed two approaches. Both approaches are designed to produce site-specific response spectra that maintain the hazard level (probability of exceedance) of the PSHA reference rock outcrop spectra used as the basis for input to the site-response modeling (BSC 2008, Section 6.1.3). The approaches used are described in

Technical Basis for Revision of Regulatory Guidance on Design Ground Motions: Hazard- and Risk-Consistent Ground Motion Spectra Guidelines (NUREG/CR-6728) (McGuire et al. 2001, Section 6.1). Both approaches are approximations to the results that would be obtained if a PSHA including site effects were to be carried out.

One approach (labeled Approach 2B in NUREG/CR-6728) (McGuire et al. 2001, Section 6.1) uses scaling of an input ground motion to obtain a site-specific uniform hazard spectrum with the same annual probability of exceedance. The input ground motion is derived from a rock uniform hazard spectrum for a probability of exceedance of interest. Scaling of the input motion is based on results of site-response modeling that determines the effect of the site materials on the input motion. The site-response modeling takes into account the distributions of earthquake magnitudes contributing to the hazard at high and low oscillator response frequencies for the probability of exceedance of interest and also the variability and uncertainty in site material properties. Site response results for the low and high oscillator frequency ranges and for different site material property base cases are enveloped to obtain the overall site response. The result is a site specific uniform hazard spectrum reflecting the effects of the site materials. This approach is used to develop the ground motions for the postclosure analyses described below.

A second approach (labeled Approach 3 in NUREG/CR-6728) (McGuire et al. 2001, Section 6.1) uses integration over multiple rock ground motion amplitude levels with the site-response dependent on the amplitude level and the associated contributing magnitude and distance distribution. As in Approach 2B, site-response modeling takes into account high and low oscillator frequency ranges and the variability and uncertainty in site properties. This approach results directly in a site-specific hazard curve. Uncertainty in site properties leads to hazard curves for each combination of base-case properties. The overall hazard curve is determined by averaging, using weights if appropriate, the hazard curves for the different base-case property combinations. When implemented for a suite of ground motion measures (e.g., spectral acceleration at a suite of response oscillator frequencies), the approach provides the results needed to construct a site specific uniform hazard curve for a probability of exceedance of interest. This approach, described in more detail in Section 1.1.5, is used to develop ground motions for preclosure probabilistic seismic safety analyses because it facilitates the weighted averaging of hazard curves associated with site material property base cases used to characterize uncertainty. The ground motions developed using Approach 3 are also used for design analyses.

A key aspect of Approach 3 is that it facilitates averaging the results of different cases that represent epistemic uncertainty in site-response model inputs. With Approach 2B, site-specific response spectra or site-response transfer functions for different cases are enveloped. The enveloping is carried out without regard to the assessed relative likelihood that the different cases reflect the true nature of the site. With Approach 3, the site response results for different cases yield a set of hazard curves. The probabilities of the ground motions for the different cases can thus be averaged, using weights that reflect assessments of their relative likelihood, if appropriate, to produce the final site-specific hazard. To develop ground motions for probabilistic preclosure seismic safety analyses, it was decided to move beyond the possible conservatism of enveloping and to use the approach that facilitates appropriate weighting of cases representing epistemic uncertainty (BSC 2008, Sections 6.1.3 and 6.4.5).

2.3.4.3.2.1 Conceptual Approach

The site-response model for Yucca Mountain addresses seismic wave propagation through the site materials and takes dynamic behavior of those materials into account (BSC 2004b, Section 6). Key inputs to the model consist of earthquake response spectra derived from the PSHA hazard results, profiles of seismic velocity as a function of depth, and curves that represent the dynamic properties of the site materials as a function of shear strain. At higher levels of ground motion, strains induced in the site materials alter the shear modulus and damping properties of the material, which in turn affect ground motion propagation.

The response of the site materials is modeled using a one-dimensional equivalent-linear formulation (BSC 2004b, Section 6.1.1). That is, nonlinear behavior of the site materials under ground motion loading is approximated with a linear equation over a limited range of its variables. The effective strain produced in the site materials by the ground motion is used to adjust the material dynamic properties, and the process is iterated to achieve a solution that is compatible with the induced strains. Random vibration theory is used to determine peak strains from which the effective strains are calculated. Thus, the site-response model is referred to as a random vibration theory–based equivalent-linear model.

The site-response approach aims to produce a location-specific response spectrum that preserves the annual probability of exceedance corresponding to the input ground motion derived from the PSHA. To reach this goal, uncertainty and variability in site material properties are taken into account (McGuire et al. 2001, Section 6). Uncertainty and variability in the ground motion that forms the basis for input into the site-response model are accounted for in the PSHA process; for postclosure analyses they are incorporated into the site-response modeling through use of mean hazard results (BSC 2004b, Section 6.2.2.7). Also, because the degree of nonlinear behavior of site materials depends on the shape and amplitude of an earthquake's response spectrum, which depends on magnitude, the site-response approach also takes into account the range of magnitudes contributing to the ground motion hazard at a particular annual probability of exceedance (McGuire et al. 2001, Section 6.1). This approach is labeled Approach 2B in NUREG/CR-6728.

Implementation of this site-response approach consists of nine steps, which are carried out for each combination of annual exceedance probability and location of interest. The steps are listed here and discussed in more detail in Sections 2.3.4.3.2.2 and 2.3.4.3.2.3:

1. For the given annual probability of exceedance, response spectral acceleration values are taken from the mean PSHA hazard curves for frequencies of 0.3, 0.5, 1, 2, 5, 10, 20, and 100 Hz (peak ground acceleration). These spectral acceleration values are plotted as a function of frequency to produce a mean uniform hazard spectrum for the PSHA reference rock outcrop (BSC 2004b, Section 6.2.2.3).

2. Based on an analysis of which earthquake magnitudes and distances contribute to the probabilistic ground motion hazard (deaggregation), earthquakes (magnitude and distance combinations) are identified from the PSHA results to form input to the site-response model. PSHA response spectral acceleration results are deaggregated for both a high (5 to 10 Hz) and low (1 to 2 Hz) frequency range; three earthquakes are determined for each frequency range to represent the range of magnitudes (mean,

5th, and 95th percentile) contributing to the hazard. Response spectra for the six earthquakes are scaled to the uniform hazard spectrum in the high or low frequency range, as appropriate, to maintain consistency with the PSHA annual probability of exceedance. These earthquakes are referred to as deaggregation earthquakes (BSC 2004b, Section 6.2.2.5).

3. Deaggregation of the PSHA response spectral acceleration results for the high (5 to 10 Hz) and low (1 to 2 Hz) frequency ranges is also used to identify reference earthquakes representing the most likely magnitude and distance combination contributing to the hazard (BSC 2004b, Section 6.2.2.4). Response spectra for the reference earthquakes are scaled to the uniform hazard spectrum in the appropriate frequency range to maintain consistency with the PSHA annual probability of exceedance. Deaggregation earthquakes and reference earthquakes are similar in that both are derived from the deaggregation of the probabilistic seismic hazard results. Both are also determined for a high (5 to 10 Hz) and low (1 to 2 Hz) frequency range to account for the different magnitude and distance characteristics of earthquakes contributing to ground motion hazard as a function of frequency. They differ in that deaggregation earthquakes incorporate a representation of the range of magnitudes contributing to hazard for a given frequency range, not just the most likely magnitude (as for the reference earthquakes). This additional factor is included in determining the site-response transfer function because the nonlinear behavior of the site materials can vary as a function of magnitude. As magnitude varies, the response spectral shape of the ground motion varies. Thus, to maintain consistency with the hazard level of the control motion, magnitude dependency is addressed in the control motions (deaggregation earthquakes) that serve as input to the site-response modeling. Transfer functions representing the site response are applied to the envelope of the reference earthquake response spectra and the uniform hazard spectrum to determine the final site-specific response spectra (Step 8). The envelope is determined by selecting, at each response structural frequency, the largest spectral acceleration value from the two reference earthquake response spectra and the uniform hazard spectrum.

4. Site-specific rock properties are characterized on the basis of geotechnical information and form an input to the site-response model. Uncertainties in the average rock properties, as well as variation in those properties across the site, are determined and incorporated into the site-response modeling for each deaggregation earthquake (BSC 2004b, Sections 6.2.3 and 6.2.4).

5. The site-response model is run for appropriate combinations of rock properties, seismic wave type, incidence angle, frequency range, and deaggregation earthquake, depending on the location and ground motion component being analyzed (BSC 2004b, Section 6.3.1). A mean spectral transfer function (also called a spectral amplification function) representing the ratio of the model output response spectrum to the response spectrum for the input deaggregation earthquake is determined for each combination. A mean PGV scaling factor, representing the ratio of the model output PGV to the input PGV, is also determined.

6. The site-response effects for the deaggregation earthquakes are combined in a weighted average. The deaggregation earthquake associated with the mean magnitude is given the most weight; those associated with the 5th and 95th percentile of the magnitude range receive lower weights. This step incorporates the effect of magnitude on the dynamic behavior of the site materials, taking into account the weighted range of magnitudes contributing to a ground motion level for a given annual probability of exceedance (BSC 2004b, Section 6.3.1).

7. For each combination of rock properties and seismic wave type, the weighted average transfer functions (or PGV scaling factors) for the high and low frequency ranges are enveloped. This step combines the effects on ground motion for high and low frequency ranges (BSC 2004b, Section 6.3.1).

8. For each combination of rock properties and seismic wave type, the envelope of the transfer functions (or PGV scaling factor) is applied to the envelope of the reference earthquake response spectra and uniform hazard spectrum (or reference rock outcrop PGVs) representing the PSHA ground motions. This step produces location-specific response spectra (i.e., for the surface facilities area or at the depth of the waste emplacement level) that incorporate the site response for each combination of rock properties and wave type (BSC 2004b, Section 6.3.1).

9. A final envelope is taken over the location-specific response spectra (or peak ground velocities) for the combinations of rock properties and wave type. This step incorporates the effects on location-specific ground motion of the uncertainty in site material properties (BSC 2004b, Section 6.3.1).

Time histories for kinematic and dynamic structural analyses are developed based on the results of the site-response modeling for the repository waste emplacement level. For a given annual probability of exceedance, strong ground motion recordings are scaled by the location-specific peak horizontal ground velocity. Scaling is carried out such that inter-component variability is preserved (BSC 2004b, Section 6.3.2.3).

2.3.4.3.2.2 Ground Motion Data and Data Uncertainty

The purpose of the PSHA process is to integrate the knowledge of experts and their assessment of uncertainty and variability into a definition of the likelihood of exceeding various levels of ground motions at the site. This process provides the range of uncertainty in the resulting ground motions. Inputs to the site-response model consist of earthquake response spectra derived from the mean PSHA hazard curves, one-dimensional profiles of seismic velocity as a function of depth, curves representing the variation with shear strain of shear modulus (normalized to its low-strain value) and material damping, the angle at which seismic waves impinge on the base of the rock and soil layers representing the site materials, and site material densities. The use of data to develop these inputs and the treatment of data uncertainties are as follows:

Control Motion Data—The ground motion determined at the reference rock outcrop (defined from the PSHA process) subsequently serves as input to the site-response analysis and is referred to as the control motion. For postclosure ground motions at Yucca Mountain, the control motion is

derived from the mean PSHA results. For a given annual probability of exceedance, the PSHA results are characterized by a uniform hazard spectrum. For input to the site-response model, deaggregation earthquakes are defined to represent the uniform hazard spectrum. This section describes development of the uniform hazard spectrum and corresponding deaggregation earthquakes based on the mean PSHA results (BSC 2004b, Section 6.2.2).

The PSHA determined, for a range of oscillator frequencies, the annual probability with which various levels of response spectral acceleration would be exceeded. To characterize the overall results for a given annual probability of exceedance, the response spectral accelerations with that annual probability of exceedance are plotted as a function of oscillator frequency to produce a uniform hazard spectrum. Given the nature of a PSHA, the uniform hazard spectrum does not represent the response spectrum of a single earthquake but rather represents the integrated contributions of the range of earthquakes that contribute to hazard at the Yucca Mountain site as expressed in the PSHA seismic source interpretations. The uniform hazard spectrum is thus a broadband representation of the ground motion for a given annual probability of exceedance (BSC 2004b, Section 6.2.2).

The use of such a broadband motion, which reflects contributions from earthquakes of varying magnitudes and distances, is inappropriate for site-response analysis. When the amplitudes of control motions cause significant nonlinear response of the site materials, broadband spectra can induce higher strains than any single earthquake scaled to the same peak acceleration level and thus perturb the calculated site response (BSC 2004b, Section 6.3.1.1.1). Accordingly, deaggregation earthquakes were developed whose individual response spectra represent the uniform hazard spectrum and are used as input to the site-response analysis (BSC 2004b, Section 6.2.2.5). Deaggregation earthquakes were developed for two response spectra frequency ranges, 5 to 10 Hz and 1 to 2 Hz, to account for differences in magnitudes and distances of earthquakes contributing to ground motion hazard in these frequency ranges. The choice of these frequency ranges conforms with guidance provided in NRC Regulatory Guide 1.165, Appendix C. Regulatory Guide 1.165 specified frequency ranges of 1 to 2.5 Hz and 5 to 10 Hz. Here, a range of 1 to 2 Hz is used for the lower range because the PSHA for Yucca Mountain determined ground motion hazard for a response spectral frequency of 2 Hz, not 2.5 Hz (BSC 2004b, Section 6.2.2).

Nonlinear behavior of site materials, which contributes to the ground motion site response, depends on earthquake magnitude as well as ground motion amplitude. As magnitude increases, the response spectral shape of the ground motion changes, and the duration and amplitude of strong ground shaking typically increases. To obtain site-specific ground motion that is consistent in probability with the control location hazard, these effects are captured in the site-response analysis through the use of deaggregation earthquakes (McGuire et al. 2001, Section 6.1; BSC 2004b, Section 6.2.2.5).

The deaggregation earthquakes are developed for the purpose of computing site-response transfer functions by deaggregating the ground motion hazard for a given annual exceedance probability and frequency range (5 to 10 Hz or 1 to 2 Hz). To represent the range of magnitudes contributing to the hazard for a given annual exceedance probability, three earthquakes are identified corresponding nominally to the mean and the 5th and 95th percentiles of the magnitude distribution contributing to hazard at a particular mean annual probability of exceedance. In some cases, different percentiles and associated weights were used to better capture the magnitude distribution resulting from the deaggregation (BSC 2004b, Section 6.2.2.5, Table 6.2-8). Response spectra for the deaggregation

earthquakes, determined from the ground motion relations for Yucca Mountain developed as part of the PSHA, are scaled to the uniform hazard spectrum in the appropriate frequency range (Figure 2.3.4-5). This scaling retains hazard consistency with the site uniform hazard spectrum by ensuring the deaggregation earthquake response spectra match the spectral acceleration level of the uniform hazard spectrum for the appropriate structural frequency range. The deaggregation earthquakes form the control motion for the site-response analysis. With three deaggregation earthquakes for each of two frequency ranges (5 to 10 Hz and 1 to 2 Hz) and two components of ground motion (horizontal and vertical), a total of 12 different control motions are involved in determining the ground motion site-response transfer functions (BSC 2004b, Section 6.2.2.5).

Similar to the process for deaggregation earthquakes, reference earthquakes representing the uniform hazard spectrum are also developed for specific annual probabilities of exceedance on the basis of deaggregation of the PSHA results. Transfer functions determined from the site-response modeling are applied to the envelope of the uniform hazard spectrum and the response spectra for the reference earthquakes to produce location-specific response spectra incorporating the effects of the site response. As for deaggregation earthquakes, reference earthquakes are determined for both a high (5 to 10 Hz) and low (1 to 2 Hz) frequency range. Based on the deaggregation results, a reference earthquake is identified for each frequency range by taking the modal magnitude and distance (BSC 2004b, Section 6.2.2.4). The response spectral shape for these earthquakes, determined from the PSHA ground motion relations, are then scaled to match the uniform hazard spectrum for the low and high frequency range, as appropriate. The scaled reference earthquake response spectra are then compared to the uniform hazard spectrum to ensure that, considered together, they adequately represent it. Development of reference earthquakes is based on guidance in NRC Regulatory Guide 1.165, Appendix C.

Reference earthquakes are identified for both the horizontal and vertical component of ground motion. Reference earthquakes for vertical motion were taken to be the same as those for horizontal motion.

Revised Vertical Spectra and Vertical Peak Ground Velocity—Examination of vertical uniform hazard spectra determined from the PSHA results reveals characteristics that are inconsistent with trends observed in recent worldwide data (BSC 2004b, Section 6.2.2.6). First, for a given annual exceedance probability, the horizontal and vertical uniform hazard spectra, determined from the PSHA, both peak at approximately the same frequency. This is in contrast to empirical observations and numerical modeling that indicate the peak of the vertical spectrum should be shifted to higher frequencies relative to the horizontal spectrum for earthquakes such as those that dominate the hazard at Yucca Mountain. Second, vertical-to-horizontal spectral ratios do not increase significantly at higher oscillator frequencies with decreasing annual probabilities of exceedance. This observation is counter to the trends seen in the empirical data in which closer, larger earthquakes (corresponding generally to lower rates of exceedance) exhibit larger vertical motions relative to horizontal motions at higher frequencies. Finally, the vertical uniform hazard spectra exhibit a dip at about a frequency of 1 Hz, which is not seen in observed spectral shapes. The expression of this dip appears to get stronger at lower annual exceedance probabilities. Thus, the vertical uniform hazard spectra derived from the PSHA for Yucca Mountain are inconsistent with empirical observations and with recent developments in understanding the factors that drive vertical-to-horizontal spectral ratios.

To address this issue, an alternative approach is employed to develop vertical spectra for the PSHA reference rock outcrop that are used in developing location-specific response spectra (BSC 2004b, Section 6.2.2.6.3). This approach follows recommendations in NUREG/CR-6728 (McGuire et al. 2001, Section 4.7). First, a vertical-to-horizontal response spectral ratio is determined for Yucca Mountain site conditions based on earthquake observations and results of numerical modeling (McGuire et al. 2001, Section 4.7). This site-specific ratio is then applied to the envelope of the uniform hazard spectrum and the reference earthquake response spectra for horizontal ground motion for given hazard levels to obtain the corresponding envelope spectrum for vertical ground motion (Figure 2.3.4-6).

Control Motion Data Uncertainty—Because they are derived from the mean PSHA results, the control motions reflect the uncertainties and variability incorporated in the PSHA through the expert elicitation process. For annual probabilities of exceedance between about 10^{-6} and 10^{-8}, mean hazard results lie between about the 85th and 95th percentiles of the overall results (Figure 2.3.4-7).

PSHA ground motion experts characterized median ground motion, its random variability, and the epistemic uncertainty in both. Variability was characterized with an unbounded lognormal distribution. Using these assessments of ground motion and its uncertainty, as lower and lower annual probabilities of exceedance are considered, associated ground motion levels continue to increase, eventually reaching levels that are inconsistent with the geologic setting. These ground motions are used in developing seismic time histories for postclosure structural response analyses. However, as discussed in Section 2.3.4.3.3, constraints on the level of ground motion that is consistent with the geologic setting at Yucca Mountain are used to condition the mean annual probability of exceedance associated with a given level of ground motion (BSC 2008, Appendix A, Section A1).

The U.S. Nuclear Waste Technical Review Board has commented on the very-low-probability ground motions determined for Yucca Mountain (Corradini 2003). They found the ground motions for annual probabilities of exceedance less than 10^{-6} to be "generally unrealistic, physically unrealizable, or outside the limits of existing worldwide seismic records or experience…" They recommended that the DOE continue its studies to bound very-low-probability ground motions on the basis of sound physical principles. Analyses that establish a bound to low-probability peak horizontal ground velocity are described in Section 2.3.4.3.3. On the basis of this work, TSPA sampling of the hazard curve for peak horizontal ground velocity at the waste emplacement level is constrained to credible values consistent with 10 CFR 63.102(j).

Material Dynamic Properties Data—Dynamic properties of the site materials form another set of inputs to the site-response model. These properties are:

- Seismic velocity as a function of depth
- Shear modulus, normalized to its small-strain value, as a function of shearing strain
- Material damping, as a function of shearing strain.

Shear modulus reduction and variation in material damping as a function of shear strain are parameters that characterize the response of site materials to dynamic strains caused by seismic wave propagation through them.

Geotechnical investigations have been carried out to help characterize these inputs. Results of the investigations are used along with other information and scientific judgment to determine parameter values and assess uncertainties. In addition, the properties vary about their geometric mean values when the spatial extent of a location of interest is considered. To determine site-specific ground motion that is consistent with the control location hazard, these uncertainties and variability are incorporated into the site-response analysis, just as uncertainties and variability were explicitly incorporated in the PSHA (BSC 2004b, Sections 6.2.2, 6.2.3.5, and 6.2.4.4).

Geotechnical Investigations—Geotechnical investigations have been carried out to collect information on the material properties of the site (BSC 2002; BSC 2004b, Sections 6.2.3 and 6.2.4). The studies focused on the two primary sites of interest: the surface facilities area and the area above the planned waste emplacement footprint. The surface facilities area is of interest for preclosure design; the area above the waste emplacement area is characterized to allow determination of subsurface ground motion for analyses supporting both preclosure design and postclosure performance assessment. Studies consisted of drilling and logging boreholes, velocity surveys, and laboratory testing of rock and soil samples to determine the dynamic response properties of the materials (i.e., the shear modulus and damping behavior as a function of imposed dynamic shear strain level). The discussion here focuses on the investigations to characterize the repository block to support postclosure analyses. Section 1.1.5.3 describes geotechnical investigations used to support preclosure analyses. For postclosure ground motion studies, the goal is to characterize the rock mass properties, including effects of fractures and features such as lithophysae (i.e., void spaces within the rock mass).

Subsequent to the development of ground motions used in postclosure analyses, additional geotechnical investigations were carried out (SNL 2008). Updated calculations of site-specific peak horizontal ground velocity that take into account the additional geotechnical information, and which also implement Approach 3 of NUREG/CR-6728 and incorporate constraints on extreme ground motion, result in lower mean annual probabilities of exceedance at the waste emplacement level for a given level of PGV (BSC 2008, Section 6.5.3.2). As described in Sections 2.3.4.4 and 2.3.4.5, postclosure seismic analyses are carried out with the ground motions based on earlier geotechnical data and the use of Approach 2B of NUREG/CR-6728. As described in Section 2.3.4.3.3.5, comparison of response spectra and seismic hazard determined using the two approaches indicates that these results provide a reasonable representation of the range of ground motions that might occur following closure of the repository and are appropriate for their intended use in evaluating seismic response of the EBS.

The following discussion describes the geotechnical data that form part of the technical basis underlying the ground motions used in postclosure analyses. A discussion of results from the additional geotechnical investigations is found in Section 1.1.5.3.

For the repository block (i.e., the block of rock containing the waste emplacement area at a depth of about 300 m below the ground surface), velocity data were obtained from existing boreholes both within and near the repository block to assess its velocity characteristics (BSC 2004b, Section 6.2.3.2). Borehole velocity data extend to depths ranging from about 1,000 ft to almost 2,600 ft for boreholes outside the repository block. Data surveys utilizing boreholes within the repository block were collected at depths ranging from about 25 to 180 ft. Spectral analyses of surface wave surveys were also used to determine velocities. Results of these analyses provide

velocity estimates for depths in the range from near surface to about 750 ft. As described below, development of velocity profiles and their use in site-response modeling take into account uncertainties resulting from the varying density of coverage.

In addition to the spectral analysis of surface wave surveys carried out at the surface of the repository block, the technique of spectral analysis of surface waves was applied within the main drift of the Exploratory Studies Facility (ESF) (BSC 2004b, Section 6.2.3.2.4). These measurements provide information on the velocity of the repository block at depths (980 to 1,150 ft) greater than those sampled using the spectral analysis of surface waves technique at the surface.

To characterize the normalized shear modulus reduction and damping properties of the repository block, laboratory testing was carried out on rock samples (BSC 2002, Section 6.2.10 and 6.3.3). Resonant column and torsional shear tests were performed to examine the nonlinear behavior of the materials as a function of shearing strain. Tested samples were from the Tiva Canyon Tuff, which has properties similar to those of the Topopah Spring Tuff that comprises the repository host horizon. Testing was carried out on right-cylindrical samples with diameters ranging from 2.11 to 3.97 cm. Testing was carried out at shear strains up to about 0.1%.

Material Dynamic Properties Data Uncertainty—Based on the results of the geotechnical investigations, other technical information, and scientific judgment, inputs to the site-response model were developed (BSC 2004b, Sections 6.2.3 and 6.2.4). The inputs reflect uncertainties in the velocity profile, material dynamic properties, and ground motion incidence angle data, as follows:

- **Velocity**—Results of the geotechnical investigations form the basis for developing base-case velocity profiles (compressional-wave and shear-wave) for the repository block (BSC 2004b, Section 6.2.3). Results of velocity surveys in deeper boreholes located near but outside the waste emplacement area, results from shallower boreholes, and results from spectral analysis of surface wave surveys indicate uncertainty in the base-case velocity profile. In addition, the density of sampling of the repository block varies spatially. To represent these uncertainties, two base-case profiles are developed and carried through the site-response analysis (Figure 2.3.4-8). The base case 1 profile is based on results from spectral analysis of surface wave profiles and from velocity measurements in shallow boreholes within the repository block. The base case 2 profile is based on velocity survey results in deeper boreholes near, but outside, the waste emplacement area. The base case 2 profile also includes an adjustment to higher velocities to account for variation in the spatial density of measurements. Results of spectral analyses of surface waves from the ESF provide the basis for the repository block velocity at a depth of about 300 m (1000 ft).

  In addition to uncertainty in the base-case velocity profile, which is addressed by developing two profiles for repository block tuff, there is also variability in velocities across the site. To incorporate this variability in the site-response modeling, each base-case profile is used as the basis to stochastically generate a suite of 60 profiles that serve as input to the site-response model. The probabilistic representation of velocity profiles consists of three elements. The first element consists of a probabilistic description of velocity layer thicknesses for the ensemble of profiles. The second element is the

median velocity profile. Although each profile consists of discrete constant-velocity layers, the median profile is smooth as if the layer boundaries are randomly located. The third element is a probabilistic description of the deviations of the velocity at the mid-point of each layer from the median and its correlation with the velocity in the layer above. The standard deviation is treated as a function of depth. Correlation between layer velocities and thicknesses is based on an analysis of the available velocity data and is site-specific. For the repository block, the logarithmic standard deviation varies from 0.36 at shallow depths to 0.20 at deeper depths (BSC 2004b, Section 6.2.3.6). For each of the stochastically generated profiles, the depth of the profile is also varied using a uniform distribution from about 200 to 450 m for the repository block. A uniform distribution is used to approximate the actual distribution of overburden thickness for the waste emplacement area. This variation accounts for the range in overburden thickness above the waste emplacement area and in the depth at which the velocity reaches the value for the reference rock outcrop from the PSHA.

Velocity data for the repository block, collected after the development of profiles used to develop ground motions for postclosure analyses, consist of additional spectral analysis of surface wave surveys (SNL 2008, Sections 6.2.5, 6.3.2, and 6.4.3). These surveys increased the spatial coverage of the repository block and used a more energetic source that allowed velocities to be determined to greater depths. Additional spectral analysis of surface wave surveys were also carried out in the ESF. When considered with the preexisting data, these additional data continue to indicate that two base case velocity profiles are appropriate to characterize the repository block. This was determined by compiling the individual velocity profiles and observing that the profiles tended to fall into two groups depending on the geographic location at which the data were acquired.

The updated profiles differ somewhat from those used in developing the ground motions for postclosure analyses (BSC 2008, Section 6.4.2.7). In particular, they reach a shear-wave velocity corresponding to the PSHA reference rock outcrop conditions at a greater depth. The PSHA reference rock outcrop conditions are interpreted to occur at the top of the Prow Pass unit beneath the Calico Hills and Topopah Spring Tuff formations. While shear-wave velocities reach those associated with the PSHA reference rock outcrop at shallower depths for one of the base-case profiles, the velocity then decreases with depth before increasing again back to the PSHA reference rock outcrop conditions (Section 1.1.5). Ground motion calculations for the waste emplacement level using the updated velocity profiles, as well as Approach 3 of NUREG/CR-6728 to address site-response and incorporating a reasonable bound to extreme ground motion at Yucca Mountain, result in lower mean annual probabilities of exceedance for the PGV levels used in postclosure analyses (BSC 2008, Section 6.5.3.2, Figure 6.5.3-17) (Section 2.3.4.3.3.5).

- **Shear-Modulus Reduction and Material Damping**—As ground motion increases and produces larger shear strains in the site materials, nonlinear behavior can take place. In the site-response computations, this nonlinear behavior is accounted for through changes in shear modulus and material damping. Laboratory testing provides information on such behavior for Yucca Mountain site materials, but because of the scale of samples tested, there is uncertainty in how these results relate to in situ rock mass properties. Consistent

with standard practice, data on shear modulus reduction and material damping were obtained using dynamic laboratory torsion testing on small core samples. These samples may not contain macroscopic fractures and voids that characterize the rock mass (BSC 2002, Section 6.2.10.2).

To accommodate this uncertainty in mean normalized shear-modulus reduction and material damping curves for tuff, two sets of base-case curves were developed (Figure 2.3.4-9) (BSC 2004b, Section 6.2.4.2). One set of curves (Base Case 1) represents the case in which in situ conditions consist of relatively unfractured rock. The laboratory testing data serve directly as part of the basis for this set of curves. The second set (Base Case 2) was developed to represent in situ conditions that reflect fracturing and heterogeneity, the effects of which are not captured in laboratory testing. Scientific reasoning and judgment were used to establish this set of curves, taking into account observed differences between laboratory and in situ measurements of seismic velocity. The shapes of the curves are based on the shape of generic curves for a cohesionless soil (EPRI 1993, Section 7.A.5). This shape also provides the basis for extending the curves beyond the site-specific laboratory testing data. The sets of curves for tuff are taken to apply to tuff units modeled. The site-response model is run for each of these base-case sets of dynamic property curves.

In addition to uncertainty in the mean dynamic property curves, variability about the mean curves is also accommodated in the site-response analysis. This variability reflects the random spatial variation of material properties across the site. As for the velocity profiles, the variability is taken into account by stochastically generating 60 sets of dynamic property curves for each base-case curve and using those stochastically generated curves in the analysis. The curves are allowed to vary between lower and upper bounds at $\pm 2\sigma$, assuming a lognormal distribution and a $\sigma(\ln)$ of 0.3. The distribution is empirical, based on examining series of laboratory dynamic test results on materials comprising the same geologic unit. The variability is taken to reflect within unit randomness (BSC 2004b, Section 6.2.4.4).

Dynamic property data for tuff, collected after the development of the dynamic property curves used to develop ground motions for postclosure analyses, consist of additional torsion testing results (SNL 2008, Section 6.5.2). These tests expanded the range of lithostratigraphic units that were tested. The tests, however, were carried out on similar size samples as the previous testing and thus do not reduce the uncertainty related to how well laboratory results represent in situ conditions. Therefore, when considering the combined data set, two sets of base-case curves are still deemed appropriate to represent the uncertainty in site dynamic material properties.

Updated sets of curves differ from those used in developing the ground motions for postclosure analyses only in that the effect of depth (confinement pressure) on the properties is taken into account (BSC 2008, Section 6.4.4). Ground motion calculations for the waste emplacement level, using the dynamic property curves that vary with depth (Section 1.1.5), as well as Approach 3 of NUREG/CR-6728 to address site-response and incorporating constraints on extreme ground motion at Yucca Mountain, result in lower

mean annual probabilities of exceedance for given levels of PGV when compared to those used for postclosure analyses (BSC 2008, Section 6.5.3.2, Figure 6.5.3-17).

- **Ground Motion Incidence Angle Data**—The incidence angle at which the control motion impinges on the site model is another input to the model. For each deaggregation earthquake, the angle of incidence is calculated based on its distance from Yucca Mountain, its depth (i.e., 7.5 km for an earthquake with magnitude greater than 5.5; otherwise, 5.0 km), and a depth profile for regional seismic velocities. Values of earthquake depth used in the incidence angle calculations are based on observations of seismicity in the western United States (BSC 2004b, Section 6.2.2.5.1).

- **Ground Motion Incidence Angle Data Uncertainty**—Uncertainty in the incidence angle of the control motion is incorporated in the modeling in two ways: (1) the velocity of the lowermost layer in the site model is stochastically varied independent of the other layers, which stochastically varies the incidence angle around its calculated value; (2) in addition to determining site response for inclined incident seismic rays, the site response is also calculated for a vertically incident ray. Final site-response results are determined by enveloping over the results for inclined and vertically incident rays (BSC 2004b, Section 6.2.2.5.1).

- **Material Density Data**—In addition to seismic velocities, material dynamic properties, and incidence angles, densities are required for input into the site-response model. Based on data for the Topopah Spring Tuff, a value of 2.2 g/cm^3 was adopted for site-response modeling (BSC 2004b, Section 6.2.3.7).

- **Material Density Data Uncertainty**—Ground motions computed from the site-response model are not very sensitive to densities. Thus, a constant density was used for the repository block (BSC 2004b, Section 6.2.3.7).

2.3.4.3.2.3 Ground Motion Site-Response Model and Model Uncertainty

The site-response model for Yucca Mountain treats seismic wave propagation through the site materials and takes into account dynamic behavior of those materials. In an elastic system, seismic wave amplitudes generally increase near the surface in response to a decrease in material velocity. However, this effect can be attenuated by material damping in the layers. Resonance can also occur in soil and rock layers and between the surface and the soil–bedrock interface and is strongly affected by material damping. To develop site-specific ground motions that include these effects, a site-response model is employed (BSC 2004b, Section 6).

Observations of seismic ground motion from sites around the world provide evidence of nonlinear behavior for the horizontal component of motion, while vertical ground motion generally shows linear behavior (BSC 2004b, Section 6.3.1.1.2). In modeling site response at Yucca Mountain, nonlinear effects are included for horizontal motion, and vertical motion is modeled in a linear fashion (BSC 2004b, Sections 6.1.9 to 6.1.11).

To propagate seismic energy through the site materials, plane-wave propagator matrices are used (Silva 1976). Silva (1976) extended the Haskell-Thompson matrix method to include the effect of

an elasticity in an exact fashion. The methodology incorporates any number of layers and treats P-SV (compression and vertically polarized shear) and SH (horizontally polarized shear) plane waves at arbitrary incidence angles. Damping is incorporated in each layer without approximation (BSC 2004b, Section 6.1.8).

Inputs to the site-response model consist of ground motions derived from the PSHA results, and material dynamic properties developed from site-specific geotechnical data, technical information, and scientific judgment (BSC 2004b, Section 6.2.4.4). Because site-response modeling was decoupled from the PSHA, PSHA ground motion results for Yucca Mountain do not include effects of the upper rock and soil layers. The site-response model was used to modify PSHA ground motions to account for the particular geologic conditions in the upper rock and soil layers. Results of the site-response modeling are then used to develop time histories for postclosure analyses (BSC 2004b, Section 6.3.2).

The computational method that is used for site-response modeling incorporates nonlinear soil and rock behavior using an equivalent-linear formulation. The equivalent-linear method is common in earthquake engineering for modeling the transmission of seismic waves through layered soil and rock sites. In this method, a linear analysis is performed with initial material properties (damping ratio and shear modulus) of the site rock and soil units defined from available geotechnical information. Representation of nonlinear material response is achieved by iterative adjustment of the material properties so that a piecewise-linear approximation can be made to nonlinear soil and rock stress–strain response (BSC 2004b, Section 6.1). The iterative procedure used is described below.

During an analysis, the maximum cyclic shear strain is recorded for each element in the model and is used to determine new or adjusted values for damping and shear modulus by reference to site-specific curves that relate damping ratio and shear modulus to amplitude of cyclic shear strain. The adjusted values of damping ratio and shear modulus are then used to conduct a new analysis. This process is iterated until changes in the material parameters are below an established tolerance level. At this point, "strain-compatible" values of damping and modulus have been defined, and the simulation using these values is representative of the response of the site (BSC 2004b, Section 6.1.1). Implementation of the approach for Yucca Mountain uses random vibration theory to determine the peak strains for each iteration. Thus, the model is referred to as the random vibration theory–based equivalent-linear site-response model.

In the model, site materials are represented as a one-dimensional layered system for the purpose of site-response computation. A series of horizontal layers, each of which is characterized by a constant velocity, density, and set of dynamic material properties, approximate the site materials. For the equivalent-linear formulation, dynamic material properties consist of curves describing how the shear modulus (normalized to its value at low strain) and material damping vary as a function of shearing strain. As nonlinear material behavior occurs with increasing shearing strain, the shear modulus decreases (the material becomes less rigid) and material damping increases (BSC 2004b, Sections 6.1, 6.2.4, and 7.1).

One-dimensional site-response analysis, using an equivalent-linear formulation, has proved successful when applied elsewhere (e.g., EPRI 1993). In a generic validation study, the random vibration theory–based equivalent-linear model was compared to three nonlinear models for three

test cases. For each test case, ground motion was recorded at a soil site and a nearby rock site. The recorded rock motions were used as the input to the site-response models, and modeling results were compared to the recorded soil site motions (BSC 2004b, Section 7.6). Each of the sites was characterized in terms of its velocities and dynamic material properties. Results of this validation study show little difference between equivalent-linear and fully nonlinear formulations for the ground motion levels examined (peak ground accelerations between about 0.05 and 0.5 g). Both equivalent-linear and nonlinear formulations also compared favorably to the recorded motions. This is especially true with respect to 5% damped response spectra, which, along with PGV, are the outputs of site response modeling used to develop artificial seismograms (time histories) for postclosure kinematic and structural response calculations. This generic validation study provides confidence that the modeling approach captures nonlinear dynamic behavior for the purpose of this analysis (BSC 2004b, Section 7.3.2).

To increase confidence in the site-response model for induced levels of shear strain that may occur at Yucca Mountain, the preexisting validation study was expanded to analyze a site at which high ground-motion-induced strains occurred. Agreement among the equivalent-linear and nonlinear models, and with the data, was comparable to the other test cases (BSC 2004b, Section 7.3.5).

Model Implementation—In the overall approach to develop seismic inputs for postclosure analyses, the role of the site-response model is to determine transfer functions for response spectra and scaling factors for PGV. Site response can be thought of as a transfer function that transposes ground motion from the PSHA reference rock outcrop (the control location) to ground motion at a specific location for which seismic inputs are needed for design or performance assessment. For earthquake response spectra, the transfer function describes the amplification or reduction of the control motion response spectrum (i.e., the response spectrum at the reference rock outcrop) as a function of frequency and is referred to as a spectral amplification function. For PGV, the transfer function consists of a single scaling value. The following discussion describes the approach for determining response spectra and PGV transfer functions for Yucca Mountain that result in location-specific ground motion that is consistent with the seismic hazard results for the control location (BSC 2004b, Section 6.3.1.1.2).

The random-vibration-theory-based equivalent-linear site-response model is used in conjunction with Approach 2B of NUREG/CR-6728 to determine ground motion inputs that have a probability of exceedance consistent with that of the input control motion (BSC 2004b, Sections 6.2.1 and 8). The following discussion describes the implementation of Approach 2B. For preclosure probabilistic seismic safety analyses and design analyses, an alternate approach is used to develop ground motion inputs (BSC 2008, Section 6.1). Implementation of this alternate approach—Approach 3 of NUREG/CR-6728—is described in Section 1.1.5.

To determine the response spectrum transfer function using Approach 2B for a given annual probability of exceedance, the model is used to calculate the site response for each of the 12 deaggregation earthquakes (low-, mean-, and high-magnitude earthquakes for frequency ranges of 1 to 2 Hz and 5 to 10 Hz and for horizontal and vertical components of ground motion). For each deaggregation earthquake (control motion), the site-response calculation is carried out for velocity profiles and sets of dynamic property curves that are stochastically generated from the base-case profiles and sets of curves. For locations where multiple base-case profiles or sets of curves were developed to represent uncertainty, the process is carried out for each combination of base-case

inputs. In addition, the process is carried out for the different seismic wave types that are considered. For horizontal motion, these consist of inclined and vertically incident horizontally polarized shear waves and vertically polarized shear waves. For vertical motion, the wave types are inclined and vertically incident compression waves and inclined shear waves. Thus, site-response calculations are carried out for appropriate combinations of deaggregation earthquake, base-case velocity profile, dynamic material property curves, and wave type (BSC 2004b, Section 6.3.1).

The result of each calculation is a response spectrum that reflects how the input motion response spectrum and PGV are modified by the site materials. For each combination of deaggregation earthquake, base-case velocity profile, dynamic material property curves, and wave type, the mean of the resulting response spectra for the 60 stochastically varied profiles and curves is taken. This mean computed response spectrum is then divided by the corresponding input deaggregation earthquake response spectrum to produce a spectral amplification function. The spectral amplification function shows how the control motion response spectrum was modified by the site response as a function of oscillator frequency. It includes the effects of variability in site material properties (BSC 2004b, Section 6.3.1).

Then, for each combination of base-case velocity profile, dynamic material property curves, and wave type, a weighted mean of the spectral amplification functions for the three deaggregation earthquakes corresponding to a given frequency range (1 to 2 Hz or 5 to 10 Hz) is computed. Most weight is given to the mean deaggregation earthquake, with lower weight given to the low and high-magnitude deaggregation earthquakes. The result of this step is a set of transfer functions for each of the two frequency ranges and ground motion components, corresponding to each combination of base-case velocity profile, dynamic property curves, and wave type. These weighted mean transfer functions include any earthquake magnitude- and amplitude-dependent effects on the dynamic response of site materials (BSC 2004b, Sections 6.2.2.5 and 6.3.1).

Next, for each combination of ground motion component, base-case velocity profile, dynamic material property curves, and wave type, the weighted mean transfer functions for the high and low oscillator frequency range are enveloped. For horizontal ground motion, the resulting transfer functions are applied to the envelope of the response spectra for the high and low frequency reference earthquakes and uniform hazard spectrum. This step results in a suite of response spectra that reflect the associated site response for each combination of base-case velocity profile, dynamic material property curves, and wave type. The final site-response spectrum for each component of ground motion is then obtained by enveloping over all the combinations of base-case velocity profile, dynamic material property curves, and wave type. The final location-specific response spectra thus reflect uncertainty in the base-case velocity profile and dynamic material properties at the site (BSC 2004b, Section 6.3.1).

In computing the site response for vertical ground motion, the same process used for horizontal ground motion is followed, except that the transfer function resulting from enveloping over the transfer functions for the high and low frequency range for each combination of base-case velocity profile, dynamic material property curves, and wave type is applied to the revised envelope vertical spectrum (Section 2.3.4.3.2.2; BSC 2004b, Section 6.2.2.6).

In addition to transfer functions for response spectra, transfer functions reflecting site response are also determined for PGV. The approach used is the same and thus includes uncertainty and

variability in site material properties, as well as magnitude dependence on nonlinear material behavior. Spectral amplification functions are replaced by PGV scaling factors. To envelop results, the largest value of PGV is taken. For vertical-component PGV, the PGV for the reference rock outcrop from the PSHA is revised to be consistent with the revised envelope vertical response spectra (BSC 2004b, Section 6.2.2.6.3) before the velocity-scaling factor is applied.

Consideration of Alternative Conceptual Models—Alternative models considered for site-response analyses include fully nonlinear as well as two- and three-dimensional models. The advantage of the equivalent-linear formulation over fully nonlinear formulations is that parameterization of complex nonlinear soil or rock models is avoided, and the mathematical straightforwardness of a linear analysis is preserved. A truly nonlinear computation requires the specification of the shapes of hysteresis curves and their cyclic dependencies through an increased number of material parameters (BSC 2004b, Section 6.1.4). Furthermore, validations have demonstrated that one-dimensional models accommodate the significant and stable features of ground motion site response (Silva et al. 1996, Section 8). For example, comparison of one-dimensional equivalent-linear models with fully nonlinear models for three sites where nonlinear soil behavior was clearly observed in response to ground motion demonstrated that the equivalent-linear and fully nonlinear models give similar results and show reasonable agreement with observed data (EPRI 1993, Appendix 6.B). This is also the case for an additional site at which high ground-motion-induced strains occurred. Agreement among the equivalent-linear and nonlinear models, and with the data, was comparable to the other test cases (BSC 2004b, Section 7.3.5).

Two- and three-dimensional formulations were also considered. While these formulations can explicitly treat lateral variability in dynamic material properties and potential topographic effects, reductions in model uncertainty are offset by increases in parameter uncertainty. Additionally, the wavefields developed within two- and three-dimensional models depend strongly upon the azimuth and depth of the seismic source, contributing to variability of the site response. These two- and three-dimensional effects are included implicitly through the PSHA results, from which inputs to the site-response model are derived. The PSHA results include two- and three-dimensional wave propagation effects because such effects are included in the ground motion database used to assess variability in ground motion as part of the PSHA. Furthermore, implementation of two- and three-dimensional formulations requires detailed knowledge of vertical and lateral variations of material properties. In the ground motion site-response model, these variations are accommodated stochastically. For the engineering and performance assessment applications addressed here, a one-dimensional approach is adequate and preferred (BSC 2004b, Section 6.1.4).

Validations have demonstrated that one-dimensional models accommodate the significant and stable features of ground motion site response (Silva et al. 1996, Section 8).

Model Uncertainty—Model uncertainty has been addressed through comparison of results for the random vibration theory–based equivalent-linear site-response model to results of one-dimensional fully nonlinear models and to recorded motions (EPRI 1993, Appendix 6B). The model was validated for three soil sites and for ground motion ranging from about 0.05 to 0.5 g. The general conclusion resulting from these analyses is that conventional one-dimensional site-response analyses, incorporating equivalent-linear and nonlinear soil behavior based upon

laboratory testing and with reasonably accurate soil profiles, can accurately determine the effects of such materials on strong ground motions (EPRI 1993, Appendix 6B).

Confirmation of model validation has been performed for a case in which large strains were generated in the site materials. In this study, the random vibration theory–based equivalent-linear site-response model was compared to another equivalent-linear model and to two one-dimensional fully nonlinear models. Response spectra produced by the random vibration theory-based equivalent-linear model are similar to those produced by the other models and to the data. Thus, the validity of the random vibration theory-based equivalent-linear site-response model to calculate response spectra is established even for a case in which large strains occurred (BSC 2004b, Section 7.3.5).

Uncertainty remains in implementation of the model at the high levels of ground motion associated with low annual probabilities of exceedance for Yucca Mountain. The model allows shear strains to occur that the rock at Yucca Mountain likely cannot sustain without suffering physical damage. Rock property testing and modeling indicate predicted strains associated with some of the low-probability ground motions would cause yield and observable, permanent damage to the lithophysal units of the Topopah Spring Tuff (BSC 2005a). As discussed in Section 2.3.4.3.3, such ground motion–induced rock damage is not observed at Yucca Mountain, providing evidence for the maximum strain levels (and thus, maximum PGV) that this rock mass has not experienced since its deposition over 12.8 million years ago.

2.3.4.3.2.4 Abstraction

For postclosure analyses, seismic inputs are abstracted as suites of time histories (seismograms) and values of PGV for the waste emplacement level. The time histories and PGV values provide input to rockfall analyses, seismic kinematic and structural response calculations for EBS features, and abstraction of the seismic consequence to the TSPA (Sections 2.3.4.4, 2.3.4.5, and 2.3.4.6).

The time histories are not a direct output of the random-vibration-theory-based equivalent-linear site-response model. Rather they are developed using the site-specific PGV levels determined from site-response modeling and actual recordings of strong ground motion from earthquakes in the western U.S. and around the world. The original recordings are modified to reflect the results of the site-response modeling for Yucca Mountain. Recordings for use are selected to have magnitude and epicentral distance characteristics similar to those earthquakes that contribute to the seismic hazard at a given annual probability of exceedance. By basing the time histories on actual earthquake recordings and choosing records consistent with the seismic hazard, the resulting time histories exhibit realistic and appropriate phase characteristics and durations (BSC 2004b, Section 6.3.2).

Postclosure seismic analyses of rockfall and EBS kinematic and structural response are aimed at determining the range of seismic effects for a given level of ground motion, taking into account the natural variation in seismic processes. Time histories that share a common measure of ground motion (e.g., the PGV on one of the horizontal components) can differ in other characteristics (e.g., duration, spectral content, relative amplitude of ground motion on the other horizontal or the vertical component). Thus, postclosure analyses are generally carried out using a suite of time histories representing the variation in earthquakes that can produce a given level of ground motion (SNL 2007c, Section 6.4).

For postclosure analyses, the selected recordings of past earthquakes are scaled by the peak horizontal ground velocity determined by the site-response modeling for the waste emplacement level at a given annual probability of exceedance. Two approaches to scaling have been used (BSC 2004b, Section 6.3.2). In one approach, each component of ground motion is scaled to the target PGV determined from the site-response modeling. In the other approach, one horizontal component is scaled to the target PGV, and the other two components are scaled to preserve the intercomponent variability of the original records.

In addition to scaling, the original strong motion recordings are, in some cases, first conditioned to make their response spectra more similar to those expected for Yucca Mountain (BSC 2004b, Section 6.3.2). There is a trade-off between the goal of maintaining the variability of the original strong motion records and having the response spectra of the records more appropriate for the Yucca Mountain site. The original records exhibit response spectral characteristics typical of the region in which they were recorded (largely California). Spectral conditioning modifies the records such that their response spectra are closer to that expected for Yucca Mountain. When spectral conditioning is employed, either the response spectra for the PSHA reference rock outcrop or the response spectra for the waste emplacement level is used as the target.

For preclosure design analyses, time histories are developed such that their response spectra closely match the target response spectra from site-response modeling (Section 1.1.5.2). This is in contrast to the spectral conditioning described above, in which only a weak match to the target spectrum is desired. Different approaches are used for time histories supporting preclosure and postclosure analyses because of the different purposes of the analyses. The purpose of the design analysis is to show that the structure, system, and component has adequate capacity to withstand the design motion. The purpose of the postclosure analyses is to determine the range of damage, if any, caused by the ground motion, taking into account the variability of ground motions associated with the target horizontal PGV (BSC 2004b, Section 6.3.2.3).

The results of implementing the overall approach to site-specific ground motions to develop seismic inputs for postclosure analyses are described below. The results reflect uncertainty and variability in the underlying ground motion hazard results, as well as in the site response (BSC 2004b, Section 6.3.3).

Waste Emplacement Level—Site-specific values of horizontal PGV for the waste emplacement level were determined for annual exceedance probabilities of 10^{-4}, 10^{-5}, 10^{-6}, and 10^{-7} (BSC 2004b, Sections 6.3.1.2.3 and 6.3.1.4). These values (0.402, 1.05, 2.44, and 5.35 m/s, respectively) support development of time histories for postclosure analyses. Results of analyses of seismic-induced rockfall (Section 2.3.4.4) and the kinematic and structural response of EBS components under seismic loads (Section 2.3.4.5) in conjunction with an analysis on bounds to low-probability PGV (Section 2.3.4.3.3) form the basis for the abstraction of seismic consequences.

For annual exceedance probabilities of 10^{-5}, 10^{-6} and 10^{-7}, the PGV-scaling approach was used to generate suites of 17 sets of time histories for each probability of exceedance. The 17 sets of recorded strong ground motion that form part of the basis for developing the time histories (Table 2.3.4-2) were selected to represent the range of magnitudes and distances consistent with the range indicated by deaggregation of the PSHA (BSC 2004b, Section 6.3.2.3).

Over the course of the analyses to develop suites of time histories, the development approach evolved as some aspects were refined. Initially, both horizontal components were scaled to the site-specific horizontal PGV value and the vertical component was scaled to the site-specific vertical PGV value. To enhance the representation of intercomponent variability, this approach was replaced by one in which only one horizontal component was scaled to the site-specific horizontal PGV value. The second horizontal component and the vertical component were scaled such that the intercomponent variability of the original records was preserved. A further enhancement was to condition the strong motion records prior to scaling so that their response spectra would reflect characteristics expected for the Yucca Mountain site rather than those of the region in which they were recorded. Conditioning involved a weak match to a response spectrum that was modified to reflect average differences between western U.S. response spectra and those at Yucca Mountain. A strong spectral match was not implemented because of the trade-off with maintaining the original intercomponent variability of the records. At first the conditioning was carried out with respect to response spectra for the PSHA reference rock outcrop. Later, conditioning was carried out with respect to response spectra for the repository waste emplacement level. Thus, as discussed below, the suites of time histories for various annual frequencies of exceedance reflect different scaling and spectral conditioning approaches. In carrying out postclosure seismic analyses of rockfall and EBS response for the various levels of PGV, the suite of time histories used was selected from the suites available when the analyses were carried out (BSC 2004b, Section 6.3.2; BSC 2004a; SNL 2007b).

For an annual exceedance probability of 10^{-5}, one suite of time histories was developed. First, the strong motion records used as a basis for the time histories were spectrally conditioned to weakly match the response spectra for the waste emplacement level. Specifically, ratios were determined between response spectra for average western U.S. conditions and response spectra for the waste emplacement level at Yucca Mountain. The western U.S. response spectra are considered typical of the strong motion records forming the basis for Yucca Mountain time histories. Next, these ratios were applied to modify the response spectrum for each component of the strong ground motion records to be used in generating time histories. Finally, the modified response spectra formed targets for weak spectral matches of the original records. Spectral matching refers to the iterative process whereby a seismic time history is adjusted such that its response spectrum matches a target response spectrum to within some fitting criterion. For time histories used in preclosure analyses, the iterative process continues until a close match is obtained. For time histories used in postclosure analyses, a single iteration of the matching process is implemented to weakly match the target response spectrum. The use of a weak match allows the time history response spectra to be representative of the Yucca Mountain site and to maintain the natural intercomponent variability of the recorded time history. Following the conditioning mentioned above, the records were scaled to the site-specific PGV. One horizontal component was scaled to the PGV, and the other components were scaled to preserve the intercomponent variability of the original records (BSC 2004b, Section 6.3.2.3).

For an annual exceedance probability of 10^{-6}, two suites of time histories were developed. The first suite consists of time histories for which both horizontal components were scaled to the site-specific horizontal PGV, and the vertical component was scaled to the site-specific vertical PGV. For this suite, observed intercomponent variability was not maintained. Also, the records used to generate the time histories were not spectrally conditioned prior to scaling (BSC 2004b, Section 6.3.2.3.1).

The second suite of time histories for an annual probability of exceedance of 10^{-6} was developed using the same method as that used for the suite with an annual probability of exceedance of 10^{-5},

with one exception. Rather than using the response spectra for the waste emplacement area as the target for spectral conditioning, the spectral conditioning was carried out with the response spectra for the PSHA reference rock outcrop as the target. Following this conditioning, the records were scaled to the site-specific PGV such that the intercomponent variability of the original records was maintained (BSC 2004b, Section 6.3.2.3.1).

Two suites of time histories were also developed for an annual exceedance probability of 10^{-7}. For these two suites, the records that form the basis for the time histories were spectrally conditioned prior to scaling. For one suite, they were spectrally conditioned to weakly match the response spectra for the PSHA reference rock outcrop, as described above for the spectrally conditioned and scaled time histories for 10^{-6} annual exceedance probability. This suite of time histories was used to evaluate the postclosure performance of the EBS. For the other suite, they were conditioned to weakly match the site-specific response spectra for the waste emplacement area as for the suite associated with an annual probability of exceedance of 10^{-5} (BSC 2004b, Sections 6.3.2.3.2 and 6.3.2.3.3). Examples of time histories for postclosure analysis are shown in Figures 2.3.4-10 and 2.3.4-11.

Time histories for the waste emplacement level, with an annual probability of exceedance of 5×10^{-4} and 1×10^{-4}, were developed using the spectral-matching approach. Although this set of time histories was developed for preclosure analyses (Section 1.1.5.2), it was also used in the evaluation of seismic-related drift degradation effects. Drift degradation effects for the preclosure ground motions were compared to those for postclosure ground motions (BSC 2004a, Section 6.3.1.2.1). One three-component set of time histories was developed (BSC 2004b, Section 6.3.2.1).

The mean annual probabilities of exceedance determined from the PSHA results are 10^{-4}, 10^{-5}, 10^{-6}, and 10^{-7} for horizontal PGV values of 0.4, 1.05, 2.44, and 5.35 m/s, respectively. These probabilities of exceedance do not reflect new information on limits to extreme ground motions at Yucca Mountain. One analysis (Section 2.3.4.3.3), based on a shear-strain threshold for ground motion related damage to lithophysal tuff, indicated that an upper bound distribution can be put on the level of extreme ground motion that has been experienced at the waste emplacement level. Adopting this distribution as a reasonable bound on the ground motions that should be considered in the TSPA conditions the hazard curve for horizontal PGV at the waste emplacement level (Section 2.3.4.3.3.4). For horizontal PGV values of 0.4, 1.05, and 2.44 m/s, the conditioned mean annual probabilities of exceedance are 10^{-4}, 10^{-5}, and 4.5×10^{-7}, respectively (BSC 2005a, Appendix D). For the conditioned mean PGV hazard curve the value of PGV never exceeds 4.07 m/s for annual exceedance frequencies greater than or equal to 10^{-8} per year (SNL 2007c, Section 6.4.3).

For postclosure analyses, time histories scaled to horizontal PGV values of 0.40, 1.05, 2.44, 4.07, and 5.35 m/s, with revised mean annual probabilities of being exceeded of 10^{-4}, 10^{-5}, 4.5×10^{-7}, 10^{-8}, and less than 10^{-12}, respectively, were used. Time history sets for horizontal PGV values of 0.40 and 4.07 m/s were developed by scaling the time histories originally developed for horizontal PGV levels of 1.05 and 5.35 m/s (SNL 2007b, Section 6.3.2.1.2). Given the similarity in the magnitude and distance deaggregation results for these similar hazard levels, simple linear scaling of the time histories is adequate.

For the purposes of the seismic damage abstractions, ground motions are characterized by the value of the first horizontal component of PGV, denoted as PGV-H1 or more simply as PGV in this section. This characterization does not imply that the second horizontal or the vertical velocity components have the same PGV value as the first horizontal component. In fact, there is substantial variability in the second horizontal and vertical components of PGV, conditional on the given value of PGV-H1.

For preclosure probabilistic seismic safety analyses and design analyses, the ground motions developed to support postclosure analyses have been supplemented. As described in Section 1.1.5, these supplemental ground motions were developed using updated geotechnical information, Approach 3 of NUREG/CR-6728 to address site-response, and incorporated two approaches to providing constraints on extreme ground motion at Yucca Mountain (BSC 2008, Section 6.1) (Section 1.1.5).

Use of Approach 3 allows a more direct determination of the seismic hazard curves needed for preclosure probabilistic seismic safety analyses. Incorporation of a reasonable bound to extreme ground motion takes into account new information that was not part of the data considered in the probabilistic seismic hazard analysis. It also provides low probability ground motions that are realistic and compatible with the geologic setting of the site. Comparison of these supplemental ground motions to those used in postclosure analyses indicate that, for a given level of ground motion, the supplemental results have a lower mean annual probability of exceedance (Section 2.3.4.3.3.5) (BSC 2008, Section 6.5.3.2).

2.3.4.3.3 Characterization of Low-Probability Peak Horizontal Ground Velocity

[NUREG-1804, Section 2.2.1.3.2.3: AC 1(1) to (4), AC 2, AC 3, AC 4(2), AC 5]

As discussed in Section 2.2.2.1.1, ground motion hazard determined in the PSHA expert elicitation is unbounded. Because of the manner in which ground motion uncertainty was characterized and incorporated into the PSHA calculations, as the calculations are extended to lower and lower annual probabilities of exceedance, the mean ground motions increase without bound, and eventually reach levels that are not credible. The U.S. Nuclear Waste Technical Review Board has commented on the very-low-probability ground motions determined for Yucca Mountain (Corradini 2003). They found the ground motions for annual probabilities of exceedance less than 10^{-6} to be "generally unrealistic, physically unrealizable, or outside the limits of existing worldwide seismic records or experience…" They recommended that the DOE continue its studies to bound very-low-probability ground motions on the basis of sound physical principles. These levels of ground motion are not credible in that they are inconsistent with the geologic setting of the site (BSC 2005a; BSC 2008, Appendix A, Section A1).

As stated in 10 CFR 63.102(j) with respect to events that are to be included in the TSPA, "the event class for seismicity includes the range of credible earthquakes for the Yucca Mountain site." Therefore, to ensure the ground motions considered in the seismic consequence abstraction and TSPA are credible, an analysis was conducted using results that became available after the PSHA to determine a reasonable bound to horizontal PGV at the repository waste emplacement level (BSC 2005a). The results of this analysis are combined with those from the PSHA to provide a horizontal PGV hazard curve for the waste emplacement level that is reasonable and credible. The conditioned hazard curve is sampled in each realization of the TSPA seismic scenario to provide

input on seismic hazard (SNL 2007c, Section 6.4.3). In addition, the resulting conditioned horizontal PGV hazard curve forms the basis for re-scaling the suite of time histories based on unbounded PSHA results with a mean annual probability of exceedance of 10^{-7}. For postclosure calculations of the kinematic and structural response of EBS components, this suite of time histories is re-scaled such that the H1 component has a PGV of 4.07 m/s, consistent with a conditioned mean annual probability of exceedance of 10^{-8}.

Subsequent to the work described in *Seismic Consequence Abstraction* (SNL 2007c), analyses and modeling were carried out that included an additional approach for determining a reasonable and credible hazard curve for horizontal PGV at the waste emplacement level (BSC 2008, Section 6.5.1). In this more recent work, a reasonable upper range distribution for the seismic source stress drop (stress parameter) was assumed and used to condition the hazard curves from the PSHA. The mean hazard curve for horizontal PGV at the waste emplacement level incorporating this additional approach for conditioning extreme ground motions is discussed in Section 2.3.4.3.3.5 and presented in more detail in Section 1.1.5. For a given value of horizontal PGV, it gives a mean annual probability of exceedance (BSC 2008, Section 6.5.3.2) that is approximately equal to or lower than that determined in *Peak Ground Velocities for Seismic Events at Yucca Mountain, Nevada* (BSC 2005a, Appendix D), and used in *Seismic Consequence Abstraction* (SNL 2007c), Table 6-3).

2.3.4.3.3.1 Conceptual Approach

One approach to characterizing extreme values of horizontal PGV at the waste emplacement level is based on physical limits of the rock strength at Yucca Mountain (BSC 2005a; Section 6). Ground-motion site-response modeling using the unbounded results from the PSHA (BSC 2004b, Section 6.3.4) indicates that, at low annual probabilities of exceedance, calculated shear strains for the rock approach 1% or higher for some realizations of the model. However, laboratory testing shows that the peak shear strain that lithophysal rock can sustain prior to yield and extensive fracture development is on the order of 0.1 to 0.2%. Numerical simulations of lithophysal rock behavior corroborate the laboratory findings. The simulations indicate that, at shear strain increments of about 0.1%, the rock would develop interlithophysal tensile fractures several tenths of a meter long. With increasing strain, the fractures would coalesce and form observable shear features with offset. Damage to lithophysae would be evident where fractures intersect them. If the shear strains were caused by transient seismic waves propagating through the rock, the fracturing would be pervasive rather than isolated. The exposed lithophysal rocks in the ESF and the Enhanced Characterization of the Repository Block (ECRB) Cross-Drift, however, do not show pervasive fracturing of this type. Moreover, most fractures in the Topopah Spring Tuff exposed in the ECRB Cross-Drift and surface-based boreholes are associated with features that formed during the cooling of the deposit. Thus, the rocks provide evidence that they have generally not experienced shear strain increments of 0.1 to 0.2% or higher since they were deposited 12.8 million years ago. By calculating the ground motion required to produce such shear strains in the lithophysal rock, a limit can be assessed for horizontal PGV that has not been experienced at the depth of the emplacement drifts (BSC 2005a, Section 6).

Note that the approach does not assert that the amplitude of ground motion is limited by the strength of the propagating medium. Rather, it concludes that a lack of physical damage to the rock that

would be expected if certain levels of ground motion had been achieved at Yucca Mountain, indicates that such levels have not been experienced.

Using this conceptual approach, the limit to the level of horizontal PGV experienced at the waste emplacement level at Yucca Mountain is determined in a two-step process. The limit is defined as a probability distribution. First, a distribution is determined for the shear-strain damage threshold based on the results of laboratory testing and corroborated by numerical modeling of mechanical deformation of lithophysal tuff. More weight is given to the values more strongly supported by the testing and modeling data. Next, that distribution is converted to one for horizontal PGV using the results of the site-response model. The site-response calculations provide the values of horizontal PGV that are associated with different levels of dynamic shear strain produced by ground motion at the waste emplacement level. The conversion is carried out for eight cases representing epistemic uncertainty in dynamic material properties at the site and two ground motion oscillator response frequency ranges (BSC 2005a, Sections 6.4.3 and 6.6).

The following three sections describe the data used to develop the limit to horizontal PGV experienced at the waste emplacement level and its uncertainty, the analysis approach and how uncertainties were incorporated, and how the limit was used in the abstraction of seismic consequences for TSPA.

2.3.4.3.3.2 Data and Data Uncertainty

Inputs to the analysis to characterize low-probability horizontal PGV consist of laboratory testing and numerical simulation of lithophysal rock behavior, geologic observations of fractures and lithophysae within the ESF and the ECRB Cross-Drift, and modeling of ground-motion site response. Laboratory testing and numerical simulations of rock behavior provide information on the shear-strain threshold at which lithophysal rock of the Topopah Spring Tuff fractures. Numerical simulations also show the expected spatial relation of such fracturing to the lithophysae within the rock. Geologic observations indicate that the type of pervasive fracturing that would be expected, if the shear-strain threshold was exceeded as a result of seismic shaking, is not evident within the rocks exposed in the ESF and ECRB Cross-Drift. Modeling of ground motion site-response determines what level of seismic shaking would be required to generate shear strains exceeding the shear-strain threshold.

Shear-Strain Threshold for Topopah Spring Lithophysal Rock: Laboratory Testing— Unconfined compressive strength tests provide data on Young's modulus, Poisson's ratio, and ultimate strength (peak stress) that form the basis for assessing the shear-strain threshold for rock failure (BSC 2005a, Section 6.4.1, Appendix B and Appendix D). The tests were conducted on large-diameter samples (288 mm) from the Topopah Spring Tuff upper lithophysal and lower lithophysal zones. The shear strain increment at failure is determined from the results of the unconfined stress compression tests, assuming a Poisson's ratio of 0.3, and accounting for the effect of in situ stress conditions at the waste emplacement level. For the 19 samples tested, the mean shear-strain increment was 0.18% with a standard deviation of 0.07% for in situ conditions at 250 m (Figure 2.3.4-12) and 0.19%, with a standard deviation of 0.07% for in situ conditions at 400 m. If seismic shaking were to generate shear strains in the rock exceeding the determined shear-strain increments, failure of the rock would be expected (BSC 2005a, Section 6.4.1, Appendix B, and Appendix D).

Shear-Strain Threshold for Topopah Spring Lithophysal Rock: Numerical Simulation—To supplement the results of laboratory testing and to examine the characteristics of fractures generated as lithophysal rock is deformed to failure, the results of numerical simulations of rock behavior were analyzed (BSC 2005a, Section 6.4.2, Appendix B, and Appendix D). Two software programs were used to conduct numerical compression tests of lithophysal material. In the simulations, lithophysae were represented as voids. The voids were either circular in shape (used in both programs) or had an irregular shape based on observed lithophysae in the ECRB Cross-Drift (used in one program). The combinations of software programs and lithophysal representation resulted in three simulation approaches. Simulations were carried out for a combined total of 119 samples. The numerical simulations were carried out as part of the characterization of subsurface geotechnical parameters (BSC 2007a, Section 6.4.4.4.2.5).

Results of the numerical compressive tests show that the lithophysal rock will fail through the development of fractures that extend generally from one lithophysal void to another (Figure 2.3.4-13). The failure mechanism is a result of tensile splitting between adjacent lithophysal voids that is caused by the induced tensile stresses in the material between the voids. Strains induced by high levels of ground motion would be expected to cause this style of deformation (i.e., fractures that connect lithophysae). Thus, seismic-induced fracturing should be distinguishable from fractures related to cooling of the deposits (BSC 2005a, Section 6.4.2). Because the ground motion would affect the entire rock mass as the seismic waves propagated through the material, it is expected that seismic-induced fracturing would be pervasive, rather than spatially limited, if extreme ground motions had ever occurred.

For the numerical samples, shear-strain increments were calculated for two failure criteria: peak stress (state at ultimate strength) and yield stress (state at volumetric strain reversal) (BSC 2005a, Section 6.4.2). Values of Young's modulus, Poisson's ratio, friction angle, peak stress, and yield stress were taken from the results of the numerical simulations. If a friction angle was not determined as part of the numerical simulation, a value of 30° was used. Shear-strain increments were calculated for in situ conditions at two representative waste emplacement level depths: 250 and 400 m (BSC 2005a, Section 6.4.2).

Shear-strain increments range from less than 0.05% to about 0.25% (Figure 2.3.4-14). Mean shear-strain increment values for the two representative depths and the two failure criteria are provided in Table 2.3.4-3 for the three simulation approaches. Mean values range from 0.09% to 0.16% (BSC 2005a, Section 6.4.2).

Geologic Data—A key element of the approach to characterize low-probability horizontal PGV at the waste emplacement level is using the geologic data collected in the ESF and ECRB Cross-Drift to determine whether pervasive seismic-induced fracturing has occurred at Yucca Mountain. In carrying out this evaluation, two types of geologic data are used: fracture characteristics gathered as part of systematic underground mapping programs and detailed studies of portions of the ECRB Cross-Drift (BSC 2005a, Section 6.3).

Yucca Mountain is a structural block, bounded by the Solitario Canyon and Bow Ridge faults, with numerous intrablock faults (Day et al. 1998pp. 8 to 12). These faults provide evidence that there has been structural disruption and various amounts of slip along the faults since the rocks were formed. For the characterization of horizontal PGV, one of the important lithostratigraphic units is the

Topopah Spring Tuff that was deposited 12.8 million years ago. Rather than focusing on the deformation along faults, the approach to characterizing horizontal PGV concentrates on the rock mass that would be subjected to the effects of propagating seismic waves, especially in the repository host rocks of the Topopah Spring Tuff. The approach has been to evaluate, through numerical simulation and comparison with geologic descriptions, whether features that were formed very shortly after the deposition of the tuff (which include lithophysae and some fractures) have been damaged by locally induced shear strains resulting from ground motions (BSC 2005a, Section 6).

A key element in evaluating fractures (or, more generically, "discontinuities") is to understand how their descriptive characteristics relate to their development and the geologic history of the rock mass that contains them. An understanding of this relationship allows identification of types of discontinuities (or sets of discontinuities). Throughout site characterization at Yucca Mountain, terms such as joint, fracture, cooling joint, "tube-bearing" joint, "early formed fracture," "fracture formed during cooling," shear, and fault have typically had similar definitions. However, as knowledge was gained, understanding was refined, and additional characteristics measured and documented, there were changes with respect to the distinguishing characteristics of and interpretations of some features. For example, early descriptions of joints (which implicitly were associated with cooling of the deposit) were identified as being relatively long, smooth, and steeply dipping, but additional characteristics were not systematically described. Subsequently, characteristics such as length and roughness were quantified, as were representative strikes and dips. This allowed classification of the discontinuities into sets that shared similar geometric values. Also, there was the recognition that "cooling joints" were not just steeply dipping but some were moderately to very shallowly dipping. Additional characteristics were recognized as being diagnostic of "cooling joints" such as tubular structures, rims, borders, and vapor-phase mineral linings. Both rims and borders are types of crystallization that form from the facture face into the rock. They formed where hot vapor interacted with the walls of the fracture. Historically, rims have been referred to by terms such as vapor-phase alteration, rinds, and bleach zones. Descriptions from previous studies often do not include enough detail (or the right type of detail) to easily interpret the data in terms of more recent definitions. Historically, the identification of "cooling joints" emphasized the larger sized features such as trace length, planarity, strike, and dip (even tubular structures) but largely overlooked the smaller features (rims, borders, vapor-phase mineral linings) that are not scale-dependant. These smaller-scale features, however, are more indicative of fractures that formed during cooling than are the larger features (BSC 2005a, Appendix A).

For the welded tuffs at Yucca Mountain, and especially the Tiva Canyon and Topopah Spring Tuffs, there are four main processes considered for the formation and orientation of fractures (Barton et al. 1993; Dunne et al. 2003; Potter et al. 2004, p. 864; Stuckless and Levich et al. 2007; Throckmorton and Verbeek 1995). These four mechanisms, which induce stress on the rock mass, include (1) thermal contraction (the only true "cooling" fracture), (2) gravitational creep along a sloping geomorphic surface, (3) movement of block-bounding faults and distribution of stress across the hanging-wall fault block, and (4) regional structural extension. All these mechanisms have been considered as being active during the time that the tuff was cooling (and typically early in this period of time). One important consequence of the fact that these mechanisms were active during the cooling of the tuff is that all fractures formed during this time would (or could) develop the characteristics of a fracture that formed during cooling. Thus, the phrase "fracture formed during

cooling" is preferred over the term "cooling joint" (except possibly for fractures formed by thermal contraction).

The distinction between these processes is not important in the context of the geologic observations for bounding PGV. Of importance to characterizing limits on the level of PGV that has been experienced at Yucca Mountain is establishing when a fracture formed (i.e., formed during cooling, formed after cooling was completed, or indeterminate as to when it formed) and whether it has been disturbed since that time. Thus, it would be important to determine if there is a lack of evidence of reactivation related to extreme ground motion for fractures that formed during cooling of the welded tuff about 12 million years ago. Similarly, it would be important to determine if fractures in the lithophysal units that appear to have developed after cooling took place exhibit spatial patterns consistent with those expected if they had been produced by extreme levels of horizontal PGV.

Fractures in the lithophysal and nonlithophysal rocks of the Topopah Spring Tuff have been systematically studied in the underground excavations of the ESF and ECRB Cross-Drift (Albin et al. 1997; Barr et al. 1996; Beason et al. 1996; Eatman et al. 1997; Mongano et al. 1999). The majority of fractures have features such as rims and/or borders, tubular structures and/or vapor-phase mineral linings, or they have geometric relations used in the identification as "cooling joints" or "vapor-phase partings." These attributes indicate the fractures formed during the cooling of the deposit (BSC 2005a, Appendix A). Most fractures in the lithophysal rocks do not exhibit shear offset, do not show damage to the fracture walls (for example, the vapor-phase mineral linings have well-developed crystal morphology), and are consistent in orientation with cooling fractures observed in the middle nonlithophysal zone. Some fractures, generally referred to as discontinuities, do show evidence of shear offset, and are identified as shears if they have less than 0.1 m offset or faults if greater than 0.1 m offset. In the ECRB Cross-Drift, for example, shears comprise 5.5% of all discontinuities, and faults are 1.6%, and the distribution along the tunnel is not systematic (i.e., they tend to form clusters) (Mongano et al. 1999). Shears and faults indicate movement and deformation along localized planes, and they are consistent with propagation of fracture and shear planes through the rock mass during earthquakes. However, the shears and faults are not widely developed as would be expected for fractures related to extreme seismic shaking (BSC 2005a, Section A1.2). Finally, many shears (and even some faults) have characteristics that indicate they are reactivated fractures that formed during cooling. Being able to identify the early history of a fracture (i.e., that it formed during cooling) provides a strong foundation upon which to determine if damage has occurred through time or the localized utilization of these fractures to accommodate slip during subsequent deformation.

Detailed examination of panel maps (1 m × 3 m detailed geologic maps of the tunnel sidewall) from the ECRB Cross-Drift (Figure 2.3.4-15) confirms the absence of fractures related to seismic shaking. Fractures observed in the panel maps are consistent with an origin of formation during cooling and do not show the spatial relations to lithophysae that numerical simulations indicate should exist for fractures related to compressive deformation. That is, the fractures do not tend to connect lithophysae and there is no evidence of damage along lithophysae margins where fractures do intersect them (BSC 2005a, Appendix A).

Data from the systematic characterization of fractures and detailed examination of panel maps in the ECRB Cross-Drift both support an origin for most fractures observed in underground exposures of lithophysal rock of the Topopah Spring Tuff that is consistent with formation during cooling and

without subsequent damage. Widespread fractures with characteristics (shear offset, interlithophysal connections) that would be expected if the shear-strain threshold for observable damage to lithophysal rock had been exceeded at Yucca Mountain are not seen. Thus, it is concluded that the shear-strain threshold for failure of lithophysal rock at Yucca Mountain has not been exceeded since the rocks were deposited about 12.8 million years ago (BSC 2005a, Section 6.3).

Ground-Motion Site-Response—Ground-motion site-response modeling has been carried out for the Yucca Mountain site (Section 2.3.4.3.2). As part of the site-response output, results are provided on the variation with depth (from the surface to the waste emplacement level) of PGV and strain. By comparing the calculated horizontal PGV and dynamic shear strain at the depth of the Topopah Spring Tuff lower lithophysal unit for a suite of ground motion levels, the shear-strain threshold determined from laboratory testing and numerical simulations is associated with a value of horizontal PGV. That is, the results of the site-response modeling are used to determine the level of horizontal PGV that would be required to generate pervasive dynamic shear strains in the lithophysal rock that exceed the threshold at which the rock will fail by producing fractures that connect lithophysae (BSC 2005a, Section 6.5).

The value of horizontal PGV at the depth of the Topopah Spring lower lithophysal unit and its associated level of dynamic shear strain are determined for the eight combinations of site-response inputs (i.e., base-case velocity profile, base-case dynamic property curves, wave propagator type, and deaggregation earthquake response spectrum). This analysis is carried out for four hazard levels (i.e., 10^{-4} per year, 10^{-5} per year, 10^{-6} per year, and 10^{-7} per year) resulting in a suite of values characterizing the relationship between horizontal PGV and dynamic shear strain and its uncertainty (Table 2.3.4-4) (BSC 2005a, Appendix C).

2.3.4.3.3.3 Model and Model Uncertainty

Rock testing data, geologic data, and ground-motion site-response data are combined to determine a bound to horizontal PGV. The analysis consists of five steps. First, laboratory testing corroborated by numerical simulations of lithophysal rock deformation are used to determine the shear-strain threshold for geologically observable rock failure. Second, the results of the numerical simulations are combined with geologic observations in the ESF and ECRB Cross-Drift to conclude that the Topopah Spring lithophysal zones have not experienced shear-strains exceeding the threshold for failure. Third, ground-motion site-response data are used to assess the level of horizontal PGV that would be required to generate shear strains exceeding the shear-strain threshold for failure. Fourth, it is concluded that such a level of horizontal PGV has not been reached at Yucca Mountain since the rocks were deposited 12.8 million years ago. Fifth, this level is taken as a reasonable bound to ground motions at Yucca Mountain for the TSPA (BSC 2005a, Section 6.6). To capture uncertainties, the horizontal PGV bound is expressed as a probability distribution.

Measurements and simulation of lithophysal rock behavior form a key element in assessing the level of horizontal PGV that has not been experienced at the waste emplacement level. For the assessment presented here, rock failure is associated with peak stress, although the numerical simulations indicate that geologically observable fractures would develop by the time the lower yield stress is attained. For the laboratory testing data and calculations for an in situ depth of 250 m, shear-strain increments range from 0.10% to 0.34% with a mean of 0.18%. When only samples with a length-to-diameter ratio greater than 1.5 are considered (i.e., the more reliable data), the range is

0.10% to 0.22% and the mean is 0.16% (BSC 2005a, Table B-2, Figure B-7, and Appendix D). When an in situ depth of 400 m is used, the calculated increments range from 0.10% to 0.35% with a mean of 0.19% for all data. For the samples with a length-to-diameter ratio greater than 1.5, the range is 0.10% to 0.24% with a mean of 0.17% (BSC 2005a, Table B-2 and Appendix D). Results from the numerical simulations based on peak stress range from 0.08% to 0.25% overall with means ranging from 0.11% to 0.16%, depending on the in situ depth used and the simulation approach (BSC 2005a, Appendix D).

For the probabilistic distribution, the laboratory results, corroborated by the numerical simulations, are used to assess a triangular distribution for shear-strain threshold with minimum and maximum values of 0.09% and 0.25%, respectively, and a modal value of 0.16%. The range is based on the range determined from the laboratory testing results for samples with length-to-diameter ratios greater than 1.5. The mode is assessed on the basis of the means determined for the same laboratory samples with length-to-diameter ratios greater than 1.5. The range and mode determined from the laboratory testing results are consistent with the results from the numerical simulations (BSC 2005a, Section 6.4.3).

To translate the shear-strain threshold probability distribution into a distribution for horizontal PGV at the waste emplacement level, the results of ground-motion site-response modeling are used (BSC 2004b, Section 6.3.4). For each of the eight site-response modeling cases, which represent epistemic uncertainty in the velocity profile and dynamic material properties at Yucca Mountain (and the two frequency ranges), the values of shear strain and corresponding horizontal PGV are used to transpose the shear-strain threshold distribution to one for horizontal PGV. The resulting eight probability distributions for horizontal PGV depart slightly from a triangular shape because the relation between shear-strain threshold and horizontal PGV is not linear (Figure 2.3.4-16). These distributions fall into two groups depending on whether the upper mean tuff or lower mean tuff set of dynamic material property curves was used in the site-response modeling. For the lower mean tuff grouping of distributions, shear strains associated with the shear-strain threshold distribution are generated at relatively lower ground motions. For the upper mean tuff grouping of distributions, higher ground motions are needed to generate the shear-strain threshold level of shear strains (BSC 2005a, Section 6.6).

2.3.4.3.3.4 Abstraction for TSPA

TSPA requires a mean hazard curve at the waste emplacement level for a wide range of annual exceedance frequencies. Based on results from the PSHA, values of horizontal PGV are available at the waste emplacement level for annual exceedance frequencies ranging from 10^{-4} per year to 10^{-7} per year. The horizontal PGV value corresponding to the 10^{-4} per year point on the hazard curve is 0.4 m/s (BSC 2004b, Table 6.3-6). The horizontal PGV value corresponding to the 10^{-5} per year point on the hazard curve is 1.05 m/s (BSC 2004b, Table 6.3-14). The horizontal PGV value corresponding to the 10^{-6} per year point on the hazard curve is 2.44 m/s (BSC 2004b, Table 6.3-16). The horizontal PGV value corresponding to the 10^{-7} per year point on the hazard curve is 5.35 m/s (BSC 2004b, Table 6.3-18). A hazard curve for unbounded horizontal PGV is constructed from these values using interpolation and extrapolation for annual exceedance frequencies ranging from 10^{-4} per year to 10^{-8} per year (BSC 2005a, Section 6.8 and Appendix D). The hazard curve is unbounded in the sense it is derived from the results of the PSHA without taking into account evidence that extreme ground motions are inconsistent with the geologic setting at Yucca Mountain.

To obtain a conditioned hazard curve that takes into account the information on the level of horizontal PGV that has not been experienced at Yucca Mountain, the triangular distributions for the bounding value of PGV (Figure 2.3.4-16) are combined with the unbounded hazard curve to generate a new composite hazard curve for the repository horizon. The conditioned ground motion exceeds a particular value, x, only if both the bounding value of PGV is greater than x and the ground motion from the original unconditioned analysis is greater than x (BSC 2005a, Section 6.8 and Appendix D). Development of the conditioned hazard curve involves two steps. First, each of the eight bounding horizontal PGV distributions is combined individually with the unconditioned hazard curve for the waste emplacement level to produce eight modified mean hazard curves (Figure 2.3.4-17). Then, for each value of horizontal PGV, the probabilities of the eight modified curves are averaged (arithmetic mean) to determine points on the final conditioned mean hazard curve (Figure 2.3.4-18). Equal weighting of the hazard curves is used to reflect the assessment that the underlying cases representing epistemic uncertainty in site conditions are equally likely to represent actual conditions at Yucca Mountain (BSC 2005a, Section 6.8 and Appendix D).

The conditioned hazard curve shown in Figure 2.3.4-18 results in a maximum PGV of approximately 4 m/s at the 1×10^{-8} annual exceedance frequency. The analyses presented for the seismic scenario class therefore fulfill the proposed 10 CFR 63.114(a)(4) requirement for performance assessment to consider events that have at least 1 chance in 10,000 of occurring over 10,000 years (10^{-8} per year) (SNL 2007c, Section 6.4.3).

An important observation from Figure 2.3.4-18 is that even the most extreme, low-probability ground motion at the 10^{-8} per year exceedance frequency will not result in a peak horizontal ground velocity at the emplacement drifts of greater than about 4 m/s. This fact limits the ground motion amplitudes that must be considered in the seismic consequence abstraction for the seismic scenario class.

2.3.4.3.3.5 Comparison to Supplemental Ground Motion Inputs for Preclosure Analyses

Subsequent to development of ground motion inputs (BSC 2004b) used in postclosure analyses (e.g., BSC 2004a; SNL 2007b; SNL 2007c) and development of a reasonable bound to horizontal PGV at the waste emplacement level (BSC 2005a), supplemental ground motion inputs were developed to support preclosure analyses (BSC 2008). For the waste emplacement level, these supplemental ground motions consist of design spectra and related time histories for mean annual probabilities of exceedance of 10^{-3}, 5×10^{-4}, and 10^{-4} per year; hazard curves for peak ground acceleration, defined at 100 Hz; PGV, and 5%-damped spectral acceleration at oscillator frequencies of 0.3, 0.5, 1, 2, 5, 10, and 20 Hertz; and associated uniform hazard spectra (Sections 1.1.5 and 1.3.2). As there is some overlap between these supplemental ground motions and the ground motion inputs used in postclosure analyses, this section compares the two.

The conceptual approach and model inputs used to develop the supplemental ground motions differ from those described in Sections 2.3.4.3.2.1 and 2.3.4.3.2.2. Specifically, development of supplemental ground motion inputs incorporated (BSC 2008, Section 6.1):

- Additional geotechnical data that formed the basis for updated inputs to site-response modeling.

- An alternate approach (McGuire et al. 2001, Section 6.1, Approach 3) for including site-response in the development of location-specific hazard curves that are consistent with the annual probability of exceedance of an input control motion.

- Two approaches to conditioning ground motion hazard curves to reflect site-specific information on limits to extreme ground motion at Yucca Mountain. The conditioned hazard curves form the control motion used in development of location-specific hazard curves that take into account site-response.

Use of Approach 3 from NUREG/CR-6728 (McGuire et al. 2001, Section 6.1; Bazzurro and Cornell 2004) is implemented to facilitate the development of location-specific hazard curves for preclosure probabilistic seismic safety analyses. As a probabilistic approach, in contrast to the deterministic basis for Approach 2B described in Section 2.3.4.3.2.1, it provides more flexibility in addressing uncertainties that are incorporated into the analysis. Implementation of Approach 3 for Yucca Mountain is described in more detail in Section 1.1.5.

The need to develop location-specific hazard curves for preclosure probabilistic seismic safety analyses also motivated the inclusion of information on limits to extreme, low-probability ground motion at Yucca Mountain. This information was used to condition the control motion used in developing supplemental ground motions such that the results are credible at low annual probabilities of exceedance and consistent with the geologic setting of the site. To increase confidence in the technical basis for characterizing extreme ground motions at Yucca Mountain, a second approach, in addition to the one described in Sections 2.3.4.3.3.1 through 2.3.4.3.3.4, was implemented. This second approach is based on an assumed distribution for the upper range of stress drop values, consistent with the geologic setting of Yucca Mountain, for the stochastic point-source ground motion model.

In developing supplemental ground motions for preclosure analyses, the shear-strain limit approach for characterizing extreme ground motions is implemented in a modified manner from the one described in Sections 2.3.4.3.3.1 through 2.3.4.3.3.4. Rather than applying the information on distributions of horizontal PGV that have not been experienced at the waste emplacement level to condition the unbounded horizontal PGV hazard curve for that location, the information is used to develop equivalent conditioned hazard curves for the PSHA reference rock outcrop (BSC 2008, Section 6.5.1). This modification was made so that the information on levels of horizontal PGV that have not been experienced at the waste emplacement level could be applied in a consistent manner in developing hazard curves for both the surface facilities area and the waste emplacement level.

The second approach to characterizing extreme ground motion at Yucca Mountain uses an assumed distribution for the upper range of stress drop values that are judged to be consistent with the geologic setting of Yucca Mountain (BSC 2008, Section 6.5.1). The assumption of a distribution for

the upper range is based on scientific judgment that was informed by discussions with a panel of ground motion experts (BSC 2008, Appendix A). The distribution for the upper range of stress drop was used in conjunction with the stochastic point-source ground motion model to characterize extreme ground motions that are credible for Yucca Mountain. These results were then used to condition the hazard curves for the PSHA reference rock outcrop (BSC 2008, Section 6.5.1), which are subsequently used in developing location-specific ground motions that incorporate site response. Implementation of the two approaches to characterizing extreme ground motion in developing supplemental ground motions for preclosure analyses is discussed in more detail in Section 1.1.5.

The results of the additional work (BSC 2008, Section 6.5.3.2) indicate that for a given level of horizontal PGV at the waste emplacement level, the mean annual probability of exceedance is lower than that determined in *Peak Ground Velocities for Seismic Events at Yucca Mountain, Nevada* (BSC 2005a, Appendix D), and used in TSPA for the seismic scenario class.

2.3.4.3.3.5.1 Comparison of Acceleration Response Spectra

As part of the development of ground motion inputs for postclosure analyses, 5%-damped acceleration response spectra were determined for the waste emplacement level for mean annual probabilities of exceedance of 10^{-5}, 10^{-6}, and 10^{-7} (BSC 2004b, Section 6.3.1.4). These response spectra reflect the site response for the waste emplacement level based on geotechnical data available at the time the analyses were carried out and using NUREG/CR-6728 Approach 2B (McGuire et al. 2001, Section 6.1). They are referred to as "target" spectra and were used in conditioning recorded accelerograms that were then used to develop site-specific time histories (Section 2.3.4.3.2.4). Also documented in *Development of Earthquake Ground Motion Input for Preclosure Seismic Design and Postclosure Performance Assessment of a Geologic Repository at Yucca Mountain, NV* (BSC 2004b, Section 6.3.1.2.3) is the development of 5%-damped design response spectra for the waste emplacement level for a mean annual probability of exceedance of 10^{-4}. None of these response spectra incorporate information on limits to the level of extreme ground motion that can occur at Yucca Mountain.

In developing supplemental ground motion inputs for preclosure analyses (BSC 2008), uniform hazard response spectra were developed for the waste emplacement level for mean annual probabilities of exceedance of 10^{-5}, 10^{-6}, and 10^{-7}. In addition, design response spectra were developed for the waste emplacement level for a mean annual probability of exceedance of 10^{-4} (Section 1.1.5). In this work, geotechnical inputs to site response modeling were updated relative to those used in *Development of Earthquake Ground Motion Input for Preclosure Seismic Design and Postclosure Performance Assessment of a Geologic Repository at Yucca Mountain, NV* (BSC 2004b, Sections 6.2.3 and 6.2.4) based on additional data and NUREG/CR-6728 Approach 3 (McGuire et al. 2001) was used. In addition, the hazard curves from the PSHA for Yucca Mountain were conditioned prior to their use in implementing Approach 3 to reflect two approaches to characterizing extreme ground motions that can occur at Yucca Mountain.

Comparison of the results of *Development of Earthquake Ground Motion Input for Preclosure Seismic Design and Postclosure Performance Assessment of a Geologic Repository at Yucca Mountain, NV* (BSC 2004b) to those of *Supplemental Earthquake Ground Motion Input for a Geologic Repository at Yucca Mountain, NV* (BSC 2008, Section 6.5.3) for mean annual

probabilities of exceedance of 10^{-4}, 10^{-5}, and 10^{-6} show that the more recent results exhibit lower ground motion levels for a given mean annual probability of exceedance (Figure 2.3.4-19). In this comparison, target response spectra from *Development of Earthquake Ground Motion Input for Preclosure Seismic Design and Postclosure Performance Assessment of a Geologic Repository at Yucca Mountain, NV* (BSC 2004b, Section 6.3) are plotted along with uniform hazard spectra from *Supplemental Earthquake Ground Motion Input for a Geologic Repository at Yucca Mountain, NV* (BSC 2008, Section 6.5.3), except for a mean annual probability of exceedance of 10^{-4} for which design response spectra are plotted for both. The target response spectra reflect the effect of site response on the smoothed envelope of the uniform hazard spectrum and the response spectra for the low and high frequency reference earthquake response spectra (Section 2.3.4.3.2.1). Thus, similar measures of ground motion are being compared.

At a mean annual probability of exceedance of 10^{-4}, the spectra from *Development of Earthquake Ground Motion Input for Preclosure Seismic Design and Postclosure Performance Assessment of a Geologic Repository at Yucca Mountain, NV* (BSC 2004b, Section 6.3.1.2.3) and *Supplemental Earthquake Ground Motion Input for a Geologic Repository at Yucca Mountain, NV* (BSC 2008, Section 6.5.3.3) are similar in amplitude and shape. The supplemental design spectrum shows slightly less amplitude at oscillator frequencies above 10 Hz and below 1 Hz. At this mean annual probability of exceedance, limits on extreme ground motion at Yucca Mountain have little effect. The updated velocity profiles and use of NUREG/CR-6728 Approach 3 in the supplemental ground motions do not result in large differences in the developed ground motions at the waste emplacement level. At lower mean annual probabilities of exceedance, the effect of including in the supplemental ground motions the impact of limits to extreme ground motion at Yucca Mountain is evident. As the mean annual probability of exceedance decreases, the amplitude of the supplemental ground motion response spectrum decreases relative to the target spectrum from *Development of Earthquake Ground Motion Input for Preclosure Seismic Design and Postclosure Performance Assessment of a Geologic Repository at Yucca Mountain, NV* (BSC 2004b, Section 6.3.1.4). Comparison of the response spectrum shapes (i.e., response spectrum normalized to its peak value) at the lower mean annual probabilities of exceedance shows that the supplemental ground motions exhibit lower amplitudes for oscillator frequencies above about 10 Hz relative to the peak response spectral acceleration. The response spectra for the supplemental ground motions are also comparable or lower for oscillator frequencies below about 1 Hz relative to the peak response spectral acceleration. In the oscillator frequency range from about 1 Hz to 10 Hz, the supplemental ground motion amplitudes are comparable or slightly higher relative to the peak response spectral acceleration.

2.3.4.3.3.5.2 Comparison of Horizontal PGV Hazard

The hazard curve for horizontal PGV at the waste emplacement level, determined as part of the supplemental ground motion development (BSC 2008, Section 6.5.3.2), exhibits comparable or lower mean annual probabilities of exceedance for a given value of PGV relative to the hazard curve determined in *Peak Ground Velocities for Seismic Events at Yucca Mountain, Nevada* (BSC 2005a, Section 6.8) (Figure 2.3.4-20). The reduction in mean annual probability of exceedance increases as larger values of horizontal PGV are considered. The reduction in mean annual probability of exceedance is primarily due to the inclusion of the second approach to characterizing extreme ground motion at Yucca Mountain (i.e., based on an assumed distribution for the upper range for

seismic source stress drop as assessed on the basis of available data and interpretations, and informed by discussions with ground motion experts during a series of workshops) (Section 1.1.5).

Supplemental Earthquake Ground Motion Input for a Geologic Repository at Yucca Mountain, NV (BSC 2008) does not determine supplemental ground motions for the waste emplacement level using only the shear-strain threshold approach to characterizing extreme ground motion at Yucca Mountain. In *Peak Ground Velocities for Seismic Events at Yucca Mountain, Nevada* (BSC 2005a) the distribution of horizontal PGV associated with the shear-strain threshold distribution was used to condition the unbounded horizontal PGV hazard for the waste emplacement level. In contrast, in *Supplemental Earthquake Ground Motion Input for a Geologic Repository at Yucca Mountain, NV* (BSC 2008, Section 6.5.1.1) the shear-strain threshold distribution is used to determine the associated distribution of horizontal PGV for the PSHA reference rock outcrop, which is then used to condition the horizontal PGV hazard curve from the PSHA. Thus, a direct comparison of the horizontal PGV hazard for the waste emplacement level using only the shear-strain threshold approach to limiting extreme ground motions cannot be made. Comparison of the effect of each approach when used to condition the ground motions for the PSHA reference rock outcrop (Section 1.1.5), however, leads to the inference that, for the shear-strain threshold approach, the supplemental ground motions using updated geotechnical data and NUREG/CR-6728 Approach 3 (McGuire et al. 2001, Section 6.1) would result in higher mean annual probabilities of exceedance for a given value of horizontal PGV than determined in *Peak Ground Velocities for Seismic Events at Yucca Mountain, Nevada* (BSC 2005a).

The fact that the shear-strain threshold approach provides less constraint on extreme ground motions than the upper range stress drop approach is not unexpected. The shear-strain threshold approach provides information on the level of ground motion that has not been experienced at Yucca Mountain. This approach does not provide information on the level that can occur. The upper range stress drop approach, on the other hand, provides a reasonable characterization of the level of ground motion that can credibly occur. The fact that this level is less than the level that has not been experienced is a logical and consistent result.

In summary, the horizontal PGV hazard curve from *Peak Ground Velocities for Seismic Events at Yucca Mountain, Nevada* (BSC 2005a, Section 6.8) is used as the basis for seismic hazard in the TSPA. Supplemental ground motions (BSC 2008, Appendix A, Section A4.5.2), based on an updated set of geotechnical data and using NUREG/CR-6728 Approach 3 (McGuire et al. 2001), indicate that, if only the shear-strain threshold approach to characterizing extreme ground motion at Yucca Mountain is considered, the mean annual probabilities of exceedance associated with the horizontal PGV hazard curve from *Peak Ground Velocities for Seismic Events at Yucca Mountain, Nevada* (BSC 2005a) should be higher. However, when the upper range stress drop approach to characterizing extreme ground motion is also included, the supplemental ground motions (BSC 2008, Section 6.5.3.2) indicate that the mean annual probabilities of exceedance for horizontal PGV at the waste emplacement level are lower, for a given level of ground motion, than those determined in *Peak Ground Velocities for Seismic Events at Yucca Mountain, Nevada* (BSC 2005a). Thus, use of the conditioned horizontal PGV hazard curve from *Peak Ground Velocities for Seismic Events at Yucca Mountain, Nevada* (BSC 2005a, Section 6.8) in the TSPA gives a reasonable representation of the expected behavior of the system. It provides slightly higher mean annual probabilities of exceedance for a given level ground motion than the more recent results in *Supplemental*

Earthquake Ground Motion Input for a Geologic Repository at Yucca Mountain, NV (BSC 2008, Section 6.5.3.2).

2.3.4.4 Rockfall Analysis

[NUREG-1804, Section 2.2.1.3.2.3: AC 1(1) to (4), AC 2, AC 3(1) to (3), AC 4, AC 5; Section 2.2.1.3.3.3: AC 1(3), (4), AC 3(3), (4), AC 4(4), AC 5(3)]

This section describes a rockfall analysis, which provides the information needed for structural analysis of drip shield response to rockfall, evaluating the impacts of rockfall on drift seepage, and estimating the impacts of rockfall on the in-drift environment. The following analyses are presented:

- Analysis of emplacement drift stability, including estimates of the rock mass damage and change in drift profile when subjected to loadings from in situ stress, transient thermally induced stress, and seismic ground motion–induced stress.

- Analysis of emplacement drift stability, including estimates of the rock mass damage and change in drift profile from time-dependent strength degradation of the rock mass when subjected to in situ and thermal loading in the presence of saturated rock conditions.

- Estimates of rockfall in terms of the block size distribution, impact velocity, impact location on the drip shield, and the total volume of rock blocks displaced during a seismic event.

- Estimates of the physical characteristics of the accumulated rubble resulting from rockfall (density or bulking factor) and the static load imposed on the drip shield from the rubble.

Ground support (Section 1.3.4.4) is not considered in the rockfall analyses described in this section. Rock bolt ground supports (Section 1.3.4.4.1) are stainless steel expansion anchors that are thin-walled. During the postclosure period, the ground supports will corrode and eventually fail. Collapse of the ground support into the drift will not damage the drip shield, since its impact is small relative to that of rockfall (excluded FEP 2.1.06.02.0A, Mechanical effects of rock reinforcement materials in EBS, Table 2.2-5).

Overview of Rockfall Analysis—Excavation of the emplacement drifts will result in the concentration of in situ stress around the openings. Since the in situ stresses are relatively small in comparison to the rock mass strength, little, if any, yield of the rock mass is expected due to in situ stress effects alone. The stability of the existing ESF and ECRB Cross-Drift tunnels (with minimal ground support) in lithophysal and nonlithophysal rocks supports this position. During the preclosure period, emplacement drifts will be ventilated, and drift temperatures will remain below approximately 75°C for a thermal loading of 1.45 kW/m (BSC 2004a, Figure Q-1), and, again, stability of the emplacement drifts is expected. At repository closure, forced ventilation is terminated, and the exhaust and main access drifts will be filled with crushed tuff. The temperature of the emplacement drifts and the surrounding rock mass will rise, reaching a peak temperature of approximately 145°C at about 20 to 30 years after closure. The temperature will then begin to decline over time, remaining above the boiling point of water at the waste package surface for approximately 1,000 years (BSC 2004a, Figures 6-25 and Q-1). Thermal expansion of

the rock will result in the addition of thermally induced stresses around the drifts, with the peak stresses occurring at the time of peak temperature, followed by a decrease in stress as the rock mass cools. The magnitude of the temperature and thermal stress change is a function of the heat output of the waste packages and the thermal properties of the rock mass. After repository closure, the walls of the emplacement drifts will be subjected to sustained loading from in situ and thermal stresses. Time-dependent microfracturing of the rock around the emplacement drifts will occur to some extent due to the environmental effects of the sustained stress and exposure to humidity (BSC 2004a, Section 6.4.2.4).

Analyses of the processes presented in this section take into account the range of uncertainty in the strength, elastic, and thermal properties of the various repository host units, and the rate of time-dependent strength degradation. In both the nominal and early failure scenarios (i.e., in the absence of seismic events), the analyses of drift stability show the following:

- Stress from in situ and thermal loading after repository closure has only a minor impact on yield around the emplacement drifts and does not result in significant drift degradation (BSC 2004a, Sections 6.3.1.3 and 6.4.2.4). Therefore, rockfall and drift collapse resulting from in situ stress and thermal effects (excluded FEPs 2.1.07.01.0A, Rockfall, and 2.1.07.02.0A, Drift collapse) have been excluded from performance assessment analyses (Table 2.2-5).

- Time-dependent strength degradation for the tuff host units varies for the expected loading conditions during the first 10,000 years after closure of the repository, depending on the rock mass quality. Substantial emplacement drift degradation is not expected for typical rock mass quality for this potential failure mechanism. In the poorest rock quality, representing less than 10% of the lithophysal rock mass, some damage and rockfall can be expected. Even in this poorest quality rock, time-dependent degradation alone is not expected to result in extensive damage or profile change in the emplacement drifts (BSC 2004a, Section 6.4.2.4.2.5, Figures S-37 and S-38). Therefore, drift collapse resulting from time-dependent rock mass strength loss (FEP 2.1.07.02.0A, Drift collapse) has been excluded from performance assessment analyses (Table 2.2-5).

Seismic events may occur after repository closure. The ground motions ensuing from an earthquake result in transient stress changes in the rock mass around the emplacement drifts. The amount of stress change is directly proportional to the PGV of the ground motion. The stability of the emplacement drifts is a function of the combined in situ, thermal, and seismic stress states, as well as the rock mass strength and deformability. In the seismic scenario, mechanical loads to the emplacement drifts include in situ and transient thermal stressing in addition to the stresses derived from low-probability seismic events. Uncertainties resulting from application of the PSHA process for prediction of the seismic hazard for the long postclosure time periods result in very conservative estimates of the magnitude of peak ground shaking (Section 2.3.4.3). Studies described in Section 2.3.4.3.3 show that bounds should be placed on the peak ground velocities based on shear strain limits of the rock mass. Nevertheless, the entire range of postclosure ground motions was used in estimating the damage potential to EBS features from rockfall and vibratory motion to allow evaluation of responses to the larger ground motions. Rockfall estimates are determined using both two- and three-dimensional discontinuum numerical modeling tools for representation of the fractured rock mass as well as the applied in situ, thermal, and seismic

loading. The models account directly for geologic structure (fractures and the effect of lithophysae, which are void spaces within the rock mass) in their formulation and have been validated through comparison against field observation and field-testing results as well as comparison to alternative modeling approaches. Data input for the models is derived from laboratory testing and in situ geotechnical characterization, and uncertainty is accounted for by using the range of expected variability in the rock mass properties and ground motions. Modeling analyses of rockfall for the full range of vibratory ground motion levels show that (Sections 2.3.4.4.4 and 2.3.4.4.5):

- Damage in the nonlithophysal rocks due to seismic shaking is characterized by small rock blocks with a median size of less than 0.2 MT. Although rare, the maximum block size can be greater than 20 MT. Structural calculations provided in Section 2.3.4.5.2 provide assessments of the damage and failure potential of the drip shield in response to impact from these rock blocks and Table 2.2-5 provides the basis for excluding the damage associated with rockfall. Note there is no propagated "failure potential" from such an effect.

- Estimates of damage in the lithophysal rock can be substantial for postclosure ground motions. Peak ground velocities of approximately 2 m/s or more can result in partial or complete collapse of the drifts.

- Loading from the seismically induced rubble that rests on the drip shield is estimated for complete collapse of the emplacement drift. The loads obtained from accumulated rubble are used as input to three-dimensional structural analysis of the drip shield. Structural calculations provided in Section 2.3.4.5.3 assess the damage and failure potential of the drip shield when subjected to the estimated static and dynamically amplified rubble load.

Analysis of the Impact of Vibratory Ground Motion—Vibratory ground motion was considered by application of site-specific ground motion time histories to the models for PGV levels of 1.05, 2.44, and 5.35 m/s. A suite of 15 three-component ground motion time histories developed at the repository horizon from actual scaled earthquake records (the waste emplacement level in Figure 2.3.4-4) is used for each postclosure PGV level. The multiple time histories ensure that a reasonable sampling of characteristics of earthquakes that make up the hazard have been incorporated into the time histories. For each set, time histories of two horizontal components (H1 and H2) and one vertical component (V) of acceleration, velocity, and displacement are supplied from the ground motion analysis, as described in Section 2.3.4.3.2. Note that the site-specific ground motions are unbounded and exceed the maximum bounded PGV of approximately 4 m/s (Section 2.3.4.3.3), and thus the estimates of rockfall and drift damage generated by the postclosure ground motions (e.g., a PGV of 5.35 m/s) are correspondingly conservative. A single three-component time history was developed for preclosure analyses with a PGV of 0.4 m/s and was also used for rockfall analysis. More recently, 15 three-component ground motion time histories at the 0.4 m/s PGV level were derived by scaling the ground motions at the 1.05 m/s PGV level (SNL 2007b, Appendix C). These 15 ground motions were used to quantify lithophysal rockfall volumes at the 0.4 m/s PGV level.

Rockfall for lithophysal units was analyzed to assess the effect of vibratory ground motion for a reasonable range or bounding of rock mass strength conditions that account for the effects of

lithophysal porosity on rock mass mechanical properties. A two-dimensional discontinuum modeling approach was used to simulate fracture and rockfall from the rock mass surrounding the emplacement drifts. Site-specific ground motion time histories appropriate for the postclosure period are used as inputs to this model. These studies found that complete drift collapse is expected for such a unit subjected to ground motions with peak ground velocities in excess of about 2 m/s. Damage to EBS components resulting from seismic-induced drift collapse (FEP 1.2.03.02.0C, Seismic-induced drift collapse damages EBS components) has been included in performance assessment analyses (Table 2.2-5).

A nonlithophysal rockfall model was developed using a three-dimensional discontinuum numerical modeling approach. This model explicitly utilizes fracture patterns generated from multiple sampling from a synthetic rock mass volume that contains a realistic fracture population based on field mapping data. Site-specific ground motion time histories appropriate for the postclosure period are used as inputs to this model (BSC 2004a, Section 6.3).

2.3.4.4.1 Conceptual Description of Rockfall Analysis

[NUREG-1804, Section 2.2.1.3.2.3: AC 1(1) to (4)]

This section provides a summary of the component parts of the rockfall analysis. Since the analysis is dependent on simulations using numerical models, the overall strategy employed in the development of the models and the geotechnical database is described first. This is followed by a discussion of the general geological features of the repository host horizon that are relevant to understanding the thermal-mechanical behavior of the rock mass. A description of the rock properties database and data uncertainty is followed by a summary of the analyses performed to estimate emplacement drift stability and rockfall for the nonlithophysal and lithophysal rock units of the repository host horizon. An analysis of emplacement drift stability when subject to in situ and transient thermal stress and analyses of seismic effects and time-dependent rock mass strength degradation are the primary analyses performed. A description of assumptions used in rockfall models is also provided. Lastly, an abstraction of the rockfall model is provided.

Model Development Strategy—The overall strategy employed in development of the rockfall analysis models involves: (1) development of a detailed understanding of the structural characteristics of the repository host rock units and how this structure affects rock mass mechanical and thermal properties, (2) development and validation of numerical modeling tools that are capable of representing the stress-strain response of site-specific repository rock units, and (3) use of the modeling tools to conduct performance analyses.

Implementation of this approach involved the following steps:

- Detailed geologic characterization of the repository host horizon rock units to provide a basic understanding of rock mass structure and its variability. These studies provide the basis for understanding the variability of rock mass properties.

- Extensive laboratory and in situ testing to define the mechanical and thermal properties and their ranges for the intact rock matrix, the fractures, and the large-scale properties of the lithophysal rock mass.

- Development and validation of two- and three-dimensional numerical models capable of representing the processes of failure and rockfall within the repository nonlithophysal and lithophysal rock units.

- Performance assessment analysis using numerical modeling to assess rockfall and time-related drift degradation as a function of in situ, thermal, and seismic loading states.

These steps provide a progression in development of understanding of the site geomechanical response, starting with basic geologic and geotechnical site description, followed by laboratory and field testing that provide basic information for development and testing of the models. An important point is that the rockfall models are formulated directly from site-specific geology and data. During the progression of this analysis, the ability of the models to adequately represent complex degradation modes, including block fallout and rock fracture resulting from stressing and time-dependence, is demonstrated (BSC 2004a, Sections 6.3 and 6.4). The stress analysis models developed are based on representing the rock mass as a "discontinuum" material (i.e., a mass that is composed of solid blocks of rock that are separated by fracture planes). These models allow direct simulation of the yield and degradation of emplacement drifts and the resulting rockfall that may occur from the applied postclosure loads. Specific analyses conducted using these models are reviewed below.

Analysis of the Impact of In Situ and Thermal Stresses—The application of in situ and thermal stress history to the emplacement drifts is part of both the nominal and early failure scenarios. Parametric thermal-mechanical stress analyses were conducted to examine the stability of emplacement drifts for nonlithophysal and lithophysal host rocks. Both the rock mass mechanical properties and thermal properties were varied over their proposed ranges. The parameter study included a base-case set of thermal properties and a sensitivity case considering the values for thermal conductivity and specific heat, which was 1σ smaller than the mean. The analyses indicate that there were only minor levels of drift yield and rockfall predicted at any time for all cases analyzed in the nominal case (BSC 2004a, Sections 6.3.1.3 and 6.4.2.4). When thermal stresses were considered in combination with the stresses resulting from postclosure seismic ground motion for the nonlithophysal rock, it was shown that thermal loading significantly reduces the amount of rockfall as a result of thermally induced tangential compression around the excavation periphery (BSC 2004a, Section 6.3.1.4).

Analysis of the Impact of Time-Dependent Rock Strength Degradation—Time-dependent effects on rock strength were examined separately for nonlithophysal and lithophysal rock units. In nonlithophysal rocks, drift degradation due to the effect of time-dependent changes of rock fracture strength was assessed based on an assumed reduction of fracture cohesion, friction, and dilation angles (BSC 2004a, Section 6.3.1.5). The dilation angle is a parameter related to the measure of how much volume increase occurs when the material is sheared. The reduced fracture strength parameters were conservatively estimated to be representative of cohesionless, smooth, and planar surfaces in which all surface roughness had been sheared off due to time-dependent effects. To achieve this condition, fracture cohesion and dilation angle (a measure of surface roughness) were reduced to zero and the fracture friction angle reduced to the postyield value of 30°. The degraded joint strength and dilational properties were applied for three of the postclosure rockfall analysis cases, including the case with most rockfall, the mean rockfall case, and a case in which no rockfall occurred. While a slight increase in rockfall is predicted for the degraded state, joint-strength

degradation has a minor impact on drift stability for nonlithophysal units. The progressive, time-dependent, stress corrosion microfracture damage of the matrix of the lithophysal rock units was represented by adjustment of the cohesive and tensile strength of the rock mass as a function of time (BSC 2004a, Section 6.4.2.4). The level of strength adjustment is based on laboratory measurements of time-dependent strength change measured by creep testing to define the static fatigue strength of the repository host horizon. Analyses show that extensive time-related degradation occurs in only the lowest-strength (i.e., having the highest lithophysal porosity content) areas of the lithophysal rocks, which represent less than 10% of the lithophysal rock mass (BSC 2004a, Section 6.4.2.4).

Output from Rockfall Analysis—Results of the rockfall analyses provide impact loading parameters for use in structural calculations described in Section 2.3.4.4.8, including rock block volume falling on the drip shield, relative impact velocity of the rock blocks to the drip shield, and impact location. Impact momentum and impact energy were also calculated as functions of block mass and impact velocity (BSC 2004a, Tables 6-11, 6-14, 6-17, and 6-20). Output also includes the static rubble load to the drip shield resulting from a complete collapse of the excavation (BSC 2004a, Section 6.4.2.5). These loads are used in drip shield structural stability analyses described in Section 2.3.4.4.8. Emplacement drift profile changes and rubble geometry resulting from seismic-induced drift collapse are also supplied to analyses of drift seepage flux and in-drift thermal and humidity environment for the seismic scenario class (BSC 2004a, Appendix R).

2.3.4.4.2 Data and Data Uncertainty for Rockfall Analysis

[NUREG-1804, Section 2.2.1.3.2.3: AC 2, AC 3(1) to (3)]

An extensive database of mechanical and thermal properties of the intact rock and fractures from the repository host horizon units is available from laboratory testing over the past 20 years. This database includes a significant amount of laboratory testing on small-diameter (25- and 51-mm-diameter) cores from surface boreholes and large-core (267- and 290-mm-diameter) samples of lithophysal rocks. These data have been supplemented by geotechnical rock mass classification and in situ mechanical and thermal testing within the repository host horizon in the ESF and ECRB Cross-Drift tunnels.

In this section, an overview of this database is presented, including a discussion of the sources and levels of uncertainty in the data. The properties of the rock mass are largely a function of the behavior of the intact rock matrix, coupled with the effects of the inherent geologic structure (i.e., the natural fracturing and the lithophysae). The term “rock mass” refers to the in situ rock material that is composed of the intact, solid rock matrix, as well as the inherent fracturing and porosity; the term “intact rock” refers to the solid rock matrix alone. The discussion in this section begins with a review of the geology of the repository host horizon, with emphasis on the geometry and structure of the fracturing and lithophysal porosity. The mechanical and thermal properties of the intact rock matrix and fractures, as determined in the laboratory, are described, as well as the impact of important environmental factors, such as pressure, temperature, and moisture. The intact matrix and fracture properties and the degree of lithophysal porosity are then used for definition of a base-case set of rock mass properties for lithophysal and nonlithophysal rock. A detailed review and analysis of the rock mass properties database is provided by *Subsurface Geotechnical Parameters Report* (BSC 2007a).

Rock Mechanical and Thermal Properties Used as Input for Design and Performance Assessment—To perform estimates of the mechanical degradation of emplacement drifts subject to stresses and time-dependent material property changes, the basic thermal and mechanical properties of fractures, intact rock, and the rock mass are required, as well as estimates of their variability within the repository host horizon. The following properties and geotechnical characteristics are required for input to rockfall analyses:

- Intact rock
  - Mechanical properties, including elastic moduli, unconfined and triaxial compressive strength (and associated shear strength properties), and tensile strength
  - Thermal properties, including thermal conductivity, thermal expansion coefficient, and heat capacity
  - Physical properties, including density and porosity.
- Rock fractures
  - Mechanical properties, including normal and shear stiffness and shear strength properties
  - Geometric properties of fracture sets (includes stochastic variability of fracture geometric parameters), including orientation (dip and dip direction), spacing, length, surface characteristics (roughness, planarity, and infilling materials), and fracture microstructure.
- Rock mass
  - Mechanical properties, including in situ compressive strength estimate (shear strength properties), in situ tensile strength estimate, deformation modulus, and surface roughness and associated dilation angle
  - Geometric properties, including engineering geotechnical classification (Q-System, Rock Mass Rating System, and Geological Strength Index) and geologic characterization of lithophysal porosity, size, shape, and distribution.

Laboratory testing of small-diameter (e.g., 25 to 51 mm) cores from surface-based boreholes and large-diameter cores (e.g., 267 to 290 mm) from drilling within the ESF and ECRB Cross-Drift and field geotechnical characterization form the bases for properties estimates and material model definition (BSC 2004a, Appendix E).

2.3.4.4.2.1 Geology of Repository Host Horizon

The rock units, their stratigraphy, and geologic evolution of the Yucca Mountain site are summarized in GI Section 5 and SAR Section 2, and have been described in detail in *Yucca Mountain Site Description* (BSC 2004c, Section 3.3). A summary of the geologic characteristics of

the repository host horizon relevant to the analysis of the mechanical degradation response of the repository excavations is provided in this section.

Site-specific characteristics of the rock units of the Topopah Spring Tuff that constitute the host rock at the repository horizon have been examined in detail through the geologic mapping of those units in both the main drift and ramps of the ESF and the ECRB Cross-Drift. These studies have been summarized for the ESF (Beason et al. 1996; Barr et al. 1996; Albin et al. 1997; Eatman et al. 1997) and for the ECRB Cross-Drift (Mongano et al. 1999). These studies are the sources for the site-specific unit descriptions presented here.

The locations of the ESF and ECRB Cross-Drift and the rock units excavated during construction of the tunnels are illustrated by a geologic map and cross section (Figure 2.3.4-21). The units that constitute the host rocks of the repository horizon are all zones of the crystal-poor member of the Topopah Spring Tuff. In descending order, the host rocks consist of the lower part of the upper lithophysal zone (Tptpul), the middle nonlithophysal zone (Tptpmn), the lower lithophysal zone (Tptpll), and the upper portion of the lower nonlithophysal zone (Tptpln). These units and their internal geologic structure are shown schematically in Figure 2.3.4-22.

The Topopah Spring Tuff includes both lithophysal and nonlithophysal rock units. The nonlithophysal rocks (the Tptpmn and Tptpln units) comprise roughly 15% of the emplacement area and are hard, strong, fractured rock masses. The lithophysal rocks (the Tptpll and Tptpul units) comprise approximately 85% of the emplacement area (about 80% of emplacement is within the Tptpll) (BSC 2003a, Attachment II). These rocks contain macroscopic voids (lithophysae) resulting from trapping of gas during the cooling process and are relatively more deformable with lower compressive strength than the nonlithophysal units. The lithophysal units have fewer fractures of significant continuous length (i.e., trace length greater than about 1 m). Lithophysal porosity in the Tptpul and Tptpll ranges from less than about 10% to approximately 30% by volume. The groundmass that makes up the rock matrix in the lithophysal units is mineralogically the same as the matrix of the nonlithophysal units, but it is heavily fractured with small-scale (lengths of less than 1 m) interlithophysal fractures in the Tptpll and is relatively free of fractures in the Tptpul (BSC 2004a, Section 6.1.4.1).

These two rock types, while compositionally similar, have very different physical and mechanical properties due to the difference in their internal geologic structure (fracture sets in nonlithophysal rock, lithophysae, and ubiquitous, short fractures in lithophysal rock) and have fundamentally different modes of failure under dynamic loading associated with seismic events. They also require different analysis methods for assessment of rockfall. Consequently, the rockfall analysis methodology described in this section has two primary approaches based on different analysis methods for lithophysal and nonlithophysal units.

2.3.4.4.2.2 In Situ Stress State

The stress state at Yucca Mountain is characterized by a vertical major principal stress equal to the gravitational gradient, and by secondary horizontal principal stresses with magnitude of approximately 0.62 and 0.36 times the vertical component. The in situ stress state at and in the vicinity of the Yucca Mountain site was determined by hydraulic fracturing (SNL 1996; Stock et al. 1985). A summary of the measurements is given in Table 2.3.4-5.

2.3.4.4.2.3 Geotechnical Data

The rock matrix material is typically strong and elastic, and, thus, the structure of the rock mass plays an important role in defining the properties and overall mechanical response of the rock mass to thermal and mechanical loading. In particular, the fracture geometry and properties in the nonlithophysal rocks and the degree of lithophysal porosity in the lithophysal units are the primary geologic structural features that impact rock mass behavior. Therefore, a significant effort was expended in describing the geometric and surface characteristics of the fractures and lithophysae and in determining the impact of these features on rock mass properties.

Extensive geotechnical mapping of fractures was performed in the ESF and the ECRB Cross-Drift (Beason et al. 1996; Barr et al. 1996; Albin et al. 1997; Eatman et al. 1997; Mongano et al. 1999). The occurrence of longer-trace-length (trace length greater than 1 m) fractures and lithophysae is roughly inversely proportional where the fracture density determined from detailed line mapping and the approximate percentage of lithophysal porosity in the ECRB Cross-Drift are shown. This is demonstrated quantitatively in Figure 2.3.4-23 for fractures with trace lengths greater than 1 m. The density of fractures with trace length greater than 1 m is significantly larger in the Tptpmn and Tptpln (20 to 35 fractures per 10 m) compared to five fractures per 10 m or less in the Tptpul and Tptpll. Conversely, lithophysae are sparse in the Tptpmn and Tptpln but abundant in the Tptpul and Tptpll.

2.3.4.4.2.3.1 Characterization of Fractures

Fracturing in the Tptpmn—Full periphery and detailed line survey maps, consisting of a description of orientation, trace length, small- and large-scale roughness, and end terminations for all fractures with trace lengths greater than or equal to 1 m, were created for all exploratory drifts (BSC 2004a, Table 4-1).

Results of this mapping indicate that there are four sets of fractures in the Tptpmn with the geometric and surface characteristics summarized in Table 2.3.4-6. The fractures have relatively short continuous trace lengths (Figure 2.3.4-24) with median values for the four sets ranging from 2.8 to 3.7 m (BSC 2004a, Table 6-1). Fracture ends often terminate either against other fractures or in solid rock.

The subvertical fractures, in particular, often have curved surfaces with large-amplitude (dozens of centimeters) asperities and wavelength of meters. Fractures sometimes terminate in solid rock with discontinuous interconnection to adjacent joint tracks (i.e., a rock “bridge”) or terminate against other joints. The subhorizontal vapor-phase partings are relatively continuous structures seen throughout the Tptpmn. These continuous but anastomosing fractures are subparallel to the dip of the rock unit, and are filled with concentrations of vapor-phase minerals. The surfaces are rough on a small scale and, unlike the subvertical fractures, have cohesion as a result of the mineral filling (BSC 2004a, Section 6.1.4.1).

Fracturing in the Tptpll—Short-length fractures (less than 1 m trace length), coupled with the presence of lithophysae, are the most important features that govern mechanical properties in the Tptpll. Whereas the Tptpul tends to have sparse, small-scale interlithophysal fracturing, the Tptpll has abundant fracturing. Thin-section analyses of fracture surfaces in the Tptpll and the Tptpmn

show vapor phase alterations on most of the fracture surfaces within the rock mass away from the tunnel wall (BSC 2005a, Appendix A). The short-length fracture geometry is also consistent with the general cooling fracture population. These factors indicate that the short trace-length fractures are cooling-related rather than induced by excavation. Near the tunnel wall, many of the fractures were disturbed by mining, and some new, stress-induced, wall-parallel fractures were created in the immediate springline (sidewall) of the tunnel. Compared to the nonlithophysal units (i.e., the Tptpmn and Tptpln), the abundant small-scale fractures that are present between lithophysae in the Tptpll result in the relatively weaker nature of this material. Wall-parallel fractures in the immediate sidewall of the tunnel were not observed in either the nonlithophysal units or in the Tptpul (which has sparse interlithophysal fracturing). It is expected that excavation or stress-induced fractures would only impact the Tptpll. The Tptpll has a ubiquitous fracture fabric composed of short trace-length, discontinuous fractures. These fractures tend to create blocks with dimensions on the order of about 10 cm or less on a side (BSC 2004a, Section 6.1.4.1). This observation in the Tptpll is important to the discussion of mechanical degradation of the emplacement tunnels. Based on the ubiquitous fracture and lithophysae fabric, it is assumed that the potential mode of failure within the Tptpll under seismic or time-dependent yield will be in a raveling mode that creates small block sizes.

2.3.4.4.2.3.2 Characteristics of Lithophysae

Although the character of the lithophysae varies between the Tptpul and Tptpll, the mineralogy of the matrix material within both of these units is the same as in the nonlithophysal units.

The lithophysae in the Tptpul have the following characteristics:

- Smaller size (roughly 1 to 30 cm in diameter) relative to the Tptpll
- Uniformity in size and distribution within the unit
- Variability of infilling and rim thicknesses (The lithophysal cavities often have a crust or rim of altered mineral coating related to movement of gas vapor through the rock mass during the cooling process, which occurred shortly after the volcanic unit was deposited.)
- Volume percentage that varies consistently with stratigraphic position
- Stratigraphic predictability (i.e., uniformity of location and thickness within the Topopah Spring unit).

In contrast, the lithophysae in the Tptpll tend to be highly variable in size, ranging from roughly 1 cm to 1.8 m in diameter. They also have the following traits:

- Shapes that are highly variable, from smooth and spherical to irregular and sharp boundaries
- Infilling and rim thickness that vary widely with vertical and horizontal spacing

- Volume percentages that vary consistently with stratigraphic position
- Stratigraphic predictability.

With the bulk of the repository located in the lower lithophysal zone, a detailed study of the lithostratigraphic features in this unit exposed in the ECRB Cross-Drift was performed (BSC 2004a, Appendix O). Results of this work document the distributions of size, shape, and abundance of lithophysal cavities, rims, and spots (i.e., poorly formed lithophysae that are filled with welded tuff of a high porosity). These data can be displayed and analyzed as local variations, variations along the tunnel, and summary statistics over the entire Tptpll (BSC 2004a, Appendix O).

In addition to variation along the tunnel for the abundance of features such as lithophysae, there is also variation in the size, shape, and distance between features. This heterogeneity is recorded as a function of distance along the ECRB Cross-Drift through the Tptpll unit (e.g., Figure 2.3.4-25). This information provides direct input to mechanical degradation studies in the following ways:

- The panel maps and porosity size and shape variations of lithophysae provide the basis for numerical estimation of impact of lithophysae on rock mass properties.
- Rock mass properties in the lithophysal rocks are primarily a function of structure and porosity. The variation in porosity across the Tptpll provided by the direct panel mapping allows the variation and ranges in rock mass properties to be estimated.

2.3.4.4.2.3.3 Mechanical Intact Rock Properties of Nonlithophysal and Lithophysal Rocks

In the late 1970s through the mid-1980s, many samples were tested from geologic units extending from the uppermost parts of the Paintbrush Tuff down through the lower regions of the Crater Flat Tuff (pre–Prow Pass volcanic group, Figure 2.3.4-21). A discussion of the available intact rock mechanical properties test data can be found in *Subsurface Geotechnical Parameters Report* (BSC 2007a, Section 6.4.2). A baseline standard set of rock test conditions was adopted with environmental conditions (e.g., temperature, saturation, sample size) examined relative to that standard. The following baseline conditions were defined: (1) test specimens were right-circular-cylinders, with a nominal diameter of 25 mm and a 2-to-1 length-to-diameter ratio; and (2) specimens were tested in a water-saturated state at room temperature, atmospheric pressure, and a nominal axial strain rate of 10^{-5}. The results from this test series (Olsson and Jones 1980; Price and Jones 1982; Price, Jones et al. 1982; Price and Nimick 1982; Price, Nimick et al. 1982; Price, Spence et al. 1984) revealed that there is some lateral (i.e., within a unit) and vertical (i.e., unit to unit) variability of properties; however, the variabilities in the elastic and strength properties of the tuffs (all having similar chemical constituents) are predominantly a function of the porosity (Price 1983; Price and Bauer 1985).

Beginning in the mid-1980s, effort was concentrated on the Topopah Spring formation and, specifically, on the Tptpmn; however, testing was also performed on the matrix material of lithophysal units as well. Most of the mechanical properties testing was conducted on small (25 to 51 mm) cores taken from surface boreholes. The properties testing was centered on conducting standard uniaxial and triaxial compression tests to define the shear strength and modulus as

functions of temperature and level of water saturation. Indirect tensile strength tests were also conducted (BSC 2005b, Sections 6.1, 6.3.2, 6.3.4, and 6.3.5). These studies reinforced previous testing results that showed that the most dominant factor in mechanical properties variability is the rock porosity (Figure 2.3.4-26). A secondary factor in the variability of strength or Young's modulus is the distribution of the porosity. Porosity in the Tptpmn was found to be in the form of intergranular openings (usually less than 5 μm across) (Price, Connolly et al. 1987). The lithophysal rocks are characterized by similar intergranular porosity in the matrix material but have additional porosity in the form of lithophysal cavities. A significant amount of data for intact mechanical properties of nonlithophysal rock exists from core testing. This testing has been conducted at a variety of environmental conditions to allow definition of the impact of temperature, moisture content, and pressure on the intact properties to be defined. The factor with the largest impact on mechanical properties is porosity; size of the rock sample also has a significant impact on rock strength. Sufficient data have been developed to adequately define the effect of both porosity and size of the rock sample on nonlithophysal rock properties (BSC 2007a, Section 6.4).

2.3.4.4.2.3.3.1 Time and Rate Dependence of Intact Rock Strength

Several studies have been conducted to determine time-dependent properties of welded tuffs (Martin, Price et al. 1993; Martin, Price et al. 1995; Martin, Noel et al. 1997a; Martin, Noel et al. 1997b). Six nonlithophysal rock samples obtained from the Tptpmn at Busted Butte and an additional eight samples from the Drift Scale Test site in the Tptpmn were used to conduct static fatigue experiments with saturated rock conditions at 125°C and 150°C. Busted Butte is a topographic feature immediately south of Yucca Mountain where surface exposures of the Topopah Spring unit can be found. The static fatigue test is a constant stress (creep) test designed to determine the relationship of the time-to-failure of a rock as a function of the applied stress. As the applied stress approaches the compressive strength of the rock, the time to failure decreases. The degree of time-dependency depends on a number of factors, including the mineral constituents of the rock, the grain structure, and the moisture and temperature conditions. These data are used in time-dependent drift stability calculations to define the rate of strength decay as a function of stress state. The uncertainty in time-dependent effects on strength of welded tuffs is considered to be high. Further investigation of uncertainty in the time-dependent models of drift degradation was performed by using the time-dependent strength degradation obtained from extensive test data from Lac du Bonnet granite as a lower bound to the time-dependent strength loss of the Topopah Spring tuff. The extent of the drift degradation predicted when using these lower-bound considerations (the overall conclusions regarding extent and timing of collapse) are not significantly different (BSC 2004a, Appendix S).

2.3.4.4.2.3.3.2 Effect of Sample Size and Anisotropy

As a result of heterogeneity within a rock mass, the compressive strength is a function of the size of the sample tested. Two separate studies to assess the effect of sample size on compressive strength were conducted for nonlithophysal samples (Price 1986; BSC 2004a, Appendix E). More than 100 samples taken from the Tptpmn and the lower, lithophysae-poor portion of the Tptpll with sizes ranging from 26 to 290 mm in diameter were tested to examine both size effect and mechanical anisotropy. The results of the sample size on unconfined compressive strength are shown in Figure 2.3.4-27. In this figure, the unconfined compressive strength is plotted as a function of the sample volume (as a log–log plot). The vertical offset of the two lines is indicative of the slightly

different average strength of the Tptpll and Tptpmn matrix material tested in the two studies. The samples from the Tptpll were taken from a large surface block found near the contact with the Tptpln. There were few lithophysae in the block, so the samples were essentially nonlithophysal in character. The size effect (slope of the lines) is virtually identical for the two studies, indicating that the matrix material from these repository units has a similar strength size effect. The mechanical anisotropy results indicate that there is a maximum anisotropy of approximately 10% in the average matrix moduli, which is considered to be a second-order effect in comparison to the impact of lithophysae and fracturing on moduli and strength (BSC 2004a, Appendix E). The uncertainty associated with size effects of nonlithophysal rock is considered to be low due to the significant size range of samples tested and the agreement of matrix strength properties from different nonlithophysal units of the Topopah Spring Tuff (BSC 2004a, Section 6.5).

2.3.4.4.2.3.3.3 Effect of Sample Saturation

The impact of saturation level on unconfined compressive strength has also been examined. Results presented in Table 2.3.4-7 indicate that moisture has a significant effect on compressive strength. In particular, samples that were heated-dry show greater compressive strength than those that were exposed to humid air conditions. Complete drying of samples increases the mean strength of the samples tested by approximately 35%. This strength decrease in the presence of moisture is consistent with other testing of silicic rocks and may be associated with a stress-corrosion mechanism involving chemical alterations due to moisture in flaws within the samples. The compression test data reported here are at room humidity conditions, unless otherwise noted. Following a conservative design approach, performance calculations for postclosure effects are conducted with strength values based on room temperature testing results with data ranges to cover fully saturated conditions. Uncertainty due to effects of saturation are accounted for by performing stability analyses of emplacement drifts for a full range of rock mechanical properties that include the effects of saturation (BSC 2004a, Appendix E).

2.3.4.4.2.3.3.4 Large-Core Laboratory Testing of Lithophysal Rocks

To obtain more representative samples of lithophysal rocks, which contain lithophysal voids, a series of large-diameter (290-mm) core samplings of the Tptpul and Tptpll were taken in the ESF and ECRB Cross-Drift. These samples were tested in addition to 267-mm diameter samples of the Tptpul that were obtained from rock outcrops at Busted Butte. Compression testing of these cores was conducted at dry and saturated rock conditions to define the unconfined compressive strength and Young's modulus variability with lithophysal porosity content. Results show unconfined compressive strength of the Tptpll and Tptpul from these large cores can vary from as high as about 25 to 30 MPa for low porosity samples to as low as about 10 MPa for high-porosity samples. The Young's modulus for these same tests can vary from 20 to 5 GPa. The primary factor influencing the variability of the unconfined compressive strength and Young's modulus is the sample porosity (BSC 2004a, Appendix E).

An appropriate way of presenting these data is in terms of the relationship between the unconfined compressive strength and Young's modulus (Figure 2.3.4-28). Some of the primary mechanical inputs to numerical stability models are the compressive strength and modulus. This plot illustrates the generally linear relationship of these parameters, the range of the data, and the scatter of the results. Those tests conducted under saturated conditions follow a similar trend but form a lower

bound to the room dry strength results. The entire range of the large-core test data is subdivided into a series of strength and modulus categories for design and performance parameter studies. As described in Section 2.3.4.4.5, variability in the mechanical properties of lithophysal rock is explored through the use of discontinuum numerical models calibrated to this large-core database. The models are used to examine the impact of variability of lithophysal porosity, shape, size, and distribution on the variability of the unconfined strength and Young's modulus as a means of defining reasonable bounding ranges of lithophysal rock mechanical properties (BSC 2004a, Section 7.5).

2.3.4.4.2.3.3.5 Summary of Mechanical Properties Laboratory Testing

A large amount of data has been collected to date on samples of tuffaceous rock from Yucca Mountain at a baseline set of test conditions. These data have shown that the variabilities in elastic and strength properties are not a function of lateral or vertical position within the repository host horizon but are primarily a function of porosity. Even though there are distinct trends in the Young's modulus and strength data as functions of porosity, the data have significant scatter. The distribution of porosity is a secondary effect that creates the scatter. Investigations have examined the effects of many other conditions; for example, sample size, saturation, pressure, temperature, deformation rate, and anisotropy have been studied. As a result, the intact rock mechanical property information collected over the last two decades has provided an understanding of many aspects of the behavior of Yucca Mountain tuffs. The greatest level of uncertainty in the mechanical properties of intact rock specimens is due to porosity of the samples. Data have been gathered to characterize the effect of porosity on the range of rock mechanical properties (Figure 2.3.4-26). This uncertainty is accounted for in rockfall modeling studies through use of ranges of properties that bound the mechanical properties as functions of porosity and environmental effects such as temperature and saturation.

2.3.4.4.2.3.4 In Situ Mechanical Testing of Nonlithophysal and Lithophysal Rock Mass Properties

In situ testing was used to provide data on the mechanical characteristics of the rock mass at a scale commensurate with the excavation dimension. Field compression testing was performed in both the nonlithophysal and lithophysal rocks. For nonlithophysal rocks (Tptpmn), the Plate Loading Test, conducted as part of the larger Drift Scale Test, was used to apply load to the drift wall adjacent to the Drift Scale Test in the Tptpmn unit. The results of the testing show an estimated rock mass modulus of the immediate drift wall from 11.4 to 29.5 GPa for ambient and thermally perturbed fractured tuffs, respectively (George et al. 1999). The relatively low value of rock mass modulus at ambient temperature is indicative of the fractured periphery of the excavation.

A series of three pressurized slot tests was conducted to perform deformation modulus (i.e., Young's modulus of the rock mass) and strength measurements in lithophysal rock units (Table 2.3.4-8). All three tests included ambient temperature compressions, and one test included compressions at elevated temperature. These tests involved using parallel saw cuts to isolate a block of rock approximately 1 m^3 in the sidewall or floor of the ESF or ECRB Cross-Drift and then compressing the block by pressurizing flatjacks placed in the slots. Deformation was monitored using instrumentation in a borehole drilled centrally between the slots (BSC 2007a, Section 6.6).

Results show a typical elastic–plastic response, in which a linear loading slope is followed by yield and plastic deformation. Yielding of the rock in the first test occurred through formation of shear fractures in the block, resulting in extensive rockfall in the form of small rock fragments in the central borehole during yield. The second test failed early by inducing movement on a through-going fracture located outside the block. The third test resulted in extensional spalling of the floor of the tunnel above the actual loaded zone without ever reaching the peak comprehensive strength of the rock. The deformation modulus and the peak pressure applied to the flatjacks (not the rock mass strength as a result of the presence of the central hole) are summarized in Table 2.3.4-8. The results show that the deformation modulus lies at the lower end of the range given in Figure 2.3.4-28. The low values of modulus in the first two tests are indicative of the fact that the tests were conducted in the immediate skin of rock at the springline of the tunnels, which has been subjected to mining disturbance and in situ stress concentration. The data, therefore, reflect the deformation modulus of this fractured and disturbed rock and not the undisturbed rock mass. Since this low-modulus region is localized, it is not taken into account in performance or design mechanical analysis (BSC 2007a, Section 6.6.4.3).

2.3.4.4.2.3.5 Mechanical Properties of Fractures

Shear properties of fractures, including fracture cohesion, shear strength, and shear dilation angle, are needed as input to rockfall models. A series of five direct shear tests was performed on 290-mm diameter Tptpmn core samples that contained fractures. Two types of fractures were tested: subvertical cooling fractures and horizontal vapor-phase partings. Cohesion and friction angle parameters were determined from repeated tests on the same fracture surface (BSC 2004a, Appendix E). Results are shown in Table 2.3.4-9. The level of uncertainty in the strength and stiffness properties of natural fractures is judged to be moderate. This level of uncertainty is accounted for in the modeling analyses through use of reasonable bounding ranges of fracture properties. For example, as described in Section 2.3.4.4.4.5, sensitivity studies of rockfall were conducted assuming lower bounding strength properties for fractures with no cohesion or dilation, and residual friction angle (i.e., friction for sheared surfaces).

2.3.4.4.2.3.6 Thermal Properties

The thermal properties used in the thermal-mechanical calculation of stresses due to heating and cooling of the repository (BSC 2004a, Section 6.2) are provided in this section. These data include thermal conductivity, specific heat, and thermal expansion for the various lithostratigraphic and thermal-mechanical units of the Yucca Mountain rock strata. The mean values for thermal-mechanical units are determined by averaging the thermal properties of the lithostratigraphic units within each thermal-mechanical unit, weighted according to the thickness of each lithostratigraphic unit (BSC 2004a, Appendix E).

Thermal properties, such as thermal conductivity, heat capacity or specific heat, and coefficient of thermal expansion of lithostratigraphic rock units at the repository host horizon are important parameters used in models supporting the TSPA. Their values are estimated primarily based on laboratory and field measurements. A majority of the data are from the following units: Tptpul and Tptpll (lithophysal) and Tptpmn and Tptpln (nonlithophysal).

Numerous laboratory tests using small specimens containing few voids or fractures show that intact rock thermal characteristics of these two types of rocks are similar (BSC 2007a, Section 6.5.1). However, rock mass characteristics of these rocks can be quite different due to their different dominant features (i.e., large-scale voids) or fractures. These impacting factors are reflected in the differences in their rock mass thermal properties.

2.3.4.4.2.3.6.1 Thermal Conductivity

Rock Matrix Thermal Conductivity—Thermal conductivity of intact rock was estimated based on laboratory thermal conductivity measurements using small specimens with nominal dimensions of 50.8 mm in diameter and 12.7 mm in length (Brodsky et al. 1997, Section 2.1, Table 2-1) and containing few voids or fractures. The results are summarized in Table 2.3.4-10 for the four rock units at the repository host horizon.

Rock Mass Thermal Conductivity—Thermal conductivity of the rock mass is the effective value of thermal conductivity that relates the heat conduction rate to the temperature gradient in a rock mass. The effective value accounts for the effects of voids, fractures, and any heterogeneity or discontinuities on thermal conductivity (BSC 2004d, Section 6.1).

A number of experimental tests were conducted to estimate rock mass thermal conductivity. They included laboratory measurements using large specimens and field measurements in the Drift Scale Test and the ECRB Cross-Drift. In the Drift Scale Test (which heated a drift-scale volume of rock mass), measurements were made on the Tptpmn unit; in the ECRB Cross-Drift, they were made on the Tptpll unit. Results show that the in situ values are within the range of those observed in the laboratory measurements on small specimens (e.g., size 50-mm diameter) (BSC 2007a, Section 6.5.3).

Analytical approaches were also developed as an alternative method of estimating rock mass thermal conductivity as a function of porosity to confirm field measurements (BSC 2004d, Section 6.1). The analytical approaches are based on models of the thermal conductivity of a two-phase (solid and fluid) rock matrix, with heterogeneity introduced in the form of lithophysal porosity (idealized as spheres, disks, and thin cracks) (BSC 2004d, Sections 6.1.7 and 6.1.8). The estimate of rock mass thermal conductivity, based on the analytical approach, is summarized in Table 2.3.4-11. Comparing the analytical approach for estimating rock mass thermal conductivity (Table 2.3.4-11), which includes the effects of lithophysae, to the laboratory measurements of thermal conductivity for intact rock (Table 2.3.4-10), it is apparent that both porosity and moisture content have a significant effect on the rock mass thermal conductivity. Given the impact of porosity and moisture content and the associated uncertainty, a range of thermal conductivities representing lithophysal and nonlithophysal rocks and saturated and dry conditions is used for the parametric thermal calculations presented in Section 2.3.4.4.3.2 (BSC 2004a, Section 6.2).

2.3.4.4.2.3.6.2 Heat Capacity

Heat capacity of a substance is defined as the amount of energy required to raise the temperature of a unit mass of the substance by 1°C and is a required material parameter used in thermal analysis for evaluation of temperature changes in rock after waste emplacement. For solid materials, heat capacity is strongly dependent on temperature. For the temperature range of interest in TSPA, heat

capacity for the repository rock units is estimated for three temperature ranges: 25°C to 94°C, 95°C to 114°C, and 115°C to 325°C, corresponding to the preboiling, transboiling, and postboiling regimes, respectively. The heat capacity values used in the design and performance assessment are largely based on the calculated values obtained from analytical methods (BSC 2004e).

Rock Grain Heat Capacity—The calculated average values of rock grain heat capacity for four repository rock units are presented in Table 2.3.4-12. These values were estimated based on available data on mineral abundance and mineral heat capacity (BSC 2007a, Section 6.5.3.2.2).

Rock Mass Heat Capacity—Rock mass heat capacity is the effective value of heat capacity that accounts for the rock matrix as well as air-filled voids and water that may exist in the voids. The rock mass heat capacity has been estimated in the Tptpll from field tests and from analytical calculations based on grain heat capacity, porosity, density, and degree of saturation (BSC 2007a, Section 6.5.3.2).

The calculated values of rock mass heat capacity for four repository rock units using analytical methods are summarized in Table 2.3.4-13. These values were estimated for the preboiling, transboiling, and postboiling regimes, based on the available data on rock matrix porosity and saturation, lithophysal porosity, rock grain heat capacity, and density (BSC 2007a, Section 6.5.3.2.2).

2.3.4.4.2.3.6.3 Coefficient of Thermal Expansion

Thermal expansion is a mechanical response in the form of displacement in response to a change in temperature. Thermal expansion is an important parameter in thermal-mechanical analysis for prediction of thermally induced rock displacements and stresses. Numerous measurements of thermal expansion coefficients have been conducted on small cores of intact nonlithophysal rock as well as large cores of lithophysal rock, and through direct measurement of rock mass thermal expansion from field heating experiments (BSC 2007a, Sections 6.5.2.3 and 6.5.3.3).

Field measurements of rock mass coefficient of thermal expansion were made for the Tptpmn unit during the Drift Scale Test (Table 2.3.4-14). The rock mass coefficient of thermal expansion for the Tptpll has been measured in the laboratory on samples with nominal diameter of 290 mm to account for lithophysae effects. Measurements were conducted on dry or saturated specimens over a temperature range of 40°C to approximately 200°C (BSC 2007a, Section 6.5.3.3).

Comparison of the rock mass and intact coefficients of thermal expansion indicate that the intact values are larger and that the difference between the two data sets decreases with increasing temperature, indicating that the effect of fractures or voids on coefficient of thermal expansion diminishes as more fractures or voids are closed as temperature increases. To deal with uncertainty in the coefficient of thermal expansion, the intact coefficient of thermal expansion, presented in Table 2.3.4-15, is selected for use in thermal-mechanical rockfall analysis as it leads to larger, and thus conservative, thermally induced stresses (BSC 2004a, Appendix E).

2.3.4.4.2.3.7 Base-Case Mechanical Property Sets for Rockfall Analysis

The base-case mechanical properties for lithophysal and nonlithophysal rock are derived from the testing of intact rock large-core and fracture testing described in the previous sections. It is typical in geomechanics to model a rock mass as an equivalent continuum material in which the mechanical properties of the rock mass are "averaged" from the combined effects of the intact rock blocks and fractures. Typically, the "averaged" properties are estimated from empirical geotechnical classification schemes. The objectives of the rockfall analyses are to provide estimates of drift stability under seismic loading and, explicitly, the rockfall block masses, velocity, and total volume as well as the final, damaged profiles of the excavations. This requires that the modeling approach explicitly represent the mechanical effects of the intact blocks and fractures rather than use a continuum-based, properties "averaging" approach. The modeling approach used in the rockfall analysis is based on the use of discontinuum models that allow explicit representation of the intact rock blocks and fractures. Therefore, the base-case mechanical properties set forth below for describing the rock mass are based on the laboratory testing of intact blocks of nonlithophysal rock and fractures and on the large-core testing of lithophysal rock (BSC 2004a, Appendix E).

Lithophysal Rock Mass Properties—The primary physical feature impacting rock mass strength and modulus in the lithophysal units is the porosity. As seen in Figure 2.3.4-28, the large-core laboratory data show a range in unconfined compressive strength from approximately 10 to 30 MPa with a corresponding range in Young's modulus from approximately 5 to 20 GPa. The estimated sample lithophysal porosity varies from approximately 10% to 30% over this range or is roughly comparable to the range of in situ values defined from mapping in the ECRB Cross-Drift. Thus, the core sampling used for the laboratory testing spans roughly the same range of lithophysal porosity as observed throughout the ECRB Cross-Drift (BSC 2004a, Appendix E).

The rockfall analyses described in Section 2.3.4.4.5 are based on sensitivity studies for reasonable bounding ranges of lithophysal rock mechanical properties. To establish the mechanical rock properties, the range of room dry test results shown in Figure 2.3.4-28 are subdivided into five categories, based on 5 MPa increments of unconfined compressive strength. The associated Young's modulus for each unconfined compressive strength category is derived from the linear data fit to the room dry test results given in Figure 2.3.4-28. The base-case strength and modulus for each of the categories and the approximate equivalent lithophysal porosity for each of these categories are given in Table 2.3.4-16. These categories represent the range of possible rock properties conditions found in the Tptpll. To determine how important each of these categories is to actual tunnel conditions, a correspondence of the rock strength category to in situ lithophysal porosity was developed. The relationship of these property ranges to their abundance in the Tptpll was determined by examining the variation in lithophysal porosity from mapping in the ECRB Cross-Drift (BSC 2004a, Appendix O). Figure 2.3.4-29 shows a histogram of the abundance of lithophysal porosity from field mapping, as well as photographs of representative drift wall sections for categories 3 (19% lithophysal porosity), 4 (13.3% lithophysal porosity), and 5 (8.5% lithophysal porosity) rock. The histogram indicates that the lowest strength categories (1 and 2) represent less than 10% of the Tptpll and that over 90% of the Tptpll is characterized by lithophysal porosity representative of category 3 or higher rock (BSC 2004a, Appendix E).

As stated in Section 2.3.4.4.2.3, the overall percentage of porosity is the primary controlling factor on lithophysal rock mechanical properties. Additionally, the distribution of that porosity, as well as

the size and shape of lithophysal cavities, affects the variability of mechanical properties at any given percentage of porosity, and, thus, the level of uncertainty in the mechanical properties of the lithophysal rock mass is high. To deal with this uncertainty, reasonable bounding ranges to the base-case properties were defined using a numerical model, PFC, which refers collectively to PFC2D and PFC3D. PFC is a commercial discontinuum numerical modeling program that represents rock as an assemblage of bonded granular particles. The program allows modeling of the development of shear and tensile fracturing of a rock mass and the ability to study the effects of the rock structure on its stress-strain behavior. This numerical model was used to explore the impact of lithophysae size, shape, and distribution on the variability of the mechanical properties (BSC 2004a, Appendix E). From these results, the bounding ranges of mechanical properties were determined. The PFC model of lithophysal rock was initially calibrated against the large-core lithophysal mechanical property database. Once calibrated, this mechanical model of lithophysal rock was used to study the impact of actual field shapes, sizes, and distribution of lithophysae on the stress-strain response and, thus, its mechanical properties. This modeling was used to provide insight into the variability of mechanical properties for a given level of porosity. Figure 2.3.4-30 presents the plot of unconfined compressive strength versus Young's modulus for the laboratory data shown previously (Figure 2.3.4-28), but with the addition of PFC results to indicate bounding ranges of lithophysal properties. These upper and lower bounding ranges, as well as the base-case data fits obtained directly from large-core testing, are used in performance assessment modeling. A lower-bound strength cutoff at 10 MPa is shown on this plot. This lower-bound strength cutoff was derived from sensitivity studies in which the stability of the existing ESF and ECRB Cross-Drift tunnels was examined. These sensitivity studies, conducted using stress analysis models, found that instability would be expected for these tunnels under the current in situ stress conditions if the in situ rock strength was below about 10 MPa. This instability would take the form of obvious shear failure of the sidewalls of the tunnel and would be easily recognizable and require additional wall ground support. On the contrary, the ESF and ECRB Cross-Drift are in excellent structural condition, with no extensive sidewall failures observed, even though the sidewalls are largely unsupported. Therefore, a lower-bound strength cutoff at 10 MPa is used. It is also noted that none of the large-core laboratory testing data show results below this lower bound (BSC 2004a, Appendix E).

Nonlithophysal Rock Properties—The nonlithophysal rock is represented as a fractured media composed of intact rock blocks separated by discontinuous fracture surfaces. The primary mechanical properties required as model input include the intact rock block elastic and strength parameters and the strength and stiffness properties of the rock fractures. The base-case properties used for simulations of nonlithophysal units are presented in Table 2.3.4-17. Uncertainty in the intact rock block and fracture properties is addressed via sensitivity studies as described in Section 2.3.4.4.4.5.2. The sensitivity studies examine the impact of a range of strength properties of the rock blocks and fractures on rockfall estimates from seismic loading.

2.3.4.4.2.4 Data Uncertainty

Fracture Geometry Data—The natural variability of fractures within a rock mass represents epistemic uncertainty in the design of engineering structures in rock. The large amount of fracture data collected at Yucca Mountain provides the basis for the representation of the range of fracture geometry anticipated at the emplacement drift horizon within the nonlithophysal rocks. The uncertainty in fracture geometry was captured in the rockfall model for nonlithophysal rock through development of a stochastically based representation of the fracturing geometry (BSC

2004a, Section 6.1.6). Representative rock volumes containing stochastically defined, representative fractures were generated using the FracMan program with the consideration of the natural variability of fractures. The representativeness of the FracMan-generated rock volume was calibrated through comparison to sampled distributions of fracture orientation, spacing, and trace length obtained from field mapping (BSC 2004a, Section 6.1.6.4). Uncertainties associated with fracture geometry data were addressed via the random selection of the fracture regions used in the discontinuum numerical simulations in the rockfall analyses (BSC 2004a, Section 6.3.1.2.2). The fracture geometry is concluded to be the dominant factor for wedge-type rockfall in nonlithophysal rock (BSC 2004a, Section 6.5).

Intact Rock Physical and Mechanical Properties Data—Intact rock physical and mechanical properties data were collected for the nonlithophysal rock units. The epistemic uncertainty associated with these data for intact nonlithophysal rock is considered low. The epistemic uncertainty associated with the rock properties data for lithophysal rock is high and has a significant impact on modeling results. However, the use of reasonable bounding properties ranges has been carried through all modeling simulations as a means of assessing properties uncertainty. As described in Section 2.3.4.4.2.3.7, bounding ranges of lithophysal rock properties have been estimated from large-core laboratory testing of room dry and saturated rock samples and are supplemented by numerical modeling extrapolations.

Fracture Mechanical Properties Data—The uncertainty associated with fracture mechanical properties data for both the nonlithophysal and lithophysal rock units is epistemic and is moderate to high. However, it is possible to account for uncertainty in fracture properties by conducting sensitivity studies using a lower bounding range of fracture properties. For example, the fracture cohesion (i.e., the bonding of the fracture surfaces) can be conservatively assumed to be zero. Similarly, the dilation angle of the fracture surfaces (i.e., the degree of roughness) can be assumed to be zero. The friction angle between adjacent surfaces can be assumed to be that of smooth fracture surfaces (i.e., the "residual" friction angle after all roughness is eliminated). To account for this uncertainty in the rockfall models, sensitivity analyses for a lower bounding range of fracture strength parameters were conducted (BSC 2004a, Section 6.3.1.6). Results of these studies, summarized in Section 2.3.4.4.4.5.2, indicate that the lower range fracture mechanical properties have an insignificant impact on rockfall (BSC 2004a, Section 6.3.1).

Rock Mass Mechanical Properties Data for Nonlithophysal Rock—As described in Section 2.3.4.4.4.1, the modeling approach used for rockfall analysis is to represent the rock mass as a fractured media consisting of intact rock blocks separated by fracture surfaces. Thus, the rock mass properties are represented by the properties of its component blocks and fractures. The uncertainties in the rock mass properties data are, therefore, a function of the geometric representation of the fractures, the uncertainty in the intact rock mechanical properties data, and the fracture mechanical properties data. The uncertainty in each of these data sources is described in the preceding paragraphs.

Rock mass mechanical properties data for nonlithophysal rock have also been estimated using common empirical rock mass classification schemes based on geologic data collected from field mapping within the ESF as well as intact rock properties data collected from laboratory testing (BSC 2007a, Section 6.4.4). Rock mass classification methods for estimating rock mass properties are used as an alternative to explicit modeling of the fractured rock using discontinuum approaches

as discussed above for the rockfall estimates. This approach is applied only in estimating preclosure drift stability and ground support design. The uncertainties associated with the intact rock properties data are described above. The uncertainties associated with the rock mass classification data are epistemic and are low since an abundance of data was collected based on established, industry-accepted methods. There is a moderate degree of epistemic uncertainty associated with the calculation approach for assessing rock mass properties because it is based on empirical methods and has an inherent imprecision. The epistemic uncertainty in estimation of nonlithophysal rock mass properties was accounted for by using two separate empirical calculation methods (Rock Mass Rating System and Q-System) and demonstrating that the results are similar (BSC 2004a, Section 6.5).

The rock mass properties data are primarily used in the thermal-mechanical calculation to determine stresses within the model (BSC 2004a, Section 6.2) and are a relatively insensitive parameter to the stress calculations (BSC 2004a, Section 6.5). The fracture geometry data have an important effect on rockfall estimates in nonlithophysal rocks when subjected to seismic loading (BSC 2004a, Section 6.3) as discussed in Section 2.3.4.4.4.2.

Rock Thermal Properties Data—The epistemic uncertainty associated with the thermal properties data for nonlithophysal rock is considered low due to the large database of thermal properties testing. The epistemic uncertainty associated with the thermal properties data for lithophysal rock is moderate to high due to the effects of lithophysal cavities on thermal properties. Field borehole heater testing has been used to determine in situ lithophysal rock thermal conductivity. This database has been supplemented by analytical estimates of the impact of lithophysal voids on thermal conductivity as a means of providing reasonable bounding ranges of thermal properties. In the rockfall analyses, thermal-mechanical simulations were performed to examine thermally induced stress around emplacement drifts in the pre- and postclosure time frames. These analyses included sensitivity calculations for thermal properties in which base-case values and values with 1σ less than the base case were used for thermal conductivity and specific heat (BSC 2004a, Sections 6.2, 6.3.1.3, and 6.4.2.3).

2.3.4.4.3 Rockfall Analysis for In Situ and Thermal Stress Effects on Nonlithophysal and Lithophysal Units

[NUREG-1804, Section 2.2.1.3.2.3: AC 4, AC 5]

2.3.4.4.3.1 Conceptual Approach for Analysis of In Situ and Thermal Stress

Both the nominal and early failure scenarios for emplacement drift stability involve examination of the effects of in situ and thermally induced stress transients over the postclosure period. Thermal-mechanical modeling was performed to estimate drift stability under combined in situ and thermally induced stresses. A heat transfer model of the emplacement drift and waste package was first run to define the evolving rock mass temperature distribution. The rock mass temperatures from these predictions were then used as input to a thermal-mechanical drift stability model to predict the associated thermally induced stresses and drift stability. This uncoupled calculation approach was used to ensure that the thermal modeling was consistent with thermal modeling approaches used in thermal-hydrologic studies (e.g., SNL 2008d; BSC 2004a, Appendix U).

Temperatures within the rock mass are determined from thermal analysis conducted using the NUFT program, which accounts for the details of heat transfer mechanisms within the drift, including heat removal due to ventilation in the preclosure period. The NUFT program is two-dimensional and, thus, assumes a cross section through a series of infinitely long emplacement drifts. Therefore, this approach represents the developing temperature distribution around emplacement drifts located centrally within the repository.

To assess the repository edge effects and topographic influences on the temperature and thermal stress distributions around the repository, the FLAC3D thermal-mechanical program was used (Figure 2.3.4-31). The results of these analyses confirm that the greatest thermal effects on drift stability occur in the center of the repository, and, therefore, limiting analysis of the thermally induced drift degradation to emplacement drifts in the center of waste emplacement panels is justified (BSC 2004a, Section 6.2).

The UDEC two-dimensional thermal-mechanical program is used to examine drift stability within the lithophysal rock mass, whereas the 3DEC three-dimensional program is used for analysis of stability within the nonlithophysal rock mass. The UDEC program calculates thermally induced stress changes resulting from the rock mass temperatures imported from the NUFT program. These stress changes are then superimposed by UDEC onto the preexisting in situ stress state around the emplacement drifts, and the stability of the drifts is examined. A similar process was used in three dimensions in which temperatures were imported into the 3DEC fractured rock model for nonlithophysal rock. In this case, the stability of the drifts is governed by the potential for shear and separation on the natural fractures as a result of the combined in situ and thermally induced stresses (BSC 2004a, Sections 6.2, 6.3.1.3, and 6.4.2.3, Appendix C).

2.3.4.4.3.2 Results and Uncertainty Analysis for In Situ and Thermal Analysis

Major cases of the emplacement drift-scale thermal calculation included:

- Case 1: Base-case calculation with 1.45 kW/m initial heat load, 50-year preclosure ventilation, and 90% heat removal ratio (BSC 2004f, Section 8)

- Case 2: Sensitivity calculation for thermal properties of repository rock material (Tptpll) with 1.45 kW/m initial heat load, 50-year preclosure ventilation, and 90% heat removal ratio. Values of thermal conductivity and specific heat 1σ less than the mean values were used:

  – Thermal conductivity (BSC 2004d, Section 6.2.1) values of 1.64 W/m·K (equal to 1.89 W/m·K – 1σ (0.25 W/m·K)) for wet conditions and 1.03 W/m·K (equal to 1.28 W/m·K – 1σ (0.25 W/m·K)) for dry conditions

  – Heat capacity value of 811 J/kg·K (equal to 954 J/kg·K – 1σ (143 j/kg·K) (BSC 2004a, Section 6.2))

- Case 3: Sensitivity calculation using a 70% heat removal ratio was used for preclosure ventilation.

Postclosure drift wall temperatures are bounded by Cases 1 and 2 (BSC 2004a, Figure 6-25). A comparison of temperature histories in the emplacement drift crown for Case 1, as determined in the drift-scale calculation (NUFT), and the coupled regional- and local-scale calculations (FLAC3D) is quite good, with the conditions in the middle of the repository representing a reasonable upper bound for thermal stress conditions since the rock mass temperatures (and stresses) are higher for centrally located emplacement drifts than for those near emplacement area boundaries (BSC 2004a, Section 6.2).

A series of thermal-mechanical calculations was performed initially for the range of lithophysal and nonlithophysal mechanical rock properties (Tables 2.3.4-16 and 2.3.4-17) to examine the potential for yield and degradation due to in situ stress and thermal loading alone. The 3DEC three-dimensional discontinuum program was used for analysis of nonlithophysal rock (Section 2.3.4.4.4), and the two-dimensional UDEC discontinuum model was used to represent lithophysal rock (Section 2.3.4.4.5).

Results of a number of thermal-mechanical simulations were analyzed in which the rock mass temperatures given by Cases 1 and 2 above are applied to an emplacement drift that has been excavated and reached equilibrium at the in situ stress condition (BSC 2004a, Sections 6.3.1.3 and 6.4.2.3). The induced stresses in the periphery of the emplacement drift can be compared to a yield criteria for the rock mass to determine if yielding of the drift walls will occur. The Mohr-Coulomb yield criteria was used to represent the rock mass failure condition and is based on the strength properties defined for the rock mass. Stability is estimated as a function of time for the entire postclosure heating and cooling cycle based on the transient temperature history of the rock surrounding the tunnel. A parametric study was conducted in which the variation in thermal properties and the rock mass Young's modulus and strength parameters were varied to account for the reasonable bounding ranges of lithophysal and nonlithophysal rock. Variation of the modulus was performed since thermally induced stress is proportional to the modulus (BSC 2004a, Sections 6.3.1.3 and 6.4.2.3).

The results of the parametric study show that no significant yield or ground collapse mode is evident for emplacement drifts in either lithophysal or nonlithophysal rocks during the pre- or postclosure time frames due to in situ or thermally induced stressing alone (BSC 2004a, Sections 6.3.1.3 and 6.4.2.3). The waste is likely to arrive at the repository in campaigns from specific generator sites and would therefore be from similar sources and of a similar type with similar thermal outputs. The operational ability of the facility to mix waste from various sources to achieve an "average" thermal load in any particular drift is expected to be limited. Therefore, while base case calculations have been performed by using 1.45 kW/m thermal loading, additional thermal-mechanical analyses were performed to determine if higher rock temperatures that are possible with a range of thermal loading would significantly change the likelihood of drift collapse or the amount of rockfall (SNL 2008e, Section 6.4.1). Thermal load was represented by average line loads from the hottest seven-package and three-package segments selected from the expected sequence of waste packages that will be received at the Yucca Mountain repository. The results show that the strength-to-stiffness ratios for the host rock units are large enough that higher temperatures will not significantly increase the amount of rockfall, even considering the lowest quality of lithophysal rock (Category 1). Complete drift collapse was not predicted as a consequence of thermal loading (SNL 2008e, Section 7.1). The additional impacts of seismic effects are addressed in Sections 2.3.4.4.4 and 2.3.4.4.5, and time-dependency of rock mass strength properties is addressed in Section 2.3.4.4.6.

2.3.4.4.4 Rockfall Analysis for Seismic Effects on Nonlithophysal Units

[NUREG-1804, Section 2.2.1.3.2.3: AC 4, AC 5]

This section on rockfall analysis for seismic effects on nonlithophysal units includes a description of the conceptual approach, an explanation of how fracture geometries were developed, an analysis of the amount and quantity of rockfall in the nonlithophysal zone due to vibratory ground motion, a description of how the model was calibrated, an explanation of the results and sensitivity studies, and a description of alternative conceptual models.

2.3.4.4.4.1 Conceptual Approach

The overall approach to estimation of rockfall in nonlithophysal rock is illustrated in Figure 2.3.4-32. The approach involves conducting a sensitivity study of the effects of various levels of earthquake ground motions on emplacement drift stability. The sensitivity study uses nonthermal loading conditions; the effect of thermal stressing is examined through a separate impact study (Section 2.3.4.4.4.5.2). As described previously, the nonlithophysal rock mass is represented as a fractured media consisting of intact rock blocks separated by fracture surfaces. The primary numerical tool used for conducting this sensitivity study is the dynamic, three-dimensional discontinuum program, 3DEC. The behavior of nonlithophysal rock is dominated by the geometry and surface properties of its fractures; therefore, a model of the fractures that reasonably represents the in situ rock mass was developed. The FracMan program was used to generate a synthetic rock mass of stochastically defined fracture sets based on data gathered from field mapping of fractures in the ESF and ECRB Cross-Drift. The strength and stiffness properties of the fractures have been defined from laboratory shearing tests. The sensitivity study involves conducting simulations of many emplacement drifts using various randomly selected realizations of the fracture geometry to represent the range of potential conditions that may be encountered in the nonlithophysal units of the repository host horizon. Rockfall, in the form of rock block mass, velocity, drip shield impact location and timing, in addition to total volume, is determined for many simulations of earthquake shaking. The resulting output is used as a basis for structural analysis of the drip shield for dynamic impact loading as well as static loading of the resulting at-rest rubble (Section 2.3.4.4.8). A number of additional sensitivity studies are used to define the effects of thermal stress, fracture surface properties, fracture continuity, and intact rock strength to provide an assessment of parameter uncertainty (BSC 2004a, Section 6.3.1.6).

2.3.4.4.4.2 Development of the 3DEC Rockfall Analysis Model for Nonlithophysal Rock

A methodology for defining statistically representative fracture distributions is required as a direct input to the 3DEC program (Figure 2.3.4-33). In particular, the input fracture geometry must provide a representation of the orientation, length, spacing, and continuity (which defines the solid rock bridges between or along fractures) of fractures and their variability. These parameters are found to have a significant impact on prediction of the size and number of blocks surrounding the drift that can be physically dislodged. Additionally, the surface characteristics, including roughness, planarity, and alteration or infilling, define the shearing and tensile resistance of the fractures under load (BSC 2004a, Section 6.1.6).

For rockfall analysis, a three-dimensional fractured cube, 100 m on each side, was generated using FracMan to represent the fractures with trace length greater than 1 m for nonlithophysal and lithophysal units. The existing fracture mapping database provided the basic input to the FracMan program, which was used to develop sets of planar, circular fractures that conform to the statistical variability of the geometric characteristics of the input data. The constructed FracMan fracture region is calibrated to the observed data for orientation and its dispersion, size and its distribution, and intensity (as measured by inter-fracture distance) and its distribution on a set-by-set basis. Essentially, the process involved fitting statistical models to the various geometric characteristics of each fracture set in the database, followed by generating a synthetic representation of each fracture set. The representative fractures are then verified against the statistical variability and geologic realism of the original sets to achieve an acceptable facsimile (BSC 2004a, Section 6.1.6).

Each fracture generated in the simulated rock mass is described by its centroid coordinate, dip, dip direction, and radius. These geometric parameters are then used as direct input to the 3DEC program, which, in turn, develops a model of the fractured media (i.e., the block and fracture geometry) for the region surrounding an emplacement drift. Fifty individual emplacement drifts are simulated for drift centroids chosen randomly within the FracMan simulated 100 m cube. The large number of simulations ensures that a statistically relevant set of rockfall responses is achieved for each level of ground motion hazard (BSC 2004a, Appendix K).

Generation of Fracture Geometry for the Middle Nonlithophysal Unit—To illustrate the methodology for fracture generation, an example of the process as applied to the Tptpmn is described below. The analysis for the Tptpmn uses a hierarchical approach to identify fracture sets based on the time-related sequence of their formation. This approach ensures that the fracture intersections are properly accounted for since the model generates fractures in the same order as occurred in reality. The detailed line survey fracture data are used to condition FracMan to develop representative fracture trace lengths and spacings. The mean orientation of the fracture sets is provided in Table 2.3.4-18. This table also provides a comparison of median fracture trace lengths and inter-fracture distances (i.e., the fracture spacing measured along the tunnel axis) from both the FracMan model and the detailed line surveys (BSC 2004a, Section 6.1.6). The mean orientation of fracture sets and a measure of the dispersion of the orientations of the set around that mean are used as a direct feed to the FracMan program for defining the synthetic fracture orientation and dispersion (BSC 2004a, Section 6.1.6).

An example comparison of full-periphery geologic maps from the ESF to synthetic full-periphery geologic maps created from FracMan is given in Figure 2.3.4-34. A full-periphery map is a structural geologic trace map of the entire visible tunnel surface. Full-periphery maps were created for the entire length of the ESF and ECRB Cross-Drift as the tunnel was driven. The realization from FracMan is not meant to replicate the field measurements but to be statistically representative. The comparison of actual to simulated full-periphery fracture maps is made initially to evaluate the general agreement of fracture orientation, intensity, and length on the scale of the emplacement drift (BSC 2004a, Section 6.1.6).

The spacing of subhorizontal fractures (e.g., vapor-phase partings) was observed to vary along the length of the tunnel in the nonlithophysal zone. In some locations it appeared to be on the order of 0.5 m spacing while in other areas it was in excess of 4 m spacing (BSC 2004a, Appendix N). The subhorizontal fractures are important to tunnel stability because these features typically form the

release plane on blocks formed by the intersection on the other three joint sets. The synthetic FracMan fracture geometry provides a relatively good fit of the underground mapping fracture geometry data, including the subhorizontal fractures, as shown in Table 2.3.4-18. The variability of fracture geometry within the tunnel is captured in the rockfall models through multiple samplings of the synthetic FracMan 100 m cube (Section 2.3.4.4.4.5).

Detailed comparisons of the fracture spacing and trace length distributions and orientation from FracMan and the observed spacing and trace length distributions, as well as comparisons of orientations from fracture stereonet plots, are used to provide quantitative verification of the representativeness of the synthetic fracture geometries. Comparison of the FracMan-generated synthetic fracture geometry to the field fracture data is performed both qualitatively and quantitatively. From a qualitative standpoint, the FracMan program is used to create equivalent full-periphery geologic maps by creation of virtual tunnels parallel to the ESF within the FracMan synthetic rock mass. Visual comparison is made between the FracMan and field full-periphery maps to ensure that the model produces the primary structural features evident in the field data. Quantitative comparisons of fracture trace length, spacing, and orientation are made by comparison of the statistical distributions. Fracture surface properties derived from laboratory direct shear tests and field characterization are associated with each of these fracture sets for input to the three-dimensional model (BSC 2004a, Section 6.1.6).

3DEC Model—An initially solid 3DEC model is cut into individual blocks using the FracMan fracture sets (Figure 2.3.4-33). The centroid, dip, dip direction, and radius of the synthetic fractures are used to cut fractures within the 3DEC block. The result is a three-dimensional model of the block structure surrounding an emplacement drift. The individual blocks within the 3DEC model are subdivided into tetrahedral finite difference elements to allow modeling of internal stresses and deformations in the blocks. The block material behavior may be elastic or conform to a desired nonlinear material law. In this case, the blocks were assumed to be elastic due to the high intact strength of nonlithophysal rock. The correctness of this assumption was verified through sensitivity analysis in which the blocks were allowed to fracture and yield under seismic loading (BSC 2004a, Section 6.3.1.6.4). The 3DEC model uses a fully dynamic solution algorithm to solve the laws of motion for the blocks, subject to contact restraints with surrounding blocks. The block element nodal points that lie along the fracture surfaces act as contact points across which forces are transmitted. If the forces dictate, the blocks may shear against one another or separate from one another. The blocks are free to dislodge and fall by gravity (or be ejected) into the emplacement drift during seismic shaking. Rockfall will eventually cease once the block system comes to a state of force equilibrium (BSC 2004a, Section 6.3.1).

2.3.4.4.4.3 Vibratory Ground Motion

Vibratory ground motion was considered by including site-specific ground motion time histories for PGV levels of 0.4, 1.05, 2.44, and 5.35 m/s. For each annual postclosure PGV level, a total of 17 sets of ground motion time histories were developed at the repository horizon, of which 15 sets for each PGV level were used for postclosure rockfall analyses (Section 2.3.4.3.2). One set of ground motion time histories was developed for the 0.4 m/s PGV preclosure level. The multiple sets of ground motion time histories at postclosure hazard levels ensure a reasonable distribution of frequency content and amplitude variability representative of the earthquakes that comprise the particular hazard level. For each set of ground motions, time histories for two horizontal components (H1 and

H2) and one vertical component (V) of acceleration, velocity, and displacement are supplied (BSC 2004a, Section 6.3.1.2.1).

2.3.4.4.4.4 Validation of the 3DEC Nonlithophysal Rockfall Model

The validation of the ability of the 3DEC program for representation of dynamic rockfall problems is based on three approaches: (1) demonstrating that the mechanical response of the fractures, which control the stability of the tunnel under shaking, properly reproduce laboratory direct shear data; (2) comparison of the 3DEC model to measurements from a field test of dynamic loading of a scaled, lined tunnel experiment conducted in jointed limestone; and (3) use of external expert technical review for validation of the overall modeling approach, which combines the FracMan fracture representation and the 3DEC dynamic modeling (BSC 2004a, Section 7.7.6). FracMan is calibrated through direct comparison of the output fracture geometry statistics against equivalent field-measured statistics as described in Section 2.3.4.4.4.2.

The 3DEC program was used to simulate the laboratory direct shear experiments discussed in Section 2.3.4.4.2.3.5. Comparison shows that 3DEC is able to adequately reproduce the shear stress–shear displacement response of the cooling and vapor phase–altered fractures (BSC 2004a, Section 7.7.3.3). Comparison of 3DEC to the lined, scaled tunnel blast–loading experiment showed good comparison of model to field experiment, including large deformation of the tunnel metal conduit lining (BSC 2004a, Section 7.7.4). Finally, the overall adequacy of the modeling approach and the specification of property ranges were validated by corroboration with the results of an alternative numerical model and by external technical review (BSC 2004a, Sections 7.7.5 and 7.7.6).

Numerous checks of the model boundary conditions and the impact of model dimensions on the problem solution were examined. Analyses indicate that the 3DEC program is able to represent dynamic boundary conditions and wave transmission through the material in an accurate fashion (BSC 2004a, Section 6.3.1). Additionally, 3DEC has undergone extensive comparison to analytic solutions through static and dynamic solution of problems of rock mechanics. Analysis shows that the FracMan program produces synthetic fracture geometries that are a reasonable facsimile of the in situ fracturing and its variability in the nonlithophysal units (BSC 2004a, Section 6.1.6).

2.3.4.4.4.5 Results and Sensitivity Studies

Several separate analyses were conducted to provide input data for assessment of drip shield response to rockfall in the nonlithophysal rock units. These include:

- The effect of vibratory ground motion on drift stability at ambient and elevated temperatures
- The effect of fracture strength degradation, over time, on drift stability
- The effect of an isolated, intensely fractured zone within the Tptpmn on drift stability
- The effect of small-scale fractures (trace length less than 1 m) on drift stability

- The effect of rock bridge strength
- The effect of model dimension.

As described previously, a cubic volume (100 m on each side) of simulated fractures was constructed from FracMan to provide the fracture network required in the 3DEC analysis. Stochastic selection of 105 emplacement drift centroid locations within this cube was performed. This sampling thus provides 105 different rock mass fracture geometries that can be used for selection in creation of 3DEC block models. These 105 centroid locations, combined with the 15 sets of ground motion time histories, served as the database from which the simulations could be sampled. The process of random generation and the coordinate of the centroid locations in the 100-m cube is described in *Drift Degradation Analysis* (BSC 2004a, Appendix J). A Latin Hypercube sampling scheme was used for the pairing of a ground motion set and fracture-modeling region (BSC 2004g). Fifty sets of paired fracturing realizations (i.e., drift centroid locations) and ground motions were made for each postclosure annual exceedance frequency (BSC 2004a, Section 6.3.1.2.2). For each of these analyses, a base case of block and fracture material properties was used so that the variability of the rockfall response was then a function of the fracture geometry and ground motion variability only. The base-case rock block and fracture properties are given in Table 2.3.4-17.

Initial Conditions—The initial stress state, characterized by the three-dimensional principal stress tensor based on data given in Table 2.3.4-5, is applied to the 3DEC model, which is allowed to equilibrate prior to excavation of the emplacement drift. Since the 3DEC model represents a finite-sized region around a typical emplacement drift, a surcharge must be applied to the top of the model to simulate the loading supplied by the overburden that extends to the ground surface (Figure 2.3.4-35). Thermally induced stresses are determined as described in Section 2.3.4.4.3.1 and added to the in situ initial stress tensor in every element in the model. The combined thermal and mechanical stress state then provides the initial condition for seismic analyses (BSC 2004a, Section 6.3.1.3).

Boundary Conditions—Ground motion at the location of the repository, in the form of three mutually perpendicular velocities (two horizontal and one vertical), is applied to the lower surface of the model, in terms of equivalent stress time histories (Figure 2.3.4-36). The effects of topography are implicitly accounted for within the ground motions, as supplied to the drift degradation modeling, and, thus, the 3DEC model does not need to explicitly account for topography (BSC 2004b, Section 6.1.6).

Nonreflecting (viscous) vertical and upper model boundaries in 3DEC allow the wave to pass through the model without reflections, and free-field boundaries on the vertical sidewalls of the model prevent damping and distortion along the vertical sidewalls of the incoming wave. In general, no material damping, in addition to that provided by sliding on fracture surfaces, is supplied to the model. Prior to the use of this model for examination of drift degradation, seismic wave propagation of models without tunnels was run to ascertain that the wave passed through the model without significant distortion (BSC 2004a, Section 6.3.1.2).

2.3.4.4.4.5.1 Results of Rockfall from Vibratory Ground Motion at Ambient Temperature

Results of the 3DEC seismic analyses conducted for ambient temperature conditions provide rockfall impact parameters for structural calculations to predict drip shield damage (Section 2.3.4.4.8). Results provided to the structural calculations include rock block volume falling on the drip shield, relative impact velocity of rock blocks to the drip shield, and impact location. Impact momentum and impact energy were also calculated as functions of block mass and impact velocity and were provided for the structural analysis. All results for rockfall simulations for the TSPA were based on the assumption of unsupported drift openings since ground support will corrode with time. The postclosure ground motion resulted in a range of response, from relatively minor drift damage due to rockfall to cases in which localized areas of rock failure were sufficient to cover the drip shield (BSC 2004a, Sections 6.3.1).

To illustrate the output from the rockfall analyses, results for a complete set of 3DEC analyses subjected to ground motions for the postclosure hazard PGV level of 2.44 m/s are presented in this section. The 3DEC model represents the drip shield with a rectangular block, with the drip shield dimensions anchored to the invert of the emplacement drift. This block has no influence on the calculations and is included only to record rock impact locations, relative velocities, timing, and forces. Figure 2.3.4-37 shows typical blocks impacting the drip shield in the 3DEC dynamic simulation for a given instant in time. Fallen blocks are automatically deleted after impacting the drip shield; the deletion is to facilitate a reasonable bounding approach to the recording of all possible rockfall on the drip shield. If the blocks are not deleted, the drip shield will be covered with fallen rocks for some of the cases in which significant rockfall occurs. In that case, some of the rockfall at the later stage of seismic shaking will not impact the drip shield. A simulation was also run without deletion of the rock blocks. As expected, results indicated less rockfall for that scenario (BSC 2004a, Figure 6-93).

A total of 50 3DEC simulations were performed at the 2.44 m/s PGV level. Each simulation represented a 21.74-meter long segment of an emplacement drift (the model simulated a 25-meter long drift, but only 21.74 meters was used to represent fractured rock (SNL 2007c, Section 6.7.2)). All simulations resulted in rockfall, with a total of 2,797 blocks dislodged (BSC 2004a, Table 6-13). It was established that 50 simulations were sufficient by examining the median and standard deviation of the rockfall mass as a function of the number of simulations. It was further established that these parameters showed little change after approximately 30 simulations (BSC 2004a, Appendix K). The associated impact parameters for these blocks from the analyses include the following:

- Rock block volume falling on the drip shields
- Relative impact velocity of rock blocks to the drip shield
- Impact location.

Rock block impact information at the 2.44 m/s PGV level is provided in the *Drift Degradation Analysis* (BSC 2004a, Section 6.3.1.2.4). The distribution of the data for each impact parameter shows that the rockfall strikes the drip shield at or around its crown with a velocity centered around 3 ± 1.5 m/s. The velocity indicates that the rock falls as the result of gravity and is not forcibly ejected from the surrounding rock mass. Summary statistics for all of the impact parameters for the

50 simulations for the 2.44 m/s PGV case are provided in Table 2.3.4-19. The maximum rockfall block mass predicted is 28.22 MT with a median block mass of 0.13 MT. The results show large variance and high skewness, with the exception of impact velocity. The block mass, impact angle, impact momentum, and impact energy show the trend of an exponentially decaying distribution with the mean at the low end of the data range. The impact velocity shows a typical normal distribution (BSC 2004a, Section 6.3.1.2.4).

Analyses similar to those discussed above were also completed for the 0.4, 1.05, and 5.35 m/s PGV level ground motions (BSC 2004a, Section 6.3.1.2.1). The exception is that 32 and 44, rather than 50, analyses were made for the 0.4 m/s and 5.35 m/s PGV level cases, respectively (BSC 2004a, Table 6-26). Analysis indicated that only about 15 simulations were required for achieving a stable mean block mass in the 0.4 m/s PGV case, and about 25 to 30 analyses were needed in the other cases (BSC 2004a, Appendix K). Figure 2.3.4-38 shows a comparison of histograms of block mass resulting from simulations for all ground motions. The results show that all motions result in the same general distribution of block sizes with median block mass of less than 0.15 MT with exponentially decaying distribution. A plot of rockfall volume as a function of the maximum PGV of the three ground motion components for all postclosure analyses is given in Figure 2.3.4-39. This plot shows that the rockfall volume is reasonably bounded by a linear relationship of total volume to PGV. At any given level of PGV, the variability of response is quite large. This is a result of the variability of the ground motion (e.g., frequency characteristics and energy) and of fracture geometry captured in these sensitivity runs (BSC 2004a, Section 6.3.1.6).

Rockfall statistics for the pre- and postclosure ground motion levels are given in Table 2.3.4-20. An important statistic for the different PGV levels is the number of blocks dislodged per kilometer, which shows an increasing number of blocks with larger PGV ground motions.

2.3.4.4.4.5.2 Sensitivity Study of the Input Parameters and Model Conditions

There are four major input data sets to the three-dimensional discontinuum analysis of nonlithophysal rock: ground motion time history characteristics, fracture geometrical properties, fracture and intact mechanical properties, and thermal stress history. Sensitivity studies of these input parameters were conducted to establish uncertainty in the predictions of rockfall and to identify the important controlling parameters. The following provides a summary of the conclusions of these parameter studies (BSC 2004a, Section 6.3.1.6).

Ground Motion Sensitivity—Fifteen sets of ground motion data were used for each hazard level in the postclosure period to ensure a reasonable distribution of frequency, amplitude, and duration variability for the earthquakes that constitute the hazard. As discussed above, the sensitivity of rockfall to ground motion is encompassed in the variability of the rockfall for any given level of PGV. The ground motion time histories were truncated at 5% and 95% energy content to shorten the time required to conduct the dynamic analyses. The analyses showed that the majority of the rockfall occurs coincident with the arrival of the strong motion, which is typically within the first 15 seconds of shaking, and that truncating the ground motion had minimal impact on the amount of rockfall (BSC 2004a, Section 6.3.1.6.1). However, the results were inspected at the end of the simulation, and, if it was determined that the simulation was terminated prematurely (i.e., there was indication of loose blocks), the simulation was continued until all loose blocks resulted in rockfall. Likewise, it was found that rotating the horizontal ground motion components by 90° had

minimal impact on rockfall. This is understandable since the horizontal motions have, in general, similar peak amplitudes.

Fracture Geometrical Properties—The variability of fracture geometrical properties is incorporated in the application of FracMan to generate a 100-m cube fracture network. A total of 50 drift locations were selected from the 100-m cube fractured rock mass for the 3DEC analyses. Results from these analyses reasonably explore the impact of the variability of fracture geometrical properties (BSC 2004a, Appendix K). This was demonstrated by examining the median rock block mass as a function of the number of simulations. It was found that there was little change in the predicted median rock block mass after approximately 30 analyses (BSC 2004a, Appendix K).

Fracture Surface Property Variation and Fracture Strength Degradation—The base-case fracture properties, listed in Table 2.3.4-17, were derived from rotary shear tests of cored specimens (BSC 2004a, Appendix E). Results from direct shear tests conducted on large-core (290-mm diameter) samples are used to provide the range of variation tested in the sensitivity studies (BSC 2004a, Section 6.3.1.6).

A range of fracture properties, as shown in Table 2.3.4-21, was selected for the sensitivity study. The values were established based on a fracture residual friction angle of 30° and three tiers of possible dilation angles. The dilation of a joint surface is a function of the roughness of the joint. The angle of dilation will increase as the roughness increases. Dilation (roughness) tends to stabilize a rock mass. The dilation angles were selected within the range of reported test results (BSC 2004a, Appendix E). The base-case rotary shear test cohesion is used in these simulations (BSC 2004a, Section 6.3.1.6.2).

A series of additional 3DEC dynamic analyses using the 1.05 m/s PGV level ground motion and three base-case analyses that had the greatest, least, and average rockfall volumes were run for the range of fracture properties. The results of these sensitivity studies (BSC 2004a, Section 6.3.1.6.2) show that the variation of fracture mechanical properties is a secondary effect compared with the variation of fracture geometrical properties (i.e., fracture pattern). Results for the three fracture properties categories are quite similar, irrespective of the variation of the mechanical properties used for each category (BSC 2004a, Section 6.3.1.6).

Time Degradation of Fracture Properties—The potential exists for time-dependent degradation of the rock mass surrounding the emplacement drifts. In the nonlithophysal rock, the potential source of time-dependency is the result of long-term shear failure along the preexisting fracture planes. A potential mechanism for time-dependent yield along rock fractures is the concentration of stress on fracture asperities (i.e., roughness along the fracture surfaces) with associated static fatigue failure of the asperities when subjected to long-term constant shear stress (BSC 2004a, Section 6.4.2.4.2). Static fatigue of hard rocks is typically associated with stress levels on the order of 60% or more of its unconfined compressive strength. Fatigue failure would presumably initiate along asperities on fracture surfaces, with the ultimate effect being a reduction of the fracture surface roughness. From a mechanical perspective, this failure would result in reducing or eliminating cohesion and dilation on the fracture surface, as well as reducing the friction angle to its residual value (BSC 2004a, Section 6.3.1.5).

The impact on drift stability due to the effect of rock fracture degradation is assessed based on a conservative estimate of the reduction of fracture cohesion and friction angle. The reduced fracture strength parameters are estimated to be in the range of the residual, post–peak shear displacement state, with fracture cohesion reduced to zero and the fracture friction angle reduced to 30°. The reduced friction angle is a typical value for a smooth fracture reported by Goodman (1980, p. 158) and is consistent with the direct shear laboratory test results for smooth cooling fractures described previously (Section 2.3.4.4.2.3.5). Dilation angle is also conservatively presumed to be zero, considering that the asperities on fracture surfaces had been sheared off. The degraded fracture strength and dilatation properties were applied in the 1.05 m/s PGV level ground motion cases that represent those cases with greatest amount of rockfall, the median case, and a case producing no rockfall. The predicted number of detached rock blocks and the total rockfall volume show only a slight increase in rockfall is predicted for the degraded state. Thus, potential time-related fracture strength degradation has a minor impact on drift stability in nonlithophysal rock (BSC 2004a, Section 6.3.1.5).

Rock Bridge Strength—As described in Section 2.3.4.4.4.2, the fracturing in the nonlithophysal rocks is nonpersistent in nature (i.e., fractures often terminate either against other fractures or simply end in solid rock as shown by the full-periphery geologic maps illustrated in Figure 2.3.4-34). Therefore, all fractures are not continuous in nature across the drift circumference, and numerous instances of solid rock bridges occur that tend to increase the gross shear and tensile strength of the rock mass. Small percentages of noncontinuous fractures result in significant increase in rock mass strength. A discussion of the significant effect of rock bridges on rock mass strength and tunnel stability can be found in a study by the Mining Research Directorate (MRD 1995, Volume 2, Section 8.2.2). The base-case 3DEC rockfall studies assumed that the rock bridges are elastic (i.e., they do not fail). The goal of this sensitivity study is to determine whether assignment of actual intact rock strength parameters to the bridges has a significant impact on rockfall volume or mass (BSC 2004a, Section 6.3.1.6).

Solid rock bridges (i.e., intact rock) between fractures were automatically generated as the extension of finite trace length fractures when forming the distinct blocks in the 3DEC model. A range of rock bridge strength parameters, in terms of cohesion, friction angle, and tensile strength, was selected for the sensitivity study. This range of intact rock strength properties was derived from the results of triaxial testing of rock cores from the Tptpmn (BSC 2004a, Appendix E). A total of three cases were included to cover the possible range of variation for bridge strength parameters. 3DEC models were run for the cases of greatest, least, and average amounts of rockfall for the 1.05, 2.44, and 5.35 m/s PGV level ground motions. Case 1 represents the bounding case in which it is assumed that the fractures are persistent (i.e., continuous) in nature and, thus, no rock bridges exist. The mean values of the intact Tptpmn strength parameters are used for Case 2. The mean $+1\sigma$ values determined from triaxial testing are assigned as the strength parameters for Category 3, which represents the upper bound for the rock bridge strength. The results show that within the range of variation for the intact strength parameters (Cases 2 and 3), rock bridge strength parameters have insignificant impact on rockfall prediction (BSC 2004a, Section 6.3.1.6.3). However, if fractures are assumed to be persistent, as represented by Case 1, a significant increase of rockfall volume occurs compared to the base case (BSC 2004a, Section 6.3.1.6.3). In this case, the fractures that previously ended in solid rock were assumed to cut completely through that given block, terminating against the fracture that formed the block boundary. Although this assumption

provides the lower bound for rock mass strength, it is considered to be unrealistic in nature as it ignores a fundamental geometric property of fracture networks that provide strength to a rock mass.

Intact Rock Block Strength—The analyses of rock bridge failure potential are also used to examine the potential for fracture of intact rock blocks as a result of seismic-induced stresses. As described in *Drift Degradation Analysis* (BSC 2004a, Section 6.3.1.6.4), less than 1% of rock bridges around the emplacement drift fail at the 1.05 m/s PGV ground motion level, about 5% at the 2.44 m/s PGV level ground motions, and approximately 20% during the 5.35 m/s PGV level motions. These fractures induced in intact blocks have a relatively minor impact on rockfall and only locally change the profile of the emplacement drift (BSC 2004a, Figures 6-89 and 6-90). Therefore, failure of the intact blocks in nonlithophysal rock under seismic stress is not considered to be a significant mechanism for rockfall in excess of that resulting from failure along preexisting fracture surfaces.

Thermal Stress Effects on Seismically Induced Rockfall—The base-case rockfall studies were conducted assuming in situ stress and seismic loading only. A 3DEC sensitivity analysis was conducted in which the base-case thermal condition (Section 2.3.4.4.3.2, Case 1) stress state was added to the in situ stress conditions, followed by application of the 1.05 m/s PGV level ground motion to examine the impact of thermal stress on rockfall. Three example cases were chosen for analysis: the case with the greatest amount of rockfall, a case showing the median amount of rockfall, and one case that showed no rockfall. The postclosure time with the highest level of rock temperature and thermally induced rock stress (within 50 years after repository closure) was chosen. The rock was also allowed to cool to examine potential hysteretic effects on fracture deformation and was followed by application of the ground motion to the model. It was found that the rockfall, in this case, is similar to the nonheated case since slip only occurs on fractures in the near vicinity of the drift (BSC 2004a, Section 6.3.1.4).

As seen in Table 2.3.4-22, the impact of thermal loading in nonlithophysal rock is to stabilize the rock mass and reduce seismically induced rockfall. The reason for this effect is that the rock mass expansion upon heating induces tangential compression around the excavations. This compression tends to provide increased normal stresses on fractures, thus increasing their shearing resistance as well as minimizing fracture opening during extensional loading during the seismic event. Thus, the reasonably bounding thermal state, from a rockfall standpoint, is actually when the rock is at or near the base-case assumption of ambient temperature conditions (BSC 2004a, Section 6.3.1.4).

2.3.4.4.4.6 Consideration of Alternative Conceptual Models

The overall approach of using FracMan to generate simulated fractures in a rock mass volume and 3DEC to compute the block geometries and solve the discontinuum static and dynamic analysis is not the only approach available for assessing block stability in the nonlithophysal units. There are alternative algorithms of simulating fracture geometries, but none so robustly address stochastic simulation as the FracMan program. In addition, FracMan is the most widely used fracture simulation program in the petroleum, mining, and nuclear waste industries. An alternative approach to simulating fractures was examined through use of a kinematic (keyblock) stability analysis program for rockfall analyses (BSC 2004a, Appendix D). Fractures are simply generated in the model along scan lines oriented perpendicular to the fracture sets in DRKBA, and thus the fracture generation algorithm is not as technically sophisticated or robust as that implemented in FracMan.

Similarly, there are alternative block stability analysis methods available besides using the 3DEC program. The DRKBA program was used for analysis of small-scale fracturing effects (BSC 2004a, Section 6.3.3). This program makes use of the limit equilibrium solution to rock block stability; however, it is not considered as appropriate as 3DEC for this particular application because in situ stress, thermal stress, and seismic loading are not explicitly represented in DRKBA. Another alternative numerical approach to the 3DEC program is the three-dimensional, discontinuous deformation analysis method, which also solves the equations of motion and can account for in situ stress, thermal stress, and seismic loading. Regardless of how this method is currently implemented, it does not provide for complex material models within the intact material. This is a significant limitation because rock blocks can internally fracture. The combination of FracMan and 3DEC was considered to provide the best approach for this analysis (BSC 2004a, Appendix N).

2.3.4.4.5 Rockfall Analysis for Seismic Effects on Lithophysal Units

[NUREG-1804, Section 2.2.1.3.2.3: AC 4, AC 5]

This section on rockfall analysis for seismic effects on lithophysal units includes a description of the conceptual approach, the identification of ground motion time histories considered in the analysis, a description of the model and model uncertainty, an explanation of the results, and a description of alternative conceptual models.

2.3.4.4.5.1 Conceptual Description for Modeling Lithophysal Units

A lithophysal rockfall model was developed using the two-dimensional discontinuum program, UDEC (Figure 2.3.4-40). In this model of lithophysal rock, the rock mass is represented as an assembly of polygonal, elastic blocks that are bonded together across the intervening contact planes. The bond strength of the block contacts is calibrated such that the overall mechanical behavior of the rock mass is representative of the material model developed for the lithophysal rock. The contact planes between blocks can be considered to be “incipient” or “potential” fractures that, from a mechanical standpoint, do not fracture until the rock mass is stressed beyond its elastic limit and yielding begins. Thus, the lithophysal rockfall model is based on a discontinuum representation to allow for the formation of fractures between blocks (i.e., the formation of internal fracturing) and block separation and instability of the rock mass around the drift as yielding occurs. Providing the capability for fractures to propagate and blocks to form is required since an objective of these analyses is to estimate rockfall volume, impact, and accumulated rubble loading to the drip shield.

Parametric rockfall analyses are conducted with the UDEC model in which the following basic approach is used:

- In situ and thermal stress states are applied to the model for various postclosure time periods as an initial condition to the ground motion application.
- Vibratory motion analyses are performed in which ground motion time histories and rock mass mechanical properties are varied to derive a reasonable bounding range of damage estimates for emplacement drifts.
- Time-dependent degradation analyses are performed to examine emplacement drift stability as a function of time under nonseismic conditions.

To examine in situ and thermal stress stability, thermal-mechanical analyses were performed for two cases of rock mass thermal properties. The transient temperature field around the repository was calculated using the NUFT program described in Section 2.3.4.4.3.1. Vibratory motion analyses were conducted using site-specific ground motion and resultant time histories appropriate for the postclosure time periods applied to the model. The vibratory motion analyses were conducted for a reasonable bounding range of lithophysal rock mass mechanical properties, characterized by the five rock strength category ranges described in Section 2.3.4.4.2.3.7 (BSC 2004a, Appendix E). Although each model assumes the rock mass is characterized by constant, homogeneous rock mass properties, heterogeneity is considered through the use of a range of rock mass properties. Analyses conducted in which true heterogeneity of properties (based on spatial variability of lithophysal porosity) is represented confirm that the approach used spans the range of expected rockfall response (BSC 2004a, Section 6.4.2.2.3.2).

2.3.4.4.5.2 Vibratory Ground Motion

Ground Motion Inputs—Drift stability in lithophysal units was analyzed for ground motion with 0.4, 1.05, and 2.44 m/s PGV levels (BSC 2004a, Section 6.4.2.2).

The ground motion time history development is discussed in detail in Section 2.3.4.3.2. Fifteen sets of ground motion time histories were considered in the analysis for 0.4, 1.05 and 2.44 m/s PGV levels. For each time history, one horizontal and one vertical component of motion were used since the drift degradation model is two-dimensional. Because the lithophysal model is two dimensional, only one horizontal component (H1) is applied to the model.

2.3.4.4.5.3 Model Description and Model Uncertainty

The rock mass is represented as an assembly of polygonal, elastic blocks that are bonded together across their boundaries to form a solid that is calibrated to the material behavior of lithophysal rock. The goal is to provide a rock mass in which the overall mechanical behavior of the mass is consistent with the mechanical behavior for the lithophysal rock, yet to allow internal fracturing to form blocks that may loosen and detach as the evolving stress state dictates. The interblock "incipient" fractures are essentially invisible to the model until yielding begins (BSC 2004a, Section 6.4.2).

Since the block boundaries can fail in tension and shear, they act as potential fracture locations should the stresses dictate that fracture is possible. The block assemblage must contain blocks that are sufficiently small so that the model discretization does not dictate where and how fractures can form and propagate. The entire tunnel domain is discretized into small blocks that are roughly consistent with the maximum block size expected from rock mass fracture spacings, as described in *Drift Degradation Analysis* (BSC 2004a, Section 6.1.4.1) (Figure 2.3.4-40). The fractures between blocks are considered to behave mechanically according to a linearly elastic, perfectly plastic model. The elastic behavior of fractures is controlled by constant normal and shear stiffness and is consistent with the Young's modulus of the intact rock blocks. The possible failure modes of the rock mass are controlled by the strength of the fractures. The fractures can sustain a finite tensile stress, whereas a Coulomb slip condition governs the onset of slip as a function of fracture cohesion and friction angle. If a potential fracture fails, either in tension or shear, tensile strength and cohesion are set to zero, whereas the friction angle is set to the residual value. This model allows for

the formation of fractures between blocks, separation, and instability (under action of gravity) of portions of the rock mass around a drift (BSC 2004a, Section 6.4.2).

2.3.4.4.5.3.1 Calibration of UDEC Discrete Element Model

Calibration of the model was performed to reproduce the mechanical properties given by the range of five lithophysal rock strength categories described in Section 2.3.4.4.2.3.7. The numerical model calibration was performed by simulating unconfined compression experiments in which the model parameters (i.e., interblock contact properties) were varied until the rock mass properties (i.e., Young's modulus and unconfined compressive strength) were matched with measurements from the actual large-core laboratory tests (BSC 2004a, Sections 7.6.3 and 7.6.4). When the calibration was completed, the UDEC model material behaved equivalently to the lithophysal rock mass (BSC 2004a, Section 7.6.4). Following calibration, the model can be used to conduct additional simulations under biaxial compression and tension to produce the yield criteria for the material. These yield criteria can be compared to typical empirically derived yield criteria for other rock types as a means of verification of the model. The lithophysal rock mass behaves, in general, as a Mohr-Coulomb material with post–peak strength strain softening, which decreases with increasing confining stress (BSC 2004a, Section 7.6.4).

2.3.4.4.5.3.2 Validation of UDEC Lithophysal Rockfall Model

Once calibrated, the UDEC model required validation against field observations and failure observations from laboratory testing. The model was validated against laboratory failure mechanisms and drift-scale response through:

- Comparison of model failure mechanisms to large-core lithophysal sample failure mechanisms observed in the laboratory
- Comparison of the model prediction of drift scale fracturing at ECRB Cross-Drift depth to observations of stress-induced tunnel sidewall fracturing in the ECRB Cross-Drift
- Comparison of roof spalling in the Drift Scale Test in the Tptpmn during thermal overdrive experiments to UDEC model predictions when calibrated to nonlithophysal mechanical properties
- Comparison of UDEC simulations to field testing of explosion-induced, lined tunnel instability in a scaled, fractured rock mass to demonstrate the capability of representing the dynamic response of a fractured rock mass.
- Corroboration of the UDEC simulations to an alternative continuum-based modeling approach.

The details of the validation tests (BSC 2004a, Section 7) showed that:

- The model reproduces the basic axial splitting fracturing and failure mode of lithophysal samples observed in unconfined compression while reproducing the proper strength and Young's modulus.

- The model reproduces the sidewall shear fracturing observed occasionally in the Tptpll in the ESF and ECRB Cross-Drift. The observed fracturing behavior, typical of local in situ stress-related yield in hard rocks, is found only directly at the springline and extends to a depth of about 0.5 m into the sidewall. Due to the high vertical to horizontal principal stress ratio, the greatest stress concentration occurs directly at the sidewall. The UDEC model reproduces the local wall-parallel fractures and yield for the lowest strength category for lithophysal rock (category 1, Table 2.3.4-16), representative of the lowest quality material. The model shows significant sidewall fracturing for rock strength category 1, with no sidewall fracturing for rock strength category 5 (BSC 2004a, Figure 7-26). The model results show that significant sidewall fracturing occurs under in situ stress conditions when the unconfined compressive strength of the rock is less than approximately 10 MPa (BSC 2004a, Section E4.1.4.1), which corresponds to rock strength category 1 (Table 2.3.4-16). This is consistent with the typical condition within the ESF and ECRB Cross-Drift, which shows no observation of sidewall yield. This observation is also consistent with the general lithophysal porosity mapped within the ECRB Cross-Drift, showing that the mean porosity is indicative of a strength category of 3 to 4, with more than 90% of the Tptpll having strength greater than category 1. The small number of observations of sidewall spalling is consistent with the relatively infrequent occurrence of low strength categories.

- The model reproduces the roof crown spalling behavior observed during the thermal overdrive portion of the Drift Scale Test conducted in a test facility in the Tptpmn. At the conclusion of this test, the rock mass temperatures were driven to approximately 200°C, at which time minor spalling in the form of plate-shaped fragments was observed in the crown of the tunnel. The UDEC model was first calibrated to reproduce the mechanical properties of the large-scale nonlithophysal rock blocks. The thermal-mechanical Drift Scale Test was modeled by imposing the in situ stress state and temperature history (as determined from field temperature measurements) onto the model. The roof crown–parallel fracturing extent and apparent mechanism were reproduced at the proper temperature levels using the calibrated model (BSC 2004a, Section 7.6.6). It was found that the fracturing was the result of the large horizontal thermally induced stresses in the immediate roof. The crown is placed in a state of unconfined compression, and when this stress reaches the strength of the rock mass (in this case, approximately 70 MPa (BSC 2004a, Figure E-22)), extensional roof-parallel fracturing occurs over a limited area of the tunnel crown. The system equilibrates when fracturing extends to a short depth. This validation test shows that the two-dimensional discontinuum approach is able to reproduce thermal stress-induced fracture development and spalling in the periphery of tunnels in welded tuff. This test also demonstrates that the estimate of in situ strength for Tptpmn is approximately correct.

- UDEC reproduces deformation induced in a large tunnel during an explosive test of dynamic tunnel stability conducted in fractured limestone for the Defense Nuclear Agency. A "blind" prediction of the experiment was performed by a number of analysts using different numerical modeling approaches to represent the dynamic response of the fractured media and the lined tunnel. The outcome of the field experiment was not known in advance. The analysts were given basic material properties data from laboratory testing and asked to predict the outcome of the test. Comparison of the model and field experiment results was then compared for all analysts by a third party. UDEC adequately matched the field dynamic response and the final shape and deformation response of the aluminum conduit–lined tunnel.

- The UDEC model was shown to produce stress distributions and yield location and extent comparable to a typical continuum-based approach for modeling of emplacement drift thermal-mechanical response.

2.3.4.4.5.4 Results for Vibratory Motion Analysis in Lithophysal Units

Initial Conditions—The approach to application of initial conditions for the two-dimensional UDEC model is similar to that used for the 3DEC model discussed in Section 2.3.4.4.4.5. In UDEC, the initial stress state consists of two components: the vertical (major principal stress) and the horizontal component. The horizontal stress component applied to the model has been determined by projecting the in situ horizontal stresses into the plane perpendicular to the axis of the emplacement drifts. This calculation results in a base-case value of 3.5 MPa, or a ratio of horizontal-to-vertical stress of 0.5. Sensitivity of the stability of emplacement drifts to the uncertainty of the horizontal-to-vertical stress ratio has been investigated with bounding values of 0.3 to 1.0 (BSC 2003b, Section 6.2.2). The results indicate that the horizontal-to-vertical stress ratio has only a minor effect on drift stability.

Boundary Conditions—Ground motion at the location of the repository, in the form of mutually perpendicular velocities (one horizontal and one vertical), is applied to the lower surface of the model, in terms of equivalent stress time histories (Figure 2.3.4-36). In the two-dimensional UDEC lithophysal models, only two time history components (one horizontal (H1) and another vertical component) are applied to the lower boundary of the model. The time histories applied to the model already include the effects of the free surface reflections, and, thus, the UDEC model does not need to account for topography (BSC 2004a, Section 6.4.2.2).

Nonreflecting (viscous) vertical and upper model boundaries in UDEC allow the wave to pass through the model, and free-field boundaries on the vertical sidewalls of the model prevent damping and distortion of the incoming wave. No material damping, in addition to that provided by sliding on fracture surfaces, is supplied to the model (0.3% of critical damping was used in a few analyses for numerical stability purposes). Prior to use of this model for examination of drift degradation, seismic wave propagation of models was run to ascertain that the wave passed through the model without significant distortion (BSC 2004a, Section 6.4.2.2 and Figure 6-119).

A series of simulations using seismic time histories appropriate for 0.4, 1.05, and 2.44 m/s PGV level was performed. The approaches for generation of preclosure and postclosure ground motion

time histories are described in Sections 1.1.5.2 and 2.3.4.3.2.4. The results in terms of emplacement drift damage are described below.

- **Results for 0.4 m/s PGV Level—**A single preclosure 0.4 m/s PGV level time history was applied to emplacement drift stability models for each of the five lithophysal rock strength category levels (BSC 2004a, Section 6.4.2.2). The analyses show that, even for the assumption of unsupported emplacement drifts, little rockfall or emplacement drift profile changes are expected for any lithophysal rock strength level. A more quantitative characterization of the rockfall volumes was required for the seismic rockfall abstraction and for the seismic seepage analysis at this PGV level. A suite of calculations was performed using 15 postclosure ground motions combined with rock strength categories (SNL 2007b, Appendix C). The results of these calculations confirm that there is little rockfall or emplacement drift profile change at the 0.4 m/s PGV level.

- **Results for 1.05 m/s PGV Level**—For the postclosure analyses, a total of 15 sets of time histories for the 1.05 m/s PGV level were applied to a reasonable bounding range of three strength category levels (categories 1, 3, and 5) for a total of 45 analyses (BSC 2004a, Section 6.4.2.2). As a result of variability of the ground motion components within the 15 time histories, the peak ground velocities considering both the horizontal and vertical directions vary from approximately 1 m/s to as high as approximately 4 m/s. As a result of this variation in PGV, the 1.05 m/s PGV level case shows a wide variation in drift damage ranging from no damage to collapse of the tunnels. Figure 2.3.4-41 shows emplacement drift damage for all three strength categories, in terms of cubic meters of rockfall per meter of drift length as a function of PGV of the greatest of the horizontal and vertical time histories applied to the model. The significant variability of damage for a given level of PGV is indicative of the variability in the particular energy content of the earthquake. The upper bound of the damage falls along an approximate linear relationship with PGV. A damage level of approximately 20 m^3/m on the vertical axis corresponds to a collapse sufficient to cover the drip shield with rubble. This damage level corresponds roughly to a PGV of approximately 2 m/s at the average rock strength category observed in the ECRB Cross-Drift (i.e., strength category 3). Analyses show that rockfall occurs within seconds of the arrival of the large amplitude peaks of the ground motion time history.

  These analyses were all conducted assuming a bounding range of constant, homogeneous strength and modulus properties for the rock mass. To examine the potential impact of actual spatial variability of rock properties within the cross section of a given model, additional analyses were performed. Estimates of the spatial variability of lithophysal porosity within the Tptpll were made based on lithophysae mapping studies conducted within the ECRB Cross-Drift (Figure 2.3.4-25). A cross-sectional model with simulated spatial variability of properties was developed to verify that the constant, homogeneous properties approach does produce damage estimates within that predicted using the bounding range approach (BSC 2004a, Section 6.4.2.2.3.2). The spatial variability model represents an average condition observed in the ECRB Cross-Drift in which the local, drift-scale variability in lithophysal porosity varies from greater than 20% to less than 10% but averages approximately 15%. The symbols labeled “spatial variability” in Figure 2.3.4-41 show the results of damage modeling using the same fifteen 10^{-5} time

histories as used for the homogenous strength cases. The results show that the damage from the spatial variability case is approximately within the range of that predicted for category 3 constant properties case, which is expected since the mean lithophysal porosity represented in both models is the same. Therefore, use of a range of rock mass properties appears to be reasonable and will provide a conservative estimate of drift damage for the case of lower rock strength property ranges (i.e., strength categories 1 or 2).

- **Results for 2.44 m/s PGV Level—**Results show that ground motion with a PGV level of 2.44 m/s causes complete collapse of the emplacement drifts irrespective of the rock mass strength category or the particular ground motion time history (BSC 2004a, Section 6.4.2.2). This is consistent with the 1.05 m/s PGV level results discussed above, since all 2.44 m/s PGV level time histories have PGV values that surpass the approximate collapse level of 2 m/s. A typical model geometry at the end of a simulation is shown in Figure 2.3.4-42. The drift completely collapses in all cases with resulting drift profile broken out to an approximate elliptical shape with a maximum diameter of 1.5 to 2 times the original emplacement drift diameter. Detailed analysis demonstrates different mechanisms of drift collapse depending on the rock mass strength category (BSC 2004a, Section 6.4.2.2). In poor quality rock masses (e.g., Table 2.3.4-16, categories 1 and 2), far-field stress (unaffected by the drift) is mostly elastic during the history of the ground shaking. However, stress amplifications and concentrations around the drift cause intense yielding in tension and shear, which eventually causes the drift to collapse. In the case of better rock mass quality (e.g., category 5), the rock mass fails in tension even for far-field conditions (away from the drift), and tensile fractures propagate throughout the rock mass. The drift creates an open space into which the loose blocks collapse, after which, the overall bulking of the collapsed material in the model causes complete closure of the drift opening (BSC 2004a, Section 6.4.2.2.2.2 and Figure 6-132).

  Because complete drift collapse was observed at the 2.44 m/s PGV level, additional rockfall at higher PGV levels were considered unnecessary (BSC 2004a, Section 6.4.2.2).

Summary of Rockfall Under Vibratory Motion for Lithophysal Rock—Analyses indicate that postclosure ground motion results in a gradation of damage level, depending on the PGV of the time history and the rock strength category. In general terms, a PGV of approximately 2 m/s or greater will result in damage sufficient to cause rubble to at least cover the drip shield for all lithophysal rock strength categories. The resulting rubble impacts the drip shield in a dynamic fashion as it falls and eventually covers the drip shield, resulting in a static loading condition due to the weight of the rubble. To examine the ultimate rubble loads on the drip shield, the final collapsed state of the rock mass was determined from the UDEC numerical model. The ultimate collapsed state for multiple realizations of rock particle shape for the lowest strength rock category was used for estimating the drip shield static load. Figure 2.3.4-43a illustrates one of these cases at final equilibrium in which the rubble has dislodged from the surrounding rock mass and has naturally bulked in volume until further collapse is choked off. The resulting pressure distribution on the 30 structural segments comprising the drip shield for six different realizations of rock particle shape are given in the histogram in Figure 2.3.4-43b. The data from this figure, which are used to supply loading input to drip shield structural analyses (Sections 2.3.4.4.8 and

2.3.4.5.3.), illustrate the variability of loading on the drip shield due to point loading by rock particles.

2.3.4.4.5.5 Evaluation of Alternative Models

The continuum representation of a fractured rock mass was considered for modeling of lithophysal rock. In the continuum model, the effect of lithophysae and fractures is accounted for directly into the material properties and yield criteria assumed for the elements in the equivalent continuum representation of the rock mass. Thus, the fractures and lithophysae are not represented explicitly in the model (as was the case with UDEC) but are implicitly represented via assignment of average properties and an appropriate yield criterion that reproduces the overall failure response of the rock mass. In this approach, rock damage is expressed as element yielding (i.e., its strength has been surpassed) rather than explicit estimates of damage and rockfall. The continuum models employed here (FLAC or FLAC3D) are representative of the lithophysal rock mass material yielding behavior with an elasto-plastic constitutive model and Mohr-Coulomb yield criteria. Yielding occurs when the stress state within the element reaches the strength criterion specified by the constitutive law (i.e., the yielding of elements in the continuum). The yielding of elements in the continuum is not equivalent to rockfall but is an indication of overall stability of the drifts. Therefore, although continuum-based models were not used for explicit estimation of rockfall or drift profile, they are used for comparison to discontinuum model stability estimates (BSC 2004a, Section 7.6.5.4).

Additional analyses were also conducted to examine the potential for rockfall controlled by the more widely spaced, longer trace length (i.e., length greater than 1 m) fractures. These analyses examined whether it is possible that larger blocks could be formed by these structures. The FracMan program was used to construct a 100-m rock mass cube populated by longer trace length fractures for the Tptpll in the same manner as was performed for the Tptpmn. The 3DEC program was then used to examine the stability and rockfall for emplacement drifts considering extremely low fracture strength properties, which provides an assessment of the formation of all possible rock blocks. It was determined that the longer trace length fractures do not form kinematically removable blocks, confirming that the failure mode in lithophysal rock is a formation of small blocks related to the short, ubiquitous fracture and lithophysae fabric (BSC 2004a, Section 6.4.3).

2.3.4.4.6 Time-Dependent Degradation of Rock Mass Strength in Lithophysal Units

[NUREG-1804, Section 2.2.1.3.2.3: AC 4, AC 5]

This section on time-dependent degradation of rock mass strength in lithophysal units includes a conceptual description of the analysis, the results of the time-dependent drift degradation analysis, and the drip shield loading from time-dependent collapse over very long time periods.

2.3.4.4.6.1 Conceptual Description of Analysis

Introduction—The degradation of the emplacement drifts is the result of two potential mechanisms—seismic loading, as described in previous sections, or the long-term, time-dependent strength loss of the rock mass around the drifts when subjected to constant or slowly varying thermal and in situ stresses. Seismic-induced drift collapse has been included in performance assessment analyses (included FEP 1.2.03.02.0C, Seismic-induced drift collapse damages EBS components Table 2.2-5), while drift collapse resulting from time-dependent rock

mass strength reduction has been excluded from the performance assessment (excluded FEP 2.1.07.02.0A, Drift collapse, Table 2.2-5). This section reviews the analyses performed to investigate the time-dependent strength loss effects on drift stability and collapse potential. Although the analyses presented here show that the time-dependent effects are expected to be small, with little impact in the first 10,000 years after closure, the bounding collapse shape and the resulting static rubble loads are also estimated for longer time periods as part of the analysis to determine maximum rubble loads. The ultimate extent of drift collapse and the rubble loads generated are primarily a function of the density of the rubble (the density is significantly less than the in-place rock mass). As the rubble falls, its volume bulks and eventually "chokes" off further collapse as it comes into contact with the drift roof. The resulting maximum loads (whether a function of rockfall from (1) repetitive seismic events; (2) a single, less frequent, low probability seismic event; or (3) bounding drift degradation for long time periods) are essentially the same. Long-term mechanical response of excavations depends on a number of factors, including:

1. Degradation due to time-dependent fracture development in the rock matrix or along joint (or existing fracture) surfaces in the presence of water vapor and driven by mechanical and thermal stresses. Large-span excavations initially created with low factor of safety against collapse and using poorly controlled excavation methods increase degradation potential.

2. Degradation due to time-dependent alteration of rock matrix or joint-filling materials due to rock mass thermal and moisture conditions. Water sensitive minerals, such as clays, increase degradation potential.

General understanding of the time dependent strength reduction of the rock mass surrounding tunnels excavated in hard rock is subject to uncertainty because most engineered excavations are designed for a relatively short life span or are typically supported to provide safe access for personnel. A detailed database of the long-term stability of unsupported man-made excavations and natural underground openings is not readily available. Therefore, it is difficult to develop general rules for time-dependent degradation based purely on empirical observations. The approach used here for estimation of time-dependent degradation effects is based on development of a mechanistic understanding of the time dependency of strength change of Yucca Mountain site-specific rocks. The approach is based on development of a database of laboratory test results defining time-related strength changes of tuff, followed by application of these data within numerical models of drift stability. This analysis accounts for the site-specific, time-evolving stress conditions over the postclosure time period, as well as environmental effects (i.e., drift temperature and humidity) on rock strength change. Uncertainty in the rock mass properties is accounted for through use of appropriate ranges of estimated rock mass strength and time-dependent variability (BSC 2004a, Section 6.4.2.2.3).

Due to the general lack of water-sensitive in-filling materials (e.g., smectite clays) in natural fractures or within the rock matrix, the impact of humidity and saturation level on alteration of minerals is expected to be inconsequential during the postclosure time period (BSC 2004a, Section 6.3.1.5). Therefore, degradation of rock or fracture strength properties due to mineral alteration is not accounted for in stability analyses. The primary driving mechanism for time dependency is expected to be strength loss of the matrix material due to subcritical microcrack growth resulting from a stress corrosion mechanism (e.g., Martin, Noel et al. 1997a; Potyondy and

Cundall 2001). This mechanism results in time-dependent crack growth due to stress, temperature, and the partial pressure of water at the tips of microcracks. These microcracks may begin as flaws in the rock or grain-boundary contacts. A crack grows either through grains or along grain boundaries due to the hydration and breaking of silicon–oxygen bonds at the tip of the crack. The rate at which the crack grows is controlled by the diffusion of water to the crack tip, which is, in turn, dependent on the crack geometry, which is stress-dependent. The overall impact of these factors is a logarithmic form of crack growth as a function of time and stress. This mechanism is commonly termed stress corrosion cracking. Experimental data on single crystals of quartz, as well as in rocks, have validated these mechanisms (e.g., Martin 1972; Kranz 1979). Laboratory testing has been performed to define the rate at which this stress corrosion mechanism occurs in Yucca Mountain tuff under saturated and heated conditions. The results of this testing have been used to develop a time-dependent strength model that has been implemented within a drift-scale stability model. This model was then used to examine time-dependent drift degradation for the postclosure in situ and thermal stress history (BSC 2004a, Section 6.4.2.4).

Observations of Existing Tunnels at Yucca Mountain—Unsupported or lightly supported tunnels can stand in a stable condition for long time periods, particularly in good quality rock masses. For example, the ESF (7.62-m-diameter) and ECRB Cross-Drift (5-m-diameter) tunnels were constructed in 1995 to 1997 and in 1998, respectively. Although the ESF main loop is located largely in the Tptpmn, the ECRB Cross-Drift cuts through and exposes all of the repository host horizon units. The tunnels are, in general, lightly supported with friction rock bolts and light wire mesh in the tunnel roof, with occasional friction bolts in the tunnel walls. There is no evidence of significant deterioration or degradation of the rock mass, and no significant episodes of rockfall have occurred (BSC 2004a, Section 6.4.2.4).

An external review panel convened to examine Yucca Mountain drift stability (Brekke et al. 1999) found that excavations of the North Ramp through the Tptpul and the ECRB Cross-Drift through the Tptpll show that both zones have properties that are favorable for stability with minimum ground support. The panel also found that rock conditions in the Tptpll in the ECRB Cross-Drift were similar to those observed in the Tptpul in the North Ramp in the following ways:

- Continuous joints were not apparent.
- Zones with more frequent short fractures were present.
- Overbreak (i.e., block fall-out that occurs immediately after excavation) and block loosening were largely absent.

Tunnel deformation measurements have been regularly monitored since excavation, showing stable conditions; tunnels in both the lithophysal and nonlithophysal rock masses are in a stable and self-supporting mode with no obvious deterioration in 9 to 12 years. Additionally, the Drift Scale Test, which involved heating a representative repository-scale tunnel in the nonlithophysal rock mass to postclosure temperature distributions, was followed by a thermal overdrive experiment to test rock strength limits. The experiment, now well into its cooldown phase, showed stable and predictable conditions at expected repository peak temperature conditions. Overdrive to approximately 200°C drift-wall temperatures showed predictable, minor spalling of a small portion of the center of the crown of the drift (BSC 2004a, Section 7.6.5.3). Cooldown has showed no

observable major or extensive instability of the tunnel. This experiment confirmed modeling estimates of stable drift conditions in the nonlithophysal rock for expected repository temperature and combined in situ and thermal stress conditions.

Time-Dependent Degradation Model—The emplacement drifts will also be subjected to in situ and slowly changing thermally induced stress conditions over a long time period. The strength of the rock mass will degrade over time due to a stress corrosion mechanism. When brittle rocks like the Topopah Spring Tuff are subjected to a constant or slowly varying stress in the presence of pore water, matrix microcracks will propagate in a time-dependent way along the boundaries of the grain structure. As microcracks grow and coalesce, a rock mass failure mechanism may develop. The time to failure for a rock mass with saturated conditions depends on stress at the crack tips, which is dependent on the ratio of the applied stress to rock strength (i.e., the lower the stress level, the longer the time to failure). Studies of basic growth of single fractures in quartz crystals and the creep strains resulting from microcrack growth in complex silicate rocks demonstrate that the same basic stress corrosion mechanism is responsible for time-dependent crack growth and the ultimate time to failure of the rock. The stress corrosion mechanism gives rise to a logarithmic relationship of time to failure as a function of the state of stress, the temperature, and the pore pressure (Scholz 1972; Martin, Noel et al. 1997a). To estimate potential long-term failure times and mechanisms in the Topopah Spring Tuff, determination of the time to failure as a function of stress level is necessary.

The relationship of time to failure as a function of applied stress level for a rock is typically determined by conducting creep experiments in the laboratory on rock samples at heated and saturated conditions. During a creep experiment, the rock sample is loaded to some percentage of its estimated compressive strength and held constant while the sample strain is monitored. The sample will eventually fail ("static fatigue limit") and the time to failure can be plotted against the ratio of applied stress to rock unconfined compressive strength ("driving stress ratio") to establish a time-dependent failure condition for the rock. The slope of this plot is indicative of the rate of strength time-dependency. Figure 2.3.4-44 shows the time to failure data for Topopah Spring welded tuff in comparison to data for the Lac du Bonnet granite from the Canadian nuclear program's Underground Research Laboratory in Manitoba (BSC 2004a, Section 6.4.2.4.2.2 and Appendix S). In this figure, the welded tuff matrix material has significantly slower time-dependency than granite due to the fine-grained nature and high silica content of the tuff.

The fundamental time-dependent failure mechanism of silicate rocks (stress corrosion cracking) has been verified for systems of increasing complexity, from single quartz crystals to silicate rocks. This mechanism leads to a logarithmic form of time to failure in terms of the applied stress levels. Since the form of time-dependency is known, even relatively short-term test data of weeks to months can be used for estimating long-term response of the matrix material (BSC 2004a, Section 6.4.2.4.2.2). The static fatigue testing on Topopah Spring Tuff at elevated temperature and saturated conditions provides the basic data required for predictive modeling of emplacement drift stability during the long post closure time period.

To assess the potential for time-dependent effects in drift stability in lithophysal rocks, a linear fit was made to the tuff static fatigue limit data representing the logarithm of the time to failure as a function of the driving stress ratio. To represent time dependence within the UDEC drift stability model described in Section 2.3.4.4.5.1, the basic rock mass strength properties must be adjusted to

reflect strength degradation as a function of time. The approach taken was to assume the rock mass cohesion and tensile strength are reduced to zero in a brittle, abrupt fashion when the time to failure, defined by the slope of the static fatigue test results, was reached. Details of the determination of the time-dependent response of lithophysal rock and the abstraction of these data into the UDEC drift-scale model can be found in *Drift Degradation Analysis* (BSC 2004a, Section 6.4.2 and Appendix S).

2.3.4.4.6.2 Results of Time-Dependent Drift Degradation Analysis

Analyses were performed for time-dependent drift degradation in which models for each rock strength category were subjected to in situ stress and the thermal stress history for the entire postclosure time period. The rock mass was allowed to yield and fracture from both the transient thermal stressing as well as the time-dependent strength degradation. At the time of peak thermal stress (within 50 years after closure) and at completion of 10,000 years, the model was subjected to multiple 0.4 m/s PGV level ground motions to determine whether rock, fractured and loosened by time-dependent damage, could be shaken down by more frequent, higher-probability seismic events. Figure 2.3.4-45a, b, and c show the results of the time-dependent degradation for in situ and thermal stress conditions (i.e., the nominal or early failure scenarios) at 10,000 years, and for the same scenarios with the 0.4 m/s PGV level seismic shaking. Three cases corresponding to lithophysal rock strength Categories 2, 3, and 5 are shown. Only Categories 2 and 5 were subjected to seismic shaking. Only relatively moderate rockfall is predicted for any of the rock categories. Shear failure of the sidewalls of the emplacement drift is the failure mode observed in Categories 2 and 3, whereas yielding in the crown of the drift occurs in Category 5. This is a function of the location of the largest thermally induced stress component which is, in turn, a function of the Young's modulus of the rock mass. The predicted microfracture network induced around the excavations in the direction parallel to the major principal stress can be seen in the left-hand column of figures. Shaking of drifts from more frequent, higher probability seismic events results in shake-down of the microfractured and damaged material, but does not result in complete collapse of the drifts. Based on these results, time-dependent damage and rockfall resulting from in situ, thermal and time-dependent stresses are not considered in the abstractions of either the nominal or early failure scenarios for TSPA (excluded FEP 2.1.07.02.0A, Drift collapse, Table 2.2-5). Rather, rockfall as a function of postclosure seismic shaking results in drift collapse and drip shield loading, which is included in performance assessment analyses (included FEP 1.2.03.02.0C, Seismic-induced drift collapse damages EBS components, Table 2.2-5). In either case—seismic shaking or drift degradation—rubble loading resulting from complete collapse is used to determine the ultimate load bearing capacity of the drip shield framework and plates (Sections 2.3.4.4.8 and 2.3.4.5.3). The following describes bounding drift degradation analyses that were performed to investigate the maximum possible drift breakout dimensions and maximum static rock rubble load applied to the drip shield.

2.3.4.4.6.3 Drip Shield Loading from Time-Dependent Drift Collapse Over Very Long Time Periods

The loading of the drip shield in response to time-dependent drift degradation was examined in a bounding fashion, assuming complete collapse over very long time periods. In Section 2.3.4.4.5.4, the drip shield loading resulting from seismic collapse of the tunnels was discussed as having a dynamic and static component. In the time-dependent drift degradation case, the drifts are assumed

to undergo cohesion and tensile strength loss, with resultant caving of the rock mass adjacent to and above the drift. Although the analyses presented in the previous section do not indicate complete time-dependent drift collapse in the initial 10,000 years after repository closure, potential drip shield loading is conservatively estimated for a completely collapsed drift. Thus, conservative estimates of the static rubble load that would accompany a slow degradation of the drip shield over very long time periods are made and used in drip shield stability calculations (SNL 2007b, Section 6.4.3.1), and presented in Section 2.3.4.5.3.

Time-dependent collapse in the lithophysal rock mass would result in microfracture development and ravelling of the rock into a number of blocks that fall onto an accumulating rubble pile surrounding the drip shield. The blocks that have fallen into the excavation do not fit together as tightly as when originally part of the rock mass, resulting in increased porosity and overall volume expansion. The increase in rock mass volume after caving is described by a bulking factor, which is a factor representing the volumetric increase of the rock after collapse. The bulking factor depends on the rock lithology, preexisting internal structure, and mechanism of collapse but is generally taken to be in the range of 0.2 to 0.4 (i.e., a 20% to 40% volume increase) (BSC 2004a, Section 6.4.2.5). Caving of underground excavations is a self-limiting process in places where the tunnel is not close to the ground surface. At a certain stage of caving, due to bulking of the rubble, the volume of the caved rock completely fills both the volume of the original excavation and the volume occupied by the collapsed rock before onset of collapse. When the cave is completely filled, the broken rock provides a backpressure to the surrounding rock mass, which prevents further collapse. The important parameters for estimation of the rubble load applied to the drip shield are the resulting cave shape, the cave height, and the bulking factor of the rubble material (BSC 2004a, Section 6.4.2.5).

The approach for analysis of the cave height and shape and the subsequent load of the broken rock on the drip shield involved the use of three different methods, each with varying assumptions and varying levels of conservatism: analytical solutions, numerical continuum modeling, and numerical discontinuum modeling (BSC 2004a, Section 6.4.2.5.3). Each of the methods uses certain conditions and assumptions regarding caving of the rock above the drifts and transfer of the stresses within the broken rock mass. The level of conservatism is the largest in analytic methods and the smallest in the discontinuum method. The analytical and continuum modeling approaches each require assumptions of the eventual shape of the caved zone as well as the bulking factor as input. The discontinuum method, which utilizes the same UDEC model used for seismic and time-dependent drift degradation estimates, requires no assumption of cave shape, height, or bulking factor. The cave shape and height are allowed to develop naturally in the model as the rock mass strength is reduced to simulate time-degradation. The rock dislodges from the roof and sidewalls of the drift and bulks and compacts in a natural fashion. Stress transfer through the rubble to the drip shield and drift invert occurs naturally during the compaction process, and interaction between the deformable drip shield and rubble occurs automatically. For these reasons, the discontinuum modeling method is considered to be the most reasonable alternative for estimation of drip shield static loading (BSC 2004a, Section 6.4.2.5).

2.3.4.4.6.3.1 Model Description and Evaluation of Alternative Methods

Analytical Method—This method assumes that the cave above the emplacement drift grows until it becomes filled with the broken rock. The vertical extent of the caved rock is calculated as a

function of the assumed bulking factor of the rubble, considering that the cave stabilizes when it is completely filled with the broken rock. An additional assumption that must be made is the ultimate shape of the cave. Two basic assumptions for cave shape and the mechanism of caving were considered for analysis. First, a piping failure condition was analyzed in which the cave is considered to propagate in a vertical direction directly above the drift. This failure condition is sometimes observed in mining applications such as longwall coal mining for conditions in which there is a relatively large ratio of the span of the excavation to its depth from ground surface and where the overburden rock is thinly bedded, as occurs in some sedimentary rocks. This mechanism provides an upper bound to drip shield load as it provides an estimate of the maximum vertical cave height (BSC 2004a, Section 6.4.2.5).

An alternative analytical method for estimating the collapse height of a tunnel utilizes a limit equilibrium method based on the Terzaghi assumption (Terzaghi 1943). This method corresponds to the limit equilibrium conditions for shear failure and collapse of the rock mass around a shallow tunnel. These two assumed mechanisms (i.e., piping and Terzaghi) and their associated analytical estimates of rubble pressure applied to the drip shield represent extreme upper bound conditions for tunnel collapse in terms of both the height of collapse and the loading applied through the rubble to the drip shield. No stress arching or load transfer through the rubble to either the solid rock sidewalls or the tunnel invert occurs in these solutions. Therefore, all of the vertical load of the rubble is assumed to act directly on the drip shield. Numerous field measurements of actual load on tunnel conduit linings show that significant vertical load is actually shed off to the surrounding rock mass and not directly on the lining, reinforcing the conservatism inherent in the use of an analytical approach. Expressions for the height of the cave were derived for each mechanism, and the pressure of broken rock on the drip shield was computed (BSC 2004a, Section 6.4.2.5) for a range of assumed bulking factors.

Numerical Continuum—The use of a continuum numerical model for estimation of rubble load provides a similar methodology to the analytical approach but is somewhat more realistic in that load transfer within the caved rock can be represented in a more realistic fashion. As was the case in the use of analytical methods, the bulking factor of rubble and general shape of the cave must be assumed. A model of the drift in the rock mass represented as a Mohr-Coulomb material was developed using FLAC. Two limiting mechanisms were considered: a vertically propagating piping mechanism and a Terzaghi mechanism, which assumes the caved region may propagate laterally as well as vertically. The model was run to determine the load on the drip shield for both mechanisms for a range of assumed bulking factors (BSC 2004a, Section 6.4.2.5).

Discontinuum Method—The caving problem was also simulated using the same UDEC model as was used for the time-dependent drift degradation analysis. As described above, the discontinuum model allows the cave shape, height, and bulking factor to develop as a result of the stress conditions and the reduction in strength properties to simulate time-dependent strength degradation. Stress transfer through the rubble is automatically accounted for by the model, as is load to the drip shield. To ensure that the model estimates are conservative, the spacing of fractures in the rock mass and, thus, the block size the fractures produce were selected so that the resulting bulking factor was equal to or less than 0.2, which is considered to be a lower bound of the bulking factor expected in rocks. Additional analyses were conducted using this method to examine the potential for seismic shaking-induced compaction of the rubble (after drift collapse

has occurred and the rubble has equilibrated) and its impact on drip shield loading (BSC 2004a, Section 6.4.2.5).

2.3.4.4.6.3.2 Static Loading to the Drip Shield from Caved Rock

The predictions of average vertical pressure of the caved rubble on the top of the drip shield for all three modeling approaches are summarized in Figure 2.3.4-46 (BSC 2004a, Section 6.4.2.5). This figure presents the average vertical pressure induced on the drip shield as a function of bulking factor for all three methods. In the case of the discontinuum model, the bulking factor is a calculated value and is the reason for the nonuniform distribution of data points along the bulking factor axis. As expected, the analytical model yields the largest loads due to highly conservative assumptions. The continuum numerical model accounts more accurately for transfer of load by friction from the caved rock to the surrounding stable rock mass. Consequently, predicted loads for small bulking factors and large cavity size are much smaller than those of analytical predictions. When the bulking factor is large, the predicted height of the cave becomes small. Stress arching cannot be realized within the small column of the cave rock, and, consequently, predictions of analytical and continuum models are identical. The most reasonable approach, using the discontinuum model, does not use an imposed condition about the shape of the caved region. It also correctly accounts for load transfer through the caved rock. The predictions of the pressures on the drip shield using this approach are smaller than the predictions of the analytical and continuum models for all values of the bulking factor. The results of the discontinuum modeling are synonymous with those shown previously in Figure 2.3.4-43 and are used as direct input to structural analysis of the drip shield (SNL 2007b, Section 6.4.3.1, and Sections 2.3.4.4.8 and 2.3.4.5.3 of this document).

The effect of shaking from seismic events occurring subsequent to rubble loading was also examined (BSC 2004a, Section 6.4.2.5). The seismic shaking may result in additional compaction of the rubble, with a potential associated decrease in the bulking factor and additional loading of the drip shield. As shown in Figure 2.3.4-46, there is an increase in average vertical pressure induced on the drip shield for compaction from ground motions with PGV greater than 0.4 m/s, corresponding to a mean annual probability of exceedance of 10^{-4}. The analyses show that there is a maximum change in the average vertical pressure on the drip shield of approximately 33% when comparing the average static pressure before and after shaking from a 2.44 m/s PGV level seismic event. The impact of seismic shaking decreases significantly for higher probability events. However, the increase in the average vertical pressure is still below the load-bearing capacity for drip shield stability, as described in Section 2.3.4.4.8.

2.3.4.4.7 Assumptions Used in Rockfall Models

[NUREG-1804, Section 2.2.1.3.2.3: AC 1(2), (3), AC 5]

Assumptions for the rockfall model are grouped into four general areas: assumptions regarding repository layout, the thermal-mechanical calculations, rockfall modeling, and ground support. The specific assumptions in each of these areas are discussed in this section.

Repository Layout Information Assumption—The repository layout data are based on preliminary design information and are subject to change before being finalized. The model results are applicable for the emplacement drift diameter and emplacement drift alignment provided by repository design requirements (SNL 2007d, Table 4-1, Item Numbers 01-08 and

01-10; Table 2.2-7). The rockfall models are sensitive to both emplacement drift diameter and alignment, and any change to this design information would require reevaluation (BSC 2004a, Section 6.5).

Thermal-Mechanical Assumption—Thermal expansion values used in the rock units underlying the repository are assumed to be equal to the repository layers. This assumption is necessary because the test data from core samples of these units are limited. This assumption does not require further confirmation because temperature increase in the underlying layers should be insignificant, and thermally induced stresses should be negligible. This assumption is used in all the thermal-mechanical calculations used to support rockfall analysis for the abstraction developed for TSPA (BSC 2004a, Section 6.2 and Appendix C).

Rockfall Modeling Assumption in Lithophysal Units—Block size distribution in the lithophysal units is assumed as a function of interlithophysal fracture density and lithophysae spacing. This assumption is needed because the size of rock blocks that are created from the lithophysal rocks is estimated from geologic and empirical evidence. This assumption does not require further confirmation. The relatively abundant, uniformly distributed lithophysae, combined with the ubiquitous fracturing fabric, provide natural breaking surfaces. Observation in the ECRB Cross-Drift for block sizes on the order of a few inches in diameter supports this assumption (BSC 2004a, Appendix O).

Ground Support Assumption—It is assumed for the rockfall analysis that ground support is not present in the emplacement drifts. Ground support will degrade and eventually fail during the postclosure period. All rock blocks predicted are, therefore, blocks that fail in an unsupported opening. The assumption is considered appropriate for the postclosure period, and does not require further confirmation.

2.3.4.4.8 Rockfall and Rubble Accumulation in the Emplacement Drifts

This section provides a summary of rockfall and rubble accumulation in emplacement drifts and includes a discussion of the following:

- Conceptual description
- Data and data uncertainty
- Model and model uncertainty
- Abstraction of rubble volumes in lithophysal rock
- Abstraction of rubble volumes in nonlithophysal rock.

2.3.4.4.8.1 Conceptual Description of Rockfall and Rubble Accumulation in the Emplacement Drifts

In this section, estimates of the rock rubble volume created by vibratory ground motions of a given PGV level are determined for emplacement drifts in the lithophysal and nonlithophysal zones. A process model and abstraction of rubble volume accumulation as a function of ground motion PGV is provided here and used to determine rubble loads for drip shield fragilities in Section 2.3.4.5.3.

2.3.4.4.8.2 Data and Data Uncertainty for Rockfall and Rubble Accumulation in the Emplacement Drifts

The primary input data governing the estimates of rock rubble volume accumulation include the following:

- Lithophysal rock mass strength and deformation modulus estimate, rock strength time-degradation estimates, and the in situ and thermally induced stress state
- Rock particle size resulting from failure of the rock mass around a tunnel in the lithophysal rock mass
- Fracture pattern in the nonlithophysal rock mass
- Ground motion level (PGV or peak ground acceleration)
- Bulking factor of the rock rubble.

2.3.4.4.8.2.1 Lithophysal Rock Strength and Modulus

The strength and modulus of the lithophysal rock mass and their variability are important in determining the stability of the drifts under in situ and thermal stresses, and the failure extent of the drift when subjected to stresses from vibratory ground motion. The in situ strength of the lithophysal rock mass was estimated from laboratory compression testing of large samples (approximately 1 foot diameter) obtained from drilling in the ECRB Cross-Drift and ESF exploration tunnels in Yucca Mountain. The strength and deformation modulus of the lithophysal rock mass has been shown to be a function of the degree of porosity of the sample. Section 2.3.4.4.2.3.7 provides a description of the estimate of the in situ lithophysal rock mass strength and deformation modulus as a function of the level of lithophysal porosity. Uncertainty in the rock mass strength has been taken into account in deterministic calculations of drift stability under thermal-mechanical and seismic loading, by subdividing the expected total range of rock mass strength into 5 categories that are roughly based on the degree of lithophysal porosity. Rock mass categories 1 through 5 represent approximately 3%, 7%, 25%, 35%, and 30% of the Tptpll stratum of the lithophysal rock mass, respectively (SNL 2007c, Section 6.7.1.1).

The rate of time-dependent degradation of the rock mass when subjected to slowly varying thermal-mechanical stresses is important in defining the timing and extent of drift failure in the absence of seismic loading. The time-dependent degradation of the rock matrix strength was determined from laboratory compression testing of tuff samples from the repository host horizon under saturated conditions, at a temperature of 100°C and confining pressure of 5 MPa. These environmental conditions ensure that the time-dependency rate was determined with conditions that promote the basic stress corrosion crack growth mechanism identified as a primary mechanism for strength degradation in tuff. Simulations of the thermal-mechanical history of emplacement drifts, presented in Section 2.3.4.4.3, indicate that drift failure and rubble accumulation resulting from degradation of the rock mass strength is expected to require thousands of years, and would be minor in comparison to loosening and rockfall resulting from vibratory ground motion effects. A description of the basis for exclusion of time-dependent drift degradation mechanisms from

consideration in rubble accumulation can be found in *Features, Events, and Processes for the Total System Performance Assessment: Analyses* (SNL 2008a, FEP 2.1.07.02A, Drift collapse). Therefore, only vibratory ground motion effects are considered in estimates of rubble accumulation.

2.3.4.4.8.2.2 Rock Particle Size in the Lithophysal Rock

In the lithophysal zones, the rock mass has a relatively low compressive strength, and is permeated with void spaces of varying size. Fracture surfaces are discontinuous but closely spaced, with short-length fractures coupled with lithophysae spaced on the order of 0.1 meters (BSC 2004a, Section 6.1.4.1). Under the dynamic stresses imposed by large vibratory ground motions, drifts in the lithophysal zone are predicted to partially or fully collapse into small fragments, with particle sizes of centimeters to decimeters (BSC 2004a, Section 8.1).

2.3.4.4.8.2.3 Fracture Patterns in the Nonlithophysal Rock

The fracture patterns in the nonlithophysal rock mass govern the size and shape of rock blocks, and have an impact on the amount of rubble produced during episodes of seismic shaking. The dynamic three dimensional discontinuum calculations described in Section 2.3.4.4.4 simulate the process of vibratory shaking of approximate 25-m-long sections of emplacement drifts in nonlithophysal zones, as well as the resulting rockfall impact to and accumulation around the drip shield. The basic stochastic description of the rock mass fracture geometry used as input to the 3DEC model was derived from a set of 105 different synthetic fracture patterns within a representative cube of nonlithophysal rock mass 100 m on a side. The synthetic fracture patterns in this cube were developed using the FracMan fracture modeling software and was based on fracture geometry data obtained from full periphery geologic fracture maps developed during construction of the ESF and ECRB Cross-Drift tunnels (Section 2.3.4.4.4). To estimate rockfall for emplacement drifts excavated in this synthetic rock mass when subjected to vibratory ground motion, dynamic simulations were conducted using various random tunnel locations paired with a range of possible ground motion time histories. A simple Latin Hypercube sampling scheme was used for the pairing of ground motions and tunnel locations (i.e., fracture modeling regions) (BSC 2004a, Section 6.3.1). Rockfall calculations for the nonlithophysal units have been performed for ground motion time histories at the 0.4 m/s, 1.05 m/s, 2.44 m/s, and 5.35 m/s PGV levels. A total of 50 rockfall calculations were performed at each of the 1.05 m/s and 2.44 m/s PGV levels, with 44 rockfall calculations at the 5.35 m/s PGV level, to provide a reasonable stochastic basis for estimation of the size, shape and energy content of the rockfall blocks dislodged. Note that the site-specific ground motions are unbounded and exceed the maximum bounded PGV of approximately 4 m/s (Section 2.3.4.3.3), and thus the estimates of rockfall and drift damage generated by the postclosure ground motions (e.g., a PGV of 5.35 m/s) are correspondingly conservative. Each of these PGV levels is represented by 15 sets of ground motion time histories. There are a total of 32 rockfall calculations at the 0.4 m/s PGV level. Additional parameter analyses using 3DEC investigated the impact of fracture and intact rock strength ranges on the block size and rubble volume as summarized in Section 2.3.4.4.4. All of these analyses have been used to derive expected distributions and ranges of rock block sizes in the nonlithophysal rock units.

2.3.4.4.8.2.4 Ground Motions

Uncertainties in the effect of ground motion level and time history variability on rockfall and rubble volumes were taken into account in calculations in both the lithophysal and nonlithophysal rock units. In the lithophysal rockfall analyses rubble volumes were estimated for 15 ground motions representative of the 0.4 m/s, 1.05 m/s, and 2.44 m/s PGV levels. Calculations were not necessary at the bounding 4.07 m/s level, since the drifts are all predicted to completely collapse, with resulting maximum rubble loading. Instead of simulating all possible combinations of the 15 sets of ground motion for the 2.44 m/s PGV level with the five rock mass categories, only the 15 realizations shown in Table 2.3.4-23 were simulated (BSC 2004a, Section 6.4.2.2 and Table 6-44). The ground motion numbers and rock mass categories in Table 2.3.4-23 are based on a Latin Hypercube sampling for these two parameters. Note that the 15 ground motions are numbered 1 through 14 in sequence, and 16, and are considered equally probable. Similarly, the rock mass categories are also treated as equally probable. Based on Latin Hypercube sampling (BSC 2004g), the 15 realizations in Table 2.3.4-23 are selected as representative of the possible response of the rock mass. In the rockfall simulations for the nonlithophysal rock mass, uncertainty in the ground motions was accounted for by conducting calculations for PGV levels of 1.05 m/s, 2.44 m/s, and 5.35 m/s. Note that the site-specific ground motions are unbounded and exceed the maximum bounded PGV of approximately 4 m/s (Section 2.3.4.3.3), and thus the estimates of rockfall and drift damage generated by the postclosure ground motions (e.g., a PGV of 5.35 m/s) are correspondingly conservative. Each of these PGV levels is represented by 15 sets of ground motion time histories. Simulations at the 0.4 m/s PGV level were conducted for a single set of ground motion time histories. These simulations cover the expected range of shaking intensity (PGV) and variability of the ground motions.

2.3.4.4.8.2.5 Bulking Factor of the Rubble

The shape of the collapsed drift varies with the local fracture pattern in the host rock, the strength and modulus of the rock mass, and the ground motion PGV level. There is significant uncertainty in the volume of intact lithophysal rock that, through caving, can generate enough rubble to fill the open volume (i.e., that volume between the original drift surface which is above the crushed tuff invert and outside the drip shield—approximately 12 m^3/m) in the drift. As the intact rock blocks detach from the surface of the drift, they fall and pack at a lower density than the intact material since it is impossible to perfectly piece together the rubble into its original condition. The increase in volume of the rubble from the original intact rock is typically expressed as a "bulking factor," which is a numerical factor in common use in the construction and mining industries for estimation of the volume of broken rock. The bulking factor is important in calculation of the vertical pressure exerted on the drip shield, since it controls the ultimate height to which a drift can collapse, and thus the static load generated on the drip shield crown. The uncertainty in the rubble volume (and thus the rubble load) is represented as a range of bulking factors for the rubble from the intact rock (BSC 2004a, Section 6.4.2.5.2). The bulking factor, B, is defined as the rubble volume, V_r, relative to its initial volume as intact rock, V_i:

$$V_r = (1 + B)V_i \qquad \text{(Eq. 2.3.4-1)}$$

An equivalent definition of the bulking factor is $\Phi/(1 - \Phi)$, where Φ is the porosity of the caved rock.

Values of the swelling factor for caved rock are 1.16 for rock masses displaying "fine" fragmentation, 1.12 for "medium" fragmentation, and 1.08 for "coarse" fragmentation (Laubscher 1994). The size scales for the lithophysal rubble (and for the nonlithophysal rock blocks) generally fall within the "fine" category of fragmentation. The swelling factor is defined as (1 + B), which implies a bulking factor of around 0.16 for caved rock (i.e., volume increase of 16% in transition from intact rock to rubble).

The El Teniente mine in Chile uses the caving method of mining. In this method, the orebody is completely undercut by a horizontal, planar slot, eventually inducing caving and fragmentation of the overlying rock mass. The caved material is drawn away, providing free volume that allows the caving process to continue upwards. If the caved material is not drawn, the cave will rapidly stop as the bulked material comes into contact with the roof. Gravimetric surveys at the mine showed the density of broken rock within the caving rock volume to be 2110 to 2200 kg/m^3 for a rock with an in situ (noncaved) solid density of 2610 to 2700 kg/m^3 (Behn and Brzovic 1996). These values lead to porosity for the caved rock between 0.16 to 0.22, which is equivalent to a bulking factor between 0.19 and 0.28, or a 19% to 28% increase in volume when transitioning from intact to caved material. Another example of field estimate of bulking factors is given by Duncan et al. (1980, Table 5), who reported that the porosity of the graded rock fill for dams is between 23% and 36%, which is equivalent to a bulking factor between 0.30 and 0.56.

An alternate approach is to estimate the bulking factors for lithophysal rock using simulations of degradation and caving of emplacement drifts conducted with the UDEC discontinuum program. The UDEC discontinuum approach is particularly useful in estimation of bulking factors since it simulates the progressive fracturing and fragmentation of the intact lithophysal rock mass during collapse of an emplacement drift. Thus, use of this model provides a methodology for prediction of bulking factors that is distinct from the field observations described above. Assuming that the intact rock will fragment into rock particles with a characteristic length scale of approximately 0.2 meters or less, as is expected to occur in the lithophysal zones, the calculated bulking factor from the UDEC drift caving simulations varies between 0.19 and 0.25 (BSC 2004a, Table P-9). These values are consistent with the measured values (0.19 to 0.28) at the El Teniente mine.

Taking into account the field and numerical results, the range of bulking factors for the caved rock is assumed to be 0.1 to 0.4 (SNL 2007c, Section 6.7.1.5). This range of values encompasses the bulking factors determined from typical swelling factors for caved rock (Laubscher 1994) and the measured values from the El Teniente mine. This range of values encompasses the calculated bulking factors for lithophysal rock with the UDEC code. Finally, this range of values encompasses part of the data for graded rock fill for dams (Duncan et al. 1980). The extreme bulking factors for a graded rock fill are considered to be not representative of the properties of ungraded caved rock.

2.3.4.4.8.3 Model and Model Uncertainty for Rockfall and Rubble Accumulation in the Emplacement Drifts

2.3.4.4.8.3.1 Rubble Accumulation in Lithophysal Zones

A series of simulations of emplacement drift stability in the lithophysal zone, when subjected to seismic shaking, was conducted using the two-dimensional discrete element program UDEC. These analyses are described in detail in *Drift Degradation Analysis* (BSC 2004a, Section 6.4.2), and are summarized in Section 2.3.4.4.5. The intact rock mass in these simulations was composed of a large number of blocks of the expected fragment size in the lithophysal zone, based on the spacings of the ubiquitous fracture fabric (Figure 2.3.4-40). The blocks were initially bonded with shear and tensile strength at their interfaces with neighboring blocks to obtain an overall rock mass strength equal to those of categories 1 to 5 (Figure 2.3.4-30). As the rock mass is stressed from thermal-mechanical and dynamic sources, the bonds between these blocks may fail, representing fracturing and loosening of the intact rock mass. The drift failure and the resulting rock rubble volumes produced have been conducted for ground motions at peak ground velocity levels of 0.4 m/s, 1.05 m/s, and 2.44 m/s PGV levels. A summary of the volume of rockfall per meter of drift from these calculations is presented in Table 2.3.4-23. The volumes in Table 2.3.4-23 are the volume of intact (in-place) lithophysal rock that caves into the drift during the seismic event. These volumes do not include the effect of bulking in the rubble, as discussed in Section 2.3.4.4.8.2. The ground motion number and rock mass category for each realization in Table 2.3.4-23 are defined in (BSC 2004a, Table 6-44).

The volume of lithophysal rock that caves during the event is based on the results for rock mass Categories 2 through 5. The results for rock mass Category 1 have not been included in the conditional rubble volumes. Rock mass Category 1 produces significantly greater rubble volume at the 0.4 m/s PGV level than rock mass Categories 2 through 5. However, rock mass Category 1 represents only 3% of the emplacement drifts in the lithophysal zones. This 3% represents a small spatial variability in the rock mass. TSPA does not represent this variability, but applies a single value for rubble volume from a seismic event throughout the lithophysal units. The data for rock mass Category 1 has therefore not been included in the abstraction because the large rubble volumes in 3% of the lithophysal zones would be applied throughout the repository (for 3% of the realizations) (SNL 2007c, Section 6.7.1.2). The assessment of the long-term strength of the rock mass indicates that the lower bound quality rock mass can be represented as rock mass Category 2 (BSC 2004a, Section 8.1).

Rock mass Categories 2 through 5 represent 97% of the emplacement drifts in the repository, and generally produce similar rubble volumes at the 0.4 m/s, 1.05 m/s, and 2.44 m/s PGV levels (Table 2.3.4-23), i.e., the rubble volume at each PGV level does not correlate strongly to rock mass strength category. More specifically, there are very small rubble volumes at the 0.4 m/s PGV level, intermediate rubble volumes at the 1.05 m/s PGV level, and large rubble volumes at the 2.44 m/s PGV level for all of the realizations with rock mass Categories 2 through 5. The results indicate a "uniform" behavior with no dependence on rock quality, therefore this dependence has not been abstracted for inclusion in the TSPA.

The initial cross-sectional volume of the 18-foot (5.5-meter) diameter emplacement drift is 254 ft^3 per foot or 23.6 m^3 per meter of emplacement drift (SNL 2007c, Section 6.7.1.5, based on the drift diameter in SNL 2007e, Figure 4-1). Part of this volume is unavailable because of the

presence of the invert and drip shield, but the solid drift walls expand outward and upward as the host rock collapses into the drift. Both of these factors need to be considered in defining the drift volume after collapse.

The unavailable volume is estimated from the volumes of the invert and drip shield. The volume of the invert is 47 ft^3 per foot (SNL 2007c, Section 6.7.1.5, based on dimensions from SNL 2007e, Figure 4-1) or 4.4 m^3 per meter of emplacement drift. The cross-sectional area of the drip shield is estimated with a simple approximation. The nominal width and nominal height of the drip shield are 99.8 in. (2535 mm) and 113.6 in. (2885 mm), respectively (BSC 2007b, Table 1). Based on these dimensions, the volume excluded by the drip shield is less than (2.533 m) (2.886 m) = 7.3 m^3 per meter (78 ft^3 per foot) of drift. The actual volume of the drip shield is somewhat less than this value because of its "mailbox" shape. The open volume is then greater than (23.6 – 4.4 – 7.3) = 11.9 m^3 per meter (127 ft^3 per foot) of the emplacement drift. The open volume is rounded up to 12 m^3 per meter of drift for TSPA.

Equation 2.3.4-1 shows that the increase in volume for the mass of rubble, $V_r - V_i$, is given by BV_i. This increase in volume must equal the unfilled drift volume (12 m^3 per meter of drift) for complete drift collapse (i.e., when rubble completely fills the drift). It follows that the volume of intact rock corresponding to complete drift collapse is (12 m^3/0.4) = 30 m^3 to (12 m^3/0.1) = 120 m^3 of intact rock per meter of emplacement drift. These volumes are applicable to both the lithophysal and nonlithophysal units in the repository, because the range of bulking factors is designed to represent a wide range of in situ response for caved rock.

It is useful to compare this range of volumes for complete collapse to the results from the UDEC rockfall calculations. At the 2.44 m/s PGV level, the volume of intact rock that caves into the drift varies between 61 m^3 per meter and 111 m^3 per meter (Table 2.3.4-23). Since these volumes are on the same order as the estimated volumes to fill the open volume within a drift, 30 m^3 to 120 m^3 per meter of emplacement drift, it follows that complete drift collapse occurs for many ground motions at the 2.44 m/s PGV level. At the 1.05 m/s PGV level, the volume of intact rock that caves into the drift varies between 0.58 m^3 and 29 m^3 per meter of emplacement drift, so complete collapse cannot occur at this PGV level. The results for the volume of intact rock that caves into the drift (SNL 2007b, Appendix C) are consistent with analyses that determined that the 2 m/s PGV level is an approximate threshold for drift collapse in the lithophysal zones of the repository (BSC 2004a, Section 6.4.2.2.2, fourth bullet under subheading "Discussion"). The rapid filling of the drifts mitigates concerns about multiple events weakening the rock mass.

The uncertainty in the volume of intact lithophysal rock corresponding to complete drift collapse is represented as a uniform distribution between 30 m^3 to 120 m^3 per meter of emplacement drift. A uniform distribution is appropriate here because the end points of the range are known, but the distribution of values within the range is not known. This distribution is used to determine the volume of intact lithophysal or nonlithophysal rock corresponding to complete drift collapse (SNL 2007c, Section 6.7.1.5). The fraction of drift that is filled with rubble or rockfall is defined as the accumulated volume of rubble/rockfall from the current state, along with all previous seismic events, divided by the sampled value of the volume corresponding to complete collapse.

2.3.4.4.8.3.2 Rubble Accumulation in Nonlithophysal Zones

In the nonlithophysal zones, large rock blocks may be shaken loose from the drift walls and fall onto the drip shield in response to vibratory ground motion (BSC 2004a, Section 6.3). The failure mode in the nonlithophysal rock results from dynamic stress induced yield in the intact rock between discontinuous joint traces, or along the joint surfaces themselves, followed by a gravity induced drop of discrete rock blocks that are shaken loose from the walls of the drift by the vibratory ground motion. The 3DEC calculations used for prediction of rockfall in the nonlithophysal rock mass are summarized in Section 2.3.4.4.4, and (BSC 2004a, Section 6.3) provides a detailed description.

The volume of rockfall per meter of drift for ground motion PGVs of 1.05 m/s, 2.44 m/s, and 5.35 m/s is presented in Table 2.3.4-24 in order to provide an equivalent basis for comparison to lithophysal volumes. The rockfall per meter is calculated with the effective drift length that can experience rockfall. The effective drift length that is modeled in 3DEC is 21.74 meters, so the rockfall volume per meter is calculated by dividing the total rockfall volume in Table 2.3.4-24 by 21.74 meters.

The rockfall volume in the nonlithophysal zones is significantly less than in the lithophysal zones at the same PGV level. This is reasonable since the nonlithophysal rock mass is significantly stronger than the lithophysal rock and is characterized by discontinuous fracture sets. Table 2.3.4-25 compares the mean and standard deviation of the rockfall volumes in the lithophysal and nonlithophysal zones for the 1.05 m/s, 2.44 m/s, and 5.35 m/s PGV levels.

The data in Table 2.3.4-25 indicate that the mean rockfall volume in the lithophysal rock is a factor of 40 to 200 greater than the mean rockfall volume in the nonlithophysal rock for the 1.05 m/s and 2.44 m/s PGV levels, respectively. This situation is expected to persist at higher PGV levels, although lithophysal calculations were not performed beyond the 2.44 m/s PGV level, because total drift collapse occurs for most lithophysal realizations at the 2.44 m/s PGV level.

2.3.4.4.8.4 Abstraction of Rubble Volumes in Lithophysal Rock Units

Probability of Nonzero Rockfall—The probability of nonzero lithophysal rockfall from a seismic event is based on computational results for 15 ground motions at the 0.4 m/s, 1.05 m/s, and 2.44 m/s PGV levels (Table 2.3.4-23). Rock mass categories 1 through 5 represent approximately 3%, 7%, 25%, 35%, and 30% of the Tptpll stratum of the lithophysal rock mass, respectively. Since the rock mass categories are not equally probable, it is appropriate to define the probability of nonzero rockfall based on a weighted average of the results for each rock mass category. The calculations for the weighted probability of nonzero rockfall at the 0.4 m/s, 1.05 m/s, and 2.44 m/s PGV levels are documented in Table 2.3.4-26 (SNL 2007c, Section 6.7.1.1).

Conditional Probability Distributions for Lithophysal Rockfall—Figure 2.3.4-47 presents the quantile-quantile plot for a gamma distribution versus the conditional (nonzero) lithophysal rock volume that caves into the drifts in response to ground motions at the 1.05 m/s PGV level. A quantile-quantile plot compares the values for the data points at their given quantiles with the values on a gamma distribution for the same quantiles. This quantile-quantile plot, abbreviated as Q-Q plot in this document, is a good measure of the degree to which a gamma distribution

matches the data. If the data exactly follow a gamma distribution, then all points in Figure 2.3.4-47 would fall on a straight line with a slope of 1.

Gamma distributions provide a very good fit to the conditional (nonzero) lithophysal rock volumes at the three PGV levels. Normal, log-normal, and Weibull distributions were also evaluated as alternate conceptual models to represent the rockfall volumes. Based on these results, gamma distributions are selected as the probability distribution for conditional lithophysal rock volume that collapses during the seismic event.

The abstraction for TSPA must represent the response for intermediate values of PGV. Quadratic fits to the mean and standard deviation of the rock volumes at the three PGV levels provide an appropriate way to represent the input parameters for the gamma distribution as a function of PGV. The resulting behavior at all PGV levels is shown in Figure 2.3.4-48. Figure 2.3.4-48 plots the 1st, 5th, 50th, 95th, and 99th percentiles of the resulting gamma distributions against the conditional lithophysal rock volume as a function of PGV. The gamma distributions provide a very good representation of the conditional lithophysal rock volume over the full range of PGV values relevant to TSPA (SNL 2007c, Section 6.7.1.2).

Q-Q plots were also prepared for the conditional lithophysal rock volumes versus log-normal distributions at the 0.4 m/s, 1.05 m/s, and 2.44 m/s PGV levels. The log-normal distribution provides a reasonable representation of the data for the three PGV levels, but quadratic fits to the mean and standard deviation of the natural logarithm of the conditional rockfall volumes produced highly anomalous behavior at intermediate values of PGV, so this approach was not considered further (SNL 2007c, Section 6.7.1.3).

The lithophysal rock volume from multiple seismic events is defined as the sum of the volumes from the individual seismic events. This approach provides a reasonable representation for the accumulation of failed rock over time (SNL 2007c, Section 6.7.1.4).

2.3.4.4.8.5 Abstraction of Rubble Volumes in Nonlithophysal Rock Units

Probability of Nonzero Rockfall—Based on the data in Table 2.3.4-24, the probability of nonzero rockfall in nonlithophysal rock is 0.98, 1, and 1 for the 1.05 m/s, 2.44 m/s, and 5.35 m/s PGV levels, respectively (note that the PGV level of 5.35 m/s is unbounded and beyond the maximum PGV level of 4.07 m/s on the bounded hazard curve abstracted for TSPA). These results are almost identical to the probabilities of nonzero rockfall in lithophysal rock, which are 1 at both the 1.05 m/s and 2.44 m/s PGV levels (Table 2.3.4-26). As noted in Section 2.3.4.3.2.4, the damage abstraction is based on the first horizontal component of PGV. Note that the magnitude of the second horizontal and vertical components of PGV may be greater than or less than the PGV value of the first horizontal component.

The lithophysal rock is generally weaker than nonlithophysal rock, and generally has greater rockfall volumes than the nonlithophysal rock, as shown in Table 2.3.4-25. Lithophysal rock will usually fail before nonlithophysal rock, so the probability of nonzero rockfall for lithophysal rock defines an upper bound for the probability of nonzero rockfall in the nonlithophysal zones (SNL 2007c, Section 6.7.2.2). This probability is defined in the previous section.

Conditional Probability Distributions for Nonzero Rockfall—Figure 2.3.4-49 presents the Q-Q plot for a gamma distribution versus the conditional nonlithophysal rock volume that caves into the drifts in response to ground motions at the 1.05 m/s PGV level. The gamma distribution provides a very good fit to the conditional nonlithophysal rock volumes at the 1.05 m/s PGV level, and at the other two PGV levels. Normal, log-normal, and Weibull distributions were also evaluated as alternate conceptual models to represent the nonzero damaged area. Based on these results, gamma distributions are selected as the probability distribution for conditional nonlithophysal rock volume that caves into the drift.

The abstraction for TSPA must represent the response for intermediate values of PGV. Quadratic fits to the mean and standard deviation of the rock volumes at the three PGV levels provide an appropriate way to represent the input parameters for the gamma distribution as a function of PGV. Figure 2.3.4-50 plots the 5th, 50th, 95th, and 99th percentiles of the resulting gamma distributions against the conditional nonlithophysal rock volumes as a function of PGV. The gamma distributions provide an appropriate representation of the conditional nonlithophysal rock volume over the 0.2 m/s to 4.07 m/s PGV levels that are relevant to TSPA (SNL 2007c, Section 6.7.2.3).

Q-Q plots were also prepared for the conditional nonlithophysal rock volumes versus log-normal distributions at the 1.05 m/s, 2.44 m/s, and 5.35 m/s PGV levels. The log-normal distribution significantly overestimates the rockfall volumes for the realizations with the highest values of rockfall volume in comparison to the gamma distributions, so this approach was not considered further (SNL 2007c, Section 6.7.2.4).

The nonlithophysal rock volume from multiple seismic events is defined as the sum of the volumes from the individual seismic events. This approach provides a reasonable representation for the accumulation of failed rock over time (SNL 2007c, Section 6.7.2.5).

2.3.4.5 Structural Response of EBS Features to Mechanical Degradation

[NUREG-1804, Section 2.2.1.3.2.3: AC 1(1) to (4), (7), AC 2, AC 3(1) to (3), AC 4, AC 5(2), (3); Section 2.2.1.3.3.3: AC 1(3), (4), AC 3(3), (4), AC 4(4), AC 5(3)]

Background-Evolution of the EBS Environment and Mechanical Degradation Processes—The concept for drift emplacement at Yucca Mountain is illustrated in Figure 2.3.4-1. Section 1.3.4 describes the emplacement drift geometry and the general arrangement of the EBS features. Section 1.5.2 describes the waste packages.Waste packages and their associated pallets and drip shields rest on the invert. The primary EBS features include: (1) the invert; (2) the emplacement pallet; (3) the waste package; (4) the drip shield; (5) the waste form; (6) the waste package internals; and (7) the emplacement drift.

The waste package and drip shield are the primary focus in this section because their response to seismic events has the potential to form new pathways for release of radionuclides from the EBS. The drift invert and emplacement pallet are included in the kinematic and structural response calculations for the seismic scenario class, but it is not necessary to develop damage abstractions for these components because they do not form new pathways for transport and release of radionuclides after strong vibratory ground motion events. The waste package internals and mass of the waste form are considered in the structural response calculations, *Mechanical Assessment of Degraded Waste Packages and Drip Shields Subject to Vibratory Ground Motion* (SNL 2007b, Sections 6.3

and 6.5; but are not represented as separate damage abstractions because the TSPA is not taking credit for any contribution of commercial SNF cladding to enhance the capability of the EBS to act as a barrier to radionuclide release (SNL 2008b, Section 6.6.1.1.3). Finally, the uneven settlement of the invert ballast from multiple seismic events does not compromise the capability of the drip shield to support static loads, as discussed in *Features, Events, and Processes for the Total System Performance Assessment: Analyses* (SNL 2008a, FEP 2.1.06.05.0B, Mechanical degradation of the invert) or *Mechanical Assessment of Degraded Waste Packages and Drip Shields Subject to Vibratory Ground Motion* (SNL 2007b, Section 6.4.6).

The waste form packaging for pressurized water reactor (PWR) and boiling water reactor (BWR) waste forms is standardized to a transportation, aging, and disposal (TAD) canister system that will be packaged primarily at the reactor sites. Details of the waste form packaging can be found in Section 1.5.1. Each TAD canister will be inserted into a waste package prior to emplacement at Yucca Mountain. The loaded TAD canister and waste package are referred to as the TAD-bearing waste package throughout Section 2.3.4. As described in Section 2.3.4.5.1.1, the TAD-bearing waste packages represent 67% of all the of waste packages to be emplaced at Yucca Mountain. The other major type of waste package in the inventory is the codisposal waste package, which includes DHLW packages of varying diameter and length. In the structural analyses described in this section, the codisposal waste packages are represented by the 5-DHLW/DOE SNF-Long waste package, which accounts for 17% of the total inventory of waste packages and roughly 60% of the inventory of the codisposal waste packages.

The major EBS components are free-standing structures. The drip shield and the emplacement pallet rest on top of the invert, while the waste package rests on top of the emplacement pallet. The effectiveness of these EBS components is potentially compromised by the direct effects from an earthquake, including vibratory ground motion, fault displacement, and drift collapse induced by ground motion (Included FEPs 1.2.02.03.0A, Fault displacement damages EBS components; 1.2.03.02.0A, Seismic ground motion damages EBS components; and 1.2.03.02.0C, Seismic-induced drift collapse damages EBS components, Table 2.2-5). The effectiveness of these components is also potentially compromised by indirect effects after an earthquake, including changes in seepage, temperature, and relative humidity as the emplacement drifts collapse and fill with rubble.

The emplacement drift environment and the mechanical state of the EBS components will evolve after closure of the repository. The occurrence of earthquakes over time is assumed to be a Poisson (random) process (SNL 2007c, Assumption 5.2) with shaking intensity at the repository horizon described by the bounded hazard curve (Section 2.3.4.3.3). The mechanical consequence of this seismic shaking on the EBS components depends not only on the intensity of the seismic event, but also on the evolving EBS environment, as explained below. The groundwater seepage, temperature, and humidity of the drift environment will evolve as the drifts initially heat and dry the rock mass in the near field of the drift, then re-saturate as the waste cools (Section 2.3.5). The EBS components will degrade over long time periods as a result of corrosion and vibratory motion from repetitive seismic events. The drift, itself, will undergo degradation and rockfall over time as it is subjected to repetitive seismic events as well as time-dependent rock mass failure mechanisms (Section 2.3.4.4). Thus, the consequences of a seismic event to EBS components may be significantly different for a given ground motion shaking intensity, depending on the elapsed time after repository closure.

To incorporate the long-term evolution of the EBS and in-drift environment into the analysis of damage due to vibratory ground motion, it is helpful to examine, in conceptual terms, the postclosure period in terms of the impacts of general corrosion and repetitive seismic events on the mechanical states of the emplacement drift and EBS components. Figure 2.3.4-51 illustrates, schematically, the evolution of the EBS over time. The future configuration of the EBS components is represented by three idealized states: (1) State 1—the as-emplaced configuration in which the drip shield is intact and minimal rockfall has occurred in the emplacement drifts; (2) State 2—an intermediate state of the system where the legs of the drip shield have buckled under the combined seismic/rockfall load, but the drip shield plates remain intact; and (3) State 3—the final state of the system in which the waste package is surrounded by rubble after rupture of the drip shield plates. A detailed description of each of these states follows, with reference to the locations within this section that describe assessment of the EBS response and the associated seismic damage abstractions.

State 1—Intact Drip Shield—Based on corrosion rates, the expected time for 10 mm of drip shield thinning (which corresponds to a highly degraded state) is estimated to be roughly 200,000 years after repository closure (Section 2.3.4.5.1.3.6). During this time, the drip shields can support the static load from rockfall and the waste packages and pallets can move freely beneath them. Seismic events may occur during the several hundred thousand years while the drip shields are expected to remain structurally intact. During this time, general corrosion of the EBS components will result in a slow, continuous thinning of the components, resulting in a decrease in their load bearing capacity over time. Section 2.3.4.5.3 provides an assessment of drip shield failure potential under the static load from rockfall, amplified by the dynamic load during a seismic event. The probability, intensity, and characteristics of the seismic events are addressed in Section 2.3.4.3. Analyses presented in Section 2.3.4.4.3 show that the drifts are expected to be stable with minimal rockfall during the thermal loading phase of the repository. Time-dependent (nonseismic) failure of the rock mass around the emplacement drifts has been excluded from TSPA because it will have a minor impact on drift degradation (excluded FEP 2.1.07.02.0A, Drift collapse, in Section 2.3.4.1). However, seismic events have the potential to result in rockfall from the drift roof and walls, with partial to complete filling of the emplacement drift with rock rubble over longer times. Section 2.3.4.4.8 provides analysis of the rockfall and rubble volume produced as the drift fails for both lithophysal and nonlithophysal rock masses. In the nonlithophysal rock unit, the possibility exists for large rock blocks to dislodge and impact and dent or even collapse the drip shield. However, damage or possible failure of the drip shield framework as a result of this rockfall has been excluded on the basis of low consequence (SNL 2008a, FEP 1.2.03.02.0B, Seismic-induced rockfall damages EBS components). The effects of rockfall on the drip shields have been quantified in terms of damaged areas and the probability of rupture of the drip shield plates (Section 2.3.4.5.2.2). However, damaged area on the drip shields is excluded from the TSPA model because advective flow through stress corrosion cracks in the drip shields is excluded from the TSPA model (see excluded FEP 2.1.03.10.0B, Advection of liquids and solids through cracks in the drip shield, Table 2.2-5), and failure of the drip shield plates is excluded because it has low consequence for the TSPA. Rupture of the axial stiffeners occurs only for an impact by a 28.3 MT rock block impact and is excluded on the basis of low probability. Finally, damage to the waste packages and waste package internals from seismically induced rockfall in jointed rock in nonlithophysal units is excluded from the TSPA model because the drip shields do not separate and because the drip shields remain intact mechanically and can deflect rockfall away from the

waste packages. Based on this analysis, the functionality of EBS features is not compromised, and seismic-induced rockfall is excluded from TSPA.

In the lithophysal units, the static load from accumulated rockfall and the dynamic amplification of this load during a seismic event may result in structural failure of the drip shield. The applied loading mechanisms and the "fragility" of the drip shield plates and framework is reviewed in Section 2.3.4.5.3. The term "fragility" is a standard term denoting the probability of structural failure, which is defined for the drip shield as buckling of its sidewalls or rupture of its plates. This probability is a function of the PGV level of the seismic event, of the static rockfall load on the drip shield, and of the thickness of the drip shield components at the time of the seismic event (SNL 2007c, Section 6.8). These analyses indicate that the drip shield is very robust, and can maintain the static and dynamic loading of the rubble even after substantial thinning has occurred from corrosion.

While the drip shields remain intact, the waste packages and pallets beneath them are free to translate in response to seismic shaking. In this configuration (State 1), the primary mechanism for mechanical damage to the waste package and drip shield is from plastic deformation (and potential stress corrosion cracking) resulting from impacts from seismic shaking (Section 2.3.4.5.1.2.1). Process modeling and abstraction of the damage areas resulting from dynamic interactions of the waste packages, pallets, and drip shields while the drip shields are intact is described in Section 2.3.4.5.2. These analyses indicate that the Alloy 22 outer corrosion barrier of the TAD-bearing waste package with intact internals is undamaged except for ground motions greater than the 2.44 m/s PGV level, so that its internal structural components are expected to remain intact during State 1. The Alloy 22 outer corrosion barrier of the codisposal waste package may be deformed by seismic events with a broad range of PGV levels. The resulting damaged areas on the outer corrosion barrier provide a pathway for water vapor to enter the codisposal waste package via diffusive transport. Once this occurs, the waste package internals are assumed to be degraded by corrosion processes, and provide no structural support to the outer corrosion barrier. The presence of damaged areas on the outer corrosion barrier also initiates double-sided corrosion of the outer corrosion barrier. Details of the corrosion process are discussed in Section 2.3.6.

States 2 and 3—Failure of the Drip Shield—As time evolves in the range of hundreds of thousands of years, general corrosion of the drip shield, coupled with static and dynamically amplified rubble loads from repetitive seismic events, are expected to buckle the drip shield framework and, eventually, lead to the rupture of the drip shield plates (Section 2.3.4.5.3) (SNL 2007c, Section 6.8). The potential for drip shield failure is important for understanding the mechanical damage mechanisms of the waste package. After the drip shield framework has buckled, the motion of the waste package is restricted because the drip shield may be pressing down on the waste package as shown schematically in Figure 2.3.4-51b. Similarly, rupture of the drip shield plates can restrict motion of the waste packages because lithophysal rubble from drift collapse can fall through the drip shield and surround the waste package. The fragility of the drip shield depends on the ultimate plastic load capacities of the drip shield plates or drip shield framework. Failure occurs when the dynamic load from lithophysal rockfall and the peak vertical acceleration of the seismic event exceeds the plastic load capacity, which is a function of the thicknesses of the drip shield components and the drip shield geometry at the time of the event. The analysis for the fragility curves is described in Section 2.3.4.5.3.

Failure of the drip shield leads to two distinct waste package configurations. These configurations are referred to as damage for a waste package beneath (loaded by) a buckled drip shield, and damage for a waste package surrounded by rubble, respectively. In these configurations, the waste packages are loaded by the weight of the lithophysal rubble and any amplification resulting from vibratory ground motion. The differentiation between the configurations is as follows. Fragility analyses of the drip shield presented in Section 2.3.4.5.3 show that the probability of sidewall buckling is always greater than that of plate rupturing, all other factors being equal. Therefore, State 2, shown schematically in Figure 2.3.4-51b, will occur before State 3 (Figure 2.3.4-51c). These analyses also indicate that buckling of the drip shield onto the waste package will not immediately impair its function of shedding seepage water because there is limited displacement between the bottom of the drip shield and the top of the waste package and because the drip shield plates are more robust than its sidewalls, as noted above (Section 2.3.4.5.4.1). With greater time and continued general corrosion thinning, the plates will eventually rupture, allowing seepage waters to directly contact the waste package via advective flow. These processes and the abstractions for fragility of the drip shield plates and drip shield sidewalls are described in Section 2.3.4.5.3.

Approach to Analysis of Mechanical Degradation of EBS Features—Figure 2.3.4-52 illustrates the interaction of the ground motions, fault displacements, and rockfall analyses presented in Sections 2.3.4.3 and 2.3.4.4, with the structural response models and abstractions provided in this section. The ground motion inputs are used to estimate drift vibratory motion and lithophysal rockfall which, in turn, provide the driving forces that generate damaged areas and rupture or puncture of the waste package and produce buckling or rupture of the drip shield. Thinning of EBS components, including the waste package outer corrosion barrier, the drip shield plates, the drip shield framework, and the emplacement pallet, from general corrosion is taken into account. As shown in Figure 2.3.4-52, process models for waste package damage assessment are dependent on the state of the drip shield. If the drip shield is intact, then the waste package and pallet are free to move beneath it. Damage or rupture are dependent on the impacts between components. Drip shield fragility analyses define the probability of failure of the plates or framework as a function of the applied loading and general corrosion thinning (SNL 2007c, Section 6.8). If the drip shield framework buckles (this is the more likely initial drip shield failure mechanism), it will rest on the waste package, and rubble load will be transmitted to the waste package via the interior bulkhead beams that support the crown of the drip shield. Damaged area on the waste package outer corrosion barrier is a result of the rubble load and amplification of this load by vibratory ground motion (Section 2.3.4.5.4). If the drip shield framework buckles, it will still maintain its seepage diversion function, as demonstrated in Section 2.3.4.5.4.1 since the plates do not tear for loads that result in buckling of the drip shield framework. Eventually, the drip shield plates will tear and the seepage diversion function of the drip shield will be lost. The tearing of the plates will allow rock rubble to come into contact with and directly load the waste package. Damaged areas and possible puncture of the waste package outer corrosion barrier is a result of the rubble load and amplification of this load by vibratory ground motion.

The process models and abstractions that describe the structural response and rockfall estimates are provided in the following sections:

- Section 2.3.4.5.1 provides a discussion of the mechanical processes and failure mechanisms utilized in the remaining sections.

- Section 2.3.4.5.2 presents kinematic structural analyses of the EBS components to vibratory ground motion and rockfall, and the abstraction of damaged area and rupture probability to the TAD-bearing and codisposal waste packages for the case of an intact drip shield. Drip shield damage from static and dynamically amplified rubble loads, as well as rock block impacts, is also described. Potential thinning from general corrosion, as well as degradation of the waste package internals, is taken into account in these process models.

- Section 2.3.4.5.3 presents an analysis of the ultimate plastic load capacity and probability of failure of the drip shield resulting from lithophysal rockfall and the dynamic amplification of the rockfall load during a seismic event. The impact of thinning of the drip shield plates and framework from general corrosion is taken into account in developing the fragility curves for the drip shield sidewalls and drip shield plates.

- Section 2.3.4.5.4 provides analyses of the potential for waste package damaged area and puncture probability for the cases where either the drip shield plates have ruptured, or where the framework has collapsed. In these instances the waste package, whose outer corrosion barrier has thinned as a result of general corrosion, is pinned in place by the drip shield and/or rock rubble. The waste package is statically loaded by the weight of the rock rubble as well as inertial loading from possible repetitive seismic events.

- Section 2.3.4.5.5 provides analyses of waste package breach from displacement on faults that cross the repository block.

- Section 2.3.4.5.6 discusses the changes in the emplacement drift environment that occur after seismic events. This includes the impacts of drift degradation on seepage flux into the drift, as well as thermal and humidity impact effects in the environment of a collapsed drift.

Section 2.3.4.6 describes the computational algorithm for seismic scenario class, and discusses how this algorithm is executed within the TSPA model.

2.3.4.5.1 Failure Criteria Used in the Seismic Scenario Class

[NUREG-1804, Section 2.2.1.3.2.3: AC 1(1) to (4), (7), AC 2, AC 3(1) to (3), AC 4, AC 5(2), (3)]

2.3.4.5.1.1 Engineered Barrier System Feature Description

A description of the design details for the EBS components is provided in Sections 1.3.4 and 1.5.2. A summary of the relevant dimensions, masses, and geometric arrangement of components is provided in this section for reference to the structural performance calculations presented in Section 2.3.4.5.

The geometry of the emplacement drift, with the emplaced drip shield, waste package, pallet, and invert showing dimensions and clearances at the time of repository closure, is provided in Figure 2.3.4-53. The emplacement drift has a nominal diameter of 18 ft (5,490 mm). Within the drift, the steel support beams and associated ballast form a level invert whose top surface is 4 ft 4 in.

(1,320 mm) above the lowest part of the drift (BSC 2007c, Figure 1; SNL 2007e, Figure 4-1). The waste package sits on an emplacement pallet that raises the bottom of the waste package above the invert.

The dimensions and number of waste packages in the design basis inventory are given in Table 2.3.4-27. The TAD-bearing waste package includes all TAD waste packages in the design basis inventory. The 5-DHLW/DOE Long waste package includes the 1S/5L and the 1D/4L codisposal waste packages in the design basis inventory.

To simplify the structural analyses presented in Sections 2.3.4.5.2 and 2.3.4.5.4, the inventory of waste packages is split into two representative groups that have similar design features or waste type. The two representative groups are as follows:

- **TAD-Bearing Package**—This includes the TAD canisters, Naval Long, and Naval Short waste packages. It is reasonable to group these waste packages together because each of these package types has a standalone stainless steel canister within the stainless steel inner vessel and Alloy 22 outer corrosion barrier (Figure 1.5.2-1 and Sections 1.5.1.1.1.2.7 and 1.5.1.4.1.2.1). Based on the information in Table 2.3.4-27, the TAD-bearing waste package constitutes 95% of the number of TAD and naval waste packages and 67% of the total number of waste packages for the license application.

- **Codisposal Waste Package**—This includes the 5-DHLW/DOE Short, the 5-DHLW/DOE Long, and the 2-MCO/2-DHLW waste packages. It is reasonable to group these waste packages together because each of these package types has HLW and/or DOE SNF inside a stainless steel inner vessel and Alloy 22 outer corrosion barrier. Based on the information in Table 2.3.4-27, the 5-DHLW/DOE Long waste package constitutes 57% of the number of codisposal waste packages and 17% of the total number of waste packages for the license application.

The detailed models for the representative waste packages are described in *Mechanical Assessment of Degraded Waste Packages and Drip Shields Subject to Vibratory Ground Motion* (SNL 2007b, Section 6.3.2.2.1). The model of the TAD-bearing waste package with intact internals is an approximate representation based on: (a) the Naval Long waste package outer corrosion barrier and inner vessel; and (b) an approximate representation of a TAD canister and fuel basket (Figure 2.3.4-54; SNL 2007b, Section 6.3.2.2.1). The model of the codisposal waste package with intact internals is an approximate representation based on the 5-DHLW/DOE SNF-Long codisposal waste package outer corrosion barrier, inner vessel, and fuel basket (Figure 2.3.4-55).

The loaded weight of the nominal TAD-bearing waste package and the representative codisposal waste package for the simulations is 73.9 and 53.1 MT, respectively (SNL 2007b, Table 4-6 and Assumption 5.23 in Section 5). The TAD-bearing waste package consists of a 1 in. (25.4 mm) thick, cylindrical Alloy 22 outer corrosion barrier, a 2 in. (50.8 mm) thick inner stainless steel vessel encasing the internals, and a TAD-canister that is loaded with racks, fuel cladding, and fuel rods. The ends of the TAD-bearing waste package consist of a series of welded end lids, including a TAD shield plug, a 316 stainless steel inner vessel lid, and two outer corrosion barrier lids. The codisposal canister consists of a 1 in. (25.4 mm) thick Alloy 22 outer corrosion barrier, and a 2 in. (50.8 mm) thick 316 stainless steel inner vessel, and the internal fuel. The ends of the codisposal waste package

consist of welded end lids, including a 316 stainless steel inner vessel lid, and an Alloy 22 outer corrosion barrier lid.

The waste package pallet consists of two end-piers constructed of Alloy 22, which are interconnected into a free-standing structure by 316 stainless steel connection tubes (Section 1.3.4.6.1; Figure 1.3.4-11). The standard pallet is 163.3 in. (4147.9 mm) in length, and 84.65 in. (2150 mm) in width.

The drip shield is a free standing structure that surrounds the waste package and rests on the invert. The components of the drip shield structure are shown in Figure 2.3.4-56 (Figure 1.3.4-15 for design details). The main structural (load bearing) elements of the drip shield are the bulkheads and the support beams which will be manufactured of Titanium Grade 29 (UNS R56404). They form four central frames that are spaced every 41 in. (1,047 mm) along the length of the drip shield. Two peripheral frames, at the ends of the drip shield, have a different geometry than the bulkhead and support beams in order to allow interlocking. The drip shield plates 1 (on the top) and 2 (on the sides), which are placed continuously over the bulkheads and the support beams, as well as the external and internal support plates that strengthen the drip shield plates 1 and 2 in the region of their junction, are manufactured of Titanium Grade 7. The plates provide the ultimate functionality of the structure to prevent (1) dripping of water from the drift roof and walls onto the waste packages; and (2) impacts of loose blocks from the drift roof and the walls directly onto the waste packages. Each drip shield is 228.5 in. (5,804 mm) in length, and 113.6 in. (2,885 mm) in height at the maximum height of the drip shield connector plate, and its total mass is 11,600 lb (5,270 kg) (BSC 2007b). The initial thickness of the drip shield plates, which are fabricated from Titanium Grade 7, is 15 mm (Table 1.3.4-3 for design details). The drip shields will be installed, prior to closure of the repository, over the waste packages and pallets. Adjacent drip shields partially overlap one another by 12.6 in. (approximately 320 mm), which is the width of the drip shield connector plate, as shown in Figure 1.3.4-15. In particular, the drip shield connector assembly on one drip shield is placed over and interlocks with the connector guide of the next drip shield to provide continuous shielding of the waste packages. In order to separate (unlock) two drip shields (or to lock them together) without significantly deforming the support beams, bulkheads, or plates or shearing off the welds, it is necessary to lift one drip shield relative to another by approximately 40 in. (approximately 1 m) (BSC 2007d, Section 6.1.1.2).

2.3.4.5.1.2 Conceptual Description of Failure Mechanisms and Failure Criteria for EBS Components

Mechanical processes resulting from seismic events that may compromise the capability of the waste packages and drip shields to prevent radionuclide release have been examined over the entire regulatory probability range. These mechanical processes include (1) impacts caused directly by vibratory ground motion during an earthquake (Section 2.3.4.5.2) and (2) impacts caused by rockfall induced by vibratory ground motions (Section 2.3.4.5.3).

Under vibratory ground motions, impacts can occur between adjacent waste packages and between the waste package and its emplacement pallet, the surrounding drip shield, and the invert. The damaged areas produced by impacts between adjacent waste packages and between the waste package and its emplacement pallet are included in the seismic damage abstractions (Section 2.3.4.5.2). The damaged areas produced by impacts between the waste package and drip

shield are not represented in damage abstractions because the damaged areas from these processes are expected to be minor in comparison to the other impact processes (SNL 2007c, Section 6.5.6). A similar reasoning for side-on impacts of the waste package on a flat surface (SNL 2007c, Section 6.5.6) also indicates that impacts between the waste package and invert will be a minor contributor to damaged area, and are not represented in the damage abstractions (Section 2.3.4.5.2).

Rockfall induced by vibratory ground motion can result in impacts on the drip shield, and may partially or fully collapse the drifts, resulting in static loads applied to the drip shield from the mass of rubblized rock surrounding it. Abstractions have been developed for damaged areas and drip shield fragility caused by the accumulated rockfall in the lithophysal units. Models have also been developed for failure of the drip shield plates and axial stiffeners due to impact from large rock blocks (Section 2.3.4.5.2), although this damage mechanism has been excluded from TSPA because of low consequence (excluded FEP 1.2.03.02.0B, Seismic-induced rockfall damages EBS components). Seismic shaking after collapse of the drifts can result in dynamic amplification of the static rubble loads (Section 2.3.4.5.3). If the dynamic loads result in failure of the drip shield framework or plates, it is possible for the weight of the rock rubble to directly load the waste package (Section 2.3.4.5.4.3.1).

The following are potential mechanical failure mechanisms of the EBS components (SNL 2007c, Section 6.1.4):

- **Mechanism 1**—Impact-related dynamic loads may dent an EBS component, resulting in permanent structural deformation with associated residual tensile stress. High levels of residual tensile stress may lead to local degradation from potential corrosion processes, primarily stress corrosion cracking. Areas that are breached from corrosion processes provide a potential pathway for diffusive transport of radionuclides out of the waste package.

- **Mechanism 2**—Dynamic loads have the potential to result in rupture (tearing) or puncture of a waste package if the local strain exceeds the ultimate tensile strain of Alloy 22. A waste package that has been ruptured or punctured provides a potential pathway for seepage to flow into and for advective transport of radionuclides out of the waste package.

- **Mechanism 3**—Static and dynamically amplified loads from rockfall rubble in the lithophysal zones may buckle the drip shield sidewalls or tear/rupture the drip shield plates. Rupture of the drip shield plates compromises the capacity of the drip shield to deflect seepage and rockfall away from the waste package.

- **Mechanism 4**—Impacts by large rock blocks in unfilled or partly filled drifts in nonlithophysal units may deform the drip shield and/or fail the plates and axial stiffeners on the crown of the drip shield. Failed plates provide a potential pathway for seepage through the drip shield. If the drip shield collapses from a rock block impact, the waste package may also be damaged or ruptured from the impact. Mechanism 4 has been examined and excluded as a result of low consequence (Excluded FEP 1.2.03.02.0B, Seismic-induced rockfall damages EBS components, Table 2.2-5 and SNL 2008a, FEP 1.2.03.02.0B). Structural analysis of rock block impacts that provides part of the

basis for excluding FEP 1.2.03.02.0B, Seismic-induced rockfall damages EBS components, is summarized in Section 2.3.4.5.2.2.3.3 and in *Features, Events, and Processes for the Total System Performance Assessment: Analyses* (SNL 2008a, FEP 2.1.03.07.0B).

- **Mechanism 5**—The static load from lithophysal rockfall combined with the dynamic load during a seismic event may deform the waste package outer corrosion barrier when lithophysal rubble comes into direct contact with the waste package after rupture of the drip shield plates. High levels of residual tensile stress on the waste package outer corrosion barrier may become sites for enhanced stress corrosion cracking that could breach the outer corrosion barrier. Areas that are breached from corrosion processes provide a potential diffusive pathway for seepage through the waste package and transport of radionuclides.

- **Mechanism 6**—Vibratory ground motion may cause adjacent drip shields to separate if there is large vertical displacement between adjacent drip shields or if the welds holding the drip shield connector guides tear loose from the drip shield plates during the dynamic response. Separation compromises the capacity of the drip shield to deflect seepage and rockfall away from the waste package. Drip shield separation has been analyzed and excluded from TSPA, as discussed in the screening justification for excluded FEP 1.2.03.02.0B, Seismic-induced rockfall damages EBS components (SNL 2008a, FEP 1.2.03.02.0B).

- **Mechanism 7**—Vibratory ground motion may cause waste package-to-drip shield impacts that could compromise the structural stability of the drip shield or tear the interior support bulkhead beneath the crown of the drip shield. A failed drip shield could provide a potential pathway for seepage through the drip shield. The potential for drip shield failures from waste package impacts has been analyzed and excluded from TSPA, as discussed in *Seismic Consequence Abstraction* (SNL 2007c, Section 6.8.5).

- **Mechanism 8**—Large displacements on known faults in the repository block may shear waste packages and drip shields if the EBS features become pinned by the fault response. Sheared components provide potential pathways for flow into and radionuclide transport out of the damaged components.

These failure mechanisms for the EBS components share the following processes that require definition as failure criteria: (1) potential stress corrosion cracking of the waste package Alloy 22 outer corrosion barrier and drip shield Titanium Grade 7 plates; (2) tensile rupture (also termed tearing or puncture) of the waste package Alloy 22 outer corrosion barrier and drip shield Titanium Grade 7 plates; and (3) buckling of the drip shield Titanium Grade 29 framework. The following section describes the basic mechanical data used to define these failure criteria, as well as the models used to describe the failure processes that are eventually abstracted to the TSPA.

There are several potential failure mechanisms that have been examined and excluded from consideration in damage abstractions for the TSPA. These mechanisms include the following:

- Time-dependent creep of the waste package Alloy 22 outer corrosion barrier or the drip shield Titanium Grade 7 plates and Grade 29 framework under the action of long-term rubble loading (excluded FEPs 2.1.07.05.0A, Creep of metallic materials in the waste package, and 2.1.07.05.0B, Creep of metallic materials in the drip shield (SNL 2008a)).

- Nonuniform settlement of the drip shield into the invert, which could result in overturning or reduction in load-bearing capacity of the drip shield under eccentric loading (SNL 2007b, Section 6.4.6; SNL 2008a, excluded FEP 2.1.06.05.0B, Mechanical degradation of the invert).

- Deformation of fuel rods and perforation of cladding resulting from dynamic loads imposed on waste package internals (excluded FEP 2.1.02.24.0A, Mechanical impact on cladding, Table 2.2-5). The seismic damage abstractions do not include a damage abstraction for the cladding because the compliance case for the license application is not taking credit for the potentially beneficial effects of commercial SNF cladding as a contributor to the ability of the EBS to act as a barrier to the release of radionuclides from the fuel rods (SNL 2008b, Section 6.6.1.1.3).

2.3.4.5.1.2.1 Conceptual Description of Failure Through Formation of Stress Corrosion Cracks

The high residual tensile stress resulting from impact and denting during vibratory motion may cause stress corrosion cracking. This is a combined mechanical-corrosion failure mechanism, and it is expected to be the most likely cause of failure for the waste package from impact processes caused by vibratory ground motions. The surface areas that exceed the residual tensile stress threshold for the particular EBS component are referred to throughout this document as the "damaged area." The effective area for transport through a damaged area will be substantially less than the actual damaged area because the cross sectional area of the stress corrosion cracks is much less than the total surface area that exceeds the RST (SNL 2007c, Section 6.1.5). The RST is often referred to as the stress threshold, with the understanding that the principal residual stress must always be tensile to initiate an accelerated corrosion process (SNL 2007c, Section 6.1.4).

Application of a residual tensile stress threshold for the seismic analysis is nonmechanistic, in the sense that detailed analyses with accelerated corrosion rates or crack propagation through the outer corrosion barrier of the waste package are not used to determine the actual failure time after a seismic event. The stress corrosion cracks are assumed to form immediately upon overcoming the RST, thereby providing potential pathways for diffusive transport through the areas exceeding the RST (SNL 2007c, Section 6.1.4]).

Figure 2.3.4-57 provides a simplified illustration of how residual stress is generated in a material by permanent (plastic) deformation when loaded in uniaxial tension. The loading path in Figure 2.3.4-57 has three phases: (1) elastic loading until reaching the elastic yield limit; (2) plastic loading above the elastic yield limit; and (3) elastic unloading when the external load reduces the local stress. Figure 2.3.4-57 also shows that plastic deformation does not always generate a

damaged area because the final residual stress state may be compressive or, if tensile, it may be below the threshold to initiate stress corrosion cracking.

The RSTs for seismic response are similar to the criteria for initiation of stress corrosion cracking on smooth surfaces of Alloy 22 (SNL 2007c, Section 6.1.4). The use of a stress corrosion cracking initiation criterion is appropriate for seismic analysis because regions where the residual stress from mechanical damage exceeds the tensile failure criterion are expected to be severely cold worked and, hence, potentially subject to enhanced stress corrosion cracking (SNL 2007c, Section 6.1.4]). Cold working is a process by which plastic deformation of a metal, in this case through impact and denting, can result in defects or dislocations in the metal. These defects can become sites for initiation and propagation of stress corrosion cracks.

The use of a nonmechanistic approach is a conservative failure criterion because detailed corrosion models will have a delay time until failure. Additionally, the assumption of stress corrosion cracks passing completely through the thickness of the outer corrosion barrier assumes that tensile stress conditions exist throughout the thickness, which may not be the case (SNL 2007c, Section 6.1.4]). This approach is appropriate because (1) it is consistent with the tensile failure criterion for the waste package closure weld (SNL 2007a, Section 6.2.2), and (2) the residual stress failure criterion is simple to apply to the complex, three-dimensional stress fields generated by the kinematic impact process.

2.3.4.5.1.2.2 Conceptual Description of Failure Through Tensile Rupture

Ultimate tensile failure (rupture) of the waste package Alloy 22 outer corrosion barrier or Titanium Grade 7 drip shield plates occurs when the "effective strain" resulting from impact, tensile stretching, or bending exceeds a threshold value that is dependent on the state of stress at the location of interest. When the surface of the waste package or drip shield is loaded, the waste package outer corrosion barrier or drip shield plates are subjected to a complex multiaxial stress state that may include both tensile and compressive components. The tensile strain limit of Alloy 22 or Titanium Grade 7 is typically measured from laboratory tensile tests in which the stress state is uniaxial tension. Therefore, the normally reported tensile elongation (strain) of a uniaxial laboratory test sample of Alloy 22 or Titanium Grade 7 at rupture (the "ultimate true elongation" in Table 2.3.4-28) needs to be adjusted to account for the effect of multiaxial (rather than uniaxial) stress states. The methodology employed for accounting for multiaxial stress states is provided below in the section on Model and Model Uncertainty.

2.3.4.5.1.2.3 Conceptual Description of Failure Through Buckling or Excessive Deformation of the Drip Shield Framework

As described in the introduction to Section 2.3.4.5, the emplacement drifts will fail over time when subjected to multiple, low probability seismic events. One result of these events is that the drifts will fill with accumulating rock rubble. The weight of this rubble will rest on the drip shield. After the drip shield is covered with rubble, ground motions will induce an additional, transient inertial loading on the drip shield that is proportional to the product of the mass of the rubble resting on the drip shield and the peak vertical ground acceleration. Over time, general corrosion processes will also thin the Titanium Grade 29 framework of the drip shield, thereby reducing its load bearing capacity. Eventually, the drip shield framework will fail under these loads, possibly by buckling of

the drip shield legs. Once the legs buckle, the drip shield bulkheads (which support the drip shield crown plates) are expected to come to rest on the top of the waste package. In this way, the rubble load will be transferred directly to the waste package structure. This buckling failure mechanism is based on loads from the lithophysal rubble because the lithophysal units encompass 80% to 85% of the emplacement drifts and because the rockfall volume in the lithophysal units is significantly greater than in the nonlithophysal units. The fragility analyses for the drip shield framework are presented in Section 2.3.4.5.3.

2.3.4.5.1.3 Data and Data Uncertainty for Failure Criteria of the EBS Components

The primary sources of data used for determination of failure criteria of the EBS components include the following:

- General mechanical material properties of the EBS components
- Corrosion thinning rates of EBS components
- RST for initiation of stress corrosion cracking of the Alloy 22 waste package outer corrosion barrier
- RST for initiation of stress corrosion cracking of the Titanium Grade 7 drip shield plates
- Tensile rupture strain for Alloy 22 waste package outer corrosion barrier
- Tensile rupture strain for the Titanium Grade 7 drip shield plates
- Fault displacement for rupture of the waste package outer corrosion barrier.

Each of these sources of data is described below.

2.3.4.5.1.3.1 Mechanical Properties of Waste Package and Drip Shield Materials

Calculation of the mechanical response of EBS components to vibratory ground motion and rock rubble loading requires basic material properties for Titanium Grade 7 (drip shield plates) and Grade 29 (drip shield framework which is assumed to have equivalent mechanical properties to Grade 24 based on ASTM B 265-02, Tables 1 and 2), Alloy 22 (waste package outer corrosion barrier, pallet end piers), Stainless Steel Type 316 (pallet connecting rods, waste package inner vessel, and internals), and the crushed tuff invert. Table 2.3.4-28 presents a summary of the specific material properties used in the structural calculations described in Section 2.3.4.5. The effects of temperature, radiation, and other processes on these material properties is provided below.

Temperature Sensitivity—The properties for the EBS structural components given in Table 2.3.4-28 are derived from standard handbook or manufacturer's catalogs (SNL 2007b, Section 4.1). The mechanical properties are somewhat temperature-dependent, with decreased yield strength and elastic modulus with increasing temperature (SNL 2007b, Section 6.3.2.2.2 and Table 6-7). An in-drift environmental temperature of 60°C was assumed as a basis for the properties specification for the EBS components, with properties interpolated from handbook

values at other temperature levels (SNL 2007b, Assumption 5.7, Section 5.7 and Appendix A). The ambient temperature of 60°C was chosen as a reasonable environmental value because the resulting material properties maximize strain and deformation for 99% of the first 1,000,000 years after repository closure (SNL 2007c, Section 8.2).

High temperatures, on the order of 300°C, can exist for relatively brief periods of time during the thermal loading phase of repository response, on the order of 100 to 200 years after repository closure (SNL 2008d, Figures 6.3-55(a), 6.3-56(a), and 6.3-57(a)). A sensitivity study of the impact of temperature-dependency of material properties on the damaged area resulting from waste package end-to-end and waste package-pallet impacts was performed for corrosion-thinned Alloy 22 outer corrosion barrier of 23 mm thickness with intact and degraded internals (SNL 2007b, Section 6.3.2.2.2). Structural calculations using finite element models were performed for impacts at various angles and velocities, and for the full range of assumed RST criteria for ambient temperatures of 60°C, 90°C, and 150°C. The effect of material properties temperature-dependence proved to be minor (SNL 2007b, Tables 6-8 and 6-9); therefore, only the 60°C temperature, representative of long time period emplacement drift conditions, was used.

Welding, Cold Work and Residual Stress Effects on Material Properties of Alloy 22—Solution heat treatment of the Alloy 22 outer corrosion barrier will eliminate precipitates formed during welding and will stress-relieve the shell. It is expected that the finished shell will have uniform material properties, and that residual stresses will not significantly affect the material properties. The resulting material properties for the structural response calculations are documented in *Mechanical Assessment of Degraded Waste Packages and Drip Shields Subject to Vibratory Ground Motion* (SNL 2007b, Appendix A). Low-plasticity burnishing of the waste package lid closure welds will induce cold-working of the surface; however, as described in Section 2.3.6.7.4, the increase in kinetics due to cold-working is insufficient to affect thermal aging and phase stability of Alloy 22 (Section 2.3.6.7.4).

Radiation Effects on Material Properties—The impact of radiation damage on the mechanical properties of the Alloy 22 outer corrosion barrier was discussed by the Waste Package Materials Performance Review Panel (Beavers et al. 2002). This panel found that there is no evidence to suggest that radiation damage to the waste package canister will alter its mechanical properties. Therefore, radiation effects on the mechanical response of the waste package is not included in calculations presented in this section.

Strain Rate Effects on Material Properties—Potential strain rate effects on Alloy 22 effective tensile strain at rupture have been incorporated into the rupture strain criteria, using the work of Zabotkin et al. (2003), as described in Section 2.3.4.5.1.4.2.

2.3.4.5.1.3.2 Residual Stress Threshold Criteria

Residual Stress Threshold for the Waste Package—The RST for initiation of potential stress corrosion cracking of the waste package outer corrosion barrier is represented by a uniform distribution with a lower bound of 90% and an upper bound of 105% of the yield strength of Alloy 22. A discussion of the basis for this RST distribution and the uncertainty in these criteria can be found in Section 2.3.6.5.3.

Residual Stress Threshold for the Drip Shield—Calculations of damaged area and the associated stress corrosion cracks on the drip shield are summarized in Section 2.3.4.5.2.2. However, advective flux of liquids through the drip shield is excluded from the TSPA, as discussed in excluded FEP 2.1.03.10.0B, Advection of liquids and solids through cracks in the drip shield, in *Features, Events, and Processes for the Total System Performance Assessment: Analyses* (SNL 2008a). Even though advective flux of liquids through stress corrosion cracks in the drip shield has been excluded, the mechanical analyses that support the exclusion basis are provided in Section 2.3.4.5.2.2. Therefore, a discussion of the RST criteria for the Titanium Grade 7 drip shield plates is provided below.

For the drip shield, the RST for initiation of potential stress corrosion cracking is represented by a fixed lower bound of 80% of the yield strength of the drip shield plate material (Titanium Grade 7) and 50% for the drip shield framework material (Titanium Grade 29). A discussion of the basis for the RST for Titanium Grades 7 and 29 and the uncertainty in these criteria are given in Section 2.3.6.8.3.

2.3.4.5.1.3.3 Tensile Rupture Criteria

The primary input data for determination of tensile rupture potential are the tensile strain limits of the Alloy 22 outer corrosion barrier or Titanium Grade 7 drip shield plates. The tensile strain limit of Alloy 22 or Titanium Grade 7 is derived from laboratory tensile tests in which the stress state is uniaxial tension. Table 2.3.4-28 provides the tensile strain limits (the ultimate engineering elongation) for these materials based on handbook and manufacturer's data. The complex stress states induced in the waste package outer corrosion barrier and drip shield plates by impact or applied pressures are typically multiaxial, rather than uniaxial in nature. In these cases, the tensile strain criteria derived from uniaxial testing results need to be adjusted. The methodology used to adjust the strain criteria based on the local stress state is described in Section 2.3.4.5.1.4.2, Tensile Rupture.

2.3.4.5.1.3.4 Buckling and Large Plastic Deformations of the Drip Shield Framework

Finite difference and distinct element structural analysis software is used to model the geometry and structural response of the drip shield to impact loading from (1) falling rock blocks prior to filling of the drift with rockfall in the nonlithophysal units (SNL 2007b, Section 6.4.7); (2) static rubble load from partially and completely filled drifts in lithophysal units; and (3) the dynamic amplification of this static load from lithophysal rubble during subsequent seismic events (Section 2.3.4.5.2.2) (SNL 2007b, Section 6.4.3). For these analyses, the Titanium Grade 29 framework is represented using a strain-hardening Tresca yield surface. Bilinear idealization of the uniaxial stress-strain relations (Figure 2.3.4-57) was used, and characterized by the initial and postyield Young's moduli and yield strength estimated at 60°C (Table 2.3.4-28). The finite difference and distinct element formulations incorporate finite strain logic that allows for determination of large distortions in the geometry of the drip shield without numerical instability. Simulations are performed with a given applied loading state. The structure modeled was allowed to either equilibrate in a stable fashion for the given loading conditions, or form a plastic hinge and undergo large deformation. Thus, the model results are used to judge the structural stability of the drip shield through recording and observation of deformations.

2.3.4.5.1.3.5 Breach Due to Fault Displacement

Given that the dose related to fault displacement is expected to be a small fraction of total dose (Section 2.3.4.5.5), detailed calculations of the structural response of EBS components to fault displacement are not warranted. Instead, the focus is on the potential for the waste package to be damaged when fault displacement exceeds the available clearance around the waste package. A fault displacement that occurs in an emplacement drift may cause a sudden discontinuity in the profile of the drift. This could result in one portion of the drift being displaced vertically or horizontally relative to the adjacent section. Such a discontinuity in the drift could cause shearing of the waste package, drip shield, and cladding located over the fault if the fault displacement exceeds the available clearances in the EBS. The comparison of fault displacements with available clearances provides a simple analysis that maximizes the potential for damage to EBS components from fault displacement.

Two distinct cases are considered in analyzing the clearances between EBS components: (1) an intact drip shield; and (2) a drip shield that has failed. The first case represents the as-emplaced configuration of the EBS, shortly after repository closure, and is expected to be applicable for several hundred thousand years after repository closure. The second case represents the late time response of the EBS after the drip shield framework and drip shield plates have failed and rockfall has partly or completely filled the emplacement drifts and surrounded the waste packages with rubble. The clearance criteria (i.e., the fault displacement criteria) for waste package and drip shield rupture are described in detail in Section 2.3.4.5.5.2.1.

2.3.4.5.1.3.6 Thinning of the EBS Components Due to General Corrosion

The uncertainty in the mechanical state of EBS components resulting from time-evolving corrosion-thinning of the waste package outer corrosion barrier and the drip shield plates and framework has been accounted for in the structural calculations described in Section 2.3.4.5. For waste package damage and rupture potential assessment, the structural analyses presented in Section 2.3.4.5.2 assume a 23 mm and 17 mm thick Alloy 22 outer corrosion barrier for TAD-bearing and codisposal waste packages. The 23 mm thick and 17 mm thick outer corrosion barrier correspond to 2.4 mm and 8.4 mm of corrosion thinning from the initial 25.4 mm thickness of the outer corrosion barrier. As seen in Figure 2.3.6-9, the median (50th percentile) general corrosion rate for Alloy 22 at 60°C for the medium uncertainty level is approximately 7 nm/year. At this rate of general corrosion, 2.4 and 8.4 mm of thinning correspond to approximately 340,000 (SNL 2007c, Section 6.5.1.2) and 1,200,000 years after emplacement. Therefore, these levels of thinning reasonably represent the ranges of thickness of the outer corrosion barrier within the period of geologic stability (SNL 2007c Section 6.1.3.3).

Drip shield structural analyses were performed for 0 (as-installed state), 5 and 10 mm of corrosion-thinning of the Titanium Grade 7 plates and Grade 29 framework (Section 2.3.4.5.3.3.1). These thickness reductions span a wide range of drip shield response, from an intact state with no corrosion thinning to a highly degraded state with 10 mm corrosion thinning. The mean corrosion rates for Titanium Grade 7 under aggressive and benign conditions are 46.1 nm/year and 5.15 nm/year, respectively (SNL 2007f, Table 8-1[a]). Assuming aggressive conditions on the top side of the drip shield and benign conditions on the underside of the drip shield, the mean double-sided corrosion rate for Titanium Grade 7 is 51.3 nm/year. The expected time for 10 mm of

thinning corresponds to roughly 200,000 years at this mean corrosion rate (SNL 2007c, Section 6.10.2.11).

These results indicate that the mean corrosion rate for the Titanium Grade 7 plates is significantly greater than for the Alloy 22 outer corrosion barrier (SNL 2007c, Section 6.1.2). Stated differently, the lifetime of the Alloy 22 outer corrosion barrier, estimated in a preceding paragraph as approximately 1,200,000 years for an 8.4 mm thickness reduction, is significantly greater than the lifetime of the Titanium Grade 7 plates, estimated as about 200,000 years for a 10 mm thickness reduction. The temperature dependence of the Alloy 22 corrosion rate can further increase the difference in lifetimes. The temperature of the EBS components will drop to ambient conditions, approximately 25°C, by 100,000 years after repository closure (SNL 2008, Figure 6.3-76[a]). The median corrosion rate for Alloy 22 at 25°C is approximately 1 nm/year (Figure 2.3.6-11), or about a factor of 50 less than the mean double-sided corrosion rate for Titanium Grade 7, 51.3 nm/yr as discussed above. The temperature dependence of the Alloy 22 corrosion rate will therefore increase the difference in lifetimes of the outer corrosion barrier versus the drip shield plates beyond 100,000 years.

2.3.4.5.1.4 Model and Model Uncertainty

2.3.4.5.1.4.1 Stress Corrosion Crack Networks

Mechanical calculations that are summarized in Sections 2.3.4.5.2 and 2.3.4.5.4 estimate damage areas on the waste package outer corrosion barrier and the drip shield plates resulting from loading from waste package-to-waste package or waste package-to-pallet impacts, rock block impacts, or from the pressure of accumulating rock rubble. The damaged areas are determined based on an RST (Section 2.3.4.5.1.3.2) for which stress corrosion cracking may occur. A conceptual model and methodology for dealing with model uncertainty for the morphology of the stress corrosion cracks and the crack area available for diffusive transport within these damaged areas are summarized in this section, based on transgranular stress corrosion cracking through the outer corrosion barrier of the waste package (SNL 2007a, Section 6.7.1).

Morphology of Damage on the Waste Package and Drip Shield—Seismically induced deformation and loading from rockfall rubble can lead to crack initiation and crack propagation on the waste package outer corrosion barrier or drip shield plates. A range of aqueous brine-type environments may form on the waste package outer corrosion barrier, or on the drip shield plates near the crown of the drip shield, producing the requisite concurrent conditions for potential stress corrosion cracking. The conditions include high residual tensile stress, an environment that supports corrosion, and a material that has been cold-worked during the seismic event. For modeling purposes, the seismic scenario conservatively assumes that stress corrosion cracking will occur if the RST is exceeded, regardless of the in-drift chemical environment. Once initiated, the strain fields produced by the seismically induced impacts can generate residual stresses that drive crack growth. The stress corrosion cracking mode (morphology) is expected to be transgranular stress corrosion cracking rather than the intergranular stress corrosion cracking (SNL 2007a, Section 6.7.1.1). Depending on the stress distribution, cracks may propagate through-wall if the stress intensity factor remains positive. If multiple cracks are initiated in the same general area, multiple cracks may intersect or coalesce, creating a continuous crack around the deformed region (SNL

2007a, Section 6.7.1). However, the occurrence of all these events in connection is improbable, as explained next.

An initiated stress corrosion crack is not expected to propagate both through-wall and to circumscribe a dent or deformed area. Any through-wall residual stress fields resulting from seismic impact loads would be a secondary type stress (displacement controlled). There is no significant stress from other sources, such as stress induced by internal pressure (volume increase from waste package internal corrosion products is not expected to affect the mechanical state of the waste package outer corrosion barrier (excluded FEP 2.1.09.03.0B, Volume increase of corrosion products impacts waste package, Table 2.2-5)). In addition, stresses and strains are generally of a higher magnitude at the outer surface, and tend to decrease through the thickness for the deformation-induced denting from a seismic event. In this situation, any crack that initiates and propagates is expected to arrest before penetrating the full thickness of the outer barrier, and is not expected to have a sufficiently positive stress intensity factor to result in both through-wall and 360° cracking around the entire dent (SNL 2007a, Section 6.7.1). However, the analyses of stress corrosion crack damage provided in Section 2.3.4.5.1.2.1 assume that stress corrosion cracks will always propagate through-wall once initiated.

Even postulating that a through-wall crack occurs and circumscribes the dented area, the nature of stress corrosion cracking will preclude the dented area from falling out. Cracks in Alloy 22 are transgranular, but the crack path, whether transgranular or intergranular, has complex local branches with a roughness and tortuosity, as illustrated for stainless steel in Figure 2.3.4-58 (SNL 2007a, Figure 6-61), that make it essentially impossible for an inner plug to disengage from the vessel in the absence of a superimposed primary load (i.e., significant internal pressure). Any internal pressure that develops from heating up of the waste package, or from corrosion-generated gas with the small amount of internal water vapor that is available, would not be sufficient to force the dented area to separate from the wall (SNL 2007a, Section 6.7.1.3).

This analysis is consistent with stress corrosion cracks in light water reactor components and other internally pressurized systems. A number of incidents of stress corrosion cracking have been observed in light water reactors involving both austenitic stainless steels and nickel based alloys. The observed stress corrosion cracking has been extensive in many of these incidents, sometimes becoming fully circumferential in response to weld-induced residual tensile stress and pressure-induced primary stresses. Even under these conditions, which are more severe than those in the postseismic environment, there is no documented case in which any section of material dropped out as a result of the observed cracking (SNL 2007a, Section 6.7.1).

Effective Area for Transport to and from the Waste Package and Through the Drip Shield— Because an expected failure mechanism from a low-probability seismic event is potential stress corrosion cracking, and because the damaged areas that exceed the residual stress failure for Alloy 22 or Titanium Grade 7 are expected to remain physically intact, it is reasonable to represent these areas as a dense network of stress corrosion cracks rather than as a plug of material that separates from the outer barrier. The effective area for transport through the crack network has been estimated from the crack density (number of cracks per unit damaged area) and from the shape and size of an individual crack opening.

The range of crack densities and crack widths has been estimated for two networks of closely spaced cracks (SNL 2007a, Section 6.7.2). The two networks are based on a densely packed hexagonal array of cracks with random orientation or parallel orientation. Figure 2.3.4-59 presents a schematic diagram of the first model for randomly oriented cracks. The wall thickness, *t*, is anticipated to be the minimum possible separation between adjacent cracks, because stress relief from propagation of adjacent cracks relieves the local stress intensity factor, thereby preventing tighter spacing between through-wall cracks.

The first model (Figure 2.3.4-59) (SNL 2007a, Sections 6.7.3 and 6.8.5) assumes the spacing between crack rows is given by *t* and the crack length is *t*, where *t* is the wall thickness. This crack network does not overlap, although the tips of adjacent cracks can abut one another on the outer surface. The second model assumes that the spacing between crack centers is given by *t*, and the length of the cracks is 2*t*. This crack network can overlap substantially, with the maximum overlap occurring for cracks in a parallel orientation. The width of each crack is estimated by assuming an elliptical opening with constant through-wall stress given by the yield strength. This approach overestimates the effective area for transport because the crack tips tend to narrow at the inner surface (as illustrated for stainless steel in Figure 2.3.4-58) and because stress relief from adjacent cracks will tend to reduce the local stress levels at the crack opening.

An analysis for a network of circumferential cracks indicates that the effective area of a typical circumferential crack network is within the range of uncertainty from the densely packed hexagonal array model (SNL 2007a, Section 6.7.2). The mechanical calculations described in Sections 2.3.4.5.2.1, 2.3.4.5.2.2, and 2.3.4.5.4 provide values of the damaged area on the waste package and drip shield. The seismic scenario class of the TSPA converts the damaged area to an effective area for diffusive transport out of the waste package.

Two numerical factors—the crack density (the number of cracks per unit area in the damaged region), and the crack opening area of an individual crack (mm^2)—determine the effective transport area through the crack network. The product of these two factors, the crack area density, is essentially a scaling factor relating the total damaged area to the area available for transport through cracks. A range of numerical values of these factors have been estimated for Alloy 22 at room temperature and at 150°C (SNL 2007a, Tables 8-13 and 8-14) for the two networks of closely spaced cracks. (SNL 2007a, Section 6.7.3). These two cases represent a range of crack area density whose epistemic uncertainty is described by a uniform distribution whose minimum and maximum values vary by four times (SNL 2007a, Section 6.7.3.3). These minimum and maximum values of the crack area density for Alloy 22 range from 0.00328 to 0.0131 and 0.00282 to 0.0119 of the total damaged area at room temperature and at 150°C, respectively.

2.3.4.5.1.4.2 Tensile Rupture

As described in Section 2.3.4.5.1.3.3, laboratory data on the tensile strain limits of Alloy 22 and Titanium Grade 7 are typically derived from laboratory uniaxial testing. The loading conditions from impact and rock loading potentially result in complex, transient, multiaxial stress states in these EBS features. The following section describes the model used to adjust the laboratory uniaxial test results to develop tensile strain criteria that can be used for more complex stress states that are determined from finite element and finite difference modeling of the mechanical response of the EBS features.

Adjustment of the Tensile Strain Limits for Multiaxial Stress States—The method of Manjoine (1983) was used to adjust the tensile elongation measured in a tensile test to the effective strains at tensile rupture for multiaxial stress states. These rupture strain limits are subsequently used as criteria for comparison to numerical strain predictions for the waste package and drip shield subjected to dynamic and static loading. This methodology (SNL 2007b, Appendix A) is used to determine an adjustment factor applied to the uniaxial test results based on the sign (i.e., compression or tension) of the components of the local stress state. This factor, termed the "triaxiality factor," (or the "knockdown factor") reduces the tensile rupture strain limit determined from the uniaxial test. This triaxiality factor is related graphically to the ratio of the effective tensile strain rupture limit for multiaxial loading states to the ultimate engineering tensile elongation limit measured in uniaxial tension in the laboratory (this ratio is termed the ductility ratio). In other words, the effective tensile strain at rupture is equal to the product of the ultimate engineering tensile elongation (Table 2.3.4-28) and the ductility ratio. Figure 2.3.4-60 illustrates the variation of triaxiality factor with ductility ratio as used in analyzing tensile rupture at nuclear containment boundaries (NNSA 2005).

A triaxiality factor of 1.0, which corresponds to a stress state of uniaxial tension, has a ductility ratio of 1.0. Negative values of triaxiality correspond to compressive stress states, and have a ductility ratio equal to 2.0. Stress states that have hydrostatic tension components have ductility ratios less than 1.0, and triaxiality factors greater than 1.0. For a case of biaxial tension (equal or unequal tension in two principal directions and zero stress in the third), the triaxiality factor can be as high as 2.0 and the ductility ratio can be as low as 0.5. For the waste package outer corrosion barrier, the surface stresses are typically biaxial tension, and the triaxiality factor is assumed to be equal to the maximum value of 2 for all calculations, meaning that the effective tensile strain at rupture is assumed to be equal to one-half of the tensile elongation as measured from uniaxial strain tests. A detailed discussion of the triaxiality factors for multiaxial stress states can be found in *Mechanical Assessment of Degraded Waste Packages and Drip Shields Subject to Vibratory Ground Motion* (SNL 2007b, Appendix A).

Strain Rate Effects—Dynamic finite element waste package model results indicate that strain rates up to 150 s^{-1} are possible during impacts (SNL 2007b, Section A2). Zabotkin et al. (2003) have indicated that the tensile elongation of Alloy 22 decreases 11% as strain rate increases from 10^{-4} s^{-1} to 200 s^{-1}. In order to account for strain rate effects, the tensile elongation is thus reduced by 11% from the 64% as defined by the laboratory tensile tests (Table 2.3.4-28) to 57% for strain rates up to 200 s^{-1}.

Effective Strain Criteria for Tensile Rupture for Alloy 22 and Titanium Grade 7—After reduction of the ultimate engineering tensile elongation of Alloy 22 (64% or 0.64—see Table 2.3.4-28) to account for strain rate effects, the effective tensile elongation at rupture is assumed to be 57% (0.570) (SNL 2007b, Section 6.2.2). This value is subsequently used for determination of the effective strain for tensile rupture. With the maximum triaxiality factor of 2.0 for the waste package outer corrosion barrier, the effective tensile rupture strain for Alloy 22 is 57%/2 or 28.5% (0.285).

The ultimate true (tensile) elongation for Titanium Grade 7 plates is 22% (0.220) (Table 2.3.4-28). For rock block impact to a drip shield plate that creates a dented region, the resulting stress state is biaxial tension, and the triaxiality factor is 2.0. Therefore, for the drip shield plates, the effective

strain for tensile rupture of Titanium Grade 7 is 22%/2 or 11% (0.110) (SNL 2007c, Section 6.10.2.2). For quasi static loading of the drip shield plates by rock rubble, the failure criteria for Titanium Grade 7 are reached when the plate snaps through, indicating that the plates would tear at the contact with the bulkheads or longitudinal stiffeners. The appropriate failure criteria for two boundary conditions are discussed in (SNL 2007, Section 6.4.3.1.2).

Implementation of Rupture Model—The implementation of the tensile rupture criteria is performed in the two- and three-dimensional structural analysis models used for simulation of the waste package and drip shield as a postprocessing procedure (SNL 2007b, Sections 6.3.3, 6.3.4, and 6.5.1.4.1). Finite element and finite difference structural analysis software is used to simulate the mechanical response of the waste package outer corrosion barrier, and the drip shield plates, to impact and to static loading. The deformations (strains) and stress states induced in the outer corrosion barrier and plates are determined as a function of time resulting from waste package-to-waste package and waste package-to-pallet collisions, and the impact of rock blocks to the drip shield plates, as well as the static loading of either the waste package outer corrosion barrier or drip shield plates due to static loading from rock rubble.

The rupture condition of a waste package is determined by comparing the maximum effective tensile strain from all elements on the outer and inner surfaces of the outer corrosion barrier to the ultimate tensile strain limit as defined above (SNL 2007b, Section 6.3.2.2.5). For uniaxial tension, the maximum effective strain limit is 0.570. For biaxial tension, the maximum effective strain limit can be as low as 0.285, based on a triaxiality factor of 2.0. If the maximum effective strain does not exceed 0.285 at any time during the analysis, rupture does not occur. If the maximum effective strain for any elements of the outer corrosion barrier exceeds 0.285 at any time, then the triaxiality factor is computed for the stress state of those elements on the appropriate surface. The elements that have effective strain exceeding 0.285 at some time during the analysis are determined visually (Figure 2.3.4-61) from examination of the computer model fringe plots. The outer corrosion barrier shell and outer corrosion barrier lids are considered simultaneously for both waste package-to-waste package impacts and waste package-to-pallet impacts, in order to obtain the rupture condition for a package.

If the stress state is compressive ($\sigma_1 + \sigma_2 + \sigma_3 < 0$) for the time that the effective strain exceeds 0.285, then rupture does not occur. If the stress state is uniaxial tension or its equivalent ($\sigma_2 + \sigma_3 < 0$), and the effective strain does not exceed 0.57 during that time, then rupture does not occur. If none of these conditions are met, then the actual effective strain limit is computed, using a triaxiality factor, then compared to the effective strain of the element. Rupture does not occur if the effective strain does not exceed the strain limit determined from the stress state of the element.

The uncertainty associated with the effects of multiple impacts on the rupture model for the Alloy 22 outer corrosion barrier is addressed using a semi-empirical methodology that provides for an assessment of rupture potential beyond simple calculation of the effective strains. A waste package is sometimes subjected to large deformation of the outer corrosion barrier; however, due to the ductile nature of Alloy 22, the effective tensile strains do not exceed the tensile strain limit for rupture. In addition to calculation of the effective strains for each element on the outer corrosion barrier, the model itself is visually inspected as the vibratory motion evolves to determine if large deformations have occurred even though the rupture limit has not been reached. If the degree of deformation is determined to be significant, based on engineering judgment, then the waste package

is determined to be in a state of "incipient" rupture, in the sense that a second severe impact has the potential to cause rupture (SNL 2007b, Section 6.3.3).

If two severe impacts occur during a given ground motion, or during a subsequent ground motion, each of which causes severe deformation to the outer corrosion barrier, then the accumulation of severe deformation is interpreted as causing an immediate rupture during the seismic event.

A similar approach is used to determine rupture of the drip shield plates. The rupture condition of a plate is determined by comparing the maximum effective tensile strain in all elements of the plate to the ultimate tensile strain limit of 11%, defined above. Plate rupture from the dynamically amplified rockfall load in lithophysal units is represented by the fragility curves for the drip shield plates. Plate rupture from impact of large rock blocks in the nonlithophysal units is modeled but not abstracted into TSPA because FEP 1.2.03.02.0B, Seismic-induced rockfall damages EBS components, has been excluded from TSPA (Table 2.2-5).

2.3.4.5.1.5 Abstraction of Residual Stress Threshold and Crack Network Transport Area

Within the seismic scenario class, the RST of Alloy 22 is represented as a uniform distribution between 90% and 105% of its yield strength (SNL 2007a, Table 6-3). The RST for Titanium Grade 7 is set to the bounding value of 80% of yield strength (SNL 2007a, Section 6.8.3.1.3).

The ratio of the effective area for transport out of the waste package to the damaged area that exceeds the RST ranges from 0.00327 to 0.0131 (SNL 2007a, Table 6-17). This ratio is represented in the seismic scenario for the TSPA as a uniform distribution with a lower bound of 0.00327 and an upper bound of 0.0131 (SNL 2007a, Section 6.7.3.3).

2.3.4.5.1.6 Abstraction of Rupture Probability

The probability of rupture for the waste package is determined from impact analyses at the 0.4 m/s, 1.05 m/s, 2.44 m/s, and 4.07 m/s PGV levels (SNL 2007b, Tables 6-122 and 6-123). The degree of deformation from waste package-to-pallet impacts during a single ground motion was used to define the probability of no rupture, the probability of incipient rupture, and the probability of complete rupture (SNL 2007b, Section 6.3.3.2). A minor degree of deformation indicates that no rupture occurs, which is consistent with the observation that the strain in the waste package outer corrosion barrier is below the ultimate tensile strain criteria for Alloy 22 for individual impacts. Even through the ultimate tensile strain is not reached, a conservative approach is adopted to determine rupture potential for multiple impacts. A significant degree of deformation, determined empirically as defined in *Mechanical Assessment of Degraded Waste Packages and Drip Shields Subject to Vibratory Ground Motion* (SNL 2007b, Section 6.3.3.2), is interpreted as causing an incipient rupture, in the sense that a second severe impact has the potential to cause rupture. Finally, if two severe impacts occur, then the accumulation of severe deformation is interpreted as causing a rupture in the waste package (SNL 2007c, Section 6.5.2.1).

2.3.4.5.2 Structural Response of the Waste Package and Drip Shield to Vibratory Ground Motion During Time Frame of Structurally Intact Drip Shields

[NUREG-1804, Section 2.2.1.3.2.3: AC 1(1) to (4), AC 2, AC 3(1) to (3), AC 4, AC 5(2), (3)]

The introduction to Section 2.3.4.5 and Figure 2.3.4-51 describe the time evolution of the EBS mechanical environment in terms of three general degradation states based on the structural condition of the drip shield. The first degradation state occurs in the time frame when the drip shields are intact and functional. Rockfall occurs primarily as a result of vibratory ground motion, accumulating in the emplacement drifts until they are filled (Section 2.3.4.4.8). As rockfall occurs, rock blocks may impact and damage the drip shields and the static and dynamically amplified load of the accumulated rubble may additionally result in damage to the drip shield plates. In both cases, the damage to the drip shields occurs primarily through stress corrosion cracking, but they do not collapse. During this state, when the drip shields are intact but pinned in place by rubble, the waste packages and pallets are free to move in response to seismic shaking (i.e., a "kinematic" condition). This movement may result in impacts to the waste packages that may damage or rupture them.

The structural response from waste package-to-drip shield impacts has also been evaluated but screened out of the TSPA. These impacts could cause failure of the drip shield and/or damaged areas on the waste package. Damaged area on the drip shield is not considered here because excluded FEP 2.1.03.10.0B, Advection of liquids and solids through cracks in the drip shield (Table 2.2-5), has been screened out of the TSPA. The potential for failure of the drip shield is considered next.

Fragility curves consider two failure modes of the drip shield: (1) rupture or tearing of the drip shield plates (Section 2.3.4.5.3); and (2) buckling or collapse of the sidewalls of the drip shield (Section 2.3.4.5.3). Both of these failure modes are represented in the TSPA. However, a third failure mode of the drip shield could occur from waste package impacts to the sidewalls and top of the drip shield. This failure mode has been analyzed with structural response calculations and with kinematic analyses for waste package-to-drip shield impacts (SNL 2007c, Section 6.8.5). A lateral impact is defined here as one with its primary velocity components in a two-dimensional cross section that is perpendicular to the drift axis, and a longitudinal impact is one with its primary velocity along the drift axis.

This third failure mode is not represented in the TSPA for two reasons. First, lateral impact of the waste package on the drip shield does not cause catastrophic failure of the drip shield. The structural stability of the drip shield subjected to lateral impacts by a waste package has been investigated with three-dimensional finite-element calculations (BSC 2005c, Section 5.6.2). The results from these calculations demonstrate that none of the lateral impacts cause catastrophic failure and the drip shield component materials remain within their true tensile (ultimate) strengths for the sidewall impacts, even under the extreme impact velocity of 11 m/s (BSC 2005c, Section VI-3.3). Based on these results, drip shield failure from lateral impacts of the waste package is excluded from the TSPA compliance case for the license application. Second, high-velocity longitudinal impacts of the waste package on the bulkhead support beams exposed on the underside of the crown of the drip shield occur infrequently, even at the 4.07 m/s PGV level (SNL 2007c, Table 6-41). The high-velocity longitudinal impacts with the potential to damage the bulkhead support beams occur with much lower probability than the probability of buckling the sidewalls of the drip shield at the 4.07 m/s PGV level for various drip shield thicknesses, as discussed in Section 2.3.4.5.3.4. It

follows that the drip shield sidewalls are expected to buckle before longitudinal impacts damage the bulkhead support beams and, after the sidewalls buckle, high-velocity longitudinal impacts are eliminated because the waste package can no longer move freely beneath the drip shield.

The potential for damage to the waste package from waste package-to-drip shield impacts is not included in the seismic damage abstractions for the TSPA, based on the discussion in *Seismic Consequence Abstraction* (SNL 2007c, Section 6.5.6). The rationale for not including damage from waste package-to-drip shield impacts is based on the observation that the damaged areas from side on impacts of a waste package on a flat elastic surface are zero or very small, and are significantly less than the damaged areas from end on impacts on a flat elastic surface. The side-on impact on a flat, elastic surface is a good representation for the lateral impact of the waste package on the drip shield because the inside surface of the drip shield side walls is a smooth surface, with no protruding bulkheads.

This section provides structural response calculations and damage estimates for EBS features that are subjected to vibratory ground motion when the drip shields are intact. Section 2.3.4.5.2.1 describes process model calculations and abstractions of the damaged area and tensile rupture/tearing potential for TAD-bearing and codisposal waste packages resulting from waste package-to-waste package and waste package-to-pallet impacts. Section 2.3.4.5.2.2 describes process model calculations and abstractions of damaged area and tensile rupture/tearing potential of drip shield plates, and possible drip shield framework collapse in response to rockfall impacts and static and dynamically amplified rock rubble loads.

2.3.4.5.2.1 Waste Package Response to Vibratory Ground Motion for Intact Drip Shields

[NUREG-1804, Section 2.2.1.3.2.3: AC 1(1) to (4), AC 2, AC 3(1) to (3), AC 4, AC 5(2), (3)]

This section reviews the results of large-scale kinematic models and detailed structural analyses of the movement and damage to waste packages resulting from impacts between adjacent waste packages, between the waste package and its emplacement pallet, and between the waste package and the drip shield as a result of vibratory ground motion. Details of these calculations can be found in *Mechanical Assessment of Degraded Waste Packages and Drip Shields Subject to Vibratory Ground Motion* (SNL 2007b, Section 6.3). These analyses are representative of those future states in which the drip shield is still functional; however, the waste package internals may have become degraded. The term "damage" as used here is synonymous with an area of the waste package outer corrosion barrier that exceeds the residual tensile stress threshold for Alloy 22, thereby resulting in enhanced susceptibility to potential stress corrosion cracking and the formation of pathways for radionuclide transport from the waste package (Section 2.3.4.5.1.2.1). In addition, the probability for rupture or tearing of the waste package outer corrosion barrier in response to impact loading is determined. Damage and rupture abstractions are developed for TAD-bearing and codisposal waste packages for three future states: (1) 23-mm-thick outer corrosion barrier with intact internals; (2) 23-mm-thick outer corrosion barrier with degraded internals; and (3) 17-mm-thick outer corrosion barrier with degraded internals. The 23-mm-thick and 17-mm-thick outer corrosion barrier correspond to 2.4 and 8.4 mm of corrosion thinning from the initial 25.4 mm thick outer barrier. The expected postclosure time periods corresponding to this amount of corrosion thinning are 340,000 years and 1,200,000 years after repository closure, based on the calculations in

Section 2.3.4.5.1.3.6. Those cases with degraded internals represent future states in which stress corrosion damage to the outer corrosion barrier of the waste package has occurred, allowing water to enter the waste package by diffusive transport and resulting in corrosion and degradation of the internal structures and fuel rods (Section 2.3.4.5.2.1.2.5).

The abstractions for damaged area are based on a three-part approach (SNL 2007c, Section 6.1.6):

- The probability of rupture occurring is defined as a function of PGV of the ground motion.
- The probability of nonzero damage is defined as a function of PGV and the RST of the Alloy 22 outer corrosion barrier.
- When nonzero damaged area occurs, a conditional probability distribution for the magnitude of the conditional damaged area is defined as a function of PGV and RST. The conditional damaged areas are always nonzero areas, by definition.

2.3.4.5.2.1.1 Conceptual Description of Analysis of Waste Package Response to Vibratory Ground Motion for Intact Drip Shields

A finite element analysis of the dynamics and impact of many waste packages and drip shields in an emplacement drift subjected to vibratory ground motion is complex. To address this issue, simplified three-dimensional finite element kinematic analyses, supplemented by a number of detailed finite element structural calculations, are used to simulate the interactions of many waste packages and pallets representing the two major waste package types in the waste package inventory (SNL 2007b, Sections 6.3.2.1 and 6.3.2.2.1). Two base case kinematic models are developed: one for estimating damage to the TAD-bearing waste package (Figure 2.3.4-62); and one for estimating damage to the codisposal waste packages (Figure 2.3.4-63), represented by the 5-DHLW/Naval Long package (Section 2.3.4.5.1.1).

Kinematic Waste Package Impact Analyses—Initial calculations with kinematic models are conducted for the complete range of ground motion time histories to establish the range of impact parameters for multiple waste packages in an emplacement drift (SNL 2007b, Section 6.3). The input ground motions include application of 17 ground motion time histories at PGV levels of 0.4 m/s, 1.05 m/s, 2.44 m/s, and 4.07 m/s. Mechanical parameters (impact time, location, relative impact velocities, and angles of impact) that describe the various impacts are recorded for each of the two base-case kinematic models.

Detailed Finite Element Damage Analyses—In addition to the kinematic models with multiple waste packages, detailed three-dimensional finite element analyses are performed for individual impacts to define the degree and mode of damage to the outer corrosion barrier over the full range of impact parameters determined from the kinematic models (SNL 2007b, Section 6.3.3). The detailed finite element models represent the TAD-bearing and the codisposal waste packages and provide a comprehensive geometric representation of the various waste package vessels and internal structures, as well as a detailed representation of the emplacement pallet. Analyses are conducted for (a) two different future states of the waste packages (defined by the level of outer corrosion barrier thinning by general corrosion); (b) degraded or intact waste package internals;

and (c) three values of the RST that cover the range for Alloy 22 (90% to 105% of yield strength) to explore the effect of yield strength uncertainty on damage area. From these analyses, lookup tables are developed relating the damaged area to impact force for the various impact locations and relative impact angle. The impact parameters for every impact recorded in the simpler kinematic models (which represent an actual emplacement drift) can then be converted to damage area through linear interpolation of damage area values from the lookup tables. The total damaged area on a waste package is defined as the sum of the damaged area from the multiple impacts that occur during a given ground motion, and are reported for each of the 17 ground motion realizations for each of the four PGV levels.

Outer Corrosion Barrier Rupture Analysis—As part of the detailed three-dimensional finite element modeling, the effective tensile strain induced in the outer corrosion barrier during impact is determined (SNL 2007b, Sections 6.2.2 and 6.3.2.2.5). The effective tensile strain is defined for the impact parameters including velocity, location, and angle. The potential for tensile rupture of the outer corrosion barrier is determined from the failure criteria for effective strain at rupture and the number of impacts that cause significant deformation (Section 2.3.4.5.1.4.2). Lookup tables are developed for waste package-to-waste package and waste package-to-pallet impacts that relate rupture potential to impact velocity and force for the various impact locations and angles. The probability that an impact causes rupture of the outer corrosion barrier is related to impact force thresholds associated with each type of waste package with intact and degraded internals (SNL 2007b, Section 6.3.4).

2.3.4.5.2.1.2 Data and Data Uncertainty of Waste Package Response to Vibratory Ground Motion for Intact Drip Shields

The input data for the waste package damage and rupture calculations for the cases where the drip shield is intact include the following (SNL 2007b, Sections 6.3.1, 6.3.2.2.1, and 6.3.2.2.2):

- 17 ground motion time histories for the 0.4 m/s, 1.05 m/s, 2.44 m/s, and 4.07 m/s PGV levels (SNL 2007b, Section 1.3)
- Friction coefficient for metal-to-metal (waste package-to-pallet, waste package-to-waste package, or waste package-to-drip shield) contacts
- Friction coefficient for waste package- to invert or pallet-to-invert (metal-to-crushed tuff) contact
- Elastic material properties of the waste package and pallet
- RST criteria for damage assessment
- Ultimate tensile strain for rupture/tearing of the Alloy 22 outer corrosion barrier
- Dimensions and masses of EBS components (drip shield, waste package, pallet)

- Three future states of the waste package: 23-mm-thick outer corrosion barrier with intact internals, 23-mm-thick outer corrosion barrier with degraded internals, and 17-mm-thick outer corrosion barrier with degraded internals.

2.3.4.5.2.1.2.1 Ground Motions and Friction Coefficients

The uncertainty in the ground motion inputs and in the metal-to-metal and metal-to-invert tuff friction coefficients is propagated into the kinematic calculations through sampled values for these input parameters. The postclosure ground motion hazard is spanned by four PGV levels: 0.4 m/s, 1.05 m/s, 2.44 m/s and the bounding PGV of 4.07 m/s as noted above. At each of these PGV levels, the ground motion hazard is adequately described by 17 ground motion time histories (SNL 2007b, Section 4.1.4). The use of 17 sets of time histories is consistent with an NRC recommendation to use 15 sets of input ground motions to perform soil-structure interaction analysis that is consistent with a probabilistically defined seismic hazard (SNL 2007b, Section 4.1.4).

For each PGV level, GoldSim provides a Latin Hypercube sampling of the metal-to-metal friction coefficient, the metal-to-invert friction coefficient, and the ground motion number. Each friction coefficient is independently sampled from a uniform distribution, with a wide range of 0.2 to 0.8. This range (approximately 11 to 38 degrees friction angle) was chosen specifically to span the range of possible conditions of sliding surfaces in the emplacement drift. The ground motion number is sampled from a discrete distribution from 1 to 17, with equal probability for each number. This sampling provides a list of input data in which a given time history (numbered from 1 to 17) is randomly paired with metal-to-metal and metal-to-invert friction coefficients for each waste package and pallet. This random pairing of friction coefficients and ground motion time history is incorporated into the kinematic calculations conducted at the 0.4 m/s, 1.05 m/s, 2.44 m/s, and 4.07 m/s PGV levels. For each of the 17 sets of ground motions, two horizontal components (H1 and H2)—and one vertical component (V) of acceleration, velocity, and displacement—were supplied (SNL 2007c, Section 1.1). The H1 component is oriented transverse to the axis of the emplacement drift, and the H2 component is oriented along the drift axis in the longitudinal direction. The waste package damage abstractions in this section are based on the first horizontal component of PGV, as described in Section 2.3.4.3.2.4.

2.3.4.5.2.1.2.2 Energy Dissipation on Impact

The energy dissipated during impact of waste packages to pallets, to other waste packages, and during impact of the pallet to the invert must be accounted for in the kinematic analyses since it has an important effect on the velocity, force and number of subsequent impacts. The dissipation of energy at impact is represented in the finite element calculations through the use of viscous contact damping. The viscous damping parameters were determined by conducting numerical canister drop tests onto a pallet (BSC 2005c, Appendix I) and pallet drop tests onto a rock base. The coefficient of restitution is defined as the ratio of incoming to outgoing velocity for an impacting body. The literature indicates that the coefficient of restitution for impact of metallic bodies is typically less than 0.6 and typically between 0.1 and 0.2 for fragmented rock (BSC 2005c, Section 3.2.28). A series of numerically simulated vertical drop tests of a canister on a waste package pallet were conducted. Viscous damping parameters were varied until a target coefficient of restitution of 0.6 was obtained.

2.3.4.5.2.1.2.3 Physical Characteristics, Material Properties, and Failure Criteria for Waste Package

The methodology for dealing with uncertainty in input properties and failure criteria in the analyses can be found in (1) physical characteristics of the waste package, particularly the dimensions, masses and degradation state of the internals; (2) waste package material properties, which are addressed in Section 2.3.4.5.1.3.1; (3) RST for estimating damage from stress corrosion cracking, which is addressed in Section 2.3.4.5.1.2.1; and (4) effective strain criteria for tensile rupture/tearing, which is addressed in Section 2.3.4.5.1.2.2.

2.3.4.5.2.1.2.4 Dimensions and Masses of the Waste Package

The dimensions and masses of the waste packages, and the number of waste packages in the inventory, are summarized in Tables 1.5.2-2, 1.5.2-3, and 1.5.2-5 as well as Section 2.3.4.5.1.1. As described in that section, the scope of the mechanical analyses described here were simplified by combining the waste package inventory into two representative groups that share similar design characteristics: the TAD-bearing group, which is represented by the TAD-bearing waste package, and the codisposal group, which is represented by the 5-DHLW/DOE Long waste package. Section 2.3.4.5.1.1 provides details on dimensions and mass of these representative groups of waste packages.

2.3.4.5.2.1.2.5 Degradation of Waste Package Internals

Uncertainty in the degradation state of the internals of the waste packages are dealt with through analysis of two general cases for the TAD-bearing and codisposal waste packages—completely intact, or completely degraded internals (SNL 2007c, Sections 6.1.2 and 6.1.3; SNL 2007b, Section 6.3). Analyses of the structural response of the waste package with intact internal structures are performed for those cases in which the waste package outer corrosion barrier has not been damaged by vibratory motion (SNL 2007c, Section 6.1.3.2). Analysis of the structural response of a waste package with degraded internals is performed to represent the case in which damage to the waste package outer corrosion barrier has occurred and the internals have degraded by corrosion processes (SNL 2007c, Section 6.1.3.2).

The assumption is made that, if the waste package outer corrosion barrier has breached, then the internal stainless steel vessels, fuel baskets, and fuel rods will have completely degraded to a soil-like material (SNL 2007c, Section 6.1.3; SNL 2007b, Sections 5.15 and 6.3.2.2.1). It is difficult to quantify the effect of degradation on the strength and stiffness of the internals. Because no test or analogue information is available, the material behavior and mechanical properties chosen to represent this material underestimate the strength and stiffness of internals irrespective of the level of their degradation (SNL 2007b, Section 5.15). In other words, assuming the material has little or no cohesive strength results in minimal supporting pressure afforded to the outer corrosion barrier of the waste package, thus resulting in a weaker outer corrosion barrier which is more susceptible to denting or puncture during external loading. The volume and mass of the degradation products is assumed to be equal to the original volume and mass of the internals but will collect in the lower half of the outer corrosion barrier (SNL 2007b, Figures 6-13 and 6-15). The material was conceptualized to degrade to a frictionless and weakly cohesive (Tresca) material which will maintain constant volume under the cyclic shear strain that accompanies strong ground motion. The

properties chosen are a cohesion of 50 kPa (7.25 psi) and bulk modulus of 10 MPa (1450 psi) (SNL 2007b, Section 5.15).

The initial porosity of the degraded internals within the outer corrosion barrier of the waste packages is estimated to be 0.5 (SNL 2007b, Section 5.10). Given the simplified representation for the corroded internals discussed above, the potential volumetric expansion of the corrosion products was not considered to affect porosity, which remains at 0.5 for degraded internals within the outer corrosion barrier (SNL 2007b, Section 5.10).

2.3.4.5.2.1.2.6 General Corrosion Thinning of the Alloy 22 Outer Corrosion Barrier

The initial thickness of the TAD-bearing and codisposal Alloy 22 outer corrosion barrier is 25.4 mm. The detailed structural analyses include examination of the impact of corrosion thinning of the outer corrosion barrier with time, as well as the effect of possible outer corrosion barrier breach and degradation of the waste package internals on mechanical performance. Future states of the waste packages were analyzed with intact and degraded internal structures for the 23-mm-thick outer corrosion barrier and with degraded internals for the 17-mm-thick outer corrosion barrier (Section 2.3.4.5.2.1). A discussion of the approximate postclosure time periods associated with this amount of corrosion thinning of the outer corrosion barrier can be found in Section 2.3.4.5.1.3.6.

2.3.4.5.2.1.3 Model and Model Uncertainty of Waste Package Response to Vibratory Ground Motion for Intact Drip Shields

Damage from waste package-to-waste package and waste package-to-pallet impacts for the TAD-bearing and codisposal waste packages in response to vibratory ground motion is determined by structural response calculations using commercially available versions of the finite-element program LS-DYNA (SNL 2007b, Section 6.3.1).

Two types of calculations are performed: (1) large-scale kinematic analyses, to determine the impact parameters for multiple waste packages in an emplacement drift for each of 17 ground motion time histories at four PGV levels; and (2) detailed finite element analyses of individual waste package-to-waste package and waste package-to-pallet impacts that encompass the impact parameters from the kinematic results. The detailed model, which accounts for plastic deformation of the waste package and pallet, provides detailed estimates of the damaged area and the rupture potential for the individual impacts. These results are used to develop lookup tables of the damaged area as a function of impact parameters. These lookup tables are used to convert the output of the kinematic analyses to the damaged area suitable for use in damage abstractions for TSPA.

2.3.4.5.2.1.3.1 Kinematic Analyses

Three-dimensional kinematic analyses are used to examine the motion and impact of multiple waste packages, pallets, and drip shields in an emplacement drift when subjected to vibratory ground motion. The main objective of these analyses is to define the history of impact parameters for collisions of the waste packages, pallets, and drip shields as a function of the suite of input ground motions. The damaged areas on the waste package, as well as the probability of rupture of the outer corrosion barrier, is determined from the impact data. A separate kinematic calculation is performed

for each of the 17 ground motion time histories, at four PGV levels that span the range of the seismic hazard described in Section 2.3.4.3.

The kinematic calculations consider a "string" of multiple waste packages in a section of an emplacement drift (SNL 2007b, Section 6.3.2). The "string" is composed of a combination of TAD-bearing waste packages and codisposal waste packages that rest on emplacement pallets which sit on a rigid invert (SNL 2007b, Section 6.3). Although the invert is rigid, impact energy is dissipated based on a coefficient of restitution characteristic of a crushed rock base. For these analyses, two waste package representations were created: one for determining the response of a typical TAD-bearing waste package (Figure 2.3.4-62); the other for the response of a typical codisposal waste package (Figure 2.3.4-63). The TAD-bearing model contains 11 total waste packages, with the central three TAD-bearing waste packages surrounded by a codisposal waste package on each side. For the codisposal model, the 11 waste package configuration was extended to 13 waste packages in order to expand the focus to include the two codisposal waste packages that surrounded the three central TAD-bearing waste packages. The additional codisposal waste package at each end of the series maintains the bounding of the internal codisposal waste packages of interest by four waste packages to either side. The appropriate mix of waste packages is chosen to make the sequence roughly representative of the percentage of TAD-bearing and codisposal packages in the inventory (Table 2.3.4-27). The number of waste packages in the sequence was chosen to make certain that the kinematic response of the central waste packages is representative of a long emplacement drift. In other words, the response of the central packages is independent of the free boundaries at either end of the string.

For computational efficiency, the kinematic calculations use relatively coarse finite-element representations of the waste package and pallet as elastic bodies that preserve the mass and dimensions of the components. The kinematic calculations represent an emplacement drift that has partially or completely collapsed, with the result that the drip shield is pinned in place, and moves synchronously with the free field. Section 2.3.4.4.8 demonstrates that complete collapse of the emplacement drifts in the lithophysal rock occurs at a PGV level of approximately 2 m/s, and that substantial rock blocks are dislodged at this level in the nonlithophysal unit as well. Even relatively small amounts of rockfall tend to prevent drip shield separation or movement relative to the tunnel invert, as demonstrated in *Mechanical Assessment of the Drip Shield Subject to Vibratory Motion and Dynamic and Static Rock Loading* (BSC 2004h, Section 5.3.3.1). Therefore, the drip shield is represented as an upper boundary that moves synchronously with the free field for the kinematic calculations.

Kinematic analyses were conducted by applying the ground motion time histories at the emplacement drifts to the top surface of the invert, which is the base of the finite element model. There is no restriction to the movement of the waste packages and pallets in the kinematic models. Impacts or sliding can occur between adjacent waste packages, the waste package and pallet, the waste package and the invert (in the event that an end of the waste package slides off the pallet), and the waste package and the drip shield. Impacts are recorded for the central waste packages in the total "string" of waste packages during the dynamic simulation. The appropriate mix of waste packages and the number of waste packages are chosen to make the number of waste packages representative of the package inventory and to make the response of the string representative of the middle of an emplacement drift, independent of the end conditions. That is, the string must have enough waste packages to make the response of the central waste packages independent of the free

boundaries at either end of the string (SNL 2007b, Section 6.3.1). At the limits of the string, packages can more easily move axially, and thus the number of waste package-to-waste package impacts will be less. The impact forces, angles, and locations for waste package-to-waste package impacts, and the impact forces, angles, and locations for the central waste package-to-pallet impacts, as well as similar data for TAD-bearing to codisposal waste package impacts, are recorded for each simulation. The resulting detailed impact data for all simulations are tabulated in *Mechanical Assessment of Degraded Waste Packages and Drip Shields Subject to Vibratory Ground Motion* (SNL 2007b, Section 6.3).

2.3.4.5.2.1.3.2 Detailed Structural Analysis and Development of Damage Lookup Tables

The kinematic calculations determine the waste package impact parameters (location, angle, velocity, force) for simulations of 17 ground motion time histories at each of the 0.4 m/s, 1.05 m/s, 2.44 m/s, and 4.07 m/s PGV levels (SNL 2007b, Section 6.3.2). These impacts then must be converted to damaged area and/or rupture on the waste package outer corrosion barrier. Detailed three-dimensional finite element structural analyses of a single TAD-bearing or codisposal waste package impacting another waste package or an emplacement pallet were conducted to provide estimates of the damage induced to the waste package as a function of the range of impact parameters as determined from the kinematic analyses (SNL 2007b, Sections 6.3.1 and 6.3.2.2). These detailed analyses are used to produce lookup tables of damage area as a function of impact parameters for two outer corrosion barrier thickness, 23 mm and 17 mm, and for intact and degraded waste package internals. Lookup tables are produced for both waste package-to-waste package and waste package-to-pallet impacts at each PGV level, and for three levels of RST (90%, 100%, and 105%) for Alloy 22 that span the range of uncertainty in the RST (Section 2.3.4.5.2.1.1).

The detailed finite element representations of the TAD-bearing and codisposal waste package with intact and degraded internals and the pallet structure are shown in Figures 2.3.4-54 and 2.3.4-55. The initial thickness of the Alloy 22 outer corrosion barrier is 25.4 mm. The detailed finite element representations examine two future states of thickness of the outer corrosion barrier of 23 and 17 mm representing 2.4 and 8.4 mm of general corrosion thinning. The 23-mm-thick outer corrosion barrier represents conditions during the initial period after repository closure and the 17-mm-thick outer corrosion barrier represents conditions at the end of the period for peak dose assessment. The basis for these levels of general corrosion thinning to represent postclosure conditions is provided in Section 2.3.4.5.1.3.6.

The model for the TAD-bearing waste package with intact internals is based on the Naval Long waste package (BSC 2006a; BSC 2006b; BSC 2006c; and BSC 2006d) as an overpack that contains an approximate representation of a TAD canister and fuel basket (SNL 2007b, Section 6.3.2.2.1). The model for the codisposal waste package with intact internals represents the 5-DHLW/DOE Long codisposal waste package (SNL 2007g, Table 4-9). For both waste package models, the outer corrosion barrier is represented with Alloy 22 material properties (Table 2.3.4-28), and the other components for intact internals are represented as 316 Stainless Steel. The temperature dependence of material properties is accounted for by using properties determined at 60°C (Section 2.3.4.5.1.3.1). Densities are scaled to obtain the correct mass for the components. Degraded internals are assumed to have properties as described in Section 2.3.4.5.2.1.2.5.

The emplacement pallet model (Figure 2.3.4-64) is an approximate representation of the pallet engineering design (Figure 1.3.4-11) (SNL 2007b, Sections 6.3.1 and 6.3.2.1). The connecting beams are represented with 316 Stainless Steel properties, and the rest of the pallet structure is represented with Alloy 22 properties (Table 2.3.4-28). For analyses representing long time periods where the waste package internals are degraded, the connecting beams are assumed to be degraded as well and are not included in the analyses. The description of the detailed finite element analyses is organized as follows: (a) the representative impact configurations of waste packages and pallets as derived from kinematic simulations is described; (b) the methodology for calculating the damaged area and rupture potential of the outer corrosion barrier for TAD-bearing and codisposal waste packages is described; and (c) the development of lookup tables of damage and rupture that summarize these calculations and can be used as a basis for conversion of impact data from the kinematic simulations to damaged area or rupture potential is given.

Impact Analysis Configurations—The impact configurations for the detailed waste package-to-waste package and the waste package-to-pallet damage lookup table analyses were determined from the ranges of impact force, location, and angle of the waste packages and pallets recorded from the kinematic analyses. Figures 2.3.4-65 and 2.3.4-66 show example plots of the detailed TAD-bearing waste package models for examining the impact location between two waste packages, and the impact angle between a waste package and pallet. Additional studies were completed for the impact angle for waste package-to-waste package impacts as well as the impact location between the waste package and pallet. All of these detailed studies were used to derive the damage area lookup tables that were, in turn, used for conversion of the impact forces from the kinematic analyses to damage area of the outer corrosion barrier. Detailed listings of all of the analyses performed and their use in developing the damage area lookup tables can be found in *Mechanical Assessment of Degraded Waste Packages and Drip Shields Subject to Vibratory Ground Motion* (SNL 2007b, Section 6.3.2.2).

Calculation of Damage from Detailed Finite Element Analyses—The damaged area related to an impact with a given force and velocity is computed from the detailed finite element analyses by determining the area of the Alloy 22 outer corrosion barrier surface (cylinder and lids) that has a residual tensile stress after impact that exceeds one of three RST levels (90%, 100%, and 105% of yield strength), as described in Section 2.3.4.5.2.1.1. Damaged area lookup tables are developed for each yield strength value for each of the three future states of outer corrosion barrier thicknesses and internals damage state (i.e., 23 mm thickness for intact and degraded internals and 17 mm thickness for degraded internals) (Section 2.3.4.5.2.1). The yield strength for Alloy 22 at 60°C is 350 MPa (51,000 psi) (SNL 2007b, Table 6-7), so the three threshold stress levels correspond to 316 MPa, 350 MPa, and 369 MPa (45,900 psi, 51,000 psi, and 53,550 psi), respectively. The values of 316 MPa and 369 MPa define the lower and upper bound of a uniform distribution for RST (SNL 2007a, Section 6.2.2 and Table 6-3). An element of the finite element mesh contributes to the damaged area if any of the outer, inner, or middle elements of the outer corrosion barrier has a residual stress that exceeds the given RST level. This approach is nonmechanistic in the sense that detailed calculations for potential crack initiation and propagation are not used to determine the time delay for a through-the-wall crack to form (SNL 2007c, Section 6.1.4). Total damage area is calculated as the summation of area of all elements that exceed the given residual stress level at the end of a simulation of vibratory ground motion. An example showing the damaged areas for the three RST levels contoured on the finite element mesh of the under surface (lower hemicylinder) of a TAD-bearing waste package, 23 mm

thickness outer corrosion barrier, degraded internals and impact velocity of 3 m/s is provided in Figure 2.3.4-67. The dark blue area is below 90% of yield strength and does not contribute to damaged area; the light blue, green, yellow, and red areas combined are above 90% of yield strength; the yellow and red areas combined are above 100% of yield strength; the red area is above 105% of yield strength. The crease in the outer corrosion barrier at the pallet impact contact is clearly visible in this figure.

Calculation of Rupture Condition—The rupture condition of the outer corrosion barrier was determined for each impact based on monitoring of the maximum effective strain and comparison to the rupture tensile strain failure criterion as described in Section 2.3.4.5.1.2.2. If the effective tensile strain overcomes the tensile rupture strain criteria for Alloy 22 during an impact, the outer corrosion barrier is breached. However, the detailed finite element calculations demonstrate that the strain in the outer corrosion barrier is always below the ultimate tensile strain for Alloy 22 from a single impact, so rupture does not occur from a single impact even at the highest PGV level on the bounded hazard curve (SNL 2007b, Section 6.3.4). A further assessment of the probability of rupture, based on deformation of the waste package, was performed using a criterion that accounts for multiple large impacts in the kinematic analyses. If an impact causes severe deformation, then additional large impacts to the deformed area have the potential to cause rupture.

For both TAD-bearing and codisposal packages, it is apparent that the overall deformation of the outer corrosion barrier resulting from impacts is insignificant for intact internals, even at the largest impact velocities. Thus, there is no rupture of waste packages with intact internals (SNL 2007, Sections 6.5.1.1 and 6.6.1.1). With degraded internals, the deformation from low velocity impacts is not judged to be severe enough to lead to rupture after multiple impacts at that level. However, the deformation becomes very large as impact velocity increases. There is an impact velocity for which the outer corrosion barrier shell starts to bulge noticeably at both sides of the deformed section, and the shell starts to have a noticeable kink where the waste package deforms into the edge of the pallet cradle. For the purposes of the rupture abstraction, it is estimated that the deformation at this velocity is a reasonable lower bound (or threshold) such that another impact of equal or greater size would potentially cause a rupture of the outer corrosion barrier. The probability that multiple impacts above the threshold could potentially cause rupture increases with increasing impact velocity, such that extremely severe deformations are judged to cause rupture after multiple impacts at that level with a probability of 1.0. The estimates of probability are qualitative and based on engineering judgment of the results from the detailed finite element calculations of a single impact (SNL 2007c, Sections 6.5.2.1 and 6.6.2.1).

These probabilities are utilized for determining the potential for rupture from the kinematic analyses. Incipient rupture is defined as a state in which a waste package has been subjected to one impact during a seismic event that causes deformation such that another large impact during a later seismic event will cause rupture of the waste package. A waste package is in a state of incipient rupture at the end of kinematic seismic analysis if one and only one impact causing deformation associated with this state occurs during the analysis. If two or more such impacts occur for a waste package during a kinematic seismic analysis, then the waste package is in a state of rupture. The probabilities of the waste packages being in either of these states are computed by statistically combining the probabilities for each impact (SNL 2007, Section 6.5.2.1 and 6.6.2.1).

Waste Package-to-Waste Package Damage Lookup Tables—Waste package-to-waste package impact analyses for determining damaged area and rupture condition for TAD bearing packages were performed for 90 configurations. The analyses were performed for impact velocities of 0.50 m/s, 1.00 m/s, 2.00 m/s, 4.00 m/s, 6.00 m/s, and 9.00 m/s; four impact locations above and below the centerline of the end lids (Figure 2.3.4-65); and one impact angle of 1.5 degrees. The impact location is defined as the normalized distance between the impact point and the outer circumference of the waste package that is being impacted on the lid by the other package. The normalization factor is the diameter of the waste package. Three configurations of the waste packages were used: 23 mm outer corrosion barrier with intact internals, 23 mm outer corrosion barrier with degraded internals and 17 mm outer corrosion barrier with degraded internals. Damaged area and rupture condition of the two waste packages are recorded separately. The results for damaged area for the TAD-bearing waste package (at 90%, 100%, and 105% of yield strength) are presented in detail in *Mechanical Assessment of Degraded Waste Packages and Drip Shields Subject to Vibratory Ground Motion* (SNL 2007b). The numerical damage results for waste package-to-waste package impacts in terms of damaged surface area for TAD-bearing and codisposal waste package types are summarized in Section 2.3.4.5.2.1.4.

Waste Package-to-Pallet Damage Lookup Tables—TAD-bearing and codisposal waste package analyses were performed for 188 and 209 configurations, respectively. These configurations include analyses for a range of impact angles, impact locations and impact velocities that encompass the range of impact configurations observed in the kinematic analyses. The damaged areas were calculated for three RST levels for the Alloy 22 outer corrosion barrier (90%, 100%, and 105% of yield strength). The results for damaged area for the TAD-bearing and codisposal waste packages (at 90%, 100%, and 105% of yield strength) are presented in detail in *Mechanical Assessment of Degraded TAD Canisters and Degraded Drip Shields Subject to Vibratory Ground Motion* (SNL 2007b, Section 6.3.2). The numerical damage results for waste package-to-pallet impacts in terms of damaged surface area for TAD-bearing and codisposal waste package types are summarized in Section 2.3.4.5.2.1.4.

Rupture Lookup Tables—Rupture potential, based on exceeding the effective rupture strain criterion, was recorded for all kinematic simulations of waste package-to-waste package and waste package-to-pallet. The rupture potential is determined for all vibratory motion cases for 23 and 17 mm thick outer corrosion barrier and for intact and damaged internals. The rupture potential is recorded as positive (rupture occurs) or negative (rupture does not occur) for each case in the rupture lookup tables. The results for rupture of the TAD-bearing and codisposal waste packages are presented in detail in (SNL 2007b, Section 6.3.4.2). A summary of the rupture probability for TAD-bearing and codisposal waste package types can be found in Sections 2.3.4.5.2.1.4.1, 2.3.4.5.2.1.4.2, and 2.3.4.5.2.1.4.3.

2.3.4.5.2.1.3.3 Confidence-Building in the Kinematic Model

The three-dimensional kinematic model for waste package damage due to vibratory ground motion was validated by two means (SNL 2007b, Section 7.3.1). First, a comparison was made of kinematic results obtained using LS-DYNA (a three-dimensional finite element computer program) to those obtained using an alternative computational kinematic model in UDEC (a two-dimensional discrete element computer program). Second, a comparison was made of the kinematic results to detailed LS-DYNA analyses of single waste packages subjected to vibratory ground motion.

Comparison of the Kinematic Model to an Alternative Modeling Approach for Rigid-Body Kinematics—The UDEC code was used to develop a two-dimensional model of many waste packages with motion restricted to the plane of the drift longitudinal axis. This is equivalent to the three-dimensional LS-DYNA kinematic model of 13 waste packages that is shown in Figure 2.3.4-63. To create similarity in boundary conditions of the models, a vertical symmetry plane parallel to the drift axis was imposed on the LS-DYNA model to suppress motion in the drift cross-sectional plane. The vertical and H2 horizontal components of ground motion 1 at 5.35 m/s PGV level (corresponding to realization 14) were applied to both models. The computed rigid-body velocity of the three central waste packages for the LS-DYNA and UDEC models was compared. The rigid-body motions computed for the two models agree well in terms of amplitude, and show similar oscillatory behavior. This general agreement, using two completely different numerical formulations, provides corroboration for the approach of using LS-DYNA to perform kinematic analyses of multiple waste packages subjected to seismic excitation, where the rigid-body behavior of the waste packages is of interest.

Validation of the Kinematic Model Using Detailed, Single Canister Deformable Models—Ideally, the waste package vibratory ground motion analyses described in Section 2.3.4.5.2.1 would have been conducted using a detailed finite element representation for all waste packages and pallets. However, as discussed previously, computational restrictions to this approach resulted in the use of the two-part calculation process for estimation of damaged area and rupture potential (i.e., large-scale kinematic model impacts interpreted via detailed finite element damage and rupture analyses). It is important to verify that this two-part approach bounds the damaged area and rupture potential that would be obtained from detailed finite element representation of all waste packages and pallets. Verification was performed by comparison of damaged area from the two-pass approach to that for a single, detailed waste package-pallet finite element model for the 0.4 m/s PGV level (SNL 2007b, Section 7.3.1). This approach is only valid for the lower PGV levels, where there is no interaction between adjacent waste packages, since the detailed finite element model was developed only for a single waste package and pallet. Two simulations were conducted for time histories at the 0.4 m/s PGV level (one for the TAD-bearing and one for the codisposal waste package, both of which had a 17-mm-thick outer corrosion barrier with degraded internals to maximize damaged area), and one simulation for the codisposal waste package at the 1.05 m/s PGV level. For each simulation, damaged area was determined for 90%, 100%, and 105% yield strength criteria.

For both the TAD-bearing and codisposal waste packages, the kinematic analyses significantly overpredict the damaged area for all simulations conducted (SNL 2007b, Tables 7-3 and 7-4). For the TAD-bearing waste package, the detailed analyses predict essentially negligible damaged areas. For the codisposal waste package, the detailed analyses predicted damaged areas significantly smaller than the corresponding kinematic analyses, with several of the detailed analyses predicting essentially negligible damaged areas. This result is reasonable since the impact forces on the detailed model are smaller than for the kinematic model due to more accurate impact energy dissipation due to plastic deformation that is not included in the kinematic model. This shows that, while the kinematic approach to modeling waste packages subjected to seismic excitation does not yield damaged area estimates that exactly match the more detailed model, the kinematic approach does overestimate the damaged areas. Thus, the relatively efficient kinematic approach is a reasonable alternative to performing computationally intensive detailed analyses with detailed

representations of multiple waste packages for multiple realizations of ground motion time histories and PGV levels.

2.3.4.5.2.1.4 Damage and Rupture Abstractions for the TAD-Bearing and Codisposal Waste Packages

Six kinematic damage abstractions have been developed for the TAD-bearing waste package and the codisposal waste package. These damage abstractions are called "kinematic" because the drip shields are intact and the waste packages are free to move and interact beneath the drip shields. The six damage abstractions are as follows:

- TAD-bearing waste package with 23-mm-thick outer corrosion barrier and intact internals
- TAD-bearing waste package with 23-mm-thick outer corrosion barrier and degraded internals
- TAD-bearing waste package with 17-mm-thick outer corrosion barrier and degraded internals
- Codisposal waste package with 23-mm-thick outer corrosion barrier and intact internals
- Codisposal waste package with 23-mm-thick outer corrosion barrier and degraded internals
- Codisposal waste package with 17-mm-thick outer corrosion barrier and degraded internals.

Each abstraction defines the probability of rupturing the outer corrosion barrier, the probability of nonzero damaged area on the outer corrosion barrier, and the conditional probability distributions for the conditional damaged area. The probability of rupture is a function of PGV, and the probability of nonzero damaged area and conditional probability distributions are functions of PGV and RST. This section illustrates the damage abstractions for three cases: (1) the TAD-bearing waste package with intact internals and a 23-mm-thick outer corrosion barrier; (2) the codisposal waste package with intact internals and a 23-mm-thick outer corrosion barrier; and (3) a codisposal waste package with degraded internals and a 17-mm-thick outer corrosion barrier. The choice of the first case is motivated by the fact that the TAD-bearing waste package with intact internals has a very low probability of nonzero damaged area, so it is almost never damaged during the time frame for kinematic response. In this situation, the dose from the seismic scenario class until drip shield failure is dominated by releases from the codisposal waste package, providing the motivation for the second and third cases. Note that the damage abstractions are very similar for either waste package type with degraded internals, so a fourth case for the TAD-bearing waste package with degraded internals is not illustrated here. The kinematic damage abstractions are documented in *Seismic Consequence Abstraction* (SNL 2007c, Sections 6.5 and 6.6).

2.3.4.5.2.1.4.1 Damage and Rupture Abstractions for the TAD-Bearing Waste Package with Intact Internals and 23-mm-thick Outer Corrosion Barrier

Probability of Rupture—The probability of rupture for the TAD-bearing waste package with a 23-mm-thick outer corrosion barrier and intact internals for single or multiple impacts is zero. The structural response calculations for kinematic response at the 0.4 m/s, 1.05 m/s, 2.44 m/s, and 4.07 m/s PGV levels demonstrate that the strain in the outer corrosion barrier from a single impact is always below the ultimate tensile strain for Alloy 22 (SNL 2007c, Section 6.5.1.1). Consideration of multiple impacts to a TAD-bearing waste package with intact internals does not change the probability of rupture for intact internals (SNL 2007b, Sections 6.3.3 and 6.3.4). In particular, the potential for damage to accumulate from multiple impacts that severely distort the outer corrosion barrier does not occur with intact internals, so the probability of rupture from multiple seismic events is judged to be zero with intact internals (SNL 2007c, Section 6.5.1.1).

Probability of Nonzero Damaged Area—Table 2.3.4-29 presents the probability of nonzero damage for the 23-mm-thick outer corrosion barrier with intact internals. The probability is zero except for a single point with a probability of 0.118 at the 4.07 m/s PGV level and 90% RST. The TAD-bearing waste package with intact internals will remain undamaged for seismic events at or below the 2.44 m/s PGV level or for simulations with an RST at or above the 100% level. This result implies that only the most extreme, low probability ground motions can damage the TAD-bearing waste package with intact internals. Since the probability of a ground motion at or greater than the 2.44 m/s PGV level is very small (see the bounded hazard curve in Figure 2.3.4-18), the TAD-bearing waste package is expected to remain undamaged during this period.

Conditional Probability Distribution for Nonzero Damaged Area—When damage does occur at the 4.07 m/s PGV level and 90% RST, a gamma distribution provides a reasonable representation of the conditional probability distribution for nonzero damaged areas. The mean and standard deviation for the gamma distribution, 0.00408 m^2 and 0.00130 m^2, respectively, are defined by the results from the structural response calculations for conditional damaged area (SNL 2007c, Section 6.5.1.3). Figure 2.3.4-68 is a plot that shows the agreement between the quantiles of the calculated values of the nonzero damaged area and the corresponding quantiles on a gamma distribution. If the agreement were exact, all points would lie on the diagonal line in Figure 2.3.4-68. Figure 2.3.4-68 is often called a quantile-quantile plot or more simply a Q-Q plot. The nonzero damaged area in Figure 2.3.4-68 is the area on the surface of the outer corrosion barrier that exceeds the RST for initiation of potential stress corrosion cracking. This area is substantially greater than the transport area through the crack network because transport is restricted to the throat area of the cracks within the damaged area, as discussed in Section 2.3.4.5.1.4.1.

The abstraction for TSPA must represent the conditional damaged area for the full range of PGV levels and RST values, rather than at the single point (4.07 m/s PGV level, 90% RST) shown in Figure 2.3.4-68. It is not possible to extrapolate the conditional damage at this single point to the range of PGV and RST values for TSPA. In this particular case, the single point results are conservative for all values of PGV less than 4.07 m/s and all values of the RST greater than 90%. In addition, the magnitude of the conditional damaged area is extremely small in comparison to the

cylindrical surface area of the TAD-bearing waste package, which is approximately 40 m^2. It is then reasonable to use the conditional damage at 4.07 m/s and 90% RST for all values of PGV and RST in TSPA.

The time dependent thickness of the outer corrosion barrier is not incorporated into the damage abstraction for the TAD-bearing waste package with intact internals. The 23-mm-thick outer corrosion barrier corresponds to a thickness reduction of 2.4 mm from the initial outer corrosion barrier thickness of 25.4 mm. The abstraction for the 23-mm-thick outer corrosion barrier provides a reasonable bound for damaged area for several hundred thousand years after repository closure, based on the estimated corrosion time for a thickness reduction of 2.4 mm (SNL 2007c, Section 6.5.1.2).

The finite element models for the waste package are based on the spatially averaged thickness of the outer corrosion barrier because the weakening of components due to general corrosion can be approximated by uniform thinning of component dimensions in the simulations (SNL 2007b, Assumption 5.13). While surface imperfections, residual stresses from welding, and local chemical environments may result in variable corrosion rates on the outer corrosion barrier, the spatially averaged thickness is most relevant to the overall structural response of the waste package during impacts with the emplacement pallet. The analyses model the occurrence of multiple impacts that are spatially distributed, so spatially averaged thickness provides an appropriate measure of structural deformation and damaged area. For example, the damaged area from the kinematic response of the waste package is dominated by waste package-to-pallet impacts. These impacts involve contact of the pallet with a significant area on the surface of the waste package, thereby averaging the impact loads across regions with multiple outer corrosion barrier thicknesses due to nonuniform corrosion. If rubble surrounds the waste package, then the seismic loads are spread over the whole surface of the waste package, again providing a mechanism to average the loads over the surface of the waste package.

The abstraction for the 23-mm-thick outer corrosion barrier is anticipated to provide a reasonable approximation to damaged area for hundreds of thousands of years after repository closure because the initial thickness of the outer corrosion barrier is 25.4 mm and because the mean time for thinning of the outer corrosion barrier from 25.4 mm to 23 mm is 340,000 years, based on the estimate in Section 2.3.4.5.1.3.6.

2.3.4.5.2.1.4.2 Damage and Rupture Abstractions for the Codisposal Waste Package with Intact Internals and 23-mm-thick Outer Corrosion Barrier

Probability of Rupture—The probability of rupture for the codisposal waste package with a 23-mm-thick outer corrosion barrier and intact internals for single or multiple impacts is zero. The structural response calculations for kinematic response at the 0.4 m/s, 1.05 m/s, 2.44 m/s, and 4.07 m/s PGV levels demonstrate that the strain in the outer corrosion barrier from a single impact is always below the ultimate tensile strain for Alloy 22 (SNL 2007c, Section 6.6.1.1). Consideration of multiple impacts to a codisposal waste package with intact internals does not change the probability of rupture for intact internals (SNL 2007c, Section 6.6.1.1). In particular, the potential for damage to accumulate from multiple impacts that severely distort the outer

corrosion barrier does not occur with intact internals, so the probability of rupture from multiple seismic events is judged to be zero with intact internals.

Probability of Nonzero Damaged Area—The kinematic analyses for the codisposal waste package with a 23-mm-thick outer corrosion barrier and intact internals provide the basic data to define the probability of nonzero damage (SNL 2007c, Section 6.6.1.2). However, these data have been modified at the 0.4 m/s PGV level to reflect the fact that the kinematic calculations produce larger for damaged areas than the single waste package calculations. In this situation, the kinematic methodology will overestimate the probability of nonzero damaged area at the 0.4 m/s PGV level.

A number of calculations were performed to investigate the potential conservatism in the probability of nonzero damage from the kinematic approach at the 0.4 m/s PGV level (SNL 2007b, Section 7.3.1.1.2). The results, which are summarized in Section 2.3.4.5.2.1.3.3, include the case of a single codisposal waste package with 17-mm-thick outer corrosion barrier and degraded internals. The results for the case with degraded internals are applicable to the codisposal waste package with intact internals because the results for the 17-mm-thick outer corrosion barrier with degraded internals should have a greater probability of nonzero damaged area relative to the results for a 23-mm-thick outer corrosion barrier with intact internals (SNL 2007c, Section 6.6.1.2).

As discussed in Section 2.3.4.5.2.1.3.3 (SNL 2007c, Section 6.6.1.2), the calculations with a single codisposal waste package provide a more accurate approach for calculating the damaged area than the kinematic approach, because of the following: (1) the finite element model for a single waste package provides a more direct representation of the structural stiffness of the waste package (in comparison to the coarser kinematic representation); and (2) the finite element model integrates the effects of multiple impacts through the stress and strain in individual elements, rather than by linear addition of damage from separate impacts in the kinematic approach. Since the single waste package calculations are more accurate, the probability of nonzero damaged area from the kinematic calculations at the 0.4 m/s PGV level has been reinterpreted. Table 2.3.4-30 presents the revised probabilities at the 0.4 m/s PGV level, based on this reinterpretation.

Conditional Probability Distributions for Nonzero Damaged Area—Figure 2.3.4-69 presents a Q-Q plot for a gamma distribution versus the conditional damaged areas at the 1.05 m/s PGV level for the 90% RST. Gamma distributions provide a representation of the conditional (nonzero) damaged areas at the 1.05 m/s PGV level, as well as for the 0.4 m/s, 2.44 m/s, and 4.07 m/s PGV levels (SNL 2007c, Figures 6-28, 6-30, and 6-31, which are not shown here). The gamma distribution provides an excellent fit to the data with only two parameters-the mean and the standard deviation-that are directly calculated from the computational results. Normal, log-normal, gamma, and Weibull distributions were also evaluated as alternate conceptual models to represent the nonzero damaged area. Based on these results, gamma distributions are selected as the probability distribution for conditional damaged areas on the codisposal waste package with intact internals (SNL 2007c, Section 6.6.1.3).

The abstraction for TSPA must represent the response for intermediate values of PGV, for intermediate of values for RST, and for the spatially averaged thickness of the outer corrosion barrier at the time of the seismic event. Two quadratic functions in PGV, with coefficients that are linear functions of RST, provide excellent fits to the mean of the damaged area and to the standard

deviation of the damaged areas at all PGV levels for RST between 90% and 100%. Simpler linear functions of the RST define the fits for the mean and standard deviation at all PGV levels and for RST levels between 100% and 105%. Figure 2.3.4-70 presents a comparison of the 1st, 5th, 50th, 95th, and 99th percentiles of the resulting gamma distributions against the conditional damaged areas as a function of PGV at the 90% RST. The quadratic fits provide an excellent representation of the conditional damaged areas at all PGV levels.

The time dependent thickness of the outer corrosion barrier is not incorporated into the damage abstraction for the codisposal waste package with intact internals. The data in Figures 2.3.4-69 and 2.3.4-70 are for a 23-mm-thick outer corrosion barrier, which corresponds to a thickness reduction of 2.4 mm from the initial outer corrosion barrier thickness of 25.4 mm. The abstraction for the 23-mm-thick outer corrosion barrier is anticipated to provide a reasonable approximation to damaged area for hundreds of thousands of years after repository closure, based on the discussion in Section 2.3.4.5.1.3.6.

Finally, the damaged area from multiple seismic events is defined as the sum of the damaged areas from the individual seismic events. This approach maximizes the total damaged area because: (1) an impact that is adjacent to an area with plastic deformation from a previous impact may relieve the preexisting residual stress in the deformed area; and (2) the summation of damaged areas from separate events ignores the potential for multiple impacts to the same location. In this situation, linear summation of the damaged area overestimates the accumulation of residual stress (SNL 2007c, Section 6.6.3).

2.3.4.5.2.1.4.3 Damage and Rupture Abstractions for the Codisposal Waste Package with Degraded Internals and 17-mm-thick Outer Corrosion Barrier

Probability of Rupture—The probability of rupture for the codisposal waste package with degraded internals is zero for a single waste package-to-pallet impact. The structural response calculations for kinematic response at the 0.4 m/s, 1.05 m/s, 2.44 m/s, and 4.07 m/s PGV levels demonstrate that the strain in the outer corrosion barrier is always below the ultimate tensile strain for Alloy 22 (SNL 2007c, Section 6.6.2.1). However, severe impacts have the potential to cause severe deformation that may accumulate from subsequent impacts during a single ground motion, or during subsequent seismic events. The methodology for assessing rupture of the outer corrosion barrier from multiple, severe impacts is described in Section 2.3.4.5.2.1.3.2 and in *Seismic Consequence Abstraction* (SNL 2007c, Section 6.6.2.1).

For the codisposal waste package with degraded internals, the degree of deformation from waste package-to-pallet impacts during a single ground motion was used to define the probability of no rupture, the probability of incipient rupture, and the probability of (immediate) rupture (SNL 2007c, Section 6.6.2.1). In effect, rupture is represented as a two step process where severe deformation from a first seismic event makes the package susceptible to rupture during a subsequent severe impact. The probability of incipient rupture defines the initial change from an unruptured state to a condition that can rupture during a subsequent severe impact. The kinematic response at the 0.4 m/s, 1.05 m/s, 2.44 m/s and 4.07 m/s PGV levels for the codisposal waste package with degraded internals (SNL 2007b, Section 6.3.2.1.2) has been assessed for the degree of deformation and the associated rupture probabilities (SNL 2007b, Section 6.3.3.2). The probabilities of incipient and

(immediate) rupture are almost identical for the 17-mm-thick and the 23-mm-thick outer corrosion barriers for each PGV level. The TSPA abstraction is based on the average of the probabilities for the 23-mm-thick outer corrosion barrier and the 17-mm-thick outer corrosion barrier, as shown in Table 2.3.4-31.

The data in Table 2.3.4-31 for incipient rupture and immediate rupture are represented in TSPA as a power law function of the form $a(\text{PGV-V}_0)^b$, where a and b are constants and V_0 is the PGV value at which the power law goes to zero. Figure 2.3.4-71 shows that there is excellent agreement between the probability data and the resulting power law functions for incipient rupture and (immediate) rupture as functions of PGV.

Probability of Nonzero Damaged Area—The kinematic analyses for the codisposal waste package with a 17-mm-thick outer corrosion barrier and degraded internals provide the basic data to define the probability of nonzero damage (SNL 2007c, Sections 6.5 and 6.5.2). However, these data have been modified at the 0.4 m/s PGV level to reflect the fact that single waste package calculations produce more accurate results at this PGV level than the kinematic calculations. The probability of nonzero damage for the TAD-bearing waste package with degraded internals is similar to the probability of nonzero damage for the codisposal waste package with degraded internals (SNL 2007, Sections 6.5.2.2 and 6.6.2.2).

A number of calculations were performed to investigate the potential conservatism in the probability of nonzero damage from the kinematic approach at the 0.4 m/s PGV level (SNL 2007c, Section 6.6.2.2). The results from the kinematic calculations at the 0.4 m/s PGV level demonstrate that the response of an individual waste package is independent of the adjacent packages for many realizations (SNL 2007c, Section 6.6.2.2). For these realizations, it is possible to perform structural response calculations for a single waste package with a fine finite element mesh, thereby avoiding the kinematic analyses and associated damage catalogs. In this case, the damaged area can be determined directly from the finite element mesh. The computational model for the single waste package calculations is identical with the detailed finite-element representation that supports the kinematic approach (Section 2.3.4.5.2.1.3.3, subsection "Validation of the Kinematic Model to Detailed, Single Canister Deformable Models").

Four single package calculations were performed for the codisposal waste package with 17 mm-thick outer corrosion barrier and degraded internals. Realizations 3 and 4 were selected because they have the greatest damaged areas without any waste package-to-drip shield impacts and without any impacts with adjacent waste packages (SNL 2007b, Section 7.3.1.1.2). Table 2.3.4-32 compares the damaged areas for the kinematic analysis and for the four single waste package calculations. A comparison of these results clearly indicates the conservatism of the kinematic approach for the waste packages. The single waste package model has zero damage for all kinematic damaged areas less than 0.057 m^2.

The calculations with a single waste package provide a more accurate approach for calculating the damaged area than the kinematic approach, as discussed in the previous subsection. Since the single waste package calculations are more accurate, the probability of nonzero damaged area from the kinematic calculations at the 0.4 m/s PGV level has been reinterpreted, based on the results in Table 2.3.4-32. Table 2.3.4-33 presents the revised probabilities at the 0.4 m/s PGV level, based on

this reinterpretation. These revised probabilities then form the basis for a linear extrapolation to the zero intercept for the probability of damaged area, which occurs at the 0.219 m/s PGV level.

Conditional Probability Distributions for Nonzero Damaged Area—Figure 2.3.4-72 presents a Q-Q plot for a gamma distribution versus the conditional damaged areas at the 1.05 m/s PGV level for the 90% RST. Gamma distributions provide an excellent representation to the conditional (nonzero) damaged areas at the 1.05 m/s PGV level, as well as for the 0.4 m/s, 2.44 m/s, and 4.07 m/s PGV levels (SNL 2007c, Figures 6-40, 6-42, and 6-43, which are not shown here). The gamma distribution provides an excellent fit to the data with only two parameters—the mean and the standard deviation—that are directly calculated from the computational results. Normal, log-normal, and Weibull distributions were also evaluated as alternate conceptual models to represent the nonzero damaged area. Based on these results, gamma distributions are selected as the probability distribution for conditional damaged areas on the codisposal waste package with degraded internals. The conditional damaged area for the TAD-bearing waste package with degraded internals is similar to the conditional damaged area for the codisposal waste package with degraded internals (SNL 2007, Sections 6.5.2.3 and 6.6.2.3).

The abstraction for TSPA must represent the response for intermediate values of PGV, for intermediate values for RST, and for the spatially averaged thickness of the outer corrosion barrier at the time of the seismic event. Two quadratic functions in PGV, with coefficients that are linear functions of RST, provide excellent fits to the mean of the damaged area and to the standard deviation of the damaged areas at all PGV levels and at all RST levels. Figure 2.3.4-73 presents a comparison of the 1st, 5th, 50th, 95th, and 99th percentiles of the resulting gamma distributions against the conditional damaged areas as a function of PGV for the 90% RST. The quadratic fits provide an excellent representation of the conditional damaged areas at all PGV levels.

The spatially averaged thickness of the outer corrosion barrier is a time-dependent (general corrosion) parameter that is predicted by other elements of the TSPA calculations. The conditional damaged area corresponding to this average outer corrosion barrier thickness is calculated by linear interpolation, if the outer corrosion barrier thickness is between 17 mm and 23 mm. The damaged area is conservatively set equal to the value at 23 mm, if the average outer corrosion barrier thickness is greater than 23 mm. The damaged area is calculated by linear extrapolation, if the thickness is less than 17 mm, using the data at 17 mm and 23 mm to define the slope for the linear extrapolation. The extrapolation is not anticipated to have a significant effect on TSPA because the spatially averaged thickness of the outer corrosion barrier will rarely be below 17-mm-thick, even at 1 million years after repository closure, as shown in Section 2.3.4.5.1.3.6.

Finally, the damaged area from multiple seismic events is defined as the sum of the damaged areas from the individual seismic events. This approach maximizes total damaged area because: (1) an impact that is adjacent to an area with plastic deformation from a previous impact may relieve the preexisting residual stress in the deformed area; and (2) the summation of damaged areas from separate events ignores the potential for multiple impacts to the same location. In this situation, linear summation of the damaged area overestimates the accumulation of residual stress (SNL 2007c, Section 6.6.3).

2.3.4.5.2.2 Drip Shield Damage in Response to Vibratory Ground Motion

[NUREG-1804, Section 2.2.1.3.2.3: AC 1(1) to (4), AC 2, AC 3(1) to (3), AC 4, AC 5(2), (3)]

As described in Section 2.3.4.4.8, rockfall and rubble accumulation may occur in the emplacement drifts. The size distribution and amount of rockfall depend on the rock type (lithophysal or nonlithophysal rock) and the PGV level of the vibratory motion. The rock blocks will impact the drip shield and, eventually, partially or completely fill the free space around the drip shield. In the lithophysal units, the static loading from rubble accumulation and the dynamic amplification of the rubble load during a seismic event may generate plastic deformation and damaged areas on the drip shield. In the nonlithophysal unit, rock volume accumulates more slowly than in lithophysal units, so rock blocks dislodged by vibratory motion may impact the drip shield. These impacts may cause denting and damaged area on the plates or, in the case of very large blocks, tensile rupture of the plates. Damaged areas are defined as regions in which the residual tensile stresses resulting from permanent deformation exceed the RST for the Titanium Grade 7 drip shield plates and can potentially lead to a network of stress corrosion cracks through the plates.

This section summarizes structural analyses, presented in *Mechanical Assessment of Degraded Waste Packages and Drip Shields Subject to Vibratory Ground Motion* (SNL 2007b, Section 6.4), of potential damage to the drip shield resulting from the static rubble load from degrading emplacement drifts, from the dynamic amplification of the rubble load occurring during vibratory ground motion, and from rockfall impacts to the drip shield. Drip shields may also be impacted by waste packages during vibratory motion (SNL 2007b, Section 6.4.5). The effect of this impact has been excluded from TSPA based on low consequence (FEP 2.1.03.07.0B, Mechanical impact on drip shield, Table 2.2-5). Further discussion of waste package-to-drip shield impacts is given in Section 2.3.4.5.3.1.

The damaged area as a function of the PGV of the ground motion provides the basis for the drip shield damage abstractions that are documented in *Seismic Consequence Abstraction* (SNL 2007c, Section 6.10). However, these models are not included in the TSPA (excluded FEP 2.1.03.10.0B, Advection of liquids and solids through cracks in the drip shield, Table 2.2-5). The discussion of the damaged area of the drip shield plates is provided here as background information in support of the excluded FEP justification.

2.3.4.5.2.2.1 Conceptual Description of Analysis for Damage to Drip Shield from Vibratory Ground Motion

Three-dimensional finite difference structural analyses using the FLAC3D program are conducted to determine drip shield plate damage and tensile tearing potential for the lithophysal and nonlithophysal zones.

In the lithophysal zones, the potential for damaged area and rupture of the drip shield plates is analyzed for the following:

- A range of three thicknesses of the drip shield plates and framework to take into account future states of general corrosion thinning
- The rockfall rubble load on the drip shield
- The vertical component of peak ground acceleration for vibratory ground motion.

Rubble loads for lithophysal rock masses provide an upper bound to rubble loading in the nonlithophysal rock mass (SNL 2007c, Section 6.9). Since the lithophysal rock mass is weaker than the nonlithophysal rock mass, the response of the lithophysal units gives the maximum possible rubble volume and thus defines an upper bound for the rubble load in the nonlithophysal units (SNL 2007c, Section 6.7.2.1). Rockfall in the lithophysal zones (SNL 2007c, Section 6.10.1.6) can cause damaged areas on the drip shield (SNL 2007c, Section 6.10.1.3) and can cause buckling of the drip shield sidewalls and failure of the drip shield plates. These latter processes are described by the fragility curves in Section 2.3.4.5.3. These abstractions of drip shield damage encompass the full range of response for the drip shield to seismically induced rockfall in the lithophysal units.

In the nonlithophysal zones, rock blocks can impact the drip shield in an unfilled or partially filled drift (SNL 2007c, Section 6.10). Block impacts may result in damaged areas on the drip shield plates and, in extreme cases, may result in tearing or rupture of the plates and failure of the axial stiffeners beneath the crown of the drip shield. The damaged areas and potential for plate or stiffener failure are analyzed as a function of the thickness of the drip shield plates and framework and for a range of rock block impact energy.

2.3.4.5.2.2.2 Data and Data Uncertainty for Analysis of Damage to Drip Shield from Vibratory Ground Motion

Lithophysal Zone—In the lithophysal zone, the rock rubble loading and corrosion thinning dominate the potential damage mechanisms to the drip shield. The primary input data of importance for damage assessment includes the following:

- Elastic and strength properties and tensile rupture failure criteria for Titanium Grade 7 plates and Grade 29 framework
- Corrosion thinning (i.e., thickness) of the drip shield plates and framework
- Static and dynamic rock rubble loading as a function of ground motion PGV (or peak ground acceleration) level.

Nonlithophysal Zone—In the nonlithophysal zone, in addition to rock rubble load, rock block impacts are of importance. Here, the additional input data of importance includes the following:

- Rock block sizes and impact energies for the nonlithophysal rock mass.

2.3.4.5.2.2.2.1 Material Properties and Failure Criteria for Titanium Grade 7 and Grade 29

The elastic and strength material properties for Titanium Grade 7 plates and the Titanium Grade 29 framework are provided in Table 2.3.4-28. The temperature dependence of Titanium Grade 7 and Grade 29 material properties are discussed in Section 2.3.4.5.1.3.1. The RST for Titanium Grade 7 is set to the bounding value of 80% of its yield strength (SNL 2007a, Section 6.8.3.1.3).

2.3.4.5.2.2.2.2 Corrosion Thinning of Drip Shield Plates and Framework

The uncertainty in the impact of general corrosion on the damage and rupture potential of the drip shield is addressed by conducting analyses for a wide range of plate and framework corrosion thinning. Analyses are conducted for 0 mm (as-installed), 5 mm, and 10 mm of uniform corrosion thinning for all drip shield components. These thickness reductions span a wide range of drip shield response, from an intact state to a highly degraded state as described in Section 2.3.4.5.1.3.6.

2.3.4.5.2.2.2.3 Rock Rubble Load

The uncertainty in the rubble rock load for a completely collapsed drift is derived from six realizations of potential rockfall geometry in the lithophysal unit as described in SNL 2007b, Section 6.4.3.2.2.2. The rock rubble loads for partially filled drifts is determined from the fraction of rubble filling the drift at the time of the seismic event (Section 2.3.4.4.8). The ratio of the accumulated rockfall volume at any given time to the maximum rockfall volume for a completely collapsed drift is multiplied by the maximum rubble load for a fully collapsed drift to determine the load for the partially filled drift. The volume of rock rubble produced by a seismic event is a function of the PGV of the vibratory ground motion.

The estimate of the lithophysal rubble volume is based on a series of 15 discontinuum UDEC calculations of rockfall in the lithophysal rock mass (BSC 2004a, Section 6.4.2). Uncertainty in the lithophysal rock strength and ground motion characteristics used as input to the UDEC calculations was propagated into the models by use of GoldSim to perform a Latin Hypercube sampling of the lithophysal rock strength category (Section 2.3.4.5.4.2.1) and ground motion number. The rubble volume can accumulate to the maximum height as multiple seismic events occur over time. The maximum height to which the drift can collapse is a function of the bulking factor of the rubble. Uncertainty in the estimate of rock rubble height (and thus the static rubble load to the drip shield) for a given rockfall volume is addressed through use of a large range (0.1 to 0.4) in the assumed bulking factor for the rock rubble as described in Section 2.3.4.4.8.3.1.

2.3.4.5.2.2.2.4 Rock Block Size in Nonlithophysal Zone

The uncertainty in detached rock block size in the nonlithophysal zone was determined from three-dimensional 3DEC parametric analyses of rockfall resulting from vibratory ground motions (Section 2.3.4.4.4). Rockfall calculations for the nonlithophysal units have been performed for ground motions at the 0.4 m/s, 1.05 m/s, 2.44 m/s, and 5.35 m/s PGV levels. These calculations were completed prior to the development of the 4.07 m/s bound to the ground motion PGV. Therefore, rockfall calculations were performed for a PGV level (5.35 m/s) exceeding the bounding ground motion level. There are a total of 50 rockfall calculations at each of the 1.05 m/s and

2.44 m/s PGV levels, and a total of 44 rockfall calculations at the 5.35 m/s PGV level. Each of these PGV levels is represented by 15 sets of ground motion time histories (Section 2.3.4.3.2.4). There are a total of 32 rockfall calculations at the 0.4 m/s PGV level. The rockfall calculations are described in detail in the *Drift Degradation Analysis* report (BSC 2004a, Sections 6.3.1.2.3 through 6.3.1.2.6).

The 3DEC model calculations for nonlithophysal units generated a series of rock blocks that impact the drip shield at varying locations and times over a 21.74-m-long section of an emplacement drift. The basic stochastic description of the rock mass fracture geometry employed for the 3DEC model was derived from a set of 105 different synthetic fracture patterns within a cube of rock mass 100 m on a side. These 105 fracture patterns represent the range of fracture geometries expected in the nonlithophysal unit within the repository host horizon SNL 2007c, Section 8.2). The synthetic fracture patterns in this cube were developed from the FracMan fracture modeling software and were based on fracture geometry data obtained from full periphery geologic fracture maps developed during construction of the ESF and ECRB Cross-Drift tunnels. A Latin Hypercube sampling scheme was used for the pairing of ground motion number and fracture modeling regions.

From the total set of detached and impacting rock blocks, a set of seven representative blocks were selected as input for detailed structural calculations. The selection of representative rocks is based on their kinetic energy since the impact energy of a rock block should provide a direct correlation with damaged area or failure of the drip shield plates from tearing. The impact energies associated with the selected rocks correspond to the 99.9th, 99th, 90th, 70th, 40th, and 20th percentiles of block impact energies for the 1.05 m/s PGV level (Table 2.3.4-34). A seventh block that corresponds to the maximum impact energy (determined at the 5.35 m/s PGV level) was added to ensure that the selected rocks encompass all significant impacts from the 0.4 m/s to 5.35 m/s PGV levels. The maximum PGV level for the 10^{-8} annual exceedance frequency is 4.07 m/s, so the kinetic energy associated with the seventh block is beyond the confines of the TSPA.

2.3.4.5.2.2.3 Model and Model Uncertainty for Analysis of Damage to Drip Shield from Vibratory Ground Motion

A series of three-dimensional finite-difference structural calculations using the FLAC3D program were used to examine the deformation and residual tensile stress induced in the drip shield plates and framework in response to both static and dynamically amplified rubble loading in the lithophysal zone and to rock block impact loading in the nonlithophysal zone.

2.3.4.5.2.2.3.1 Damaged Area Results for the Lithophysal Zone

This section discusses the potential for the static load from lithophysal rubble and the dynamic load from vibratory ground motion to form damaged areas on the drip shield plates in the lithophysal zone. The probability of tensile tearing of plates in the lithophysal zone is addressed in the fragility analyses presented in Section 2.3.4.5.3. As described previously, advective flow of liquids through the drip shield has been excluded from the TSPA due to low consequence (excluded FEP 2.1.03.10.0B, Advection of liquids and solids through cracks in the drip shield, Table 2.2-5). While the TSPA does not include advective flow through potential crack networks on the drip shield, the computational results provide a model for damaged area on the drip shield plates. This section therefore describes the damage abstraction for the drip shield plates in the lithophysal zones.

The potential source of damaged area on the drip shield plates in the lithophysal zone is based on plastic deformation and exceedance of the RST (80% of yield stress for Titanium Grade 7) as a result of static rock rubble loading and possible amplification of this load from the vertical peak ground acceleration during vibratory ground motion (SNL 2007c, Section 6.10). The potential for collapse of the drip shield framework or rupture of the drip shield plates under these loading conditions is described in separate fragility analyses presented in Section 2.3.4.5.3, and is not considered further here.

A series of three-dimensional finite-difference calculations were used to examine the deformation and residual stress distribution in the drip shield plates as a function of plate thickness and external load (SNL 2007b, Section 6.4.3.1). The emphasis in this approach is on the crown plates, rather than the plates on the sides of the drip shield, because seepage through the crown plates may fall directly on the waste package, while seepage through the sides of the drip shield is expected to flow down the sides of the drip shield rather than drip directly onto the waste package. Three plate thicknesses were examined representing intact and highly degraded states: 15 mm (no corrosion thinning), 10 mm (5 mm corrosion thinning), and 5 mm (10 mm corrosion thinning). The mechanical response of a symmetrical section of a drip shield crown plate was determined that included the area between two bulkheads, the middle stiffener and the shoulder (where the crown attaches to the legs) of the drip shield (Figure 2.3.4-74). Using symmetry of the segment geometry with respect to the vertical plane perpendicular to the drip shield axis, located half-way between the stiffeners, and symmetry of loading, only half of the segment was analyzed. All of the presented results are for half of the segment between the bulkheads, middle stiffener and the shoulder. To obtain the "damaged area" for the entire drip shield, the results for the symmetric section are multiplied by 20 since there are five bulkheads in a drip shield and the region modeled represents one-fourth of the region between two bulkheads (Figure 1.3.4-15).

Because of uncertainty in the distribution of rubble load along the drip shield (BSC 2004a, Section 6.4.2.5.1) and the fact that only one segment was considered, the analysis was carried out for two sets of boundary conditions. In one case (case 1), the plate boundaries along the middle stiffener and the bulkhead are considered fixed (for both translation and rotation). In the other case (case 2), those boundaries are allowed to move laterally, but the rotation is fixed. These two cases bound the resulting damage estimates (SNL 2007b, Section 6.4.3).

To establish the relationship between the applied rubble load and damage (i.e., the area of stress corrosion cracking), vertical load was applied uniformly across the crown of the drip shield (BSC 2004a, Section 6.4.2.5.1) and those areas exceeding the RST for Titanium Grade 7 determined (SNL 2007b, Section 6.4.3). The average pressure applied to the drip shield crown was increased incrementally from less than 500 kPa until ultimate rupture of the drip shield plates occurred for each plate thickness. The purpose of this analysis is to define the relationship of applied pressure to damaged area; the pressure was raised to ultimate plate tensile rupture to define damage over the complete range of plate response including failure. At each load increment, equilibrium is achieved, and the damaged area determined as the total area of the elements on the inner and outer surfaces of the drip shield crown plate with the major principal tensile stress greater than the RST of 80% of the yield strength of Titanium Grade 7 at 60°C (Section 2.3.4.5.1.3.2). If damaged areas on the inner and outer surfaces overlap, they should not be counted twice. However, for this analysis, the overlap is not considered and the damage area is the sum of the areas on the inner and outer surfaces, irrespective of their relative geometrical position. Although the reported damaged area

overestimates the actual damage area, the overestimate is not great for a significant portion of the load range, while bending, which causes tension on one side and compression on the other side of the plates, is the dominant mode of deformation (SNL 2007, Section 6.10.1.3). The overestimate of damage increases (but never exceeds 100%) when the plate enters a failure mode and the membrane forces become dominant.

The resulting total damage area, given as a function of the applied rubble pressure, is summarized in Figure 2.3.4-75 for three thicknesses of the drip shield plate (15 mm, 10 mm, and 5 mm), where the initial plate thickness is 15 mm. From this figure, the applied pressure at rupture can be seen as the vertical asymptote of each curve. The results for both model boundary condition assumptions are shown, indicating only a minor difference in damaged area and limit load for the two cases.

The relationship of damaged area to applied pressure, given in Figure 2.3.4-75, can be used to determine the damage to the drip shield at the time of a seismic event. The dynamic rubble pressure during a seismic event has two components: the static load resulting from the accumulation of rubble on the drip shield, and a dynamic amplification resulting from the peak vertical acceleration of the ground motion. The static rubble load is related to the fraction of the drift that is filled and the accumulated rubble volume. This accumulated rubble volume is a function of the number and intensity of the vibratory ground motion events that have occurred as well as the lithophysal rock strength category (Section 2.3.4.4.8). The total rubble pressure (*Ptotal*) is the sum of the static vertical pressure (*Pstatic*), which is a result of the weight of the rubble on the drip shield and the dynamic amplification resulting from the peak vertical ground acceleration.

The damaged area for the plate thickness at the time of the seismic event in the TSPA is determined by interpolation on the data presented in Figure 2.3.4-75, based on the total dynamic load for the seismic event.

The bounded hazard curve (Section 2.3.4.3.3.4) defines the horizontal PGV for each seismic event, rather than the vertical component of peak ground acceleration. Since this analysis utilizes the vertical component of peak ground acceleration for drip shield damage and stability calculations, its relationship to the peak horizontal ground velocity (the basis of the bounded hazard curve) must be defined. The peak vertical acceleration is available for each of the 17 ground motions at the 1.05 m/s, 2.44 m/s, and 5.35 m/s peak horizontal ground velocity levels. Least-squares regression analysis for the vertical component of peak ground acceleration as a function of the peak horizontal ground velocity (PGV) was performed for all of the ground motions (Figure 2.3.4-76).

2.3.4.5.2.2.3.2 Static Rockfall Loads in the Lithophysal Zone

Lithophysal rockfall is expected to vary significantly because of the variability in mechanical properties in the host rock at the repository horizon and because of the variability in the fracture pattern and fracture spacing in the host rock. The resulting variability of rockfall loads from lithophysal rubble has been evaluated with six quasi-static calculations for collapsed drifts in lithophysal rock (BSC 2004a, Appendix P), as shown in Table 2.3.4-35. The basis for selection of rock rubble load distributions is discussed in Section 2.3.4.5.3.2.1.

2.3.4.5.2.2.3.3 Damaged Area Results for the Nonlithophysal Zone

Vibratory ground motions have the potential to dislodge larger rock blocks in the crown and sidewalls of drifts in the nonlithophysal units. These blocks will fall by gravity, may impact the drip shield, and will accumulate around it, eventually covering the drip shield, and precluding further direct impacts to the drip shield. The mechanical response of the drip shield to impact by a rock block could result in damage to the drip shield as a barrier to seepage flow and rockfall directly on the waste package. This section describes the structural response calculations that have been performed to evaluate the mechanical response of intact and degraded drip shields to these impacts.

The technical approach for this analysis and for developing the damaged area model for the drip shield due to large block impacts in the nonlithophysal units is summarized in Figure 2.3.4-77. The methodology for calculation of the rockfall resulting from vibratory ground motion was described in Section 2.3.4.5.2.2.2.4. The output parameters for each calculation include the mass, relative impact velocity, impact location, impact angle, and impact energy associated with each block that strikes the drip shield.

A set of seven representative rock blocks were selected from this suite of calculations that span the full range of impact energies. These rock blocks and their impact velocities were used to conduct detailed three-dimensional structural analyses of the deformation of the drip shield due to impact using FLAC3D. The seven representative blocks include blocks with small impact energies that do minimal or no damage to the drip shield and the block with the maximum impact energy recorded from all simulations. The properties of the seven representative blocks are given in Table 2.3.4-34. This set of damage calculations provides the basis for estimating the response of the drip shield when multiple blocks are shaken loose from the drift boundary during a seismic event. These calculations are used to develop a damage catalog that provides a direct correlation of damaged area or failure of the drip shield by tensile tearing/rupture to block impact energy. Interpolation between these values can be used to define damage for intermediate block impact energies.

The structural response calculations were performed for three states of general corrosion thinning for the drip shield plates and framework: the initial state with 15-mm-thick plates, 5 mm thinning with 10-mm-thick plates, and 10 mm thinning with 5-mm-thick plates. Section 2.3.4.5.1.3.6 describes the approximate time frame associated with these levels of general corrosion thinning. These thickness reductions are uniformly applied to the dimensions of the drip shield plates and the components of the drip shield framework.

Rock block impact is represented as an edge-on impact at the center of the drip shield, with the center of mass of the block directly above the impact point (Figure 2.3.4-78). An edge-on impact at the center of the drip shield crown is reasonable for several reasons. First, seepage through a dent or failed plate at the center of the drip shield is more likely to drip onto the waste package than a dent for a failed plate at the "shoulder" (where the crown meets the vertical side) or side of the drip shield. Second, a corner or side impact will generally create a crease that diverts the flow of seepage toward the side(s) of the drip shield, rather than forming a central depression that could collect seepage. The collection of seepage in a depression is potentially important because the resulting hydrostatic head from the pooled seepage could facilitate advective flow through stress corrosion cracks. Finally, the alignment of the block's center of mass with the impact point maximizes deformation for a given kinetic energy, maximizing the damaged areas in the damage catalogs. Although advective flow of

liquids through the drip shield is excluded from the TSPA (excluded FEP 2.1.03.10.0B, Advection of liquids and solids through cracks in the drip shield, Table 2.2-5), a model has been developed to quantify the damaged areas from rock block impacts.

The damaged area is determined as the area of the drip shield plates that exceeds the RST for Titanium Grade 7 (Section 2.3.4.5.1.2.1). The effective tensile strain criteria for tearing of the plates is taken to be 0.11 (11%) as described in Section 2.3.4.5.1.2.2. This effective tensile tearing/rupture strain is based on the engineering elongation strain of 0.22 (22%) for tensile rupture of Titanium Grade 7 observed in laboratory uniaxial tension testing. As described in Section 2.3.4.5.1.2.2, permanent deformation of the drip shield plates resulting from block impact typically induces a state of biaxial residual tensile stress, with a resulting triaxiality factor of 2 (Section 2.3.4.5.1.4.2). This factor is used to reduce (by a factor of 2) the laboratory tensile elongation to derive the tensile tearing strain of 0.11 (SNL 2007b, Section 6.4.7.3).

The results of the damage calculations, in terms of damaged area, maximum effective strain in the drip shield plates, and maximum stiffener displacement as a function of rock block impact energy for the three plate and framework corrosion thinning assumptions is given in Table 2.3.4-36. The results in this table demonstrate that impacts by rock blocks 1, 2, and 3 may cause plate failure by tensile tearing, while the stiffeners fail only for impact by the maximum rock block observed in all rockfall simulations (block 1). The abstraction for drip shield failure is based on the plastic strain in the plates, rather than plastic strain in the axial stiffeners, because the plates are expected to fail before the stiffeners (SNL 2007c, Section 6.10.2.3).

The results in Table 2.3.4-36 also demonstrate that the maximum stiffener deflections are 0.171 meters (6.7 inches) and 0.204 meters (8.0 inches) for the intact drip shield and for the drip shield with 5-mm thickness reduction in all components, respectively. These values are less than the minimum clearance of 1 foot 2 inches (SNL 2007e, Figure 4-1) for the 5-DHLW/DOE SNF waste package or the clearance of 1 foot 9 inches for the TAD-bearing or Naval waste packages. The drip shield therefore does not collapse onto the waste package for the calculations in Table 2.3.4-36 that ran to completion, and the trend in Table 2.3.4-36 for rock block 1 makes it unlikely that the drip shield collapses onto the waste package for any of the block impacts and drip shield states examined. This conclusion does not mean that the drip shield never collapses onto the waste package. The fragility for the drip shield framework (Section 2.3.4.5.3) defines the probability of drip shield collapse in response to the static and dynamically amplified load from lithophysal rubble, rather than the probability of collapse from individual block impacts.

2.3.4.5.2.2.4 Models for Damage to Drip Shield from Vibratory Ground Motion

2.3.4.5.2.2.4.1 Damaged Area Model for the Lithophysal Zone

This section discusses the model for damaged area on the drip shield plates in response to vibratory ground motion in the lithophysal zones of the repository. This model is not used in the TSPA because advective flow through crack networks on the drip shield is screened out.

The total dynamic load on the drip shield is a function of the fraction of drift filled with accumulated rubble, of the static rockfall load for a completely collapsed drift, and of the vertical component of peak ground acceleration.

The total dynamic load follows a log-normal distribution (SNL 2007c, Section 6.10.1.2). When a seismic event occurs, this log-normal distribution is sampled within TSPA to determine the dynamic load on the drip shield. The value of the mean of this distribution is a function of the PGV level of the seismic event and the fraction of filled drift, *f*, at the time of the event. The value of the standard deviation of this distribution is constant. Once the sampled value of the dynamic load has been determined for a seismic event, the damaged plate area for 5 mm, 10 mm, and 15 mm thick plates is determined by using Table 2.3.4-37 as a lookup table. Table 2.3.4-37 is based on the boundary condition (either case 1 or case 2 as discussed in Section 2.3.4.5.2.2.3.1) that defines the larger value for damaged area at 5 mm, 10 mm, and 15 mm plate thicknesses.

The damaged plate areas for 5 mm, 10 mm, and 15 mm plate thicknesses provide the basis for a linear interpolation that determines the damaged area at the current drip shield plate thickness, *t*, at the time of the seismic event. If *t* is less than 5 mm, then the values at 10 mm and 5 mm are used to extrapolate to the final damaged area. The use of extrapolation is not expected to be a significant factor in TSPA because the plates become increasingly likely to fail (via the drip shield fragility curves) for plate thicknesses less than 5 mm (Section 2.3.4.5.3).

The damaged area from multiple seismic events is defined as the sum of the damaged areas on the drip shield from the individual seismic events. This approach maximizes total damaged area because work hardening of dented or deformed areas on the drip shield plates makes it more difficult to damage these areas during a subsequent event and because the summation of damaged areas from individual events ignores the potential for the physical overlap of damage from multiple events. In this situation, linear summation of damaged area overestimates the accumulation of residual stress.

2.3.4.5.2.2.4.2 Damaged Area Model for the Nonlithophysal Zone

This section discusses the models for damaged area and failure of the drip shield plates in response to impacts of nonlithophysal rock blocks induced by vibratory ground motion. This model is not used in TSPA because advective flow through crack networks on the drip shield is screened out of TSPA and because advective flow through failed plates from rock block impacts has been shown to be of low consequence for dose in TSPA (SNL 2008a, FEP 1.2.03.02.0B, Seismic-induced rockfall damages EBS components).

Probability of Nonzero Damage/Plate Failure—Table 2.3.4-38 presents the probability of nonzero damaged area/plate failure. Note that there is a high probability of nonzero damaged area or plate failure at and above the 1.05 m/s PGV level.

The model represents the probability of nonzero damaged/plate failure for intermediate values of PGV and of the plate thickness. Linear interpolation between the values in Table 2.3.4-38 provides a reasonable method to represent the probability of nonzero damaged area/plate failure as a function of PGV and plate thickness. Damaged area on the plates occurs when the residual stress exceeds the threshold for stress corrosion cracking, and plate failure occurs when the strain in the plate exceeds the ultimate tensile strain for Titanium Grade 7 as described in Section 2.3.4.5.1.2. The probability of nonzero damaged area/plate failure at 0.4 m/s is conservatively used for all PGV values less than 0.4 m/s.

Conditional Probabilities for Damaged States—The 3DEC model that was used for prediction of rockfall for the nonlithophysal rock encompasses 21.75 m of emplacement drift, which corresponds to approximately 4 drip shields. If the drip shield is damaged by multiple block impacts, then each realization may experience one of five states:

- State 1: Damaged areas on 4 drip shields with no plate failure
- State 2: Damaged areas on 3 drip shields and failure of plates on 1 drip shield
- State 3: Damaged areas on 2 drip shields and failure of plates on 2 drip shields
- State 4: Damaged areas on 1 drip shield and failure of plates on 3 drip shields
- State 5: Failure of plates on 4 drip shields.

A sixth state, with 1 drip shield failure and no damaged area, is also encountered. Four realizations have a single rock block that causes 1 drip shield plate failure with no damaged area to the other drip shields. These four cases are combined into State 2 for the conditional probability calculations for the abstraction. Table 2.3.4-39 presents the conditional probabilities of States 1 through 5 as a function of PGV level and plate thickness. These are conditional probabilities because they depend on the probability of having nonzero damage or failure as determined by the probabilities in Table 2.3.4-38.

The model represents the response for intermediate values of PGV and of the plate thickness. Linear interpolation between the values in Table 2.3.4-39 provides a reasonable method to define the conditional probability for the drip shield states as a function of PGV and plate thickness (SNL 2007c, Section 6.10.2.5). If the PGV value is less than 0.40 m/s, then the value at 0.40 m/s should be used because extrapolation of the data in Table 2.3.4-39 could produce unphysical results, with the potential for probabilities that are less than zero. Similarly, if the plate thickness is less than 5 mm, then the values for the 5 mm thickness should be used because extrapolation of the data in Table 2.3.4-39 could produce questionable values.

Conditional Probability Distributions for Nonzero Damaged Areas—Figure 2.3.4-79 is a Q-Q plot for the gamma distribution versus the conditional damaged area at the 2.44 m/s PGV level for the 15 mm thick plate. These damaged areas are the damaged area per rockfall realization and include a factor of 4 to compensate for the quarter symmetry in the structural response model. The values of the mean and standard deviation of the conditional damaged areas, which are the input to the gamma distribution, are shown in Table 2.3.4-40. Gamma distributions provide a very good fit to the conditional (nonzero) damaged areas. Q-Q plots for the gamma distributions versus the conditional damaged areas for the 2.44 m/s PGV level with 10 mm and 5 mm thick plates show similar comparisons to Figure 2.3.4-79, as shown in Figures 6-99 through 6-101 in *Seismic Consequence Abstraction* (SNL 2007c, Section 6.10.2.6). Based on these results, gamma distributions are selected as the probability distribution for conditional damaged areas on the drip shield in response to block impacts in the nonlithophysal units.

The model represents the response for values of PGV between the four PGV levels of 0.4 m/s, 1.05 m/s, 2.44 m/s, and 5.35 m/s. Linear interpolation between the values of the mean and standard deviation of the data in Table 2.3.4-40 provides a convenient way to represent the input parameters for the gamma distribution as a function of PGV. Figure 2.3.4-80 is a typical comparison of the damaged area data across the full range of PGV at the 15 mm plate thicknesses. These figures

indicate that linear interpolation in PGV for the mean and standard deviation provides a reasonable representation (SNL 2007c, Section 6.10.2.7).

The model also represents the response for the full range of values for the plate thickness, from 15 mm to 0 mm. A linear interpolation between the responses at 15 mm, 10 mm, and 5 mm provides a reasonable representation of conditional damaged area as a function of plate thickness. Conditional damaged areas for plate thicknesses less than 5 mm can be based on linear extrapolation of the results at 10 mm and 5 mm.

Damage to the drip shield from rock block impacts in nonlithophysal units will continue until the drip shield plates rupture, as described in this section, or until the drifts in the nonlithophysal units become 50 percent filled with rubble (SNL 2007c, Section 6.10.2.9). The damaged area from multiple seismic events is defined as the sum of the damaged areas from the individual seismic events. The number of drip shields with ruptured plates from multiple seismic events is defined as the sum of the failed drip shields from the individual seismic events. The linear summation of damaged area overestimates the accumulation of residual stress, and maximizes damage area (SNL 2007c, Section 6.10.2.9).

2.3.4.5.3 Drip Shield Fragility

[NUREG-1804, Section 2.2.1.3.2.3: AC 1(1) to (4), AC 2, AC 3(1) to (3), AC 4, AC 5(2), (3)]

2.3.4.5.3.1 Conceptual Description of Drip Shield Fragility

Mechanical failure of the drip shield can occur as a result of the accumulated weight of rock rubble, combined with amplification of this load from the acceleration of subsequent vibratory ground motions. The failure can be characterized as one of two forms shown conceptually in Figure 2.3.4-51: (1) rupture of the drip shield plates; or (2) buckling of the drip shield framework.

Analysis of the probability of plate tearing or framework collapse, both of which alter the mechanical loading on the outer corrosion barrier of the waste package, is described in this section. Integral to this analysis is the continuous action of general corrosion over time, resulting in a long-term thinning and, thus, weakening of the drip shield plates and framework. In the case of the tearing of drip shield plates, the drip shield will lose its ability to divert seepage water away from the waste package. In addition, rock rubble will come into contact with the waste package outer corrosion barrier (Section 2.3.4.5.4). In the case of drip shield framework collapse, the leg(s) buckle near the invert and the framework will collapse directly onto the waste package without significant distortion to the shape of the structure ("Results" in Section 2.3.4.5.3.3.3). Since the drip shield plates are structurally more robust than the framework under the applied loads, they will remain intact after the framework legs buckle, and will retain their water diversion function. In both cases, the waste package outer corrosion barrier will be mechanically loaded by the overlying rock rubble load and will no longer be free to move beneath the drip shield. Mechanical analysis of the waste package loaded by the drip shield or rubble is provided in Section 2.3.4.5.4.

Fragility analysis determines the probability of failure based on the relationship of the ultimate plastic load capacity for drip shield plate tensile tearing or framework collapse to the total dynamic load on the drip shield. The ultimate plastic load capacity is a function of the thickness of the plates

and framework at the time of the seismic event. The analysis for ultimate plastic load capacity is based on quasi-static three-dimensional finite difference structural analyses of the deformations of the drip plates and framework under a range of static rock rubble loads and their amplification from accelerations resulting from vibratory ground motion. The loads from the acceleration are accounted for in a quasi-static fashion through use of an amplification factor based on the peak vertical ground acceleration multiplied times the static gravitational rubble load. An alternative conceptual model of drip shield framework collapse is provided through a companion series of fully dynamic two-dimensional discontinuum calculations (Section 2.3.4.5.3.3.3) in which the time-dependent interaction of the drip shield and rock rubble is simulated explicitly (Section 2.3.4.5.3.3.3). The loads corresponding to collapse of the drip shield derived from these more complex dynamic calculations are compared to the simpler, quasi-static approach, verifying that the simpler approach yields smaller collapse loads than the dynamic calculations. The abstraction of the fragility analysis determines the probability of these failure mechanisms as a function of the PGV of the ground motion.

Additional calculations that complement these fragility analyses were performed to examine the impact of other factors on stability of the drip shield. These factors, described below, are not included in the fragility assessments or in the drip shield plate or framework failure probability abstractions. The reasons for the exclusion of these factors from TSPA are given.

- Analysis of the effects of nonuniform invert settlement due to corrosion of the invert steel structure on drip shield stability when subjected to static rubble loading. Three dimensional finite difference stability assessments (SNL 2007b, Section 6.4.6) of a drip shield with uneven settlement of as much as 25 cm of the two sides was conducted for static rubble loading and for impact by large rock blocks. It was found that the uneven settlement does not result in drip shield overturning or framework buckling as a result of increased stresses. Based on these calculations, nonuniform settlement of the drip shield has been excluded from further consideration in drip shield performance (excluded FEP 2.1.06.05.0B, Mechanical degradation of invert, Table 2.2-5).

- Analysis of the impact of time-dependent deformation mechanisms (creep) of Titanium Grade 7 plates or Grade 29 framework on failure potential. Analyses presented in *Creep Deformation of the Drip Shield* (BSC 2005d) show that the impact of creep on drip shield stability under long-term static load of rubble is not significant (excluded FEP 2.1.07.05.0B, Creep of metallic materials in the drip shield, Table 2.2-5).

- Analysis of the effect of potential waste package impacts on the structural stability of the drip shield framework during high ground motion level shaking. The response of the drip shield to impact of the waste packages on the sides and interior bulkhead supports of the drip shield was investigated by three-dimensional finite element structural simulations (BSC 2005c, Section 5.6.2). These calculations simulated high velocity lateral impact of a waste package against the interior sidewalls of the drip shield as well as high velocity longitudinal impacts to the bulkheads at the crown of the drip shield. These calculations indicate that waste package impacts to the drip shield can be excluded from consideration in drip shield fragility abstractions for the following reasons (SNL 2007c, Section 6.8.5). First, lateral impact of the waste package on the drip shield does not cause catastrophic failure of the drip shield. Second, high velocity longitudinal impacts of the waste package

on the bulkhead support beams exposed on the underside of the crown of the drip shield occur infrequently, only at the 4.07 m/s PGV level (SNL 2007c, Table 6-41). The high velocity longitudinal impacts with the potential to damage the bulkhead support beams occur with much lower probability than the probability of buckling the sidewalls of the drip shield. It follows that the drip shield sidewalls are likely to buckle before longitudinal impacts damage the bulkhead support beams and, after the sidewalls buckle, high velocity longitudinal impacts are eliminated because the waste package can no longer move freely beneath the drip shield.

2.3.4.5.3.2 Data and Data Uncertainty for Drip Shield Fragility

The key input parameters for the fragility analysis are the static load of rockfall on the crown of the drip shield, the vertical component of peak ground acceleration from a seismic event, and the plastic load capacity of the drip shield plate or framework, which is a function of the drip shield structural design, the thickness of the plates and framework, and their material properties.

2.3.4.5.3.2.1 Static Rockfall Rubble Load

The static rockfall rubble load on the crown of the drip shield is a key parameter in the potential for buckling of the drip shield structural framework and in the potential for rupture of the drip shield plates (SNL 2007c, Section 6.8.1). There are two important aspects in estimating the degree and level of uncertainty in rock rubble load on the drip shield. The first is the volume and associated height of rubble (and thus the average magnitude of the applied crown pressure) that lies above the drip shield crown and how this volume is related to vibratory loading. The second is the degree of nonuniformity of load both around the circumference of the drip shield and along its length. The nonuniformity is important in that highly nonuniform loads can lead to stress concentrations and bending moments that need to be accounted for in the structural assessments. The relationship of the volume of rubble to the ground motion level and the occurrence of multiple seismic events was discussed in Section 2.3.4.4.8.

The uncertainty in rubble load applied to the drip shield was addressed by estimating a reasonable maximum static collapse rubble volume for the emplacement drifts (BSC 2004a, Section 6.4.2.5.1). This maximum volume was determined by simulating the complete (100%) collapse of drifts in the lithophysal rock mass using the two-dimensional discontinuum program UDEC as described in Section 2.3.4.4. These analyses simulate the vertical and lateral progression of collapse until the resulting bulked rubble volume eventually "chokes" off further collapse (because the rubble eventually contacts the roof of the drift). The collapse volume and load distribution from complete collapse of emplacement drifts is expected to vary significantly in the lithophysal unit due to the variability in mechanical properties in the host rock at the repository horizon and because of the variability in the fracture pattern and fracture spacing in the host rock. The resulting variability of rockfall loads for complete drift collapse from lithophysal rubble has been evaluated with six calculations for degradation of drifts in lithophysal rock (BSC 2004a, Appendix P4). The load distributions on the drip shield are summarized for 30 segments around the circumference of the drip shield (Figure 2.3.4-43).

To examine uncertainty of the load distribution on the drip shield, two patterns of applied drip shield rubble load, determined from the UDEC analyses, were used in the fragility analysis. The first load

pattern for determining plastic load capacity is based on averaging the results from the six two-dimensional UDEC lithophysal realizations on a segment-by-segment basis around the drip shield. Figure 2.3.4-43 defines the averaged pressure on all segments of the drip shield. These average loads retain the nonuniform character of the loads from the six UDEC realizations.

This averaging process is appropriate because the UDEC calculations are based on a two-dimensional model that does not represent spatial variability in the rubble loading along the length of the drip shield (BSC 2004a, Section 6.4.2.1). This spatial variability will be significant because the typical rubble size of 0.1 to 0.3 meters (BSC 2004a, Section 6.4.1.1) is much less than the 5.8-meter nominal length of the drip shield (Figure 1.3.4-15). This spatial variability may also be significant because the porosity and unconfined compressive strength of the lithophysal rock mass will vary along the emplacement drift, resulting in different rockfall volumes. In this situation, the rockfall load will vary between axial locations on the drip shield, and the average load on each segment provides a reasonable estimate of the effective load on the drip shield with axial variability (SNL 2007c, Section 6.8.3.2). This averaged nonuniform load pattern is referred to as the "mean" load pattern.

The second load pattern is based on rubble Realization 3, which has the maximum average load on the 10 segments on the crown of the drip shield (Table 2.3.4-35). This second load pattern provides a nonuniform load that is biased toward the highest total load on the crown of the drip shield.

The static load from rockfall used in the fragility calculations is based on rubble volume produced in the lithophysal zone because the static lithophysal load is greater than the static load from nonlithophysal rockfall. Rockfall in lithophysal rock has significantly greater volume per cubic meter of drift length (Section 2.3.4.4.8.3.2) than rockfall in nonlithophysal rock because the lithophysal rock is generally weaker than the nonlithophysal rock. The lithophysal rubble therefore has greater static loads than the nonlithophysal rockfall at a given point in time. The load from lithophysal rubble is treated as uniformly distributed over the drip shield plates because the typical particulate sizes in the lithophysal rubble, on the order of 0.1 to 0.3 meters, are less than the typical dimensions of the drip shield plates. For example, the half-span across the crown of the drip shield is approximately 1.3 m (SNL 2007c, Table 4-1, Nominal Width of the Drip Shield, 2,535 mm), much greater than the typical dimensions of rubble particulates.

2.3.4.5.3.2.2 Peak Ground Acceleration

The fragility analysis accounts for the amplification of the static rubble loading during vibratory ground motion. The amplification is based on the vertical component of peak ground acceleration because the vertical load is expected to be directly correlated with buckling of the legs or rupture of the plates forming the crown of the drip shield. In other words, the primary effect of the seismic wave impacting the rubble filled drift will be a transient "spike" in the vertical loads applied to the drip shield components. This viewpoint is confirmed by calculations for lithophysal rockfall loads on the drip shield. These calculations demonstrate that the average loads on the crown are significantly greater than the average loads on the sides of the drip shield (SNL 2007c, Section 6.8.1), indicating that vertical loads are likely to be the critical loads for failure.

The bounded hazard curve (Figure 2.3.4-18) defines the value of horizontal PGV for each seismic event, rather than the vertical component of peak ground acceleration. Since the fragility analysis

utilizes the vertical component of peak ground acceleration for drip shield stability calculations, its relationship to the peak horizontal ground velocity (the basis of the bounded hazard curve) is described in Section 2.3.4.5.2.2.3.1.

2.3.4.5.3.2.3 Plastic Load Capacity of the Drip Shield Plates and Framework

The plastic load capacity of the drip shield plates and framework is a function of the strength of the plates and framework, as well as the nonuniformity of the rockfall loads, as described above. The strength of the plates and framework is a function of their thickness and material properties. The thickness of all drip shield components are reduced as a function of time due to general corrosion processes.

The elastic and strength material properties for Titanium Grade 7 plates and the Titanium Grade 29 framework are provided in Table 2.3.4-28. The uncertainties in the elastic and strength properties are primarily a result of temperature dependence. The temperature dependence of Titanium Grade 7 and Grade 29 are discussed in Section 2.3.4.5.1.3.1. The methodology for dealing with model uncertainty in the morphology of stress corrosion cracks and the crack area for diffusive transport through the Titanium Grade 7 plates is provided in Section 2.3.4.5.1.4.1.

To investigate the impact and uncertainty of general corrosion thinning, structural calculations are performed for a range of thickness reductions for all drip shield components, including the plates and the individual structural members in the framework (SNL 2007b, Section 6.4.3). The thickness of these units is reduced by a constant value of 0 mm (the as-installed state), 5 mm, or 10 mm for these calculations. These three specific thickness reductions encompass the full range of structural response of the drip shield in degraded states. Although the drip shield fragility curves depend on thickness at the time of the seismic event, they do not have any dependence on corrosion rates, which are determined within the TSPA model. The general corrosion rate basis for these thickness reductions was described in Section 2.3.4.5.1.3.6.

The drip shield plates are fabricated from Titanium Grade 7, and the framework is fabricated from Titanium Grade 29. The physical/chemical mechanisms for the general corrosion processes on Titanium Grades 7 and 29 are expected to be similar, although the absolute corrosion rates can be somewhat different (SNL 2007f, Section 6.2[a]). However, this difference is not represented in the calculations, which have equal thickness reductions in all structural elements based on corrosion rates for Grade 29. Equal thickness reduction is a reasonable approach because the buckling or collapse of the framework is insensitive to plate thickness. The framework is observed to fail when a side buckles or collapses (SNL 2007b, Section 6.4.4, particularly Figures 6-60, 6-61, and 6-62). This failure typically occurs at a location close to the base because the physical/chemical mechanisms and the general corrosion processes are similar, and because the data for the ratio of the general corrosion rates for Grade 29 and Grade 7 are less than 1 approximately 50% of the time and greater than 1 approximately 50% of the time (SNL 2007f, paragraph preceding Table 6-8[a] in Section 6.2.2[a]). In addition, the side walls and its stiffeners are thinnest close to the base. The response at the leg base is essentially independent of the plate thickness because the crown of the drip shield remains intact when the sidewalls buckle (SNL 2007b, Section 6.4.4, particularly Figures 6-60, 6-61, and 6-62). In addition, the plastic load capacity of the plates is significantly greater than the capacity of the framework for a given thickness reduction (SNL 2007c, Section 6.8.3.2). These results are confirmed by the dynamic calculations of drip shield response,

which demonstrate that the failure mode for the fragility analysis of the drip shield framework is buckling or collapse of the sidewalls of the drip shield (SNL 2007c, Section 6.8.3.1).

2.3.4.5.3.3 Model and Model Uncertainty for Drip Shield Fragility

The mechanical failure mechanisms for the drip shield plates and drip shield framework are represented as a set of fragility curves which define the probability that the dynamic vertical load is greater than the plastic load capacity of the plates or framework. Within this context, mechanical failure refers to rupture of the drip shield plates or collapse/buckling of the drip shield sidewalls. The fragility curves are based on detailed three-dimensional numerical calculations of the plastic load capacity of the drip shield plates and drip shield framework.

A series of quasi-static three-dimensional and dynamic two-dimensional finite-difference calculations are used to examine the plastic load bearing capacity of the drip shield plates when loaded to the point of ultimate tensile failure (i.e., rupture) (SNL 2007b, Section 6.4.3). These calculations also examine the failure modes of the drip shield framework, such as buckling of the "legs" (sides) and possible snap-through failure of the crown of the drip shield. Based on these calculations, limit load curves are developed which relate the plastic load-bearing capacity of the plates or framework to their thickness. In addition, a limited number of two-dimensional, dynamic simulations that simulate full interaction between the drip shield and surrounding rubble are used to investigate modes of framework collapse and to demonstrate that a quasi-static approach conservatively predicts failure loads in comparison to a fully dynamic approach.

An abstraction, in terms of the probability of plate tearing or framework buckling, can be developed from the plastic load capacity analyses and the applied static and dynamic loading (SNL 2007c, Section 6.8). The average static load from lithophysal rockfall, combined with the peak vertical acceleration from vibratory ground motion, can be compared to the capacity of the plates and framework. If the combined static load from rockfall plus dynamic load from ground motion is greater than the load-bearing capacity, then the structure has failed. Since the peak vertical load varies as a function of PGV level, the results are represented as a probability of failure that is a function of plate thickness and static load at each PGV level. The resulting estimate of probability of mechanical failure for the drip shield plates or drip shield framework is abstracted for use in the TSPA.

2.3.4.5.3.3.1 Ultimate Plastic Load Capacity of the Drip Shield Plates

A three-dimensional finite difference analysis using FLAC3D for the plastic load capacity of the drip shield plates was conducted for a simplified geometry of a drip shield crown plate. This model is the same as that used for investigation of drip shield damaged areas in the lithophysal zones (Section 2.3.4.5.2.2). One half of the plate within one segment between two bulkheads is included in the calculation. Such a reduction in the size of the analyzed domain was done using symmetries of drip shield geometry and rockfall load. The analyzed region of the drip shield crown plate, shown in outline in Figure 2.3.4-74, is bounded by (a) the vertical symmetry plane along the center of the middle stiffener, (b) the vertical plane along the contact between the crown and the legs, (c) the vertical plane perpendicular to the drip shield axis between two bulkheads, and (d) the vertical plane perpendicular to the drip shield axis along the bulkhead.

Three drip shield plate thicknesses were analyzed to establish the impact of general corrosion: 15 mm (the initial thickness), 10 mm (accounting for 5 mm uniform thinning), and 5 mm (accounting for 10 mm uniform thinning). Two sets of mechanical boundary conditions were used to address uncertainty in the load distribution (SNL 2007b, Section 6.4.3.1.2), one case representing the uniform loading case and one representing a nonuniform loading case.

For each loading case, the vertical load was applied over the entire top surface of the plate and increased incrementally until a failure mechanism developed (SNL 2007b, Section 6.4.3.1.2). For each load increment, the equilibrium deformations and stress state of the plate was determined. At a certain load level, the region of the plate between the stiffener and the support over the legs snaps through, when the rupture criteria for Titanium Grade 7 is reached. Criteria based on both accumulated plastic strain and maximum yield stress (SNL 2007b, Section 6.4.3.1.3) were used to determine the plate failure. The plate failure load was considered to be the smallest applied load in which plate failure from either criteria occurred. If the failure criterion is reached anywhere in the modeled plate, it is considered to have failed. This minimum plate failure load defines the ultimate plastic load capacity of the plates.

All plate fragility results are summarized in Figure 2.3.4-81, which shows the drip shield plate failure limit load as a function of plate thickness for the two cases of boundary conditions (SNL 2007b, Section 6.4.3). The two boundary conditions represent uncertainty in load distribution between the neighboring drip shield segments. The results show that the limit loads increase with plate thickness as would be expected. Considering bending stresses only, the limit load is expected to be proportional to the square of the plate thickness. However, the shear and membrane forces result in a relationship between limit load and plate thickness that is nearly linear.

The drip shield fragility results indicate that a high safety margin against plate tearing is evident. As shown in the note to Table 2.3.4-35, the average applied crown rubble pressure is estimated to be 127 kPa. For an intact drip shield (15-mm-thick plate), the plate limit load is approximately 2500 kPa, and approximately 1000 kPa for a 5-mm-thick plate. Thus, even accounting for dynamic load amplification from earthquakes, there is a substantial design margin against tensile rupture of the plates.

2.3.4.5.3.3.2 Ultimate Plastic Load Capacity of the Drip Shield Framework

The plastic load capacity of the drip shield framework was determined from quasi-static numerical analysis in which vertical loading on the drip shield crown is increased incrementally until the structure fails by collapse.

Static Loading from Rockfall Rubble—The limit load of the drip shield framework is a function of the magnitude and distribution of pressure resulting from rock rubble loading as described in Section 2.3.4.5.3.2.1. A series of quasi-static three-dimensional finite difference analyses using FLAC3D were conducted to establish the plastic load limits of the structural framework from the static gravity load of the rubble. Rock rubble pressure is applied along the drip shield surface which was discretized over 30 segments of approximately equal length (Figure 2.3.4-43). The limit load of the drip shield framework was based on two load distributions: (1) rock-load Realization 3, which was selected as the most severe load realization among the six rubble load

simulation cases; and (2) an average of the 6 load realizations of complete drift collapse. The rationale for these two load configurations is explained in Section 2.3.4.5.3.2.1.

The drip shield is loaded primarily in a vertical direction from the rubble. This vertical loading results in lateral movement (i.e., a "bowing") of the drip shield legs into the rubble confining the sides of the drip shield. This movement into the rubble results in a lateral reactive pressure which is applied to the sides of the drip shield, thus effectively increasing the load-bearing capacity of the structure. This lateral confining effect was accounted for in the model by representing the rubble adjacent to the drip shield sides as a series of elastic springs whose stiffness is a function of the elastic modulus of the rubble (SNL 2007b, Section 6.4.3.2). If the sides of the drip shield attempt to displace into the rubble, a reaction force proportional to the stiffness of the spring is applied back to the side of the drip shield. If the drip shield deforms inward, away from the rubble, no reaction force is applied.

Analyses of drip shield collapse were completed by applying increased vertical rubble load incrementally until the applied crown pressure results in buckling of the sidewalls or rupture of the bulkheads and axial stiffeners beneath the crown of the drip shield (SNL 2007b, Section 6.4.3). Analyses presented in this reference show that the buckling of the sidewalls or rupture of the bulkheads and stiffeners is dependent on the vertical rubble load applied, and thus the completely collapsed drift represents a more conservative case for drip shield stability than intermediate states of a partially collapsed drift. These analyses automatically generate the lateral rubble loads applied to the drip shield legs generated by rubble–drip shield interaction under the vertical seismic loading. The pressure increment was refined near the collapse load to more accurately define the limiting load. Effective plastic strain, maximum stress, and maximum stress difference were monitored for all elements of the drip shield framework during the simulation.

Typical drip shield framework failure modes are illustrated in Figure 2.3.4-82. For the initial, nondegraded drip shield framework, the drip shield bulkhead snaps through approximately in the middle of the crown span. Uniform reduction in the thickness of the drip shield structural components weakens the lower part of the drip shield legs. Consequently, the typical mode of failure of the degraded and thinned drip shield structure is buckling of the legs.

Drip shield framework limit load as a function of thickness is shown in Figure 2.3.4-83 for the two applied load cases: load distributions from Realization 3 and from the average of the six load realizations (SNL 2007b, Section 6.4.3). These plots show that the limiting load increases almost linearly with increased thickness of the structural components. The particular loading case does not have a significant effect on the predicted plastic load capacity of the drip shield framework. This is a consequence of the significant confining effect of the rubble reactive pressure along the drip shield legs; the asymmetry of loading introduced by the different loading cases is compensated for by an increase in reactive rubble pressures as the drip shield structure starts deforming excessively to one side. Table 2.3.4-35 provides the average drip shield rubble pressures exerted on the drip shield crown from 6 realizations of complete drift collapse. These 6 realizations show an average static crown pressure of approximately 127 kPa resulting from the weight of the column of rubble lying on top of the drip shield. This can be compared to the limit load capacity of the drip shield framework in Figure 2.3.4-83 indicating a load limit of the as-installed drip shield framework at approximately 1600 kPa. Even with 10 mm of corrosion thinning, the limit load capacity of the drip shield sidewalls is in excess of 400 kPa. Therefore, under static rubble loading conditions, the drip

shield framework has a substantial design margin against buckling failure, even for significant degrees of thinning caused by general corrosion.

Dynamic Amplification of Static Load During Vibratory Ground Motion—When the drip shield is either partially or completely surrounded by rock rubble, vibratory ground motion will result in an amplification of the static rubble load. This amplification is taken into account in a simple fashion by determining an amplification load factor that is a function of the peak vertical ground acceleration of the ground motion. When the amplified (dynamic) load is greater than the limit load given in Figure 2.3.4-83, the drip shield framework fails by buckling (SNL 2007c, Section 6.8.1.1).

The correspondence between PGV and the dynamic load factor ($1 + A$) was provided in Figure 2.3.4-76 (SNL 2007c, Section 6.8.1.1). Since the seismic hazard curve is given in terms of PGV (Figure 2.3.4-18), an approximate relationship of the dynamic load factor to annual exceedence frequency can be obtained. The drip shield framework in the as-installed state has an approximate load capacity of 1600 kPa. This is approximately 12 times the average static rubble pressure of 127 kPa. It follows that a dynamic amplification factor of 12 would be required to collapse the drip shield. Even after 5 mm of thinning of the framework supports, the load capacity is about nine times the average static rubble loads estimated.

A comparison of Figures 2.3.4-81 and 2.3.4-83 show that the load limit of the plates in tensile rupture is substantially greater than the load limit of the framework for any given level of corrosion thinning. It is for this reason that the drip shield framework is expected to fail in a buckling mode of the legs near the invert before the plates fail by tensile rupture. Therefore, as stated in the introduction to Section 2.3.4.5, the plates are structurally more robust than the framework.

2.3.4.5.3.3.3 Alternative Modeling Approach—Dynamic Analysis of the Drip Shield and Rubble Under Vibratory Ground Motion

The limit failure loads for the drip shield framework described above assume that the use of quasi-static rubble loads bounds the dynamic collapse loads of the drip shield (SNL 2007b, Section 6.4.3). To verify this assumption, fully dynamic modeling of the kinematics and deformation modes of the drip shield when subjected to vibratory motion were conducted for a selected group of strong ground motion time histories. This section summarizes these analyses and demonstrates that the quasi-static limit load analyses provide a reasonable and conservative representation of drip shield deformation modes and plastic load capacity when subjected to the complex loading that occurs when the rubble and drip shield interact under vibratory ground motion.

Model and Scope of Simulations Performed—To investigate the full interaction of the drip shield, waste package, and rubble during strong ground motion characteristic of the highest levels of potential seismic shaking (i.e., the 2.44 and 4.07 m/s PGV levels), a detailed analysis of a drip shield, waste package, and pallet within a rubble-filled emplacement drift was performed. A two-dimensional analysis was performed using the discontinuum program UDEC. The numerical representation of the drip shield surrounded by rubble at three different geometric scales is shown in Figure 2.3.4-84. This model was not intended for detailed analysis of waste package damage mechanisms, but to investigate the general effects of potential drip shield-waste package impacts

as well as rubble loading on drip shield collapse. In this regard, the important aspect of the waste package representation is that it has the proper dimensions and mass. The internals of the waste package were assumed to be degraded and represented as a relatively soft and weak, elastic-perfectly plastic material as described in Section 2.3.4.5.2.1.2.5.

In these analyses, a two-dimensional model of the drip shield is used to represent the response of the three-dimensional structure. The height of the cross section and the mechanical properties (i.e., Young's modulus, yield strength) of the drip shield representation were calculated in such a way that flexural stiffness and bending moment as a function of the curvature of the approximating rectangular cross-sectional match or underestimate those of the actual drip shield cross section. The two dimensional representation reasonably and conservatively represents the structural stiffness, strength, and the induced forces and, thus, the failure response of the fully three-dimensional structure. The methodology of approximation and validation of the two-dimensional model is documented in detail in *Mechanical Assessment of Degraded Waste Packages and Drip Shields Subject to Vibratory Ground Motion* (SNL 2007b, Appendix B).

Analyses Conducted—The dynamic UDEC drip shield simulations were carried out in several steps. The emplacement drift is first allowed to completely collapse in order to develop the full static rubble loading on the drip shield. Once the drip shield-rubble system equilibrates under the rubble load, the vertically propagating ground motion time histories are applied at the base of the model and the emplacement drift, rubble and drip shield allowed to interact dynamically for the entire period of the strong ground motion (SNL 2007b, Section 6.4.4.4). These analyses automatically generate the lateral rubble loads applied to the drip shield legs generated by rubble-drip shield interaction under the vertical seismic loading. Nonreflecting boundary conditions were applied at the top and bottom boundaries of the domain, with free field boundaries applied on the vertical domain boundaries. After completion of the dynamic simulation of the ground motion time history, all outside boundaries were fixed and the model allowed to come to final gravitational equilibrium.

Twenty-four simulations were carried out. As in the fragility analyses described previously, three different drip shield structural component thicknesses (15 mm [initial case], 10 mm, and 5 mm) were used to assess the effect of uniform general corrosion on mechanical response. Models of each of these configurations were subjected to four sets of ground motion time histories at the two highest PGV levels: 2.44 m/s and 4.07 m/s. The ground motion time histories were selected from the set of 17 time histories available at each PGV level to provide the maximum vertical components of peak ground acceleration and PGV and the maximum total power spectral density for all three components. The time histories selected were numbers 3, 7, 9, and 13. Ground motion 9 has the largest vertical peak ground acceleration, ground motions 7 and 3 have the largest vertical PGV, and ground motion 13 has the largest power spectral density (the greatest energy content) (SNL 2007, Section 6.4.4.5).

The rock rubble particle distributions on the drip shield are random in nature. The initial rock block structure within the lithophysal rock mass is represented using a random block structure characterized by a large number of blocks of the expected fragment size in the lithophysal zone, based on the spacings of the ubiquitous fracture fabric (Section 2.3.4.4.8.3.1). A total of 17 different randomly generated realizations of the block structure of the lithophysal rock mass was used, resulting in 17 distinct initial rubble particle size and shape distributions and thus the static rubble

load distributions on the drip shield. Each initial rubble block geometry realization was then paired with one of the four vibratory ground motion time histories for the dynamic analysis of the drip shield at thicknesses representing the initial and two degraded thicknesses. This was done using a Latin Hypercube sampling, resulting in the 24 total simulations given in Table 2.3.4-41.

Results—The stability of the drip shield under dynamic loading is assessed through examination of the effective plastic strain in the structural framework and comparison to the tensile effective strain failure criterion for Titanium as described in Section 2.3.4.5.1.2.2 (SNL 2007b, Section 6.4.4). Additionally, large deformations of the structure and regions of localized strain and plastic hinge formation can be observed visually from the model output. In the majority of the calculations, the maximum effective plastic strain, usually greater than the failure limit, occurs at the bottom of the legs where large forces occur in the region of the footing contact with the invert or the rubble. Because the large deformation and plastic strains are localized to the leg-invert contact area, the observed damage at the bottom of the legs will not appreciably affect the overall stability and performance of the drip shield structure. In other words, the leg can buckle near the base and not completely lose its load-bearing capacity as it is confined by rubble along its sidewalls. An example of the deformed drip shield shapes and contours of the effective strain for the cases of 10 mm drip shield component thickness (5 mm thinning) are summarized in Figure 2.3.4-85.

It is observed from these fully dynamic simulations that the drip shield structure does not typically fail as a result of snap-through in the middle of the crown. Only in Case 11, at the 4.07 m/s PGV level for all geometrical configurations, are there indications of failure in the crown, but it occurs in the corner. Typically, the drip shield is observed to fail by buckling of the legs near the bottom, approximately 20 to 30 cm from the contact with the invert.

A summary of drip shield stability assessments based on comparison of dynamic simulations and estimates from the quasi-static drip shield fragility analysis is provided in Table 2.3.4-42. This table provides a comparison of the load limits from the quasi static fragility analysis and the maximum load computed for the dynamic simulations. The fragility analysis indicates the drip shield framework fails if the load limit is less than the total static and dynamically amplified rubble load; otherwise, “stable” is indicated. Failure for the dynamic analyses is determined from inspection of whether buckling is indicated in the model. This table shows that the quasi-static (fragility analysis) approach underestimates stability of the drip shield covered with rubble during strong seismic ground motions for all cases except Case 13 at 4.07 m/s PGV level and 15 mm (initial) plate thickness. In this case, the predicted ultimate load is considerably lower than for the other three realizations at 4.07 m/s. The maximum extensile effective plastic strain for this case is 0.16, which is only slightly greater than the failure strain of 0.152. Clearly, this case is right at the stability limit from the perspective of both the quasi-static and dynamic modeling approaches. In addition, the location of predicted failure in the dynamic simulation is relatively low on the drip shield leg; if failure occurs there, it would not have a significant effect on drip shield performance. Based on these results, the limit loads determined from the quasi-static fragility analyses of the drip shield structural framework provide a reasonable and conservative estimate of both the failure mode and limit loads for the complex case of strong ground motion shaking of the drip shield and rubble.

2.3.4.5.3.4 Abstraction for Probability of Drip Shield Plate and Framework Failure

Numerical integration for the total probability of plate rupture has been performed for similar conditions as the plate rupture calculations. The results of the numerical integrations are presented in Table 2.3.4-43. Table 2.3.4-43 also includes a column for a 0-mm-thick plate in order to encompass the full range of thicknesses for TSPA. The 0-mm-thick plate is assigned a probability of failure of 1 for a seismic event at any PGV level. Figure 2.3.4-86 illustrates the probabilities for the 100% rockfall load.

Numerical integration for the total probability of buckling of the sidewalls (i.e., framework failure) has been performed for PGV levels of 0.2 m/s, 0.4 m/s, 1.05 m/s, 2.44 m/s, and 4.07 m/s, for plate thicknesses of 2 mm, 5 mm, 10 mm, and 15 mm and for static rockfall loads for drifts that are 10%, 50%, and 100% filled with lithophysal rock. The results of the numerical integrations are presented in Table 2.3.4-44. Table 2.3.4-44 also includes a column for the framework reduced by 15 mm, corresponding to a 0-mm-thick plate, in order to encompass the full range of thicknesses for TSPA. The 0-mm-thick plate is assigned a probability of failure of 1 for a seismic event at any PGV level. Figure 2.3.4-87 illustrates the probabilities of framework failure for the 100% rockfall load. A comparison of Figures 2.3.4-86 and 2.3.4-87 clearly indicates that the probability of sidewall buckling is always greater than the probability of plate rupture for a given PGV level, rockfall load, and component thickness. This result demonstrates that buckling of the sidewalls will usually occur before rupture of the plates in TSPA.

2.3.4.5.4 Structural Analysis of the Waste Package After Drip Shield Failure

[NUREG-1804, Section 2.2.1.3.2.3: AC 1(1) to (4), AC 2, AC 3(1) to (3), AC 4, AC 5(2), (3)]

2.3.4.5.4.1 Conceptual Description of Analysis of Structural Analysis of the Waste Package After Drip Shield Failure

Failure of the drip shield changes the configuration of the EBS components. The configuration of the EBS and the mechanical response of the waste packages to seismic events must be defined for three states of the system: (1) the initial state, with an intact drip shield; (2) the final state, with the waste packages surrounded by rubble after failure of the drip shield plates; and (3) an intermediate state, where the legs of the drip shield have buckled, but the plates remain intact.

The waste package damage and tensile rupture potential estimates derived from the dynamic kinematic calculations in Section 2.3.4.5.2.1 are appropriate when the drip shield is intact and the waste package can move freely beneath it. In this condition, end-to-end impacts between adjacent waste packages and impacts between the waste package and its emplacement pallet may occur. The damage to an intact drip shield subjected to rockfall and rubble load was described in Section 2.3.4.5.2.2.

In the final state, after the drip shield plates rupture, the relatively small rock rubble particles (e.g., 0.1 to 0.3 m side length) (BSC 2004a) are able to flow beneath the drip shield and directly accumulate around the waste package outer corrosion barrier. In this case, the drip shield no longer functions as a seepage barrier, and the degraded waste package outer corrosion barrier will be

loaded directly by the weight of the rock rubble and by the amplification of this load during vibratory motion.

In the intermediate state, the legs of the drip shield structural framework may buckle, resulting in collapse of the drip shield onto the waste package. In this case, the drip shield will contact the waste package and transmit load from the rubble directly to the waste package via the framework. This intermediate state can occur because the plastic load capacity of the plates is significantly greater than the plastic load capacity of the drip shield framework for a given reduction in thickness of the drip shield components from general corrosion (Section 2.3.4.5.3). Stated differently, the drip shield framework is expected to buckle before the plates rupture, all other factors being equal.

Although the drip shield sidewalls have collapsed in the intermediate state, the drip shield plates remain intact and still prevent seepage water from contacting the waste package. The drip shield fragility analyses indicate that drip shield collapse will occur as a result of buckling of the legs at a location near the invert (Figures 2.3.4-82 (bottom) and 2.3.4-85). Once buckling occurs, the vertically applied rubble load will force the drip shield down into contact with the waste package. As shown in Figure 2.3.4-53, the clearance between the drip shield bulkheads and the waste package outer corrosion barrier is 2 ft 3 in. (0.68 m) or less. Therefore, large vertical movements of the drip shield are not required for contact to occur between the drip shield bulkheads and the upper surface of the waste package. Since the primary strain, or distortion, of the drip shield frame is expected to occur in the legs at the site of the buckling (Section 2.3.4.5.3.3.3), the drip shield may be resting on top of the waste package (SNL 2007c, Section 6.8.4). Thus, the drip shield will maintain its basic water diversion function even after collapse resulting from buckling of the side walls until the drip shield plates rupture.

Section 2.3.4.5.4 provides a summary of the mechanical analysis of the damage and rupture potential of the outer corrosion barrier of the TAD-bearing waste package for vibratory loading for these two long-time-frame drip shield failure possibilities—rubble in direct contact with the waste package and the drip shield in direct contact with the waste package (SNL 2007b, Section 6.5.2). Damage and rupture potential are examined for models of the TAD-bearing waste package with 17 and 23 mm outer corrosion barrier with intact or degraded internals subjected to static rubble loads and dynamic amplification from vibratory ground motions with PGV levels of 0.4 m/s, 1.05 m/s, 2.44 m/s, and 4.07 m/s.

2.3.4.5.4.2 Data and Data Uncertainty of Structural Analysis of the Waste Package After Drip Shield Failure

The input data for these calculations include the following:

- Static rock rubble loading
- 17 ground motion time histories for the 0.4 m/s, 1.05 m/s, 2.44 m/s, and 4.07 m/s PGV levels
- Elastic and plastic material properties of the waste package

- Dimensions and masses of EBS components (waste package, pallet)

- Damage criteria for the waste package outer corrosion barrier (Sections 2.3.4.5.1.2.1 and 2.3.4.5.1.2.2).

2.3.4.5.4.2.1 Rock Rubble Load on Waste Package and Ground Motion Application

The structural response of a waste package surrounded by rubble is determined from a series of two dimensional discontinuum simulations of drift collapse in the lithophysal rock units similar to that described in Section 2.3.4.5.3.2.1. The initial rock block structure within the lithophysal rock mass is represented using a random block structure characterized by a mean rock block dimension of 0.3 m, which is roughly consistent with the average block size of the rubble expected to form in the lithophysal rock mass (BSC 2004a, Section 6.4.1.1). A total of 17 different randomly generated realizations of the block structure of the lithophysal rock mass was used in a UDEC analysis of emplacement drift collapse resulting in 17 distinct initial static rubble load distributions on the waste package.

The uncertainty in ground motions is provided via 17 different ground motion time histories at each PGV level. The uncertainty in the ground motions and in the rock block pattern at a given PGV level is propagated into these calculations through sampled values for these input parameters. GoldSim provides a Latin Hypercube sampling of the rock block pattern and the ground motion number (Table 2.3.4-45) (SNL 2007b, Section 6.5.1.1). The ground motion number is sampled from a discrete distribution from 1 to 17, with equal probability for each integer. This sampling provides a list of input data in which a given ground motion is randomly paired with one of the 17 rock block patterns.

In all, 136 dynamic simulations of the waste package surrounded by rubble and subjected to vibratory ground motion were carried out using UDEC. These simulations consisted of the following parameter variations:

- Two different waste package outer corrosion barrier thicknesses were analyzed: 17 mm, and 23 mm. The waste package internals were assumed to be degraded for these simulations because this final state represents the late time response of the system, when the outer corrosion barrier is expected to have damaged areas, allowing the internals to degrade as structural components (Section 2.3.4.5.2).

- For each outer corrosion barrier thickness, 17 sets of ground motion/rock block realizations (Table 2.3.4-45) at four PGV levels: 0.4 m/s, 1.05 m/s, 2.44 m/s, and 4.07 m/s were simulated. The ground motions at the 0.4 m/s and 4.07 m/s PGV levels were derived by rescaling the velocity time histories from the available ground motions at the 1.05 m/s and 5.35 m/s PGV levels, respectively.

2.3.4.5.4.2.2 Alloy 22 Outer Corrosion Barrier Material Properties and Damage Criteria

Elastic and plastic material properties are set to constant values at 60°C as given in Table 2.3.4-28. The uncertainty in temperature-dependence of the material properties is addressed by use of

properties at 60°C, which is an upper bound for the waste package temperature for 99% of the 1,000,000 year period after closure (SNL 2007b, Section 5.7). The full rationale for the choice of 60°C for material properties is presented in Section 2.3.4.5.1.3.1.

The uncertainty in the RST for initiation of stress corrosion cracking in the Alloy 22 outer corrosion barrier is defined as a range from 90% to 105% of the yield strength of Alloy 22 (Section 2.3.4.5.1.3.2). The uncertainty represented by this range is propagated into TSPA by abstracting damaged area at several representative values of the RST. The TSPA model interpolates between the damaged areas for these representative values to capture the uncertainty.

2.3.4.5.4.2.3 Waste Package Outer Corrosion Barrier Thinning Due to General Corrosion

The structural response of the waste package is affected by the thickness of the outer corrosion barrier which will thin as a function of time due to general corrosion. The uncertainty in the structural response of the waste package outer corrosion barrier as a result of general corrosion thinning was included by performing analyses for two future degraded states. Two degraded thicknesses of the outer corrosion barrier are analyzed: 23 mm and 17 mm. These states represent the response of the waste package over the long-term evolution of the EBS components, as described in Section 2.3.4.5.

A simplification in these models relates to the use of the spatially averaged thickness of the outer corrosion barrier (SNL 2007b, Section 6.3.1). While surface imperfections, residual stresses from welding, and local chemical environments may result in variable corrosion rates on the outer corrosion barrier, the spatially averaged thickness is most relevant to the overall structural response of the waste package. The applied rubble load to the waste package occurs over the full surface of the waste package outer corrosion barrier, thus occurring over regions with the potential to have multiple thicknesses due to nonuniform corrosion rates. For example, the damaged area from the kinematic response of the waste package is dominated by waste package-to-pallet impacts. These impacts involve contact of the pallet with a significant area on the surface of the waste package, thereby averaging the impact loads across regions with multiple outer corrosion barrier thicknesses due to nonuniform corrosion. If rubble surrounds the waste package, then the seismic loads are spread over the whole surface of the waste package, again providing a mechanism to average the loads over the surface of the waste package. The spatially averaged thickness of the outer corrosion barrier therefore provides an appropriate measure of structural deformation and damaged area because the dynamic loads are spread over the whole outer corrosion barrier (Assumption 5.13 in *Mechanical Assessment of Degraded Waste Packages and Drip Shields Subject to Vibratory Ground Motion* (SNL 2007b)).

2.3.4.5.4.3 Model and Model Uncertainty of Structural Analysis of the Waste Package After Drip Shield Failure

The following section describes two models of the waste package mechanical performance after drip shield failure. First, a model of the waste package surrounded by rubble (drip shield plates fail in tensile tearing) is given. Second, a model of the waste package directly in contact with a buckled drip shield is described. For each of these process models, the waste package damage and tensile tearing (rupture) potential is assessed, and each described by an abstraction.

2.3.4.5.4.3.1 Waste Package Surrounded by Rubble

2.3.4.5.4.3.1.1 Model

A two-dimensional mechanical analysis of the waste package surrounded by rubble subjected to vibratory ground motion was conducted using UDEC). The UDEC model initially represents an intact emplacement drift containing a waste package and pallet resting on the invert. The drift is then allowed to fail and collapse onto the waste package by successively reducing the shear and tensile strength of the rock mass until complete drift collapse occurs. The rock rubble is represented as distinct, randomly shaped polygonal blocks whose average dimension is 0.3 m (Figure 2.3.4-88) (SNL 2007b, Section 6.5.1.2.1).

Once static equilibrium of the collapsed drift and rubble load to the waste package is established, the model is subjected to vibratory ground motion, resulting in dynamic amplification of the static rock rubble loads. During this stage of the simulation, incoming ground motions, propagating vertically upward, were applied at the base of the model. The analyses were carried out dynamically, and nonreflecting boundary conditions were applied at the top and bottom boundaries. The rubble particles and waste package are free to move and impact one another as the time-developing forces dictate. The static and dynamic forces of the accumulated rubble are transmitted to the waste package via direct contact with the rock particles, thus realistically determining the dynamic amplification of the static rubble load. The analyses result in a determination of the residual tensile stress and effective tensile strains in the outer corrosion barrier as well as the general observed deformed shapes of the outer corrosion barrier for 17 mm and 23 mm thicknesses (SNL 2007b, Sections 6.5.1.2.2 and 6.5.1.2.3).

The magnitude of damage and the tensile tearing (rupture) potential of the Alloy 22 outer corrosion barrier were determined for each analysis. The damage was determined from the surface area in which the tensile residual stress exceeds the RST of 90%, 100%, and 105% of the yield strength of Alloy 22 (Section 2.3.4.5.1.3.2). The tensile tearing or rupture potential of the outer corrosion barrier was determined by calculating the magnitude of the effective tensile strain and comparison of this strain to the effective tensile strain criteria for Alloy 22 as described in Section 2.3.4.5.1.2.2.

The analyses described here utilize a two-dimensional representation of the waste package due to the great complexity of a fully three-dimensional analysis in which the rubble and waste package are modeled explicitly. To verify that the two-dimensional approach bounds the predicted damage of the outer corrosion barrier, a detailed comparison of two and three-dimensional models of a waste package subjected to a vertical pressure was conducted (SNL 2007b, Appendix D). The vertical pressure applied to the crown of the waste package outer corrosion barrier was increased in increments until collapse of the outer corrosion barrier shell occurred. The collapse load estimates from the three-dimensional analyses were found to be between 3.5 to 6.0 times greater than those from two-dimensional analyses. The two-dimensional model thereby provides a conservative estimate of deformation when subjected to external loading as compared to the actual three-dimensional waste package structure.

Separate models are not developed for the TAD-bearing and codisposal waste packages surrounded by rubble because the results from the TAD-bearing waste package provide a reasonable estimate of damage for the codisposal package waste package. With degraded internals, the computational

model for the TAD-bearing waste package has a 23-mm-thick or 17-mm-thick outer corrosion barrier, and all internal components (inner vessel, TAD canister, fuel baskets, and fuel assemblies) are represented as a material that is similar to weakly cohesive soil, with no significant strength and with very limited cohesion as described in Section 2.3.4.5.2.1.2.5 (SNL 2007b, Section 6.5.1.1). Table 2.3.4-46 provides a more detailed comparison of total loaded weight and outer diameter for both waste package types. Based on this comparison, the computational model for the codisposal waste package with degraded internals is expected to be similar to the model for the TAD bearing waste package because the outer corrosion barrier thicknesses of both waste packages are the same and because the outer diameter and total loaded mass of both waste packages are similar (SNL 2007c, Section 6.9.10).

The concept that the TAD-bearing and codisposal waste packages will have similar structural response with degraded internals can also be confirmed by comparing the damaged areas in Section 2.3.4.5.2.1 for the kinematic response of the TAD-bearing and codisposal waste packages with degraded internals and a 17-mm-thick outer corrosion barrier.

2.3.4.5.4.3.1.2 Results—Outer Corrosion Barrier Damage

Outer corrosion barrier surfaces with tensile residual stresses greater than specified RSTs (90%, 100%, and 105% of Alloy 22 yield strength) are characterized as damaged areas (Section 2.3.4.5.1.2.1). Figure 2.3.4-89 shows percentages of the outer corrosion barrier surface area that is in a damaged state for the two degraded thicknesses of the outer corrosion barrier (23 and 17 mm) for averages of the 17 realizations of ground motion/rubble load patterns for all four PGV levels. This plot shows that the damage areas are generally a small percentage of the total waste package surface area. If the residual strength threshold is 90% of the yield strength, the average damage area is less than 0.2% of the total outer corrosion barrier surface area. If the RST is 105% of the yield strength, the average damaged area is less than 3% of the surface area. These results show, in general, that increase in damage area correlates with an increase in PGV level as well as a thinner outer corrosion barrier. An exception occurs at the 4.07 m/s PGV level in which the damage area is greater for the 23-mm-thick outer corrosion barrier than for the 17-mm-thick outer corrosion barrier at and above the 90% RST. The reason for this apparent discrepancy is the nonlinear and nonmonotonic response of the outer corrosion barrier as it deforms sufficiently to close the initial open space around the degraded internals.

2.3.4.5.4.3.2 Waste Package Loaded by a Collapsed Drip Shield

After the drip shield framework buckles or collapses, the drip shield may be resting on top of the waste package. The deformation and stresses in the outer corrosion barrier of a TAD-bearing waste package that is loaded by a collapsed drip shield has been investigated with the FLAC3D three-dimensional finite-difference model (SNL 2007b, Section 6.5.2). Structural analyses were completed for the TAD-bearing waste package with intact and degraded internals. The basic geometry of these models is shown in Figure 2.3.4-90. The entire drip shield is not explicitly represented in the model only the bulkhead flanges that are expected to contact the waste package after collapse of the framework.

For intact internals, the finite difference representation includes the inner vessel, the TAD canister, and the fuel baskets and plates inside the canister (Section 2.3.4.5.2.1.3.2). For degraded internals,

all internal components inside the outer corrosion barrier are represented as a very weak continuum that fills 50% of the interior volume of the outer corrosion barrier; the continuum is considered to be a weakly cohesive, soil-like material (Section 2.3.4.5.2.1.2.5). Outer corrosion barrier thicknesses of 17 mm and 23 mm were analyzed for both the intact and degraded internals.

Each simulation was performed by moving the bulkhead flanges vertically downward at a velocity that was sufficiently small to maintain quasi-static mechanical response in the outer corrosion barrier (SNL 2007b, Section 6.5.2.2.3). The structural deformation and the residual stress state induced in the outer corrosion barrier were monitored as a function of the average vertical pressure exerted on the outer corrosion barrier by the drip shield bulkhead flanges. For these analyses, damaged area was determined as a function of the effective quasi-static load on the waste package for a single value, 90%, of the RST for Alloy 22 (SNL 2007b, Section 6.5.2). The results at 90% RST provide a measure of the damage levels at this point. The final abstraction for TSPA includes the response for the full uncertainty range of RST, from 90% to 105%.

In determining damaged area, the damage to interior and exterior surfaces were added and then divided by the surface area of the cylinder to obtain a percent surface area damaged. The effective load on the waste package was expressed as an average vertical pressure (i.e., the total vertical force between the flanges and the waste package divided by the area of the horizontal cross section through the center of the waste package). Figures 2.3.4-91 and 2.3.4-92 show example views of predicted damage area and residual tensile stress contours in the outer corrosion barrier for the 23-mm-thick case and degraded and intact internals at two applied pressures.

2.3.4.5.4.3.2.1 Results—Outer Corrosion Barrier Damage

Figure 2.3.4-93 presents the resulting damage area percentage of the outer corrosion barrier surface area as a function of the effective vertical load. The results for intact internals at a 17-mm- or 23-mm-thick outer corrosion barrier indicate very small damage, less than 0.025%, up to an average vertical pressure of 1200 kPa. For reference, the average vertical static pressure from lithophysal rockfall for a completely collapsed drift exerted on the crown of the drip shield is 127 kPa (Table 2.3.4-35). The results of the calculations indicate that, if the internals are degraded, the damage area of the outer corrosion barrier is less than 0.1% of the total area for loads less than or equal to 350 kPa.

2.3.4.5.4.4 Abstraction of Waste Package Damage and Rupture Potential After Drip Shield Failure

2.3.4.5.4.4.1 Abstraction of Waste Package Response After Drip Shield Buckling But Before Plate Rupture

After the drip shield sidewalls buckle or collapse, the drip shield may be resting on top of the waste package. Separate analyses, described above, have been performed to determine the damaged areas in the outer corrosion barrier for thicknesses of 17 mm and 23 mm with intact and degraded internals in this intermediate state when the legs of the drip shield have buckled but the plates remain intact. Figure 2.3.4-93 presents the resulting damaged areas as a function of the effective vertical load.

The intermediate state is expected to persist for a limited period of time. The probability of plate failure is less than the probability of the legs buckling for a given thickness reduction (Section 2.3.4.5.3). However, general corrosion will continue to reduce the plate thickness after the framework buckles, eventually resulting in plate failure during a subsequent seismic event. This delay until plate failure is expected to be modest relative to the period beyond 10,000 years, within the period of geologic stability, because titanium corrosion rates are significantly greater than the corrosion rates of Alloy 22, as explained in Section 2.3.4.5.1.3.6. Given the limited duration of the intermediate state, separate damage abstractions have not been developed. Rather, the damage levels shown in Figure 2.3.4-93 have been approximated and bounded by other damage abstractions.

For intact internals, Figure 2.3.4-93 indicates damaged areas are less than 0.025% of the surface area of the drip shield up to an average vertical pressure of 1,200 kPa. Even at the highest value of vertical pressure in Figure 2.3.4-93, 1,500 kPa, the maximum damaged area is approximately 0.3% or less. It follows that the expected damaged area for a waste package surrounded by rubble provides an upper bound for the damage shown in Figure 2.3.4-93 for the case of intact internals. For example, the mean damaged area for a waste package surrounded by rubble with a 17-mm-thick outer corrosion barrier is 2.2% and 0.4% of the surface area for the 90% RST and 100% RST, respectively, as shown in Table 2.3.4-47. These values are greater than the maximum value of damaged area for the drip shield resting on a waste package, which is 0.3% at 1,500 kPa (SNL 2007c, Section 6.8.4).

The results for degraded internals at a 17-mm or 23-mm-thick outer corrosion barrier rise rapidly to damaged areas in the 1% to 10% range for average vertical pressure of 500 kPa or greater (Figure 2.3.4-93). This higher level of damage with degraded internals is consistent with the kinematic damage abstraction for the TAD-bearing waste package with degraded internals (SNL 2007c, Section 6.8.4). For example, the TAD-bearing waste package with 17-mm-thick outer corrosion barrier and degraded internals has damaged areas between 2 m^2 and 10 m^2 over a wide range of PGV levels (Figure 2.3.4-94). These damaged areas are equivalent to approximately 6% to 30% of the surface area of the TAD-bearing waste package (SNL 2007c, Section 6.8.4), thereby providing an upper bound to the damaged area for the drip shield resting on the waste package.

In summary, the damage abstraction for a waste package surrounded by rubble provides an upper bound for the damage shown in Figure 2.3.4-93 for the case of intact internals, and the kinematic damage abstractions for the TAD-bearing waste package with degraded internals provide an upper bound for the damage shown in Figure 2.3.4-93 for the case of degraded internals. These abstractions have been used in TSPA to represent the response of the waste package in the intermediate state, after the drip shield framework has collapsed but before the drip shield plates fail.

2.3.4.5.4.4.2 Abstraction of Waste Package Response After Plate Rupture

Two damage abstractions have been developed for a waste package after plate failure, when it is surrounded by lithophysal rubble:

- 23-mm-thick outer corrosion barrier with degraded internals
- 17-mm-thick outer corrosion barrier with degraded internals.

The waste package becomes surrounded by rubble after the drip shield framework and drip shield plates have failed during a seismic event. This is expected to occur well after repository closure, when the outer corrosion barrier is expected to be breached by stress corrosion cracking, resulting in degraded internals inside the waste package. Regardless of the time scale, the damage abstractions for degraded internals will have greater probability of damage occurring and greater damaged areas relative to the response with intact internals.

Each abstraction defines the probability of rupture, the probability of nonzero damage, and the conditional probability distributions for conditional damaged area, all as functions of PGV alone or of PGV and RST (SNL 2007c, Section 6.9). The abstractions are based on the TAD-bearing waste package because the response of the TAD-bearing waste package is expected to be similar to, but provide an upper bound, relative to the response of the codisposal waste package when the internals are degraded. A single damage abstraction has therefore been developed for both types of waste packages, as explained in the last subsection of this section. Lithophysal rubble was selected for the dynamic load on the waste package because the mass of lithophysal rubble accumulates more quickly than the mass of nonlithophysal rubble, resulting in greater rockfall loads.

The damage abstraction for the 23-mm-thick and 17-mm-thick outer corrosion barriers are very similar. Only the damage abstraction for the 17-mm-thick outer corrosion barrier is illustrated in this section.

Probability of Rupture/Puncture—The probability of rupture for the (TAD-bearing) waste package surrounded by rubble for the 17-mm-thick and 23-mm-thick outer corrosion barriers with degraded internals is zero. The structural response calculations for the waste package surrounded by rubble at the 0.4 m/s, 1.05 m/s, 2.44 m/s, and 4.07 m/s PGV levels demonstrate that the strain in the outer corrosion barrier is always below the ultimate tensile strain for Alloy 22 (SNL 2007b, Section 6.5.1.4.1). However, a severely deformed outer corrosion barrier may be punctured by the sharp edges of fractured or partly degraded internal components. In this conceptualization, the volume reduction in a severely deformed outer corrosion barrier is hypothesized to have the potential to puncture the outer corrosion barrier.

The deformation of the outer corrosion barrier is assessed by calculating the ratio of the volume within the deformed outer corrosion barrier, at the end of the ground motion, to the initial volume within the outer corrosion barrier (SNL 2007b, Section 6.5.1). This ratio is 1 at the start of each calculation, when the interior is 50% free space and 50% degraded internals. This ratio can become as low as 0.5 if the outer corrosion barrier collapses around the degraded internals, eliminating all free space within the outer corrosion barrier. As this ratio is reduced from 1.0 to 0.5, the probability of puncture increases monotonically from 0 to 1. In other words, the probability of puncture becomes 1 when all of the free space within the outer corrosion barrier is eliminated by the dynamic response of the system. Table 2.3.4-48 displays the resulting probabilities for the 17-mm-thick outer corrosion barrier, based on calculations with 17 ground motions at each of the 0.4 m/s, 1.05 m/s, 2.44 m/s, and 4.07 m/s PGV levels.

The probability for puncture of the waste package surrounded by rubble is represented in TSPA as a power law function of the form $a(\text{PGV}-0.4)^b$. This function goes to 0 at the 0.40 m/s PGV level, consistent with the data in Table 2.3.4-48. This power law provides an excellent fit to the probability of puncture at the 1.05 m/s, 2.44 m/s, and 4.07 m/s PGV levels, judging by the R^2 value of

0.9958 for the least squares fit to the logarithmic values for the probability data shown in Figure 2.3.4-95. A similar approach defines the power law fit for the 23-mm-thick outer corrosion barrier.

The spatially averaged thickness of the outer corrosion barrier is a time-dependent parameter that is predicted by other elements of the TSPA calculations. The probability of puncture corresponding to this average outer corrosion barrier thickness at the time of the seismic event is calculated by linear interpolation if the outer corrosion barrier thickness is between 17 mm and 23 mm. The probability is set equal to the value at 23 mm if the average outer corrosion barrier thickness is greater than 23 mm. The probability is calculated by linear extrapolation if the thickness is less than 17 mm, using the data at 17 mm and 23 mm to define the slope for the linear extrapolation. The extrapolation is not anticipated to have a significant effect on TSPA because the spatially averaged thickness of the outer corrosion barrier provides a reasonable basis for determining the response of the waste package at around 1,000,000 years, as discussed in Section 2.3.4.5.1.3.6.

When the waste packages are punctured, the failed area is determined by sampling a uniform distribution with a lower bound of 0 m^2 and an upper bound of 0.10 m^2 (SNL 2007c, Section 6.9.1). The upper bound of the uniform distribution is based on two estimates for the area of a hypothetical puncture. The first estimate assumes that a puncture occurs from a sharp fragment of a fuel rod. An upper bound for this puncture area is estimated to be a "hole" that is 1 foot-by-1 foot, or (0.3048 m) (0.3048 m) = 0.092 m^2. This value allows for the possibility that multiple fragments may puncture the outer corrosion barrier. In the second estimate, one of the fuel basket plates is conceptualized to form a lengthwise slice through the outer corrosion barrier whose area is estimated as (3,968.5 mm) (25.4 mm) = 100,800 mm^2 or 0.10 m^2. The area of the slice, which is slightly greater than the first estimate, is used for the upper bound of the distribution (SNL 2007c, Section 6.9.1). This failed area allows advective flow through the punctured waste package and advective and diffusive transport out of the ruptured waste package. This failed area is conceptualized to be a small patch on the surface of the outer corrosion barrier.

Probability of Nonzero Damaged Area—Table 2.3.4-49 presents the probability of nonzero damaged area from the calculations for the (TAD-bearing) waste package with degraded internals, surrounded by rubble. With the 23-mm-thick outer corrosion barrier, the probability of nonzero damage is 0 except at the 4.07 m/s PGV level. With the 17-mm-thick outer corrosion barrier, the probability of nonzero damage is 0 at the 0.4 m/s and 1.05 m/s PGV levels, and nonzero at the 2.44 m/s and 4.07 m/s PGV levels.

The probability of nonzero damage in Table 2.3.4-49 is based on three independent parameters: the value of PGV for the *j*th seismic event, the value of RST for a given realization, and the time-dependent thickness of the outer corrosion barrier. Linear interpolation is used to define the variation of the probability of nonzero damage as a function of PGV and RST.

Conditional Probability Distributions for Nonzero Damaged Area—Relatively few data points have nonzero damaged area for the 17-mm-thick outer corrosion barrier. There are only 7 points, 3 points, and 2 points with nonzero damaged areas at the 90%, 100%, and 105% RSTs, respectively, for the 4.07 m/s PGV level. There are only 2 points with nonzero damaged area for the 90% RST at the 2.44 m/s PGV level. Since most of the nonzero data occur at the 4.07 m/s PGV level, a reasonable approach is to abstract these data as a function of RST at this PGV level.

Figure 2.3.4-96 is a Q-Q plot for a gamma distribution versus the conditional damaged areas at the 90% RST and the 4.07 m/s PGV level. The values of the mean and standard deviation of the conditional damaged areas, which are the input to the gamma distributions, are shown in Table 2.3.4-47 for all RST levels. The data for the standard deviations at the 100% RST and 105% RST levels in Table 2.3.4-47 are based on the observed coefficient of variation at the 90% RST level because the available data at 100% RST and 105% RST are very limited and produced unrealistically small values for the standard deviation. Figure 2.3.4-96 demonstrates that the gamma distribution provides a very good fit to the damaged area data (SNL 2007c, Section 6.9.3).

The abstraction for TSPA must represent the response for intermediate values of RST, between 90% and 105% (SNL 2007c, Section 6.9.3). Simple quadratic fits to the mean and (modified) standard deviations of the data sets at the 3 values of RST shown in Table 2.3.4-47 provide a representation of the input parameters for the gamma distribution as a function of RST. Figure 2.3.4-97 plots the 1st, 5th, 50th, 95th, and 99th percentiles of the resulting gamma distributions against the conditional damaged areas. The quadratic fits to the mean and standard deviation result in gamma distributions that provide a reasonable representation of the conditional damaged areas over the complete RST range, from 90% to 105% (SNL 2007c, Section 6.9.3).

The abstraction for TSPA must represent the response for a range of PGV levels (SNL 2007c, Section 6.9.5), rather than the damage at the single 4.07 m/s PGV level shown in Figure 2.3.4-97. It is difficult to extrapolate the conditional damage at the 4.07 m/s PGV level to the full range of PGV values for TSPA. In this particular case, the results for 4.07 m/s PGV level are conservative for all values of PGV less than 4.07 m/s. It is then conservative to use the conditional damage at the 4.07 m/s PGV level for all values of PGV in TSPA.

Alternate Conditional Probability Distributions—The gamma distribution produces a better match to the sum of the squared differences than a log-normal distribution and approximately the same match as a Weibull distribution for this data set (SNL 2007c, Section 6.9.4). The gamma distribution is the preferred approach because it is straightforward and does not involve the numerical adjustment of parameters for the Weibull distribution.

TAD-Bearing Versus Codisposal Waste Packages Surrounded By Rubble—Separate abstractions are not being developed for the TAD-bearing and codisposal waste packages surrounded by rubble because the results from the TAD-bearing waste package provide a reasonable estimate of damage for the codisposal waste package. With degraded internals, all internal components (inner vessel, TAD canister, fuel baskets, and fuel assemblies) are represented as a material that is similar to sand, with no significant strength and with very limited cohesion (SNL 2007b, Section 6.5.1). The computational model for the codisposal waste package with degraded internals is similar to the model for the TAD-bearing waste package because the load-bearing structural component, the cylindrical outer corrosion barrier, has the same thickness for either waste package, and because the differences in outer diameter of the outer corrosion barrier and fully loaded weight are modest, as discussed in Section 2.3.4.5.4.3.1.1. Separate damage abstractions for the two waste package types are therefore not necessary.

2.3.4.5.5 Structural Response to Fault Displacement

[NUREG-1804, Section 2.2.1.3.2.3: AC 1(1) to (4), AC 2, AC 3(1) to (3), AC 4, AC 5(2), (3)]

2.3.4.5.5.1 Conceptual Description of Analysis

Fault displacement could impact key EBS components by causing mechanical damage to the waste packages and drip shields. Potential faulting within the emplacement drifts generally results in small displacements along the faults. With the exception of the Solitario Canyon Fault and the Ghost Dance Fault, which are immediately outside the western and eastern boundaries of the emplacement drifts, a fault displacement of greater than 0.1 cm is associated with a mean annual exceedance frequency of less than 10^{-5} per year (SNL 2007c, Section 6.11). In addition, only the small number of waste packages located directly above faults are subject to damage from fault displacement. It follows that the dose related to fault displacement is expected to be a small fraction of the total dose for the seismic scenario class because damage from fault displacement affects at most a small fraction of the inventory and because this damage occurs only for events with very low exceedance frequencies. Although the contribution to total dose is expected to be small, the contribution is calculated in the fault displacement modeling case in TSPA (Section 2.4).

Given that the dose related to fault displacement is expected to be a small fraction of the total dose, simplified calculations of the structural response of EBS components to fault displacement are sufficient for TSPA. The focus in this abstraction is on the potential for the waste package to be damaged when fault displacement exceeds the available clearance around the waste package. For example, a fault displacement that occurs in an emplacement drift may cause a sudden discontinuity in the profile of the drift. This could result in one portion of the drift being displaced vertically or horizontally relative to the adjacent section. Such a discontinuity in the drift could cause shearing of the waste package, drip shield, and cladding located directly over the fault if the fault displacement exceeds the available clearances in the EBS. The comparison of fault displacements with available clearances provides a simple analysis that maximizes the potential for damage to EBS components from fault displacement.

Fault displacement is assumed to occur concurrently with ground motion during a low probability seismic event (SNL 2007c, Section 6.12.1). More specifically, the annual exceedance frequency for the ground motion and fault displacement are assumed to be equal during each seismic event. This approach is reasonable because a significant nearby earthquake simultaneously will induce both ground motion and fault displacement at the repository (SNL 2007c, Section 6.12.1).

2.3.4.5.5.2 Data and Data Uncertainty

The primary input data required for the fault displacement analysis (SNL 2007c, Section 6.11) are:

- Inventory of waste package types and their dimensions
- Clearances of EBS components (drip shields and waste packages) to drift walls/fault intersections
- Failure criteria for waste packages under fault displacement

- Numbers and locations of faults intersecting repository excavations
- Fault displacement hazard curves.

2.3.4.5.5.2.1 Clearances for EBS Components

Two distinct cases are considered in analyzing the clearances between EBS components: (i) an intact drip shield and (ii) a drip shield that has failed (SNL 2007c, Section 6.11.1). The first case represents the as-emplaced configuration of the EBS, shortly after repository closure, and is expected to be applicable to the first 10,000 years after repository closure. The second case represents the late time response of the EBS after the drip shield framework and drip shield plates have failed and rockfall has partly or completely filled the emplacement drifts and surrounded the waste packages with rubble. Each of these cases is considered separately in the following sections.

2.3.4.5.5.2.1.1 Clearances with an Intact Drip Shield

To determine the response of EBS components to fault displacement with an intact drip shield, consider the emplacement drift layout, shown schematically in Figure 2.3.4-53. The emplacement drift has a nominal diameter of 216 inches or 18 feet (5,490 mm) (BSC 2007e). Within the drift, the steel support beams and associated ballast form a level invert whose top surface is 52 inches (1,320.8 mm) above the lowest part of the drift (BSC 2007e, invert height). The waste package sits on an emplacement pallet that raises the bottom of the waste package above the invert. While the elevation difference between the top of the invert and the bottom of the waste package varies depending on the waste package diameter, the exact value is not important for this analysis because this elevation difference is not actually used in the analysis.

Table 2.3.4-50 summarizes the exterior dimensions of the various waste package designs. The most important parameter for the analyses presented herein is the outside diameter of the waste package outer corrosion barrier, which is seen to vary between 1749 mm to 2045 mm (SNL 2007h, Table 4-3, for outside diameter of the outer corrosion barrier and for nominal length of the TAD waste package; SNL 2007g, Tables 4-6 through 4-10, for the outside diameter of the outer corrosion barrier and nominal length of the other waste package types). Also shown in Table 2.3.4-50 is the calculated clearance between the top of the waste package and the underside of the drip shield, without the pallet. This clearance is defined as the interior height of the drip shield less the outside diameter of the waste package outer corrosion barrier. The elevation of the package above the invert is not included in calculating the clearance, as explained below. This clearance varies between 673 mm and 969 mm, as shown in Table 2.3.4-50.

The actual response of the EBS components to a fault displacement scenario is complicated. As a conservative simplification, the fault displacement is analyzed considering:

- The fault is perpendicular to the drift axis with the displacement being purely vertical.
- The fault displacement occurs at a discrete plane, creating a sharp discontinuity.
- The temporal evolution of rockfall in the emplacement drifts is not addressed. Clearances are conservatively based on emplacement drifts in the lithophysal and nonlithophysal zones that are fully collapsed (i.e., filled with rockfall) at the time of the seismic event.

The technical basis for this approach is discussed in detail in (SNL 2007c, Section 6.11.1).

Movement along a sudden discontinuity will affect the rubble surrounding the drip shield after drift collapse. The lithophysal rubble is a loosely packed material with bulking factors in the 0.1 to 0.4 range, which are equivalent to porosities between 0.09 and 0.29 (Section 2.3.4.4.8 for definition of the bulking factor and the relationship between bulking factor and porosity). With this free space, the rubble has substantial movement in the plane of the discontinuity and longitudinally along the drift axis during the fault displacement. The potential for substantial movement of the drip shield after drift collapse has been confirmed in ground motion analyses for the 1.05 m/s PGV level (BSC 2004a, Appendix P2.1). The rockfall loads from lithophysal rubble have the capability to move the entire drip shield by sliding it along the invert and by lifting it from the invert. The inertial forces during seismic shaking can also cause movement of the drip shield. It follows that the clearance between the top of the drip shield and the roof of the drift will be partly available, but the exact value is difficult to quantify.

The dynamic response of the rubble, invert and emplacement pallet during a fault displacement is difficult to predict. As a simplification, the approximation is made that the clearance between the top of the waste package and the bottom of the drip shield is determined without the pallet. This is a reasonable approximation because the clearance from the crown of the drip shield to the roof of the drift (1270 mm in Table 2.3.4-51) is much greater than the difference in clearance due to the pallet, as shown in Table 2.3.4-50. Since the porosity and dynamic motion of the rubble allows the drip shield to displace horizontally and vertically during the ground motion, the difference in clearance due to the pallet can be accommodated by drip shield displacements that are a small percentage of the height of the rubble. It follows that the potential for upward displacements of the drip shield into the large rubble filled space between the top of drip shield and roof of the drift allows for vertical motions that can exceed the maximum difference (317 mm) in clearance due to the pallet. In addition, the dynamic response of the invert ballast during a very low probability seismic event may result in the pallet settling downward into the invert. It is then reasonable to exclude the presence of the pallet in defining clearance between components because of the potential for upward displacement of the drip shield. This representation is conservative because no credit is taken for any shifting of the ballast into the portion of the tunnel that has displaced downward during the seismic event and because lack of clearance does not necessarily result in shearing of the waste package outer corrosion barrier, as is assumed here (SNL 2007c, Section 6.11.1.1). The calculated clearances are summarized in Table 2.3.4-52.

2.3.4.5.5.2.1.2 Clearances with a Failed Drip Shield

After closure, the waste package can become surrounded by rubble after the drip shield plates rupture (see the plate fragility analysis in Section 2.3.4.5.3), allowing the accumulated rubble and rockfall in the drifts to fall through the drip shield. The presence of the rubble eliminates the free space between the top of the waste package and the bottom of the drip shield shown in Figure 2.3.4-53. The potential for fault displacement to cause rupture of the waste package in the presence of rockfall needs to be evaluated for this system configuration.

Movement along a sudden discontinuity will affect the rubble surrounding the drip shield after drift collapse (SNL 2007c, Appendix D). The lithophysal rubble is a loosely packed material with a range of bulking factors between 0.1 to 0.4, corresponding to a porosity range of 0.09 to 0.29. With this free space, the rubble has substantial movement in the plane of discontinuity and longitudinally along the drift axis during the fault displacement. The movement of the rubble will allow the waste package to move with the fault displacement, rather than being rigidly fixed. A similar range of porosities should exist for the rockfall in the nonlithophysal zones because its range of bulking factors are similar to those for the lithophysal rubble (Section 2.3.4.4.8.3.1; SNL 2007c, Section 6.7.2.6).

As a conservative simplification, the approximation is made that fault displacement has to exceed one-quarter of the outer diameter of the outer corrosion barrier in order to cause failure of the waste package. One quarter of the outer corrosion barrier outer diameter is between 437 mm to 511 mm, or about 0.4 meters to 0.5 meters, based on the outer diameters of the waste package outer corrosion barriers in Table 2.3.4-50. The rationale for this simplification is based on the typical size of lithophysal rubble fragments and the potential for substantial movement of the rubble surrounding the waste package. A more detailed discussion is presented in (SNL 2007c, Section 6.11.1.2).

A more complete representation of the minimum fault displacement that can rupture the waste package could depend on the size distribution of the rock fragments, the state of the waste package internals, the fraction of the drift that is filled with rockfall at the time of the fault displacement, the state of the pallet (intact or failed) and the exact positioning of the waste package and drip shield relative to the fault. In this situation, there is clearly significant uncertainty in the value of the minimum fault displacement. This uncertainty is not being included in TSPA because the current analysis provides a lower bound estimate of the minimum fault displacement that could rupture the waste package.

The displacements corresponding to one-quarter of the outer diameter of the outer corrosion barrier are summarized in Table 2.3.4-53.

2.3.4.5.5.2.2 Failure Criteria for EBS Components in Response to Fault Displacement

The displacement values in Tables 2.3.4-52 and 2.3.4-53 represent the failure criteria for waste packages and drip shields (if appropriate) in response to fault displacement for two possible states of the EBS: a case for intact drip shields (Table 2.3.4-52) and a case for a failed drip shield (Table 2.3.4-53). Fault displacement in excess of these values is considered to fail the waste package and the overlying drip shield through direct shearing, allowing advective flow through the

sheared components (SNL 2007c, Section 6.11.1.3). The cladding within the affected waste package(s) would also be failed, but is not considered here because TSPA is not taking credit for commercial SNF cladding as a feature that contributes to barrier performance in the license application (SNL 2008b, Section 6.6.1.1.3). The values from Table 2.3.4-53 are used for TSPA because these values are less than the values in Table 2.3.4-52, thereby maximizing the number of damaged waste packages from fault displacement in TSPA.

2.3.4.5.5.2.3 Faults Intersecting Emplacement Drifts

The location, frequency, and magnitude of potential fault displacements within the footprint of the emplacement drifts must be analyzed to determine the potential impacts of fault displacement on the Yucca Mountain repository. Fault displacements are considered to occur at known faults that intersect the emplacement drifts (based on surface mapping), and to occur at generic locations within the repository (SNL 2007c, Section 6.11.2).

2.3.4.5.5.2.3.1 Location of Known Faults

Information on known faults intersecting the emplacement drifts is obtained from several sources. The traces for the Sever Wash Fault, Drill Hole Wash Fault, Pagany Wash Fault, and the western splay off the main Ghost Dance Fault relative to the repository are provided in *Total System Performance Assessment Data Input Package for Requirements Analysis for Subsurface Facilities* (SNL 2007d, Table 4-1, Item Number 01-03). The intersection of these traces with individual emplacement drifts, as well as the intersections for the Sundance Fault with the emplacement drifts, are summarized in *Seismic Consequence Abstraction* (SNL 2007c, Section 6.11.2). The intersections of known faults with the emplacement drifts are summarized in Table 2.3.4-54. As can be seen from Table 2.3.4-54, there are a total of 43 locations where a known fault intersects an emplacement drift.

2.3.4.5.5.2.3.2 Faulting at Generic Locations

During a major seismic event, faulting could occur not only coincident with the location of well characterized, known faults, but also elsewhere in the repository. In characterizing the potential for fault displacement elsewhere in the repository, rock conditions ranging from intact rock to the presence of existing small faults with about 2 meters of cumulative offset have been considered. The generic rock conditions and the corresponding fault displacement hazard curves are summarized in (SNL 2007c, Section 6.11.3). Table 2.3.4-55 summarizes the fault displacement hazard curves for generic rock conditions, denoted as Sites 7a-7d and 8a-8d (SNL 2007c, Table 6-61). Only the locations identified as Site 7a and Site 8a, for an existing fault with a cumulative offset of about 2 meters, have the capacity to produce significant fault displacements for exceedance frequencies greater than 10^{-8} per year (SNL 2007c, Section 6.11.2.2). The exact number or location of these small faults is not known because they are not readily identified through surface mapping. Thus, it is necessary to estimate the density of such small faults based on either site data or natural analogues.

One means of quantifying the likelihood of such smaller faults is through use of the data obtained from the characterization of the ECRB Cross-Drift (Mongano et al. 1999, pp. 51 to 59). The ECRB Cross-Drift extends through the repository footprint near its north/south midpoint and spans the

approximate east/west extent of the repository. Over the length of this drift, three small faults were identified with cumulative displacement of between about one meter and a few meters. This is thought to be generally representative of the density of small faults throughout the repository, so one can make an estimate of the number of such small faults that might intersect the emplacement drifts. In reviewing the repository layout (BSC 2007f, Figure 1), it can be seen that there are 57 emplacement drifts that span the entire north to south extent of the repository (designated 3–1 W through 3–22 W, 1–1 through 1–8, and 2–1 through 2–27). Some of these drifts are much shorter than the ECRB Cross-Drift. However, for abstraction purposes, the three unknown small faults in the ECRB Cross-Drift are taken to intersect the repository footprint along its entire north to south extent (SNL 2007c, Section 6.11.2.2). This conservative treatment results in 57 drifts, each of which has three unknown small faults, for a total of 3 × 57 or 171 locations where small faults have the potential to intersect the emplacement drifts (SNL 2007c, Section 6.11.2.2).

2.3.4.5.5.2.4 Fault Displacement Hazards

Magnitudes of fault displacement along two of the known faults (Sundance and Drill Hole Wash) as a function of probability are obtained from *Probabilistic Seismic Hazard Analyses for Fault Displacement and Vibratory Ground Motion at Yucca Mountain, Nevada* (CRWMS M&O 1998). Fault displacement hazard curves for fifteen faulting conditions mapped within the immediate vicinity of Yucca Mountain have been developed in *Probabilistic Seismic Hazard Analyses for Fault Displacement and Vibratory Ground Motion at Yucca Mountain, Nevada* (CRWMS M&O 1998). Mean fault displacement hazard curves are used in the following analyses (SNL 2007c, Section 6.11.3). The fault displacement hazard curves relevant to this abstraction are as follows:

- Site 4 – Ghost Dance Fault
- Site 5 – Sundance Fault
- Site 7 – A generic location within the repository, approximately 100 meters east of the Solitario Canyon Fault. The ground conditions at the generic location include intact rock (7d), a hypothetical fracture with no cumulative displacement (7c), a hypothetical shear with 10 cm of offset (7b), and a hypothetical small fault with 2 meter offset (7a).
- Site 8 – A generic location within the repository, midway between the Solitario Canyon Fault and the Ghost Dance Fault. The ground conditions at the generic location include intact rock (8d), a hypothetical fracture with no cumulative displacement (8c), a hypothetical shear with 10 cm of offset (8b), and a hypothetical small fault with 2 meter offset (8a).

Five known faults intersect the emplacement areas of the repository. These five faults are the Drill Hole Wash Fault, the Sundance Fault, the Pagany Wash Fault, the Sever Wash Fault and the western splay of the Ghost Dance Fault (called the West Ghost Dance Fault). It is assumed that displacements on the Pagany Wash Fault and Sever Wash Fault are identical to those on the Drill Hole Wash Fault. The hazard curve for the main Ghost Dance Fault provides a conservative estimate of the fault displacement on the West Ghost Dance Fault. Generic locations identified as Site 7a and Site 8a apply throughout the repository. There are 171 intersections of these small faults with the emplacement drifts, based on the estimate provided in Section 2.3.4.5.5.2.3.2.

Table 2.3.4-55 provides the displacement values from the mean hazard curves as a function of the mean annual exceedance frequency (or probability) associated with sites 2, 3, 4, 5, 7a to 7d and 8a to 8d (SNL 2007c, Table 4-1).

2.3.4.5.5.3 Model and Model Uncertainty

The model for the consequences of fault displacement by waste package type is defined in *Seismic Consequence Abstraction* (SNL 2007c, Section 6.11.4) and summarized in this section. To simplify the analysis, the inventory of waste packages is split into two groups. Waste packages of similar design and similar waste type are grouped together. The two groups are defined as follows:

- **TAD:** Includes the TAD, Naval Long, and Naval Short waste packages.
- **Codisposal Waste Package:** Includes the 5 DHLW/DOE Short, the 5-DHLW/DOE Long and the 2-MCO/2-DHLW waste packages.

The waste package designs with the smallest diameter in the group are chosen to represent the diameter for all packages in that group (SNL 2007c, Section 6.11.4). The impact of this approximation is small because it affects only the 2-MCO/2-DHLW waste packages, which are small in number relative to the total number of waste packages in the design basis inventory.

The percentage of inventory of the waste packages in each group is calculated based on the total length of the waste package types in the group versus the total length of all emplaced waste packages. Length is the appropriate parameter here because it more accurately represents the probability that a waste package is directly on a fault. These results are shown in Table 2.3.4-56.

The data in Table 2.3.4-53 define the allowable fault displacement before a waste package is pinned. The allowable displacement for all packages in the TAD group is 470 mm (47.0 cm). The allowable displacements for the packages in the codisposal waste package group are 511 mm (51.1 cm) or 437 mm (43.7 cm) for the 5-DHLW/DOE package types or the 2-MCO/2-DHLW waste package, respectively. This abstraction conservatively uses the minimum of these two values (437 mm) for the 2-MCO/2-DHLW waste package, even though this package constitutes less than 7% of the inventory in the codisposal waste package group.

Waste package failure occurs when displacements on the fault displacement hazard curve(s) exceed the maximum allowable displacements in Table 2.3.4-53. The fault displacement hazard curves from the *Probabilistic Seismic Hazard Analyses for Fault Displacement and Vibratory Ground Motion at Yucca Mountain, Nevada* (DTN: MO0401MWDRPSHA.000) define which fault displacement events are severe enough to cause waste package failure. A comparison of the allowable displacements (Table 2.3.4-53) with the individual hazard curves defines the range of exceedance frequencies that can cause waste package failure. The ranges of exceedance frequencies are listed in Table 2.3.4-57 for each fault and each waste package group. The Solitario Canyon Fault and main Ghost Dance Fault are not included in this discussion because these faults lie outside the emplacement areas of the repository.

There are six locations where the Sundance Fault intersects the emplacement drifts, 26 locations where either the Drill Hole Wash Fault, Pagany Wash Fault, or Sever Wash Fault intersect the

emplacement drifts, and 11 locations where the West Ghost Dance Fault intersects the emplacement drifts (Table 2.3.4-54). There are 171 locations where additional small faults are assumed to intersect the emplacement drifts (SNL 2007c, Section 6.11.2.2). Combining this information with the probability of finding a particular waste package group at a given point in the repository (last column in Table 2.3.4-56), an estimate can be made of the expected number of each type of waste package at the five known faults under the modeled, hypothetical conditions. This result is shown in Table 2.3.4-58. Note that the number of waste packages is not an integral number because it represents an average expectation of finding a particular waste package along a particular fault. The Pagany Wash Fault, Sever Wash Fault, and Drill Hole Wash Fault have been combined in Table 2.3.4-58 because they have the same fault displacement hazard curves.

2.3.4.5.5.4 Abstraction for Fault Damage

The expected number of waste package failures as a function of annual exceedance frequency is calculated by combining the data in Tables 2.3.4-57 and 2.3.4-58 and the results are summarized in Table 2.3.4-59. Smaller values of the exceedance frequency result in sequential failures on the West Ghost Dance Fault, the Sundance Fault, and at Sites 7a/8a, producing incremental increases in the number of package failures. In other words, lower values of exceedance frequency cause additional waste package failures on multiple faults within the repository.

When a waste package fails by fault displacement, the damaged area on the waste package is determined by sampling a uniform distribution with a lower bound of 0 m^2 and an upper bound equal to the area of the waste package lid (SNL 2007c, Section 6.11.5). The lower bound is appropriate for annual exceedance frequencies near 10^{-7} per year because a waste package that is minimally pinned from fault displacement is expected to have only minor crimping and is unlikely to rupture. The upper bound is only appropriate for a large fault displacement that shears a waste package near its lid. In this case, the lid welds have the potential to fracture, separating the lid from the package and potentially exposing the entire waste form to seepage and release. The use of a uniform distribution is appropriate here because reasonable upper and lower bounds can be defined and because the use of this type of distribution maintains the uncertainty in the damaged area for this abstraction. The area of the lid for the TAD and codisposal waste package groups is 2.78 m^2 and 3.28 m^2, respectively, based on the diameters of 1.8816 m, and 2.0447 m shown in Table 2.3.4-50.

When a waste package fails from modeled fault displacement, the associated drip shield is modeled to fail if it has not already failed (SNL 2007c, Section 6.11.5). A sheared drip shield is modeled to allow all seepage to pass through it; that is, there is no flux splitting (diversion of seepage) on the drip shield. This damage abstraction for the drip shield represents a bounding approximation, particularly for annual exceedance frequencies near 10^{-7} per year where the fault displacement is only slightly greater than the clearance around the waste package. In this situation there will be little deformation of the waste package and a shear is unlikely.

2.3.4.5.6 Postseismic Changes for the In-Drift Environment

[NUREG-1804, Section 2.2.1.3.2.3: AC 5(2), (3)]

A large seismic event, involving both vibratory ground motion and fault displacement, has the potential to change the local environment around the emplacement drifts. Drift collapse can alter

the shape of the drift and fill it with a natural backfill (Section 2.3.4.4), resulting in the following potential process-level changes in and around the EBS:

- Seepage may increase because of the irregular drift shape and because the presence of rubble in the drift reduces the capillary barrier at the rock interface.

- Temperature of the drip shield and waste package may increase relative to an unfilled drift because the backfill provides an insulating blanket on top of the drip shield (SNL 2008d, Section 6.3.7.1). General corrosion may increase because of increased temperature and because of rock and water contact with the drip shield or waste package.

In-drift chemistry is not changed in the rubble or invert after drift collapse and remains the same as in-drift chemistry for the nominal scenario class, based on excluded FEP 1.2.03.02.0E, Seismic-induced drift collapse alters in-drift chemistry, in Table 2.2-5.

2.3.4.5.6.1 Change in Seepage Flux into the Drift

The change in seepage flux to the emplacement drifts resulting from drift degradation is described in Section 2.3.3.2.4.2.2. As described in this section, the drift seepage conditions at any given time are categorized by assessing the rockfall volume that has accumulated in response to the multiple seismic events considered to occur up to this point in time. The rockfall volume, in turn, is linked to the magnitude of a seismic event by rocktype-specific regression functions given in *Seismic Consequence Abstraction* (SNL 2007c, Section 6.7.2.3), while the rockfall volume from multiple seismic events is calculated as the sum of the rockfall volumes from individual events.

A threshold rockfall volume of 0.5 m^3 per meter drift length is defined for nonlithophysal rocks as indicating minor to moderate levels of drift degradation. If the cumulative volume in a given drift section at a given time is smaller than this threshold, seepage is handled in the TSPA in the same manner as the nominal scenario, which assumes a 20% increase in the seepage rate for an intact drift based on the possibility that there may be some local rockfall even without seismic activity. If this threshold is exceeded, significant drift degradation is assumed and seepage is set equal to the local percolation flux arriving at the drift (i.e., the seepage percentage is set to 100%) as the capillary barrier is assumed to be destroyed.

In lithophysal zones, drifts are considered intact or moderately degraded in the seepage calculation if the cumulative volume is smaller than 5 m^3 per meter drift length (Section 2.3.3.2.4.2.2). If the cumulative volume in a given drift section at a given time is smaller than this threshold, seepage is handled in the TSPA in the same manner as the nominal scenario, which assumes a 20% increase in the seepage rate for an intact drift based on the possibility that there may be some local rockfall even without seismic activity. Drifts are considered fully collapsed if the cumulative rockfall volume is larger than 60 m^3 per meter drift length and the seepage is set equal to the local percolation flux (Section 2.3.3.2.4.2.2). In intermediate cases, seepage is interpolated between the results obtained for intact and collapsed drifts, using the cumulative rockfall volume as the interpolation parameter. Seepage lookup tables for collapsed and partially collapsed drifts were developed as described in Section 2.3.3.2.4.2.2.

2.3.4.5.6.2 Changes for a Collapsed Drift

The presence of rubble around the drip shield would cause changes in the temperature and relative humidity of EBS features. A parameter study was conducted to examine the impact of drift collapse on in-drift thermal-hydrologic parameters (SNL 2008d, Section 6.3.7). The multiscale thermal-hydrologic model was used to examine the effect of a collapsed drift on waste package and invert temperature and relative humidity at the waste package and invert. A collapsed drift is represented as having twice the initial diameter (i.e., 11-m collapsed diameter) and is filled with rubble with a bulking factor of 0.231. The thermal conductivity of the rubble (K_{th}) is defined as the intact rock thermal conductivity of the Tptpll multiplied by the factor, $1/(1 + BF)$, where BF is the bulking factor. Two thermal conductivity values (a high case based on a bulking factor of 0.231, and a low case which is taken to be half the high case value) of the dry and wet rubble thermal conductivity were used in the analyses.

Figure 2.3.4-98 shows the in-drift thermal-hydrologic parameters as functions of time from repository closure for the case of the hottest waste package. These plots show three cases: (1) an open, noncollapsed drift; (2) a collapsed, rubble-filled drift with high-K_{th} for the rubble; and (3) rubble-filled drift with low-K_{th}. The temperature (or any of the other environmental parameters plotted) will follow the intact drift curve until the assumed time of collapse. At that point, the temperature (or other parameters) is expected to increase or decrease toward the range defined by the curves for the collapsed drift with high and low thermal conductivity of the rubble.

Examination of the waste package temperature time history (Figure 2.3.4-98) shows that significant impact to peak waste package temperature results only if drift collapse occurs within the first 100 to 200 years after closure. After that time, the waste package temperature will always be below the peak temperature for the intact drift case, which occurs within about 20 to 30 years after closure. The total time at which the waste package surface remains above the boiling point of water for the hottest waste package case is approximately 1,000 years for the intact drift, 1,500 years for the high-K_{th} case, and 2,000 years for the low K_{th} case (SNL 2008d, Table 6.3-43). The relative humidity at the waste package decreases significantly in a collapsed drift because of the increase in local temperature. Results for the temperature and relative humidity time histories for nine representative waste package and drift configurations are defined by the calculations documented in *Multiscale Thermohydrologic Model* (SNL 2008d, Section 6.3.7 and Table 6.3-42).

For TSPA, degradation of the emplacement drifts in lithophysal rocks is determined from the abstraction for rubble accumulation presented in Section 2.3.4.4.8. This abstraction provides a relationship between the PGV of the ground motion and the volume of accumulated rubble in the drift. Temperature and humidity changes within the emplacement drift are determined based on the computational results in *Multiscale Thermohydrologic Model* (SNL 2008d).

2.3.4.6 Computational Algorithm for Seismic Scenario Class

[NUREG-1804, Section 2.2.1.3.2.3: AC 3(2), (3), AC 5(3)]

Complete details of the computational algorithm for the seismic scenario class are presented in *Seismic Consequence Abstraction* (SNL 2007c, Section 6.12). This section summarizes the key information from this report.

The dose calculation for the seismic scenario class is based on a set of *R* realizations that have robust sampling of all levels of seismic events (i.e., for the full ranges of PGV levels and fault displacement amplitudes) with the potential to generate releases from the EBS. The *R* realizations represent the future performance of the repository for the seismic hazards of ground motion and fault displacement. These realizations represent the combined epistemic and aleatory uncertainty in TSPA for the seismic scenario class. Epistemic uncertainty is captured by those stochastic parameters that represent the "lack of knowledge" uncertainty in various processes. Aleatory uncertainty is captured by the stochastic parameters that represent the randomness of processes, such as the uncertainty in the timing and amplitude of seismic events.

The seismic scenario class is very similar to the nominal scenario class, with the following notable differences: (1) breach of the waste package can occur from rupture, puncture, and stress corrosion cracking, in addition to damaged areas from general corrosion processes; (2) buckling and breach of the drip shield can occur from the dynamic amplification of static rockfall loads during a seismic event, in addition to general corrosion processes; (3) damaged area on the waste package is determined by sampling stochastic parameters in the seismic damage abstractions; and (4) the damaged area on the waste package is represented as a network of stress corrosion cracks, rather than as large breaches on the waste package or drip shield. The primary output from each of these *R* realizations is a time history of dose to the reasonably maximally exposed individual.

Seismic events occur randomly in time, and multiple seismic events will occur in each realization. For each seismic event, the value of the horizontal PGV, PGV_j, and its associated annual exceedance frequency, λ_j, are determined in a manner that is consistent with the mean bounded hazard curve. Once the value for PGV_j is known, the seismic damage abstractions for the waste package and drip shield are evaluated and sampled for each seismic event. This evaluation also requires: (1) the RST for Alloy 22 in the realization, denoted as RST_i; (2) the spatially averaged thickness of the outer corrosion barrier at the time of the seismic event; (3) the accumulated volume of lithophysal rubble in the emplacement drifts; and (4) the state of the internals. This approach explicitly propagates the variability from the structural response calculations and rockfall calculations into the TSPA through this sampling process (SNL 2007c, Section 6.12.1).

Damage from fault displacement occurs simultaneously with damage from vibratory ground motion (SNL 2007c, Section 6.12.1). The sampled value of λ_j determines the number of damaged waste packages by type. Simultaneous damage from fault displacement and vibratory ground motion is a reasonable approach for the seismic scenario class. A significant nearby earthquake simultaneously induces both ground motions and fault displacements. In the TSPA, all known onsite faults and generic (hypothetical) faults with a 2 m cumulative offset (Sites 7a/8a in the PSHA) are assumed to move simultaneously. This approach is conservative because it maximizes the potential for damage from the low probability seismic events with significant fault displacements.

2.3.4.6.1 Computational Approach

The abstractions for rupture/puncture and damaged area on the waste package are based on a three-part approach (SNL 2007c, Section 6.1.6):

- The probability of rupture or puncture occurring is defined as a function of PGV.
- The probability of nonzero damaged area is defined as a function of PGV and RST.
- When nonzero damaged area occurs, a conditional probability distribution for the magnitude of the conditional damaged area is defined as a function of PGV and RST. The conditional damaged areas are always nonzero areas, by definition.

This approach is useful because it eliminates zero values from the conditional probability distributions (SNL 2007c, Section 6.1.6).

The probability of rupture or puncture of an EBS feature is represented as a power law function with PGV as the independent variable (SNL 2007c, Section 6.1.6). The probability of nonzero damage is represented as simple lookup tables or as a quadratic function, each of which uses PGV and RST as the independent variables (SNL 2007c, Sections 6.5.1.2, 6.5.2.2, 6.6.1.2, and 6.6.2.2). The typical lookup table for probability of nonzero damage has 12 entries defined by four values of PGV (0.4 m/s, 1.05 m/s, 2.44 m/s, and 4.07 m/s) and by three values of RST (90%, 100%, and 105% of the yield strength of Alloy 22). A piecewise linear interpolation scheme is used between the points in the lookup table, avoiding the need for a functional fit to a probability surface. This is a simple and transparent approach that is consistent with the Monte Carlo computational approach in TSPA (SNL 2007c, Section 6.1.6).

When a seismic event occurs within a TSPA realization, the corresponding probability for rupture/puncture or for nonzero damage is calculated by evaluation of the power law function or by interpolation (or sometimes extrapolation for small values of PGV) within the lookup table (SNL 2007c, Section 6.1.6). These probabilities are compared to random numbers between 0 and 1 that are generally sampled for each seismic event. If the random number is less than or equal to the probability of rupture or puncture, then the component has failed by rupture or puncture during this event, and if the random number is greater than the probability of rupture or puncture, then the component remains intact. A similar procedure is used to determine if nonzero damage occurs during a seismic event. This sampling procedure is consistent with the Monte Carlo approach in TSPA, wherein rupture/damage does or does not occur during a given event.

The nonzero damaged areas, which are more precisely called the “conditional damaged areas,” are defined by conditional probability distributions whose parameters are functions of PGV and RST (SNL 2007c, Section 6.1.6). There are potentially 12 separate distributions for each of the four values of PGV and three values of RST, although it is often possible to simplify this representation. Five types of probability distributions have been considered to represent the conditional damaged areas: gamma, log-normal, normal, Weibull, and log-triangular.

A similar approach has been used for the abstractions for rubble volume in the lithophysal and nonlithophysal zones (SNL 2007c, Section 6.1.6). These abstractions are based on a two part approach:

- The probability of nonzero rockfall volume is defined as a function of PGV.
- When nonzero rockfall occurs, a conditional probability distribution for the magnitude of the conditional rockfall volume is defined as a function of PGV.

When a seismic event occurs within a TSPA realization, the corresponding probability for nonzero rockfall volume is calculated, based on the functional dependence on PGV (SNL 2007c, Section 6.1.6). This probability is compared to a random number between 0 and 1 that is sampled for each seismic event. If the random number is less than or equal to the probability of nonzero rockfall, then rockfall occurs for this event and its volume is determined by sampling the distribution for the conditional rockfall volume. If the random number is greater than the probability of rupture, then there is no rockfall for this event. The conditional rockfall volumes are defined by conditional probability distributions whose parameters are functions of PGV.

For each seismic event, the seismic damage abstractions are performed in the following sequence (SNL 2007c, Section 6.12.2):

- Volume of Rubble Abstraction (Section 2.3.4.4.8)
- Drip Shield Fragility Assessment (Section 2.3.4.5.3)
- Waste Package Damage Abstractions (Sections 2.3.4.5.2 and 2.3.4.5.4)
- Damage to the EBS Components from Fault Displacement (Section 2.3.4.5.5).

Volume of Rubble Abstraction—The volumes of lithophysal and nonlithophysal rockfall is defined as a function of the event PGV and total volume of rockfall for multiple events determined.

Drip Shield Fragility Assessment—The fragility of the drip shield plates in response to the event PGV (and estimated peak ground acceleration) is determined. The thickness of the Titanium Grade 7 plates is calculated by other components within the TSPA model based on the time of the event, the top-side and bottom-side corrosion rates for Titanium Grade 7, and the initial plate thickness. The static rubble load on the drip shield (based on the rubble volume from step 1) and the dynamic amplification based on the event peak vertical acceleration (on the basis of the PGV), is determined. Rubble load for lithophysal rock is used as it is the maximum load for lithophysal or nonlithophysal units.

The probability of plate failure is determined as a function of plate thickness, PGV of the seismic event, and rubble load on the drip shield. If the drip shield plates fail by tensile rupture, all drip shields in the repository are assumed to allow advection of liquids (i.e., there is no spatial variability in drip shield failure response in the seismic scenario in TSPA) (SNL 2007c, Section 6.8.2.2). This represents a permanent change in drip shield performance for the remainder of the realization. Waste package damage assessment is based on the waste package surrounded by rubble (see below).

If plates do not fail, then the fragility of the drip shield framework is examined. The fragility of the drip shield framework in response to the event PGV (and estimated peak ground acceleration) is determined. The thickness of the Titanium Grade 29 framework is calculated based on information from other components within the TSPA model based on the time of the event, the corrosion rates for Titanium Grade 29, and the initial framework thickness. The static rubble load on the drip shield (based on the rubble volume from step 1) and the dynamic amplification based on the event peak vertical acceleration (on the basis of the PGV) is determined. Rubble load for lithophysal rock is used as it is the maximum load for lithophysal or nonlithophysal units.

The probability of structural framework failure is determined as a function of the thickness of framework components, PGV of the seismic event, and rubble load. If the structural framework collapses, but the plates are not failed, the drip shield rests on the waste package, but continues to function as a feature that contributes to seepage barrier capability (Section 2.3.4.5.4.1). If a drip shield framework collapse occurs, all drip shields are assumed to collapse simultaneously as spatial variability is not taken into account in the seismic scenario (SNL 2008b, Section 6.6.1.2.2.1). This represents a permanent change in drip shield performance for the remainder of the realization. After drip shield collapse, waste package damage assessment is based on the degradation state of the internals (intact or degraded) (SNL 2007c, Section 6.8.4).

Waste Package Damage Abstractions—The waste package damage abstractions described in Section 2.3.4.5.2.1 are applicable when the drip shield remains intact. For a TAD-bearing or codisposal waste package, probability of rupture is determined based on the thickness of the outer corrosion barrier due to general corrosion thinning, the event PGV, intact or degraded internals, and accumulated deformation from multiple impacts. In the event of a rupture, the rupture is conceptualized as a circumferential tear of the outer corrosion barrier due to impact on the pallet. If the outer corrosion barrier of the waste package and the drip shield plates have ruptured, advective flow into the ruptured package and diffusive and advective flow out of the package is possible if seepage is present (SNL 2007c, Sections 6.5.2.1 and 6.6.2.1).

The next step is to determine the probability of nonzero damage. If damage has occurred, then damage area is determined based on the event PGV, the thickness of the general corrosion-thinned outer corrosion barrier, the RST for Alloy 22, and the state of the waste package internals (intact or degraded). The damaged area is predominantly on the cylindrical sides of the outer corrosion barrier because waste package-to-pallet impacts are the main cause of plastic deformation and damaged area. Diffusive transport of water vapor into and diffusive transport of radionuclides out of the package occurs through the network of stress corrosion cracks. The effective area for flow and transport is based on the crack density model and associated scaling factor for Alloy 22 defined in *Stress Corrosion Cracking of the Waste Package Outer Barrier and Drip Shield Materials* (SNL 2007a). The numerical values for the scaling factor are summarized in Section 2.3.4.5.1.4.1. The scaling factor for Alloy 22 is sampled once per realization because it represents epistemic rather than aleatory uncertainty. The effective flow and transport area for the waste package is much smaller than the damaged area because diffusion occurs through a network of stress corrosion cracks, rather than through the total damaged area that exceeds the RST.

The damage abstraction for the waste package surrounded by rubble (Section 2.3.4.5.4) is based on a TAD-bearing waste package with degraded internals, and is applied to all waste packages. Probability of puncture is determined based on the thickness of the outer corrosion barrier due to

general corrosion thinning, the event PGV, and the final deformed volume of the outer corrosion barrier. Failed area is determined and conceptualized as a small rip or tear on the surface of the outer corrosion barrier. Advective flow is assumed into the ruptured package and diffusive and advective flow out of the package (SNL 2007c, Section 6.9.1).

The next step is to determine the probability of nonzero damage. If damage has occurred, then damage area is determined based on the event PGV, the thickness of the general corrosion-thinned outer corrosion barrier, the RST for Alloy 22, and the state of the waste package internals (intact or degraded). The effective area for flow and transport is based on the crack density model and associated scaling factor for Alloy 22 defined in *Stress Corrosion Cracking of Waste Package Outer Barrier and Drip Shield Materials* (SNL 2007a), as discussed above.

Damage to the Drip Shield—Damage models for damaged area on the drip shield and tensile rupture of drip shield plates from rock block impacts have been developed but are not included in TSPA.

Damage to the EBS Components from Fault Displacement—The number of failed waste packages and the failed area on each package are based on the annual exceedance frequency corresponding to the PGV value for a seismic event. The number of failed waste packages is defined by Table 2.3.4-59. The failed area is based on a sampled value from a uniform distribution with a lower bound of zero and an upper bound defined by the lid area (Section 2.3.4.5.5.4). If a waste package fails from fault displacement, then any seepage can advect through the drip shield associated with this waste package.

2.3.4.6.2 Validation of Seismic Damage Abstractions

The validation activities for the seismic damage abstractions are documented in *Seismic Consequence Abstraction* (SNL 2007c, Section 7 and Appendix C). Validation activities were performed for the seismic damage abstractions for: (1) volume of rubble that accumulates in the drifts; (2) drip shield fragility curves and the damaged area on the drip shield plates in the lithophysal units; (3) rupture/puncture and damaged area on the waste package outer corrosion barrier; (4) rupture and damaged area on the drip shield plates in the nonlithophysal units; and (5) damage to EBS components from fault displacement. The waste package damage abstractions include those for the kinematic damage to the waste package (while the drip shield is intact), for the waste package surrounded by rubble, and for the waste package after the drip shield framework buckles. Each seismic damage abstraction has been validated by: (1) corroboration of the abstraction model results to the results of the validated structural response model or validated rockfall model from which the abstraction is derived; and (2) a technical review by an independent reviewer for postdevelopment model validation. Based on these validation activities, the seismic damage abstractions are considered to be sufficiently accurate and adequate for the representation of seismically induced damage to EBS components in the TSPA model.

2.3.4.7 Evaluation of Material Supporting Mechanical Disruption of the EBS

[NUREG-1804, Section 2.2.1.3.2.3: AC 1(1) to (4), AC 5; Section 2.2.1.3.3.3: AC 1(3), (4), AC 5(3)]

The material presented in Section 2.3.4 shows that the requirements of proposed 10 CFR 63.114 are addressed regarding the abstraction of mechanical disruption of the EBS in the performance assessment. In particular, Section 2.3.4 shows the following:

- Data from the site and surrounding region, uncertainties and variabilities in parameter values, and alternative conceptual models have been used in the analyses (Sections 2.3.4.3, 2.3.4.4, and 2.3.4.5).

- Specific FEPs have been included in the analyses, and appropriate technical bases have been provided (Section 2.2.1.2; Table 2.2-5; SNL 2008a, Section 6).

Coupling of processes is included in the analyses, as appropriate. The mechanical response of EBS features to rockfall induced by vibratory ground motion is included in the damage assessments for the seismic scenario class (Sections 2.3.4.4.8 to 2.3.4.5.4). The mechanical response of EBS features has taken into account the occurrence of multiple seismic events over long time periods in assessment of damage or rupture. In particular, the combined effect of static rock rubble load and the dynamic amplification from vibratory ground motion has been addressed in the damage assessments and assessment of structural stability (Sections 2.3.4.4.8 to 2.3.4.5.4). The coupled effects of drip shield plate or framework failure on waste package mechanical response and damage has been addressed in the seismic consequence abstraction (Sections 2.3.4.5.3, 2.3.4.5.4, and 2.3.4.6). General corrosion thinning of EBS features over time is included in structural models of the drip shield and waste packages (Sections 2.3.4.5.2 to 2.3.4.5.4). Potential degraded states of the waste package internals on the damage and rupture assessments of the waste package when subjected to combined static and dynamically amplified loading has been assessed and included in the seismic consequence scenario (Sections 2.3.4.5.2, 2.3.4.5.4, and 2.3.4.6). The thermal and hydrologic response of the in-drift environment to the presence of natural backfill after drift collapse is included in the assessment of seepage into the drifts, waste package temperature, waste package relative humidity, and in the potential for localized corrosion (Section 2.3.4.5.6).

2.3.4.8 Conclusions

The capability of the barriers at Yucca Mountain may be impacted by disruptive natural events, including igneous or seismic activity. Analyses have shown that the effect of seismic events on natural barrier capability is small, and the associated FEPs (e.g., changes in rock properties or hydrologic conditions due to seismic activity) have been excluded from performance assessment analyses (Table 2.2-5). In contrast, analyses indicate that mechanical disruption of the EBS after repository closure may have a significant effect on repository performance.

2.3.4.8.1 Summary of Significant Processes for Mechanical Degradation of the EBS

Three seismic-related included FEPs (Table 2.3.4-1) have been determined to be important to the capability of the EBS at Yucca Mountain (Tables 2.2-5 and 2.3.4-1):

- **Seismic Ground Motion Damages EBS Components**—Seismic activity that causes repeated vibration of the EBS components (drip shield, waste package, pallet, and invert) could result in severe disruption of the drip shields and waste packages, through vibration damage or through contact between EBS components. Such damage mechanisms could lead to degraded performance.

- **Seismic Induced Drift Collapse Damages EBS Components**—Seismic activity could produce jointed-rock motion and (or) changes in rock stress leading to enhanced rockfall that could impact drip shields, waste packages, or other EBS components.

- **Seismic Induced Drift Collapse Alters In-Drift Thermal Hydrology**—Seismic activity could produce jointed-rock motion and/or changes in rock stress leading to enhanced drift collapse and/or rubble infill throughout part or all of the drifts. Drift collapse could impact flow pathways and condensation within the EBS, mechanisms for water contact with EBS components, and thermal properties within the EBS.

Seismic hazard assessments account for both variability in vibratory ground motion and fault displacement due to the inherent randomness of earthquake processes and epistemic uncertainties. Large ground motions predicted by applying the PSHA ground motion models at annual exceedance probabilities of 10^{-6} and below overestimate the severity of low-probability ground motions at Yucca Mountain. A realistic and reasonable bound on peak horizontal ground velocity at the waste emplacement level was developed based on the physical and geologic properties of the tuff units at Yucca Mountain. Seismic and tectonic effects on the natural systems at Yucca Mountain will not significantly affect repository performance, as deformation rates are too slow to have significant mechanical impacts to the mountain during the period of geologic stability.

Industry-standard, state-of-the-art approaches and models have been used to assess rockfall and EBS structural response (Sections 2.3.4.4 and 2.3.4.5). Models developed for analysis of rockfall represent the thermal-mechanical and dynamic response of the lithophysal and nonlithophysal fractured rock mass units. The models are based on site-specific geology of the repository and account for variability and uncertainty in geologic structure and properties. Analysis of the static, dynamic, and long-term creep response of EBS features was performed using two- and three-dimensional structural analyses in which the applied loading, corrosion-related thinning of the materials, material property, and material failure criteria assumptions incorporate uncertainty and variability.

The mechanical degradation of EBS features is abstracted for the TSPA (Section 2.3.4.6). Mathematical relationships of rockfall accumulation and drip shield and waste package damage and rupture probability in terms of the magnitude of the seismic event (expressed in terms of the PGV) have been developed for application in the TSPA. The impact of multiple seismic events on rockfall and rubble accumulation, static and dynamically amplified loading, and the accumulation of damage and rupture potential for the drip shield and waste package over time have been abstracted

to the TSPA. Future states of degradation of EBS components occurring over long time frames have been taken into account in the mechanical response calculations. These include the following: (1) the impact of long-term corrosion of EBS features on load-bearing capacity and mechanical response; (2) degradation of the waste package internal structures and its impact on mechanical response of the waste package outer corrosion barrier; (3) degradation of the invert and its impact on settlement and stability of the drip shield; (4) accumulation of deformation and damage on the drip shield and waste package and the impact on damage and rupture potential resulting from multiple seismic events; and (5) the effect of the ultimate failure of the drip shield on the damage and rupture probability of the waste package. Finally, the effects of emplacement drift collapse on the in-drift environment after a seismic event are defined as boundary conditions for other process model abstractions within the TSPA (Section 2.3.4.5.6).

The results presented in Section 2.3.4.5 indicate that the EBS features are robust and remain robust under seismic loads and will contribute to the ability of the EBS to prevent or substantially reduce the release of radionuclides from the waste and the movement of water and radionuclides to the accessible environment. Various damage mechanisms to EBS features are possible as the mechanical response of EBS features evolve. These damage modes include the following: (1) development of a network of stress corrosion cracks on the waste package surface in areas where the RST for Alloy 22 has been exceeded; (2) tensile rupture or puncture of the drip shield or waste package when the tensile strain limit of Alloy 22 or Titanium Grade 7 is exceeded or when multiple, high-deformation impacts to the waste package outer corrosion barrier occur; and (3) collapse of the framework of the drip shield. These damage modes are the result of three basic mechanisms: (1) rockfall on the drip shield or waste package due to seismic loading of the rock mass; (2) dynamic amplification of the rockfall loads by multiple seismic events; and (3) multiple events of vibratory motion of the waste package, pallet, and drip shield. As described in the previous paragraph, the evolution of the EBS features due to future degradation states results in additional considerations related to these basic mechanisms that are important to understand EBS feature damage.

The seismic scenario class considers the full range of PGV levels with the potential to cause damage to the waste package and drip shield. Vibratory ground motions with PGV levels below 0.219 m/s do not damage the waste package with intact or degraded internals (Section 2.3.4.5.2.1.4.3; SNL 2007c, Section 6.6.2.2). The methodology for redefining the probabilities of nonzero damaged area at the 0.4 m/s PGV level and the extrapolation of these results to 0.219 m/s are described in Section 2.3.4.5.2.1.4.3. This PGV level corresponds to the 4.3×10^{-4} annual exceedance frequency on the bounded hazard curve. PGV levels above 4.07 m/s are not considered in the seismic scenario class because these levels occur with less than a 10^{-8} annual exceedance frequency, the lower limit in NRC regulations (10 CFR 63.114(d)).

The kinematic response of the waste packages, when the drip shields are intact, may cause damaged areas in the outer corrosion barrier from end-to-end impacts and waste package-pallet impacts. The magnitude of the damaged area is a function of the type of waste package, TAD-bearing or codisposal, and of the state of the internals, intact or degraded. The TAD-bearing waste package with intact internals will not experience (0 probability) a damaged area below the 2.44 m/s PGV level for an RST of 90% of the yield strength of Alloy 22. The mean damaged area at the 4.07 m/s PGV level is 0.004 m^2, insignificant in comparison to the typical surface area of the TAD-bearing waste package of approximately 40 m^2. The TAD-bearing waste package with degraded internals has mean conditional damaged areas of 0.7 m^2 and 4.5 m^2 for the 90% RST and a 23-mm-thick outer

corrosion barrier at the 1.05 m/s and 4.07 m/s PGV levels, respectively. Mean conditional damaged areas are a factor of 3 to 4 less for the 105% RST. Conditional damaged areas are slightly greater for a 17-mm-thick outer corrosion barrier and 90% RST: 0.8 m^2 and 5.4 m^2 at the 1.05 m/s and 4.07 m/s PGV levels. The mean conditional damaged areas for the codisposal waste packages with degraded internals have similar magnitudes.

A waste package with a 23-mm-thick outer corrosion barrier and degraded internals that is surrounded by rubble also will not experience (0 probability) a damaged area below the 2.44 m/s PGV level. The mean conditional damaged area at the extreme 4.07 m/s PGV level is 3.8 m^2, 1.2 m^2, and 1.0 m^2 at the 90%, 100%, and 105% RST levels, respectively. The mean conditional damaged areas at the 2.44 m/s PGV level are 0 at these RST levels.

Ground motion and fault displacement are assumed to occur simultaneously in each seismic event in TSPA. The sampled value of the annual exceedance frequency for each seismic event is applied to the hazard curves for PGV and for fault displacement. However, no damage from fault displacement is predicted for mean fault displacements with annual exceedance probabilities greater than 2.5×10^{-7}. Even at the smallest annual exceedance probability considered by the TSPA (10^{-8}), a total of 214 waste packages (Table 2.3.4-59) are predicted to be damaged by fault displacement out of a total of 11,162 waste packages expected in the repository (Table 2.3.4-56).

The impact of seismically induced drift collapse on the in-drift temperature and humidity environment and on seepage has also been determined. Analyses indicate that even the conservative case of complete emplacement drift collapse has only minor effects on waste package temperature if it occurs more than a few hundred years after closure of the repository, and the rare seismic events that could trigger such a collapse are not likely during the first few hundred years. Humidity within the emplacement drifts decreases substantially in the event of rubble filling the emplacement drifts.

2.3.4.8.2 Summary of Key Uncertainties Associated with Mechanical Degradation of the EBS

Variability and uncertainty has been incorporated into models and analyses of mechanical degradation of the EBS through several methods. In the PSHA, expert teams with a broad range of experience and background used a formal, documented process of expert elicitation to generate ground motion and fault displacement hazard curves (Section 2.2.2.1). The teams used available site-specific information and their expertise in tectonics and seismic hazard evaluation to develop alternative seismic-source models. The seismic source characterization was integrated with ground motion attenuation evaluations to develop seismic hazard curves. Characterization of uncertainties was a key element of the PSHA, and several approaches were used (Section 2.2.2.1.5). A logic tree approach was used to document and incorporate the uncertainties related to different interpretations permitted by the available data (epistemic uncertainty) (Section 2.2.2.1.1.1). Alternative models reflecting the uncertainty in scientific understanding were identified and assigned weights that address their likelihood. Variability in earthquake location, timing, and magnitude due to the random nature of earthquake occurrences (aleatory uncertainty) was expressed by defining random variables that are specified in each model.

Each hazard curve incorporates the variability in ground motion due to the inherent randomness of earthquake processes, and the range of hazard curves reflects scientific uncertainty due to limits on

available information about earthquake ground motions (Section 2.3.4.3.2, particularly Approach 3). The variability and uncertainty are carried forward into the TSPA through the use of mean hazard curves as the basis for development of multiple ground-motion time histories for postclosure rockfall and structural response calculations (Section 2.3.4.3.2.1).

In addition to the PSHA, each of the major analyses that contribute to the assessment of the mechanical degradation of the EBS consider and incorporate uncertainty and variability in both data and models. These analyses include ground motion, rockfall, structural damage to EBS features (drip shield, waste package and emplacement pallet, and invert) due to drift degradation, vibratory ground motion and fault displacement, and postseismic changes to the in-drift environment. Each analysis accounts for the uncertainty and variability of site properties (e.g., rock mechanical properties, fault and fracture properties, thermal properties), and engineered material properties (Alloy 22 and Titanium Grades 7 and 29) as well as uncertainties associated with the processes used to simulate repository behavior. Detailed descriptions of the treatment of uncertainty are presented throughout Sections 2.3.4.3 (ground motion analyses), 2.3.4.4 (rockfall analyses), and 2.3.4.5 (structural response of EBS features). Uncertainties associated with future conditions or states of degradation of the EBS features over the long time frames of the peak dose assessment has been accounted for in the calculation of damage. These future states include multiple seismic events, general corrosion thinning of structural components, degradation of waste package internals, accumulation of deformation and damage, and the impact of failure of the drip shield on waste package damage response.

The nonzero damaged areas or nonzero rockfall volumes are represented in TSPA by conditional probability distributions. Normal, log-normal, log-triangular, Weibull, and gamma distributions were evaluated as alternate conceptual models for the computational data. The gamma distribution has usually been selected because it provides a good to excellent fit to the computational data and because its input parameters, which are the mean and standard deviation of the computational data set, are defined without recourse to engineering judgment or other numerical adjustment.

The TSPA abstraction for mechanical degradation of the EBS incorporates uncertainty by utilizing a stochastic approach to represent the variability and uncertainty in the underlying process models. Multiple realizations represent the combined epistemic and aleatory uncertainty for the seismic scenario class. These uncertainties include the likelihood and magnitude of seismic events, as expressed in hazard curves for ground motion and fault displacement. Uncertainty in the extent of damage to EBS features is represented by probability distributions of damaged areas and rupture of the waste package and drip shield, as well as collapse potential of the drip shield as a function of the number and amplitude of multiple seismic events.

2.3.4.8.3 Summary of Key Limitations/Conservatisms in Models Used to Assess Mechanical Degradation of the EBS.

The major limitations of the postclosure abstractions for the seismic scenario class and any associated conservatisms are as follows (SNL 2007c, Section 6.13):

- Waste package internals are assumed to degrade as structural elements after the outer corrosion barrier is first damaged by a seismic event (SNL 2007c, Assumption 5.4, Section 5) or by general corrosion processes as described in Section 2.4. This approach is

conservative because a waste package with degraded internals has significantly greater deformation and probability of rupture relative to a waste package with intact internals (SNL 2007c, Sections 6.5.1 versus 6.5.2 and 6.6.1 versus 6.6.2). This approach also underestimates the structural capacity of stainless steel internal components, such as the two-inch-thick inner vessel or the TAD canister itself.

- Spatial variability in the mechanical response of waste packages and drip shields to vibratory ground motion has not been represented in the TSPA. In other words, damage to the waste package and drip shield from vibratory ground motion is constant throughout the repository for each seismic event. Although spatial variability is not included within the TSPA, it has been included in the kinematic calculations through the variability of friction factors on a package-by-package basis and in the abstraction of damaged areas for the two or three central waste packages in the kinematic calculations.

- Structural response calculations for the waste package surrounded by rubble are based on the TAD-bearing waste package with degraded internals. *Seismic Consequence Abstraction* (SNL 2007c, Section 6.9.10) provides the rationale for using the results for the TAD-bearing waste package with degraded internals for the codisposal waste package with degraded internals.

- The waste package internals, including the inner vessel and TAD canister, are always degraded when surrounded by rubble. The use of degraded internals is consistent with the fact that the waste package becomes surrounded by rubble at late times, after the drip shield plates have failed and allowed rubble to contact the waste package. The use of degraded internals is conservative because damage to a waste package with degraded internals is observed to be significantly greater than damage to a waste package with intact internals (SNL 2007c, Sections 6.5.1 versus 6.5.2 and 6.6.1 versus 6.6.2).

2.3.4.8.4 Summary of Consistency Between TSPA Model Abstractions and Process Models

Mechanical degradation of the EBS is incorporated in the seismic scenario modeling case in a way that is consistent with the underlying process models and analyses, as explained in detail in *Seismic Consequence Abstraction* (SNL 2007c, Section 8.2). The outputs of the process models are used to generate abstractions that correlate damage to EBS features with the range of effects caused by seismic events (Section 2.3.4.6). The abstractions incorporate the variability and uncertainty in both the causative seismic and drift degradation processes and the resulting damage to EBS features. The abstractions account for future degradation states and multiple seismic events that will occur over the extended time periods of the peak dose assessment of TSPA.

Both the process models and abstractions are also treated consistently with other components of the TSPA models. The seismic scenario modeling case utilizes the same downstream process models for EBS flow and transport, flow and radionuclide transport through the unsaturated and saturated zones, and biosphere transport to calculate dose to the RMEI as the nominal scenario class does. Input from the nominal scenario, including general corrosion rates of EBS features, are taken into account. As appropriate, outputs from the model for mechanical damage to the EBS are represented

as postseismic changes to the in-drift environment for seepage and for a collapsed drift (Section 2.3.4.5.6).

2.3.4.8.5 Summary of Key Output Parameters Provided to TSPA

The seismic scenario class is represented by two modeling cases (Section 2.4.2.3.2.1.12.3). The first case is the ground motion modeling case, where waste packages can be breached by the effects of vibratory ground motion and the drip shield fragility is a function of vibratory ground motion and lithophysal rockfall induced by vibratory ground motion. The second modeling case is the fault displacement case, where waste packages and drip shields can be breached by the effects of fault displacement.

The outputs from the process models for mechanical degradation of the EBS to the seismic consequence abstraction include ground motion and fault displacement hazard curves, as well as information related to drift collapse and ground motion-related damage to EBS features. This information includes dynamic and static loads on the drip shield resulting from rockfall and seismically induced dynamic and residual stresses in the drip shield and waste package and considers stress corrosion cracking and rupture or puncture failure thresholds for Alloy 22 and Titanium Grade 7 as well as the plastic collapse load limit of the drip shield framework. The impact of future states including multiple seismic events, general corrosion thinning, degradation of waste package internals, accumulation of deformation and damage from multiple events, and the eventual failure of the drip shield are included in the abstractions. Evaluation of postseismic changes to the in-drift environment is also provided to the abstraction.

The abstraction of mechanical degradation of the EBS is used to generate inputs to the TSPA model. These include the horizontal PGV hazard curve at the repository, the results of the waste package damage and rupture probability abstractions and drip shield damage, plate rupture or framework collapse probability abstractions for vibratory ground motion, and the results of the waste package and drip shield damage abstractions for fault displacement (Figure 2.3.4-2 and Section 2.3.4.6). The abstraction results are probabilistic distributions that correlate the extent of waste package damage or rupture probability and drip shield rupture or collapse probability to the EBS feature with the amplitude of the seismic event.

2.3.4.9 General References

Albin, A.L.; Singleton, W.L.; Moyer, T.C.; Lee, A.C.; Lung, R.C.; Eatman, G.L.W.; and Barr, D.L. 1997. *Geology of the Main Drift—Station 28+00 to 55+00, Exploratory Studies Facility, Yucca Mountain Project, Yucca Mountain, Nevada.* Milestone SPG42AM3. Denver, Colorado: Bureau of Reclamation and U.S. Geological Survey. ACC: MOL.19970625.0096.

Altman, W.D.; Donnelly, J.P.; and Kennedy, J.E. 1988a. *Peer Review for High-Level Nuclear Waste Repositories: Generic Technical Position.* NUREG-1297. Washington, D.C.: U.S. Nuclear Regulatory Commission. TIC: 200651.

Altman, W.D.; Donnelly, J.P.; and Kennedy, J.E. 1988b. *Qualification of Existing Data for High-Level Nuclear Waste Repositories: Generic Technical Position.* NUREG-1298. Washington, D.C.: U.S. Nuclear Regulatory Commission. TIC: 200652.

ASTM B 265-02. 2002. *Standard Specification for Titanium and Titanium Alloy Strip, Sheet, and Plate.* West Conshohocken, Pennsylvania: American Society for Testing and Materials. TIC: 254000.

Barr, D.L.; Moyer, T.C.; Singleton, W.L.; Albin, A.L.; Lung, R.C.; Lee, A.C.; Beason, S.C.; and Eatman, G.L.W. 1996. *Geology of the North Ramp—Stations 4+00 to 28+00, Exploratory Studies Facility, Yucca Mountain Project, Yucca Mountain, Nevada.* Denver, Colorado: U.S. Geological Survey. ACC: MOL.19970106.0496.

Barton, C.C.; Larsen, E.; Page, W.R.; and Howard, T.M. 1993. *Characterizing Fractured Rock for Fluid-Flow, Geomechanical, and Paleostress Modeling: Methods and Preliminary Results from Yucca Mountain, Nevada*. Open-File Report 93-269. Denver, Colorado: U.S. Geological Survey. ACC: NNA.19931026.0008.

Beason, S.C.; Turlington, G.A.; Lung, R.C.; Eatman, G.L.W.; Ryter, D.; and Barr, D.L. 1996. *Geology of the North Ramp—Station 0+60 to 4+00, Exploratory Studies Facility, Yucca Mountain Project, Yucca Mountain, Nevada.* Denver, Colorado: U.S. Geological Survey. ACC: MOL.19970106.0449.

Beavers, J.A.; Devine, T.M., Jr.; Frankel, G.S.; Jones, R.H.; Kelly, R.G.; Latanision, R.M.; and Payer, J.H. 2002. *Final Report, Waste Package Materials Performance Peer Review Panel, February 28, 2002*. Las Vegas, Nevada: Waste Package Materials Performance Peer Review Panel. ACC: MOL.20020614.0035.

Behn, G. and Brzovic, A. 1996. *Determinacion Gravimetrica de la Densidad del Material Quebrado Remanente del Crater Teniente.* Santiago, Chile: CODELCO, Division El Teniente. TIC: 259287.

Brekke, T.L.; Cording, E.J.; Daemen, J.; Hart, R.D.; Hudson, J.A.; Kaiser, P.K.; and Pelizza, S. 1999. *Panel Report on the Drift Stability Workshop, Las Vegas, Nevada, December 9–11, 1998.* Las Vegas, Nevada: Management and Technical Support Services. ACC: MOL.19990331.0102.

Brodsky, N.S.; Riggins, M.; Connolly, J.; and Ricci, P. 1997. *Thermal Expansion, Thermal Conductivity, and Heat Capacity Measurements for Boreholes UE25 NRG-4, UE25 NRG-5, USW NRG-6, and USW NRG-7/7A.* SAND95-1955. Albuquerque, New Mexico: Sandia National Laboratories. ACC: MOL.19980311.0316.

BSC (Bechtel SAIC Company) 2002. *Geotechnical Data for a Potential Waste Handling Building and for Ground Motion Analyses for the Yucca Mountain Site Characterization Project.* ANL-MGR-GE-000003 REV 00. Las Vegas, Nevada: Bechtel SAIC Company. ACC: MOL.20021004.0078.

BSC 2003a. *Underground Layout Configuration.* 800-P0C-MGR0-00100-000-00E. Las Vegas, Nevada: Bechtel SAIC Company. ACC: ENG.20031002.0007; ENG.20050817.0005.

BSC 2003b. *Scoping Analysis on Sensitivity and Uncertainty of Emplacement Drift Stability.* 800-K0C-TEG0-00600-000-000. Las Vegas, Nevada: Bechtel SAIC Company. ACC: ENG.20031125.0002.

BSC 2004a. *Drift Degradation Analysis*. ANL-EBS-MD-000027 REV 03. Las Vegas, Nevada: Bechtel SAIC Company. ACC: DOC.20040915.0010.

BSC 2004b. *Development of Earthquake Ground Motion Input for Preclosure Seismic Design and Postclosure Performance Assessment of a Geologic Repository at Yucca Mountain, NV.* MDL-MGR-GS-000003 REV 01. Las Vegas, Nevada: Bechtel SAIC Company. ACC: DOC.20041111.0006.

BSC 2004c. *Yucca Mountain Site Description.* TDR-CRW-GS-000001 REV 02 ICN 01. Two volumes. Las Vegas, Nevada: Bechtel SAIC Company. ACC: DOC.20040504.0008.

BSC 2004d. *Thermal Conductivity of the Potential Repository Horizon*. MDL-NBS-GS-000005 REV 01. Las Vegas, Nevada: Bechtel SAIC Company. ACC: DOC.20040928.0006.

BSC 2004e. *Heat Capacity Analysis Report.* ANL-NBS-GS-000013 REV 01. Las Vegas, Nevada: Bechtel SAIC Company. ACC: DOC.20041101.0003.

BSC 2004f. *Ventilation Model and Analysis Report*. ANL-EBS-MD-000030 REV 04. Las Vegas, Nevada: Bechtel SAIC Company. ACC: DOC.20041025.0002.

BSC 2004g. *Sampling of Stochastic Input Parameters for Rockfall and Structural Response Calculations Under Vibratory Ground Motion.* ANL-EBS-PA-000009 REV 01. Las Vegas, Nevada: Bechtel SAIC Company. ACC: DOC.20040901.0004.

BSC 2004h. *Mechanical Assessment of the Drip Shield Subject to Vibratory Motion and Dynamic and Static Rock Loading.* CAL-WIS-AC-000002 REV 00A. Las Vegas, Nevada: Bechtel SAIC Company. ACC: DOC.20041028.0004.

BSC 2004i. *Estimation of Mechanical Properties of Crushed Tuff for Use as Ballast Material in Emplacement Drifts.* 800-CYC-SSE0-00100-000-00A. Las Vegas, Nevada: Bechtel SAIC Company. ACC: ENG.20040309.0023.

BSC 2005a. *Peak Ground Velocities for Seismic Events at Yucca Mountain, Nevada.* ANL-MGR-GS-000004 REV 00. Las Vegas, Nevada: Bechtel SAIC Company. ACC: DOC.20050223.0002.

BSC 2005b. *Intact Rock Mechanical Properties of Yucca Mountain Stratigraphic Units.* 800-K0C-SS00-00800-000-00A. Las Vegas, Nevada: Bechtel SAIC Company. ACC: ENG.20051108.0007.

BSC 2005c. *Mechanical Assessment of the Waste Package Subject to Vibratory Ground Motion.* CAL-WIS-AC-000001 REV 0B. Las Vegas, Nevada: Bechtel SAIC Company. ACC: DOC.20050823.0001.

BSC 2005d. *Creep Deformation of the Drip Shield*. CAL-WIS-AC-000004 REV 00A. Las Vegas, Nevada: Bechtel SAIC Company. ACC: DOC.20050830.0007.

BSC 2006a. *Naval Long Waste Package for License Application*. 000-MWK-DNF0-00101-000-00A. Las Vegas, Nevada: Bechtel SAIC Company. ACC: ENG.20060227.0002.

BSC 2006b. *Naval Long Waste Package for License Application*. 000-MWK-DNF0-00102-000-00A. Las Vegas, Nevada: Bechtel SAIC Company. ACC: ENG.20060227.0003.

BSC 2006c. *Naval Long Waste Package for License Application*. 000-MWK-DNF0-00103-000-00A. Las Vegas, Nevada: Bechtel SAIC Company. ACC: ENG.20060027.0004.

BSC 2006d. *Naval Long Waste Package for License Application*. 000-MWK-DNF0-00104-000-00A. Las Vegas, Nevada: Bechtel SAIC Company. ACC: ENG.20060227.0005.

BSC 2007a. *Subsurface Geotechnical Parameters Report.* ANL-SSD-GE-000001 REV 00. Las Vegas, Nevada: Bechtel SAIC Company. ACC: ENG.20070115.0006.

BSC 2007b. *IED Interlocking Drip Shield.* 800-IED-SSE0-00101-000 REV 00C. Las Vegas, Nevada: Bechtel SAIC Company. ACC: ENG.20070913.0011.

BSC 2007c. *IED Emplacement Drift Configuration and Environment.* 800-IED-MGR0-00501-000 REV 00B. Las Vegas, Nevada: Bechtel SAIC Company. ACC:ENG.20070716.0006.

BSC 2007d. *Drip Shield and Waste Package Emplacement Pallet Design Report*. 000-00C-SSE0-00100-000-00B. Las Vegas, Nevada: Bechtel SAIC Company. ACC: ENG.20070810.0008.

BSC 2007e. *Drift Cross Section Showing Emplaced Waste Package and Drip Shield.* 800-M00-WIS0-00101-000 REV 00B. Las Vegas, Nevada: Bechtel SAIC Company. ACC: ENG.20070412.0003.

BSC 2007f. *IED-Subsurface Facilities Layout Geographical Data*. 800-IED-WIS0-01701-000 REV 00C. Las Vegas, Nevada: Bechtel SAIC Company. ACC: ENG.20071211.0007.

BSC 2008. *Supplemental Earthquake Ground Motion Input for a Geologic Repository at Yucca Mountain, NV.* MDL-MGR-GS-000007 REV 00. Las Vegas, Nevada: Bechtel SAIC Company. ACC: DOC.20080221.0001.

Budnitz, R.J.; Apostolakis, G.; Boore, D.M.; Cluff, L.S.; Coppersmith, K.J.; Cornell, C.A.; and Morris, P.A. 1997. *Recommendations for Probabilistic Seismic Hazard Analysis: Guidance on the Uncertainty and Use of Experts.* NUREG/CR-6372. Two volumes. Washington, D.C.: U.S. Nuclear Regulatory Commission. TIC: 235076.

Buzzard, P. and Cornell, C.A. 2004. "Nonlinear Soil-Site Effects in Probabilistic Seismic-Hazard Analysis." *Bulletin of the Seismological Society of America, 94,* (6), 2110–2123. El Cerrito, California: Seismological Society of America. TIC: 257584.

Corradini, Michael L. 2003. "Responses and Evaluation from the Nuclear Waste Technical Review Board to the U.S. Department of Energy: Presentations given at the February 2003 Joint Meeting held by the Natural System and Engineered System Panel Discussing Seismic Issues." Letter from Michael L. Corradini (NWTRB) to Dr. Margaret Chu (DOE/OCWRM), June 27, 2003. ACC: HQO.20031017.0002.

CRWMS M&O (Civilian Radioactive Waste Management System Management and Operating Contractor)1998. *Probabilistic Seismic Hazard Analyses for Fault Displacement and Vibratory Ground Motion at Yucca Mountain, Nevada.* Milestone SP32IM3, September 23, 1998. Three volumes. Las Vegas, Nevada: Civilian Radioactive Waste Management System Management and Operating Contractor. ACC: MOL.19981207.0393.

Day, W.C.; Dickerson, R.P.; Potter, C.J.; Sweetkind, D.S.; San Juan, C.A.; Drake, R.M., II; and Fridrich, C.J. 1998. *Bedrock Geologic Map of the Yucca Mountain Area, Nye County, Nevada.* Geologic Investigations Series I-2627. Denver, Colorado: U.S. Geological Survey. ACC: MOL.19981014.0301.

Duncan, J.M.; Byrne, P.; Wong, K.S.; and Mabry, P. 1980. *Strength, Stress-Strain and Bulk Modulus Parameters for Finite Element Analyses of Stresses and Movements in Soil Masses.* UCB/GT/80-01. Berkeley, California: University of California, College of Engineering, Office of Research Services. TIC: 253873.

Dunne, W.M.; Ferrill, D.A.; Crider, J.G.; Hill, B.E.; Waiting, D.J.; La Femina, P.C.; Morris, A.P.; and Fedors, R.W. 2003. "Orthogonal Jointing During Coeval Igneous Degassing and Normal Faulting, Yucca Mountain, Nevada." *Geological Society of America Bulletin*, *115*, (12), 1492–1509. Boulder, Colorado: Geological Society of America. TIC: 256766.

Eatman, G.L.W.; Singleton, W.L.; Moyer, T.C.; Barr, D.L.; Albin, A.L.; Lung, R.C.; and Beason, S.C. 1997. *Geology of the South Ramp—Station 55+00 to 78+77, Exploratory Studies Facility, Yucca Mountain Project, Yucca Mountain, Nevada.* Denver, Colorado: U.S. Department of Energy. ACC: MOL.19980127.0396.

EPRI (Electric Power Research Institute) 1993. "Appendices for Ground Motion Estimation." *Volume 2 of Guidelines for Determining Design Basis Ground Motions*. EPRI TR-102293. Palo Alto, California: Electric Power Research Institute. TIC: 226496.

George, J.T.; Finley, R.E.; and Riggins, M. 1999. "Conduct of Plate Loading Tests at Yucca Mountain, Nevada." *Rock Mechanics for Industry, Proceedings of the 37th U.S. Symposium, Vail, Colorado, USA, 6–9 June, 1999*, Amadei, B.; Kranz, R.L.; Scott, G.A.; and Smeallie, P.H.; eds. *2,* 721–727. Brookfield, Vermont: A.A. Balkema. TIC: 245246.

Goodman, R.E. 1980. *Introduction to Rock Mechanics*. New York, New York: John Wiley & Sons. TIC: 218828.

Kotra, J.P.; Lee, M.P.; Eisenberg, N.A.; and DeWispelare, A.R. 1996. *Branch Technical Position on the Use of Expert Elicitation in the High-Level Radioactive Waste Program*. NUREG-1563. Washington, D.C.: U.S. Nuclear Regulatory Commission. TIC: 226832.

Kranz, R.L. 1979. "Crack Growth and Development During Creep of Barre Granite." *International Journal of Rock Mechanics, Mining Sciences & Geomechanical Abstracts, 16*, 23–35. New York, New York: Pergamon. TIC: 255955.

Laubscher, D.H. 1994. "Cave Mining—State of the Art." *Journal of the South African Institute of Mining and Metallurgy, 94,* (10), 279–293. Johannesburg, South Africa: South African Institute of Mining and Metallurgy. TIC: 259288.

Manjoine, M.J. 1983. "Damage and Failure at Elevated Temperature." *Transactions of the ASME, 105,* 58-62. New York, New York: American Society of Mechanical Engineers. TIC: 258853.

Martin, R.J., III 1972. "Time-Dependent Crack Growth in Quartz and Its Application to the Creep of Rocks." *Journal of Geophysical Research, 77* (8), 1406–1419. Washington, D.C.: American Geophysical Union. TIC: 224770.

Martin, R.J.; Noel, J.S.; Boyd, P.J.; and Price, R.H. 1997a. "Creep and Static Fatigue of Welded Tuff from Yucca Mountain, Nevada." *International Journal of Rock Mechanics and Mining Sciences, 34* (3/4), 382. New York, New York: Elsevier. TIC: 250241.

Martin, R.J.; Noel, J.S.; Boyd, P.J.; and Price, R.H. 1997b. *Creep Properties of the Paintbrush Tuff Recovered from Borehole USW NRG-7/7A: Data Report.* SAND95-1759. Albuquerque, New Mexico: Sandia National Laboratories. ACC: MOL.19971017.0661.

Martin, R.J., III; Price, R.H.; Boyd, P.J.; and Noel, J.S. 1993. *Unconfined Compression Experiments on Topopah Spring Member Tuff at 22°C and a Strain Rate of 10^{-9} s^{-1}: Data Report.* SAND92-1810. Albuquerque, New Mexico: Sandia National Laboratories. ACC: NNA.19930728.0088.

Martin, R.J., III; Price, R.H.; Boyd, P.J.; and Noel, J.S. 1995. *Creep in Topopah Spring Member Welded Tuff.* SAND94-2585. Albuquerque, New Mexico: Sandia National Laboratories. ACC: MOL.19950502.0006.

McGuire, R.K.; Silva, W.J.; and Costantino, C.J. 2001. *Technical Basis for Revision of Regulatory Guidance on Design Ground Motions: Hazard- and Risk-Consistent Ground Motion Spectra Guidelines.* NUREG/CR-6728. Washington, D.C.: U.S. Nuclear Regulatory Commission.TIC: 251294.

MO0401MWDRPSHA.000. Results of the Yucca Mountain Probabilistic Seismic Hazard Analysis (PSHA). Submittal date: 03/13/2008.

Mongano, G.S.; Singleton, W.L.; Moyer, T.C.; Beason, S.C.; Eatman, G.L.W.; Albin, A.L.; and Lung, R.C. 1999. *Geology of the ECRB Cross Drift–Exploratory Studies Facility, Yucca Mountain*

Project, Yucca Mountain, Nevada. Deliverable SPG42GM3. Denver, Colorado: U.S. Geological Survey. ACC: MOL.20000324.0614.

MRD (Mining Research Directorate) 1995. *Rockburst Research Handbook, Canadian Rockburst Research Program 1990–1995.* Six volumes. Sudbury, Canada: Canadian Mining Industry Research Organization, Mining Division. TIC: 256095.

NNSA (National Nuclear Security Administration) 2005. *Design and Development Guide for NNSA Type B Packages.* SG1-00, Rev. 2. Albuquerque, New Mexico: U.S. Department of Energy, National Nuclear Security Administration. ACC: MOL.20070220.0128.

Olsson, W.A. and Jones, A.K. 1980. *Rock Mechanics Properties of Volcanic Tuffs from the Nevada Test Site.* SAND80-1453. Albuquerque, New Mexico: Sandia National Laboratories. ACC: NNA.19870406.0497.

Potter, C.J.; Day, W.C.; Sweetkind, D.S.; and Dickerson, R.P. 2004. "Structural Geology of the Proposed Site Area for a High-Level Radioactive Waste Repository, Yucca Mountain, Nevada." *GSA Bulletin*, *116*, (7-8), 858–879. Boulder, Colorado: Geological Society of American. TIC: 257982.

Potter, C.J.; Dickerson, R.P.; Sweetkind, D.S.; Drake, R.M., II; Taylor, E.M.; Fridrich, C.J.; San Juan, C.A.; and Day, W.C. 2002. *Geologic Map of the Yucca Mountain Region, Nye County, Nevada.* Geologic Investigations Series I-2755. Denver, Colorado: U.S. Geological Survey. TIC: 253945.

Potyondy, D. and Cundall, P. 2001. *The PFC Model for Rock: Predicting Rock-Mass Damage at the Underground Research Laboratory.* Report No. 06819-REP-01200-10061-R00. Toronto, Ontario, Canada: Ontario Power Generation, Nuclear Waste Management Division. TIC: 253569.

Price, R.H. 1983. *Analysis of the Rock Mechanics Properties of Volcanic Tuff Units from Yucca Mountain, Nevada Test Site.* SAND82-1315. Albuquerque, New Mexico: Sandia National Laboratories. ACC: NNA.19870406.0181.

Price, R.H. 1986. *Effects of Sample Size on the Mechanical Behavior of Topopah Spring Tuff.* SAND85-0709. Albuquerque, New Mexico: Sandia National Laboratories. ACC: NNA.19891106.0125.

Price, R.H. and Bauer, S.J. 1985. "Analysis of the Elastic and Strength Properties of Yucca Mountain Tuff, Nevada." *Research & Engineering Applications in Rock Masses, Proceedings of the 26th U.S. Symposium on Rock Mechanics, Rapid City, South Dakota, June 26–28, 1985*, Ashworth, E., ed. 89–96. Boston, Massachusetts: A.A. Balkema. TIC: 218790.

Price, R.H.; Connolly, J.R.; and Keil, K. 1987. *Petrologic and Mechanical Properties of Outcrop Samples of the Welded, Devitrified Topopah Spring Member of the Paintbrush Tuff.* SAND86-1131. Albuquerque, New Mexico: Sandia National Laboratories. ACC: NNA.19870601.0013.

Price, R.H. and Jones, A.K. 1982. *Uniaxial and Triaxial Compression Tests Series on Calico Hills Tuff.* SAND82-1314. Albuquerque, New Mexico: Sandia National Laboratories. ACC: NNA.19900810.0480.

Price, R.H.; Jones, A.K.; and Nimick, K.G. 1982. *Uniaxial Compression Test Series on Bullfrog Tuff.* SAND82-0481. Albuquerque, New Mexico: Sandia National Laboratories. ACC: HQS.19880517.1700.

Price, R.H. and Nimick, K.G. 1982. *Uniaxial Compression Test Series on Tram Tuff.* SAND82-1055. Albuquerque, New Mexico: Sandia National Laboratories. ACC: HQS.19880517.1699.

Price, R.H.; Nimick, K.G.; and Zirzow, J.A. 1982. *Uniaxial and Triaxial Compression Test Series on Topopah Spring Tuff.* SAND82-1723. Albuquerque, New Mexico: Sandia National Laboratories. ACC: NNA.19870406.0063.

Price, R.H.; Spence, S.J.; and Jones, A.K. 1984. *Uniaxial Compression Test Series on Topopah Spring Tuff from USW GU-3, Yucca Mountain, Southern Nevada.* SAND83-1646. Albuquerque, New Mexico: Sandia National Laboratories. ACC: NNA.19870406.0252.

Regulatory Guide 1.165. 1997. *Identification and Characterization of Seismic Sources and Determination of Safe Shutdown Earthquake Ground Motion.* Washington, D.C.: U.S. Nuclear Regulatory Commission. TIC: 233774.

Scholz, C.H. 1972. "Static Fatigue of Quartz." *Journal of Geophysical Research, 77* (11), 2104–2114. Washington, D.C.: American Geophysical Union. TIC: 224772.

Silva, W.J. 1976. "Body Waves in a Layered Anelastic Solid." *Bulletin of the Seismological Society of America*, *66*, (5), 1539–1554. El Cerrito, California: Seismological Society of America. TIC: 241277.

Silva, W.J.; Abrahamson, N.; Toro, G.; and Costantino, C. 1996. *Description and Validation of the Stochastic Ground Motion Model*. PE&A 94PJ20. El Cerrito, California: Pacific Engineering and Analysis. TIC: 245288.

SNL (Sandia National Laboratories) 1996. *Hydraulic Fracturing Stress Measurements in Test Hole ESF-AOD-HDFR#1, Thermal Test Facility, Exploratory Studies Facility at Yucca Mountain*. WA-0065. Albuquerque, New Mexico: Sandia National Laboratories. ACC: MOL.19970717.0008.

SNL 2007a. *Stress Corrosion Cracking of Waste Package Outer Barrier and Drip Shield Materials.* ANL-EBS-MD-000005 REV 04. Las Vegas, Nevada: Sandia National Laboratories. ACC: DOC.20070913.0001.

SNL 2007b. *Mechanical Assessment of Degraded Waste Packages and Drip Shields Subject to Vibratory Ground Motion*. MDL-WIS-AC-000001 REV 00. Las Vegas, Nevada: Sandia National Laboratories. ACC: DOC.20070917.0006.

SNL 2007c. *Seismic Consequence Abstraction.* MDL-WIS-PA-000003 REV 03. Las Vegas, Nevada: Sandia National Laboratories. ACC: DOC.20070928.0011.

SNL 2007d. *Total System Performance Assessment Data Input Package for Requirements Analysis for Subsurface Facilities.* TDR-TDIP-PA-000001 REV 00. Las Vegas, Nevada: Sandia National Laboratories. ACC: DOC.20070921.0007.

SNL 2007e. *Total System Performance Assessment Data Input Package for Requirements Analysis for Engineered Barrier System In-Drift Configuration.* TDR-TDIP-ES-000010 REV 00. Las Vegas, Nevada: Sandia National Laboratories. ACC: DOC.20070921.0008.

SNL 2007f. *General Corrosion and Localized Corrosion of the Drip Shield*. ANL-EBS-MD-000004 REV 02 ADD 01. Las Vegas, Nevada: Sandia National Laboratories. ACC: DOC.20070427.0004.

SNL 2007g. *Total System Performance Assessment Data Input Package for Requirements Analysis for DOE SNF/HLW and Navy SNF Waste Package Physical Attributes Basis for Performance Assessment.* TDR-TDIP-ES-000009 REV 00. Las Vegas, Nevada: Sandia National Laboratories. ACC: DOC.20070921.0009.

SNL 2007h. *Total System Performance Assessment Data Input Package for Requirements Analysis for Transportation Aging and Disposal Canister and Related Waste Package Physical Attributes Basis for Performance Assessment.* TDR-TDIP-ES-000006 REV 00. Las Vegas, Nevada: Sandia National Laboratories. ACC: DOC.20070918.0005.

SNL 2007i. *Thermal Testing Measurements Report.* TDR-MGR-HS-000002 REV 01. Las Vegas, Nevada: Sandia National Laboratories. ACC: DOC.20070307.0010.

SNL 2008a. *Features, Events, and Processes for the Total System Performance Assessment: Analyses*. ANL-WIS-MD-000027 REV 00. Las Vegas, Nevada: Sandia National Laboratories. ACC: DOC.20080307.0003.

SNL 2008b. *Total System Performance Assessment Model-Analysis for the License Application*. MDL-WIS-PA-000005 REV 00 ADD 01. Las Vegas, Nevada: Sandia National Laboratories. ACC: DOC.20080312.0001.

SNL 2008c. *Technical Report: Geotechnical Data for a Geologic Repository at Yucca Mountain, Nevada*. TDR-MGR-GE-000010 REV 00. Las Vegas, Nevada: Sandia National Laboratories. ACC: DOC.20080206.0001.

SNL 2008d. *Multiscale Thermohydrologic Model*. ANL-EBS-MD-000049 REV 03 ADD 02. Las Vegas, Nevada: Sandia National Laboratories. ACC: DOC.20080201.0003.

SNL 2008e. *Postclosure Analysis of the Range of Design Thermal Loadings*. ANL-NBS-HS-000057 REV 00. Las Vegas, Nevada: Sandia National Laboratories. ACC: DOC.20080121.0002.

Stock, J.M.; Healy, J.H.; Hickman, S.H.; and Zoback, M.D. 1985. "Hydraulic Fracturing Stress Measurements at Yucca Mountain, Nevada, and Relationship to the Regional Stress Field." *Journal of Geophysical Research, 90* (B10), 8691–8706. Washington, D.C.: American Geophysical Union. TIC: 219009.

Stuckless, J.S. and Levich, R.A., eds. 2007. *The Geology and Climatology of Yucca Mountain and Vicinity, Southern Nevada and California.* Memoir 199. Boulder, Colorado: Geological Society of America. TIC: 259378.

Terzaghi, K. 1943. *Theoretical Soil Mechanics.* New York, New York: John Wiley & Sons. TIC: 223827.

Throckmorton, C.K. and Verbeek, E.R. 1995. *Joint Networks in the Tiva Canyon and Topopah Spring Tuffs of the Paintbrush Group, Southwestern Nevada*. Open-File Report 95-2. Denver, Colorado: U.S. Geological Survey. TIC: 235000.

YMP (Yucca Mountain Site Characterization Project) 1997. *Methodology to Assess Fault Displacement and Vibratory Ground Motion Hazards at Yucca Mountain.* Topical Report YMP/TR-002-NP, Rev. 1. Las Vegas, Nevada: Yucca Mountain Site Characterization Office. ACC: MOL.19971016.0777.

Zabotkin, K.; O'Toole, B.; and Trabia, M. 2003. "Identification of the Dynamic Tensile Properties of Metals Under Moderate Strain Rates." *16th ASCE Engineering Mechanics Conference, July 16-18, 2003, University of Washington, Seattle, Washington.* New York, New York: American Society of Civil Engineers. TIC: 259107.

Table 2.3.4-1. Seismic-Related Features, Events, and Processes for the Total System Performance Assessment

FEP Number and FEP Name	FEP Description	Summary of Technical Basis/Approach for FEP Inclusion
1.2.02.03.0A Fault displacement damages EBS components	Movement of a fault that intersects drifts within the repository may cause the EBS components to experience related movement or displacement. Repository performance may be degraded by such occurrences as the tilting of components, component-to-component contact, or drip shield separation. Fault displacement could cause a failure as significant as the shearing of drip shields and waste packages by virtue of the relative offset across the fault, or as extreme as exhumation of the waste to the surface.	An analysis is performed that examines how fault displacement may contribute to mechanical disruption of the EBS. In this analysis, estimates of very low probability fault displacement (Section 2.3.4.5.5) are compared with the dimensions of the EBS features. Potential damage to the EBS is estimated, and the results are used to create an abstraction for TSPA.
1.2.03.02.0A Seismic ground motion damages EBS components	Seismic activity that causes repeated vibration of the EBS components (drip shield, waste package, pallet, and invert) could result in severe disruption of the drip shields and waste packages, through vibration damage or through contact between EBS components. Such damage mechanisms could lead to degraded performance.	Structural calculations were used to simulate the response of the drip shield and waste package to vibratory ground motion (Section 2.3.4.5). These calculations utilize a three-dimensional, dynamic structural analysis model that incorporates the details of the EBS design. Ground motion time histories input into the calculations represent postclosure hazard levels at the emplacement depth (Section 2.3.4.3.2). The potential for structural damage and for separation of the drip shields is examined. The potential damage to the waste package due to ground motion-induced interactions of the waste packages, the pallet, and the drip shield are examined (Section 2.3.4.5.2). Surface area damage and tensile rupture probability are determined for input to the abstraction of seismic consequence. Results of these studies are used in creating abstractions for TSPA.

Table 2.3.4-1. Seismic-Related Features, Events, and Processes for the Total System Performance Assessment (Continued)

FEP Number and FEP Name	FEP Description	Summary of Technical Basis/Approach for FEP Inclusion
1.2.03.02.0C Seismic Induced Drift Collapse Damages EBS Components	Seismic activity could produce jointed-rock motion and (or) changes in rock stress leading to enhanced drift collapse that could impact drip shields, waste packages, or other EBS components.	The potential for drift collapse and (or) rubble infill associated with vibratory ground motion was assessed using detailed two- and three-dimensional tunnel stability models (Section 2.3.4.4). Ground motion time histories input into the calculations represent postclosure hazard levels at the emplacement depth (Section 2.3.4.3.2). The rockfall accumulation from multiple seismic events was determined as a function of the PGV of multiple seismic events (Section 2.3.4.4.8). The effect of drift collapse and rubble load on the probability of drip shield plate tearing and framework collapse was determined from three-dimensional structural models (Sections 2.3.4.5.2.2 and 2.3.4.5.3). After drip shield framework collapse and drip shield plate tensile rupture, the effect of rock rubble load surrounding the waste package on damage and rupture potential was determined. Results of these studies (damage or rupture potential) resulting from vibratory motion and rockfall have been abstracted to TSPA.
1.2.03.02.0D Seismic-induced drift collapse alters in-drift thermal-hydrology	Seismic activity could produce jointed-rock motion and (or) changes in rock stress leading to enhanced drift collapse and (or) rubble infill throughout part or all of the drifts. Drift collapse could impact flow pathways and condensation within the EBS, mechanisms for water contact with EBS components, and thermal properties within the EBS.	The potential for drift collapse and (or) rubble infill associated with vibratory ground motion was assessed using detailed two- and three-dimensional tunnel stability models (Section 2.3.4.4.8). Ground motion time histories input into the calculations represent postclosure hazard levels at the emplacement depth (Section 2.3.4.3.2). Emplacement drift profiles and the porosity of rubble material in the drift following a seismic event or from long-term degradation are estimated to use in examination of potential impacts on drift seepage and the in-drift environment (Section 2.3.4.5.4). Results of these studies are used in creating abstractions for TSPA.
1.2.03.03.0A Seismicity associated with igneous activity	Seismicity associated with future igneous activity in the Yucca Mountain region may affect repository performance.	Seismicity associated with igneous activity was considered as part of the probabilistic seismic hazard analysis for Yucca Mountain (Section 2.2.2.1). The seismic source characterization expert teams either included specific seismic sources for seismicity associated with igneous activity or determined that such seismicity was included in their areal source zones representing background seismicity not associated with specific faults. Thus, seismicity associated with igneous activity is included in the ground motion hazard results that form the basis for developing seismic inputs for postclosure analyses.

Table 2.3.4-1. Seismic-Related Features, Events, and Processes for the Total System Performance Assessment (Continued)

FEP Number and FEP Name	FEP Description	Summary of Technical Basis/Approach for FEP Inclusion
2.1.06.05.0C Chemical Degradation of the Emplacement Pallet	Degradation of the materials used in the pallet supporting the waste package may occur by chemical or microbial processes, and may affect the long-term performance of the repository.	The detailed structural response calculations for damaged areas from waste package-to-pallet impacts are described in Section 2.3.4.5.1.3. As noted in Section 2.3.4.1, the Alloy 22 components of the pallet are thinned from general corrosion at the same rate as the Alloy 22 outer corrosion barrier of the waste package. The pallet thus becomes structurally weaker and more deformable as the outer corrosion barrier thins from general corrosion.

Table 2.3.4-2. Summary of Strong Ground Motion Recordings Used as a Basis for Postclosure Time Histories

	Earthquake	Date	Magnitude (M)	Station	Distance (km)	Peak Ground Acceleration (g)			Peak Ground Velocity (cm/s)		
						H1	H2	V	H1	H2	V
1	Coalinga, California	7/22/83	5.8	Oil City	8.2	0.866	0.447	0.568	42.2	24.7	12.5
2	Whitter Narrows, California	10/1/87	6.0	Garvey Res. - Control Bldg.	12.1	0.384	0.457	0.362	15.8	19.0	9.9
3	Helena, Montana	10/31/35	6.2	Carroll College	8.0	0.15	0.173	0.102	5.8	16.5	7.3
4	Parkfield, California	6/28/66	6.1	Cholame #8	9.2	0.246	0.273	0.116	10.2	11.3	4.3
5	Parkfield, California	6/28/66	6.1	Temblor (pre-1969)	9.9	0.375	0.272	0.136	21.5	15.0	4.4
6	San Fernando, California	2/9/71	6.6	Pacoima Dam	2.8	1.226	1.16	0.699	112.5	54.3	56.5
7	Gazli, USSR	5/17/76	6.8	Karakyr	3.0	0.608	0.718	1.264	65.4	71.6	54.2
8	Morgan Hill, California	4/24/84	6.2	Coyote Lake Dam (SW abutment)	0.1	0.711	1.298	0.388	51.6	80.8	15.6
9	Morgan Hill, California	4/24/84	6.2	Gilroy Arr #6	11.8	0.222	0.292	0.405	11.4	36.7	14.1
10	Whitter Narrows, California	10/1/87	6.0	San Gabriel - E Grand Ave	9.0	0.304	0.199	0.227	23.0	11.0	5.5
11	Loma Prieta, California	10/18/89	6.9	Corralitos	5.1	0.644	0.479	0.455	55.2	45.2	17.7
12	Northridge, California	1/17/94	6.7	Pacoima Kagel Canyon	8.2	0.301	0.433	0.169	31.4	51.5	15.1
13	Loma Prieta, California	10/18/89	6.9	Gilroy Arr #6	19.9	0.126	0.17	0.101	12.8	14.2	9.5
14	Landers, California	6/28/92	7.3	Lucerne	1.1	0.721	0.785	0.818	97.6	31.9	45.9
15	Chi-Chi, Taiwan	9/20/99	7.6	TCU025	54.3	0.058	0.075	0.034	10.5	19.0	13.8

Table 2.3.4-2. Summary of Strong Ground Motion Recordings Used as a Basis for Postclosure Time Histories (Continued)

	Earthquake	Date	Magnitude (M)	Station	Distance (km)	Peak Ground Acceleration (g)			Peak Ground Velocity (cm/s)		
						H1	H2	V	H1	H2	V
16	Kobe, Japan	1/16/95	6.9	Kobe University	0.2	0.29	0.31	0.38	54.8	34.2	20.2
17	Koaceli, Turkey	8/17/99	7.4	Izmit	7.7	0.152	0.22	0.149	22.6	29.8	11.9

Source: McGuire et al. 2001, Appendix B, Tables B-1 and B-2.

Table 2.3.4-3. Mean Shear-Strain Increments Determined from Numerical Simulation of the Mechanical Behavior of Lithophysal Rock

Depth for In Situ Conditions (m)	Simulation Approach	Failure Criterion = Peak Stress	Failure Criterion = Yield Stress
		Shear Strain Increment[a] (%) (mean ±σ)	Shear Strain Increment (%) (mean ±σ)
250	PFC2D+Circles[b]	0.15 ±0.02	0.14 ±0.02
	PFC2D+Actual[c]	0.13 ±0.03	0.11 ±0.04
	UDEC+Circles	0.11 ±0.02	0.09 ±0.03
400	PFC2D+Circles	0.16 ±0.02	0.15 ±0.02
	PFC2D+Actual	0.15 ±0.03	0.12 ±0.05
	UDEC+Circles	0.12 ±0.02	0.10 ±0.03

NOTE: [a]Shear strain increment is the increment in shear strain from the in situ stress state to the failure criterion. Failure criterion is based on either a peak failure stress or on yield stress condition.
[b]Lithophysae are represented in the model as circular holes.
[c]Lithophysae are represented in the model as actual complex shapes traced from geologic field maps.

Source: BSC 2005a, Table 6-2.

Table 2.3.4-4. Modeled Horizontal Peak Ground Velocity for Modeled Shear Strain Values

	Frequency Range	Annual Probability of Exceedance (per year) for Modeled Horizontal PGV Values (cm/s)				Annual Probability of Exceedance (per year) for Modeled Shear Strain (Syz,%) Values			
		10^{-4}	10^{-5}	10^{-6}	10^{-7}	10^{-4}	10^{-5}	10^{-6}	10^{-7}
Velocity Profile P1 + Upper Mean Tuff Dynamic Material Property Curves	1 to 2 Hz	45.26	110.67	242.65	512.01	0.020	0.050	0.118	0.270
	5 to 10 Hz	31.63	99.29	246.20	520.46	0.016	0.051	0.124	0.286
Velocity Profile P1 + Lower Mean Tuff Dynamic Material Property Curves	1 to 2 Hz	47.27	104.48	231.98	499.27	0.023	0.076	0.263	0.869
	5 to 10 Hz	29.65	93.24	237.70	522.41	0.018	0.072	0.276	0.905
Velocity Profile P2 + Upper Mean Tuff Dynamic Material Property Curves	1 to 2 Hz	45.17	111.40	244.31	519.61	0.018	0.048	0.116	0.272
	5 to 10 Hz	31.33	99.70	249.51	540.36	0.016	0.049	0.127	0.297
Velocity Profile P2 + Lower Mean Tuff Dynamic Material Property Curves	1 to 2 Hz	43.67	105.82	231.41	494.90	0.024	0.089	0.331	1.041
	5 to 10 Hz	30.00	93.86	235.68	518.23	0.021	0.085	0.351	1.089

Source: BSC 2005a, Table 6-3.

Table 2.3.4-5. In Situ Stress Estimates at Yucca Mountain Site

Stress Component	Magnitude (MPa)	Direction
σ_1	4.7 (at a depth of approximately 244 m)	Vertical
σ_2	2.9 (0.62 × σ_1)	N15°E
σ_3	1.7 (0.36 × σ_1)	N105°E

Source: SNL 1996.

Table 2.3.4-6. General Characteristics of Fracture Sets in the Middle Nonlithophysal Unit

Set Number	Observed Orientation (Strike/Dip)	Inter-fracture Distance (m)	True Spacing (m)	Trace Length Median from Full Periphery Geologic Maps (m)
Set 1	120°/84°	0.48	0.48	3.3
Set 2	215°/88°	1.08	1.08	2.8
Set 3	302°/38°	3.40	2.09	3.7
Vapor-Phase Partings	329°/14°	2.46	0.60	3.5

NOTE: Inter-fracture distance is the fracture spacing measured along the tunnel axis. For flat-lying tunnels (0% grade), true fracture spacing is equal to the product of the inter-fracture distance and the sine of the fracture dip angle.

Source: BSC 2004a, Table 6-1.

Table 2.3.4-7. Impact of Moisture Conditions on Unconfined Compressive Strength of Nonlithophysal Tptpll Samples

Test Condition	Moisture Condition	Mean Strength (MPa)
1	Samples dried by slow heating to 200°C, tested at 200°C	213
2	Samples dried by slow heating to 200°C, then slowly cooled in dry environment, exposed to room humidity for about 30 minutes and tested at room temperature	176
3	Samples allowed to equilibrate with room humidity, tested at room temperature	158
4	Samples water saturated, tested at room temperature	149

NOTE: Strengths are mean values from testing of 51-mm diameter samples at each moisture condition.

Source: BSC 2004a, Table E-12.

Table 2.3.4-8. Summary of Mechanical Properties Results from the Pressurized Slot Tests

Test	Temperature (°C)	Tuff Unit	Deformation Modulus (GPa)	Peak Flatjack Pressure (MPa)
PST#1	25	Tptpll	0.5	6.1
PST#2	25	Tptpul	3.0	3.4
PST#2	90	Tptpul	1.5	10.7
PST#3	25	Tptpll	1.0	6.8

Source: BSC 2007a,Table 6-99.

Table 2.3.4-9. Summary Statistics of Direct Shear Tests on Fractures

Joint	Peak Cohesion (MPa)	Peak Friction Angle (°)	Dilation Angle (°)
Cooling[a]	0	33	2
Vapor Phase Parting	0.7 ±0.1	44 ±2	14 ±2

NOTE: [a]Two samples.

Source: BSC 2004a, Table E-5.

Table 2.3.4-10. Intact Rock Matrix Thermal Conductivities for Repository Units

	Saturated (W/m·K)		Oven Dried (W/m·K)			
	~70°C		50-70°C		~290°C	
Rock Units	Mean	Standard Deviation	Mean	Standard Deviation	Mean	Standard Deviation
Tptpul	1.99	0.08	1.08	0.01	1.16	0.29
Tptpmn	2.14	0.31	1.59	0.33	1.52	0.22
Tptpll	2.11	0.14	1.73	0.26	1.49	0.05
Tptpln	NA	NA	NA	NA	NA	NA

Note: NA = not applicable.

Source: BSC 2007a, Tables 6-78 and 6-79.

Table 2.3.4-11. Rock Mass Thermal Conductivities for Repository Units

Rock Units	Dry Bulk (W/m·K)		Wet Bulk (W/m·K)	
	Mean	Standard Deviation	Mean	Standard Deviation
Tptpul	1.18	0.24	1.77	0.25
Tptpmn	1.42	0.27	2.07	0.25
Tptpll	1.28	0.25	1.89	0.25
Tptpln	1.49	0.28	2.13	0.27

Source: BSC 2007a, Table 6-90.

Table 2.3.4-12. Rock Grain Heat Capacities for Repository Units

Rock Units	25°C to 94°C		95°C to 114°C		115°C to 325°C	
	Average (J/kg·K)	Standard Deviation (J/kg·K)	Average (J/kg·K)	Standard Deviation (J/kg·K)	Average (J/kg·K)	Standard Deviation (J/kg·K)
Tptpul	780	90	870	90	990	110
Tptpmn	780	110	870	110	990	130
Tptpll	780	100	870	100	990	120
Tptpln	780	70	870	70	990	90

Source: BSC 2007a, Table 6-93.

Table 2.3.4-13. Rock Mass Heat Capacities for Repository Units

Rock Units	25°C to 94°C		95°C to 114°C		115°C to 325°C	
	Average (J/kg·K)	Standard Deviation (J/kg·K)	Average (J/kg·K)	Standard Deviation (J/kg·K)	Average (J/kg·K)	Standard Deviation (J/kg·K)
Tptpul	940	300	3,600	1,000	990	300
Tptpmn	910	300	3,000	900	990	300
Tptpll	930	300	3,300	1,000	990	300
Tptpln	900	300	2,800	800	990	300

Source: BSC 2007a, Table 6-94.

Table 2.3.4-14. Coefficients of Rock Mass Thermal Expansion for Repository Units

Rock Units	Rock Mass Thermal Expansion (10^{-6}/°C)													
			50°C	70°C	75°C	80°C	100°C	117°C	120°C	125°C	150°C	160°C	175°C	200°C
Tptpmn	Drift Scale Test[a]	Mean	2.03	NA	2.41	NA	4.19	NA	NA	4.40	7.43	NA	9.80	12.55
		Std Dev	1.29	NA	0.93	NA	2.07	NA	NA	1.95	0.46	NA	0.80	NA
Tptpll	290-mm diameter specimens	Mean	NA	NA	NA	6.50	NA	NA	6.60	NA	NA	10.04	NA	15.34
		Std Dev	NA	NA	NA	1.49	NA	NA	1.73	NA	NA	1.69	NA	5.58

NOTE: [a]SNL 2007i, Table 6.3-21 (mean thermal coefficients for Drift Scale Test reported at upper end temperature range; for example, value for 75°C to 100°C reported at 100°C).
NA = not applicable.

Table 2.3.4-15. Coefficients of Intact Rock Thermal Expansion for Repository Units

Rock Units		Intact Rock Thermal Expansion (10^{-6}/°C) from Air-Dried Specimens										
		25°C~ 50°C	50°C~ 75°C	75°C~ 100°C	100°C~ 125°C	125°C~ 150°C	150°C~ 175°C	175°C~ 200°C	200°C~ 225°C	225°C~ 250°C	250°C~ 275°C	275°C~ 300°C
Tptpul	Mean	7.78	8.21	9.00	9.62	10.81	14.94	23.36	31.07	33.71	42.41	45.98
	Standard Deviation	0.62	0.48	0.68	0.53	0.83	4.44	7.77	10.97	9.76	20.22	16.80
	Number of Samples	12	12	12	12	12	12	12	12	12	12	12
Tptpmn	Mean	8.06	9.00	9.11	9.77	10.46	11.42	12.94	16.55	21.87	33.56	49.17
	Standard Deviation	0.73	0.82	0.56	0.57	0.74	0.89	1.68	3.43	4.80	9.28	11.24
	Number of Samples	71	71	71	71	71	71	71	65	65	65	65
Tptpll	Mean	7.71	8.51	8.84	9.09	9.88	10.82	12.96	15.06	17.77	21.77	28.51
	Standard Deviation	0.69	0.38	0.56	0.51	0.57	0.87	2.57	3.06	3.16	3.41	4.58
	Number of Samples	10	10	10	10	10	6	6	6	6	6	6
Tptpln	Mean	7.18	8.19	8.97	9.74	10.69	11.33	12.22	12.95	14.27	15.48	18.62
	Standard Deviation	1.31	0.68	0.79	1.26	2.19	2.62	2.07	1.56	1.46	2.51	4.91
	Number of Samples	10	10	10	10	10	10	10	10	10	10	10

Source: BSC 2007a, Table 6-84.

Table 2.3.4-16. Categories of the Lithophysal Rock Mass Selected for Analysis

Category	Unconfined Compressive Strength (MPa)	Estimated Young's Modulus[a] (GPa)	Approximate Lithophysal Porosity From Laboratory Tests[b] (%)
1	10	1.9	35 ±8
2	15	6.4	28 ±6
3	20	10.8	21 ±4
4	25	15.3	13 ±5
5	30	19.7	7 ±7

NOTE: [a]The calculation of Young's modulus values is documented in *Drift Degradation Analysis (*BSC 2004a, Appendix E).
[b]Approximate lithophysal porosity estimates are provided in *Drift Degradation Analysis* (BSC 2004a, Appendix E).

Source: BSC 2004a, Table E-10.

Table 2.3.4-17. Base-Case Material Properties for Analysis of Nonlithophysal Rock

Property	Parameter	Value
Joint strength properties	Joint cohesion (MPa)	0.1
	Joint friction (°)	41
	Joint dilation (°)	0
	Joint normal stiffness, K_n (MPa/m)	5.0×10^4
	Joint shear stiffness, K_s (MPa/m)	5.0×10^4
Intact rock deformation properties	Young's Modulus (GPa)	33.03
	Poisson's ratio	0.21
	Bulk modulus (GPa)	19.2
	Shear modulus (GPa)	13.6
Intact bridge strength properties	Cohesion (MPa)	47.2
	Friction angle (°)	42
	Tensile strength (MPa)	11.56

NOTE: Values of cohesion and friction angle were derived from preliminary data with a slight deviation from the reported values (BSC 2004a, Section 6.3). An impact analysis was conducted with no difference in the results for rockfall prediction (BSC 2004a, Section 6.3.1.6). Joint dilation (BSC 2004a, Table 6-3) is set to zero for the base-case analysis. With no dilation, joints are modeled as perfectly planar and smooth, resulting in a greater estimation of rockfall.

Source: BSC 2004a, Table 6-3.

Table 2.3.4-18. Comparison of FracMan Output for the Tptpmn, Data from Detailed Line Survey, and Full-Periphery Geologic Maps

Set Number	Observed Orientation (Strike/Dip)	FracMan Orientation (Strike/Dip)	Inter-Fracture Distance (m)		Trace Length Median from Full-Periphery Geologic Maps (m)	Trace Length Median from FracMan (m)
			Observed	FracMan		
Set 1	120°/84°	125°/84°	0.48	0.79	3.3	2.8
Set 2	215°/88°	214°/86°	1.08	1.29	2.8	3.1
Set 3	302°/38°	299°/43°	3.40	3.16	3.7	3.6
Vapor-Phase Parting	329°/14°	327°/08°	2.46	1.48	3.5	3.4

NOTE: Inter-fracture distance is the fracture spacing measured along the tunnel axis. For flat-lying tunnels (0% grade), true fracture spacing is equal to the product of the inter-fracture distance and the sine of the fracture dip angle. True spacing data for the observed fractures are provided in Table 2.3.4-6. Trace length medians are taken from a compilation of tunnel mapping and synthetic tunnel samples from FracMan.

Source: BSC 2004a, Table 6-2.

Table 2.3.4-19. Statistic Summary of the Nonlithophysal Rockfall Impact Parameters for 2.44 m/s PGV Level, Nonlithophysal Rock

	Block Mass (MT)	Relative Impact Velocity (m/s)	Impact Angle[a]	Impact Momentum (kg·m/s)	Impact Energy (J)
Mean	0.43	3.23	136°	1,217	2,350
Median	0.13	2.97	124°	337	576
Standard Deviation	1.30	1.74	93°	3,464	7,704
Skewness	11.61	1.06	0.87°	11	12
Range	28.19	12.03	359°	79,001	163,657
Minimum	0.02	0.07	0°	2	0
Maximum	28.22	12.10	360°	79,003	163,657

NOTE: [a] Impact angle is measured counterclockwise from a horizontal line emanating from the midpoint of the drip shield. Thus, angles greater than 180° (horizontal plane) can occur. Range is maximum minus minimum values for the rockfall parameters and subject to rounding differences.

Source: BSC 2004a, Table 6-14.

Table 2.3.4-20. Nonlithophysal Rockfall Statistics for Preclosure and Postclosure Ground Motion Levels

Statistic	Ground Motion Level (PGV m/s)			
	0.4	**1.05**	**2.44**	**5.35**
Runs Completed	32	50	50	44
Total Number of Rockfalls	428	1,764	2,797	3,387
Total Volume of Rockfall (m^3)	39.4	255.4	497.7	705.2
Total Length of Drift Simulated (m)	800	1,250	1,250	1,100
Number of Blocks per km	535	1,414	2,238	3,079
Volume of Rockfall per km (m^3/km)	49.3	204.3	398.2	641.1

NOTE: The Total Length of Drift Simulated, the Number of Blocks per km, and the Volume of Rockfall per km are based on a length of 25 meters per model simulation (BSC 2004a, Section 6.3.1). The effective drift length that can generate rockfall is 21.74 meters per simulation, which accounts for the solid continuum at the ends of the model domain and the aximuthal angle of the drift relative to the model boundaries (SNL 2007c, Section 6.7.2).

Source: BSC 2004a, Table 6-26.

Table 2.3.4-21. Three Categories of Joint Properties Used in Sensitivity Study, Nonlithophysal Rock

Joint Category	Joint Cohesion (Pa)	Joint Dilation Angle (degrees)	Peak Friction Angle (degrees)	Joint Shear Stiffness (Pa/m)	Joint Normal Stiffness (Pa/m)
1	1.0×10^5	1.4	31.4	5.3×10^9	7.2×10^{10}
2	1.0×10^5	4.4	34.4	1.1×10^{10}	9.4×10^{10}
3	1.0×10^5	11	41	1.7×10^{10}	1.2×10^{11}

Source: BSC 2004a, Table 6-29.

Table 2.3.4-22. Impact of Thermal Loading on Rockfall for 1.05 m/s PGV Level, Nonlithophysal Rock

Case	Nonthermal Analysis			Thermal Stress Addition		
	Time of Event (year)	Number of Blocks Dislodged (Nonthermal)	Rockfall Volume (m^3)	Time of Event (year)	Number of Blocks Dislodged (Thermal)	Rockfall Volume (m^3)
Greatest Rockfall Case	0 (Nonthermal)	173	42.03	80	56	13.59
Median Rockfall Case	0 (Nonthermal)	14	2.49	80	5	1.07
No Rockfall Case	0 (Nonthermal)	0	0.00	80	2	5.93

Source: BSC 2004a, Table 6-23.

Table 2.3.4-23. Model Predictions of Rubble Volume in the Lithophysal Zones

Realization Number	Ground Motion Number	Rock Mass Category Number	Rubble Volume (m^3/m) by PGV Level		
			0.4 m/s	1.05 m/s	2.44 m/s
1	4	3	0.06	2.26	104.75
2	8	5	0	7.63	67.92
3	16	4	0	3.22	69.3
4	12	1	2.13	5.62	109.77
5	2	3	0	3.62	84.2
6	8	1	2.46	3.11	109.85
7	14	2	0.06	5.52	76.59
8	4	4	0	3.42	94.52
9	10	2	0.03	0.58	94.28
10	6	3	0	11.84	60.83
11	9	1	7.16	21.95	82.53
12	1	1	2.12	4.35	111.21
13	1	3	0	0.79	103.52
14	7	4	0	28.96	62.22
15	11	4	0	14.38	72.16

Source: SNL 2007c, Table 6-28; Ground motion numbers and rock mass category numbers from (BSC 2004a, Table 6-44).

Table 2.3.4-24. Model Predictions of Rockfall Volume in Nonlithophysal Rock

1.05 m/s PGV Level			2.44 m/s PGV Level			5.35 m/s PGV Level		
Case	Total Vol. (m^3)	Vol. per m (m^3/m)	Case	Total Vol. (m^3)	Vol. per m (m^3/m)	Case	Total Vol. (m^3)	Vol. per m (m^3/m)
14	1.844	0.085	14	2.118	0.097	14	2.347	0.108
15	7.067	0.325	15	16.514	0.760	15	38.033	1.749
16	4.264	0.196	16	10.652	0.490	16	23.029	1.059
17	0.045	0.002	17	0.647	0.030	17	2.828	0.130
18	0.544	0.025	18	1.417	0.065	18	5.632	0.259
19	7.375	0.339	19	15.123	0.696	20	1.456	0.067
20	0.417	0.019	20	0.602	0.028	21	3.532	0.162
21	1.041	0.048	21	1.445	0.066	22	2.260	0.104
22	1.846	0.085	22	2.055	0.095	23	33.630	1.547
23	5.217	0.240	23	8.316	0.383	27	13.322	0.613
24	1.308	0.060	24	1.620	0.075	29	8.469	0.390
25	14.296	0.658	25	12.913	0.594	31	0.981	0.045
27	5.661	0.260	27	6.512	0.300	32	6.058	0.279
28	3.520	0.162	28	5.974	0.275	33	19.501	0.897
29	1.386	0.064	29	2.919	0.134	34	13.436	0.618
31	0.149	0.007	31	0.221	0.010	35	1.421	0.065
32	0.193	0.009	32	2.404	0.111	36	6.543	0.301
33	0.725	0.033	33	13.741	0.632	39	36.451	1.677
34	2.845	0.131	34	5.374	0.247	40	51.291	2.359
35	1.449	0.067	35	1.753	0.081	41	8.866	0.408
36	2.697	0.124	36	2.954	0.136	42	21.141	0.972
38	42.030	1.933	38	58.486	2.690	43	26.606	1.224
39	8.179	0.376	39	17.014	0.783	44	36.713	1.689
40	21.902	1.007	40	35.204	1.619	45	14.267	0.656
41	2.145	0.099	41	5.194	0.239	46	25.590	1.177
42	0.111	0.005	42	1.820	0.084	48	14.942	0.687
43	6.232	0.287	43	18.513	0.852	49	36.387	1.647
44	8.815	0.405	44	21.158	0.973	50	7.720	0.355

Table 2.3.4-24. Model Predictions of Rockfall Volume in Nonlithophysal Rock (Continued)

1.05 m/s PGV Level			2.44 m/s PGV Level			5.35 m/s PGV Level		
Case	**Total Vol. (m^3)**	**Vol. per m (m^3/m)**	**Case**	**Total Vol. (m^3)**	**Vol. per m (m^3/m)**	**Case**	**Total Vol. (m^3)**	**Vol. per m (m^3/m)**
45	2.489	0.114	45	4.188	0.193	51	13.863	0.638
46	0.891	0.041	46	1.891	0.087	53	36.445	1.676
48	0.276	0.013	48	4.445	0.204	54	17.647	0.812
49	24.099	1.109	49	9.695	0.446	55	3.057	0.141
50	5.812	0.267	50	6.449	0.297	56	7.132	0.328
51	1.056	0.049	51	4.173	0.192	57	10.432	0.480
52	15.880	0.730	52	63.335	2.913	58	4.505	0.207
53	4.525	0.208	53	25.427	1.170	59	9.584	0.441
54	6.371	0.293	54	11.759	0.541	60	9.565	0.440
55	1.285	0.059	55	2.377	0.109	61	8.212	0.378
56	6.056	0.279	56	10.011	0.460	62	8.736	0.402
57	1.435	0.066	57	3.893	0.179	63	9.204	0.423
58	0.133	0.006	58	0.323	0.015	64	58.927	2.711
59	2.130	0.098	59	4.972	0.229	65	6.050	0.278
60	0.526	0.024	60	8.221	0.378	66	22.520	1.036
61	0.299	0.014	61	7.074	0.325	67	16.889	0.777
62	1.807	0.083	62	4.921	0.226	Mean	16.028	0.737
63	0	0	63	0.480	0.022	Std Dev	14.062	0.647
64	13.611	0.626	64	25.130	1.156	—	—	—
65	3.020	0.139	65	3.034	0.140	—	—	—
66	2.776	0.128	66	8.815	0.405	—	—	—
67	7.601	0.350	67	14.415	0.663	—	—	—
Mean	5.108	0.235	Mean	9.954	0.458	—	—	—
Std Dev	7.563	0.348	Std Dev	12.944	0.595	—	—	—

NOTE: Volume per meter defined by dividing the Total Volume by the effective length of the drift in the 3DEC calculations, 21.74-meters.
Stnd Dev = standard deviation.

Source: SNL 2007c, Table 6-31.

Table 2.3.4-25. Comparison of Statistical Parameters for Rock Volumes in Lithophysal and Nonlithophysal Rock

	Conditional Rock Volumes (m^3 per Meter of Emplacement Drift)					
	1.05 m/s PGV Level		**2.44 m/s PGV Level**		**5.35 m/s PGV Level**	
	Lith	**Nonlith**	**Lith**	**Nonlith**	**Lith**	**Nonlith**
Mean	7.8	0.24	86.9	0.46	NA	0.74
Standard Deviation	8.2	0.35	18.2	0.60	NA	0.65

NOTE: NA = Not Available.

Source: SNL 2007c, Table 6-32.

Table 2.3.4-26. Probability of Nonzero Rubble Volume Weighted by Rock Mass Category in Lithophysal Units

Rock Mass Category Number	**Weight (%)**	**Probability of Nonzero Rubble Volume for each Rock Mass Category (Unweighted)**		
		0.4 m/s	**1.05 m/s**	**2.44 m/s**
1	3	1	1	1
2	7	1	1	1
3	25	0.25	1	1
4	35	0	1	1
5	30	0	1	1
Weighted Probability		0.1625	1	1

Source: SNL 2007c, Table 6-29.

Table 2.3.4-27. Waste Package Dimensions and Design Basis Inventory

Waste Package Configuration	Nominal Length (mm)	Outer Diameter of Outer Corrosion Barrier (mm)	Nominal Quantity
TAD-Bearing	5850.1	1881.6	7483
Naval Fuel – Long	5850.1	1881.6	310
Naval Fuel – Short	5215.1	1881.6	90
5-DHLW/DOE SNF – Short	3697.4	2044.7	1207
5-DHLW/DOE SNF – Long	5303.9	2044.7	1862
2-MCO/2-DHLW	5278.6	1749.3	210

NOTE: The TAD waste package in this table includes all medium and small TAD waste packages in the design basis inventory. The 5-DHLW/DOE SNF-Long waste package includes the 1S/5L and the 1D/4L codisposal waste packages in the design basis inventory.
Waste package diameters presented in Tables 1.5.2-3 and 1.5.2-5 are clearance diameters that include the end sleeves.
DHLW = defense high-level radioactive waste; MCO = multicanister overpack; SNF = spent nuclear fuel; TAD = transportation, aging, and disposal (canister).

Source: SNL 2007c, Table 6-62.

Table 2.3.4-28. Material Properties of EBS Components Used in Mechanical Calculations

Property	Value	Sources
Material Properties for SB-265 R52400 (Ti-7)		
Density (room temperature)	4,520 kg/m^3	SNL 2007b, Table 4-3.
Yield Strength (60°C)	316 MPa	SNL 2007b, Table 4-3 and Table A-1.
Poisson's Ratio (room temperature)	0.32	SNL 2007b, Table 4-3.
Modulus of Elasticity (60°C)	105 GPa	SNL 2007b, Table 4-3 and Table A-1.
Tangent (Hardening) Modulus (60°C)	368 MPa	SNL 2007b, Table A-1.
True Tensile Strength (60°C)	396 MPa	SNL 2007b, Table A-1.
Ultimate engineering elongation e_u (60°C)	0.25	SNL 2007b, Table A-1.
Ultimate true elongation ε_u (60°C)	0.22	$\varepsilon_u=\ln(1+e_u)$ SNL 2007b, Table A-1.
Material Properties for SB-265 R56405 (Ti-24)		
Density (room temperature)	4430 kg/m^3	SNL 2007b, Table A-2.
Yield Strength (60°C)	862 MPa	SNL 2007b, Table A-2.
Poisson's Ratio (room temperature)	0.34	SNL 2007b, Table A-2.
Modulus of Elasticity (60°C)	112 GPa	SNL 2007b, Table A-2.
Tangent (Hardening) Modulus (60°C)	1.66 GPa	SNL 2007b, Table A-2.
True Tensile Strength (60°C)	1.12 GPa	SNL 2007b, Table A-2.
Ultimate engineering elongation e_u (60°C)	0.18	SNL 2007b, Table A-2.
Ultimate true elongation ε_u (60°C)	0.16	$\varepsilon_u=\ln(1+e_u)$ SNL 2007b, Table A-2.
Material Properties for SB-575 N06022 (Alloy 22)		
Density (room temperature)	8690 kg/m^3	SNL 2007b, Table 4-3.
Yield Strength (60°C)	350 MPa	SNL 2007b, Appendix A2
Poisson's Ratio (room temperature)	0.278	SNL 2007b, Assumption 5.5 and Table 4-3.
Modulus of Elasticity (60°C)	204 GPa	SNL 2007b, Table 4-3 and Appendix A.

Table 2.3.4-28. Material Properties of EBS Components Used in Mechanical Calculations (Continued)

Property	Value	Sources
Tangent (Hardening) Modulus (60°C)	1.94 GPa	SNL 2007b, Appendix A2.
Ultimate engineering elongation e_u (60°C)	64%	SNL 2007b, Appendix A2.
Effective Strain at Failure	28.5%	SNL 2007b, Appendix A2.
Material Properties for SA-240 S31600 (Stainless Steel Type 316)		
Density (room temperature)	7,980 kg/m^3	SNL 2007b, Table 4-3.
Yield Strength (60°C)	193 MPa	SNL 2007b, Appendix A3.
Poisson's Ratio (room temperature)	0.30	SNL 2007b, Table 4-3.
Modulus of Elasticity (60°C)	192 GPa	SNL 2007b, Appendix A2.
Tangent (Hardening) Modulus (60°C)	1.58 GPa	SNL 2007b, Appendix A3.
Material Properties for Crushed Tuff Invert		
Modulus of Elasticity	50 MPa	BSC 2005c, Attachment IX-5
Poisson's Ratio	0.2	Selected from the max and min range in BSC 2004i, Table 5
Density	2000 kg/m^3	Selected based on BSC 2004i, Table 5
Friction Angle	45°	Selected based on BSC 2004i, Table 5
Friction Angle Between Crushed Tuff and Invert Walls	35°	Brady and Brown (1985), p. 117.

NOTE: Titanium Grade 24 properties used as representative of Titanium Grade 29.

Table 2.3.4-29. Probability of Nonzero Damage for the TAD-Bearing Waste Package with 23-mm-thick Outer Corrosion Barrier and Intact Internals

	RST (% of Yield Strength)		
PGV Level (m/s)	**90%**	**100%**	**105%**
0.40	0	0	0
1.05	0	0	0
2.44	0	0	0
4.07	0.118	0	0

Source: SNL 2007c, Table 6-4.

Table 2.3.4-30. Revised Probability of Nonzero Damage for the Codisposal Waste Package with 23-mm-Thick Outer Corrosion Barrier and Intact Internals

	RST (% of Yield Strength)		
PGV Level (m/s)	**90%**	**100%**	**105%**
0.40	0.029	0	0
1.05	0.559	0	0
2.44	0.941	0.147	0
4.07	1	0.412	0

Source: SNL 2007c, Table 6-16.

Table 2.3.4-31. Average Probabilities for Incipient Rupture and Rupture for the Codisposal Waste Package with Degraded Internals

PGV Range (m/s)	Average Probability of Incipient Rupture	Average Probability of Rupture
0.4	0	0
1.05	0	0
2.44	0.029	0
4.07	0.123	0.118

Source: SNL 2007c, Table 6-21.

Table 2.3.4-32. Comparison of Damaged Area for the Codisposal Waste Package with 17-mm-Thick Outer Corrosion Barrier and Degraded Internals at the 0.4 m/s PGV Level

	Damaged Area (m^2)					
	90% RST		100% RST		105% RST	
WP ID / Rlz	Kinematic	Single Package	Kinematic	Single Package	Kinematic	Single Package
H / 3	0.059	0.0222	0.030	0	0	0
L / 3	0.061	0.0154	0.018	0	0	0
H / 4	0.192	0	0.057	0	0.003	0
L / 4	0.099	0.0026	0.038	0	0	0

Source: SNL 2007c, Table 6-23.

Table 2.3.4-33. Revised Probability of Nonzero Damage for the Codisposal Waste Package with 17-mm-Thick Outer Corrosion Barrier and Degraded Internals

	RST (% of Yield Strength)		
PGV Level (m/s)	90%	100%	105%
0.40	0.147	0.059	0.029
1.05	0.676	0.676	0.382
2.44	0.941	0.941	0.882
4.07	1	1	1

Source: SNL 2007c, Table 6-26.

Table 2.3.4-34. Characteristics of Representative Rock Blocks

Block Number (-)	Rock Block Mass (Metric Tons)	Rock Block Volume (m^3)	Total Velocity (m/s)	Kinetic Energy (J)
1	28.29	11.7	7.07	706914
2	7.49	3.1	4.81	86559
3	1.86	0.77	4.50	18846
4	0.38	0.16	4.24	3412
5	0.15	0.062	3.58	949
6	0.14	0.056	1.83	228
7	0.13	0.054	1.14	84

NOTE: Rock block 1 has the maximum kinetic energy for all calculations. Rock blocks 2 through 7 are based on the 99.9th, 99th, 90th, 70th, 40th, and 20th percentiles of impact kinetic energy for the 1.05 m/s PGV level. The largest block (28.29 MT) occurs during simulations at a PGV level of 5.35 m/s, which is beyond the bounding ground motion level of 4.07 m/s (SNL 2007c, Sections 6.10.2.2 and 6.4.3).

Source: SNL 2007c, Table 6-50.

Table 2.3.4-35. Data for Average Rockfall Pressure on the Crown of the Drip Shield

Segment No. (–)	Pressure Real 1 (Pa)	Pressure Real 2 (Pa)	Pressure Real 3 (Pa)	Pressure Real 4 (Pa)	Pressure Real 5 (Pa)	Pressure Real 6 (Pa)
11	2.466×10^3	7.790×10^4	5.219×10^5	2.549×10^3	2.389×10^4	0
12	1.373×10^5	9.381×10^4	6.983×10^3	2.280×10^5	6.474×10^3	1.463×10^5
13	1.850×10^3	2.755×10^5	1.369×10^3	6.830×10^4	1.966×10^5	1.513×10^5
14	2.339×10^5	1.037×10^5	1.984×10^5	6.566×10^4	1.438×10^5	1.293×10^5
15	3.072×10^3	4.556×10^4	3.396×10^5	0	5.439×10^4	1.788×10^5
16	3.033×10^4	7.905×10^2	5.462×10^3	3.252×10^5	5.622×10^5	2.543×10^4
17	6.782×10^5	1.258×10^5	1.987×10^5	1.138×10^5	0	2.776×10^3
18	0	1.696×10^5	9.350×10^4	3.015×10^4	4.419×10^3	1.591×10^5
19	2.018×10^3	0	1.802×10^5	4.638×10^5	1.355×10^5	3.457×10^5
20	0	5.780×10^5	2.002×10^3	0	0	0
Average Crown Pressure	1.089×10^5	1.471×10^5	1.548×10^5	1.297×10^5	1.127×10^5	1.139×10^5
Ln (Average Crown Pressure)	11.60	11.90	11.95	11.77	11.63	11.64
Mean of Ln (Average Crown Pressure)			11.75			
Standard Deviation of Ln (Mean Crown Pressure)			0.149			

NOTE: Average pressure is the average for segments 11 through 20 on the crown of the drip shield. All values have been rounded to four significant digits. The mean of the six pressure realizations is given by exp (11.75) = 1.27×10^5 Pa = 127 kPa (SNL 2007c, Section 6.8.4).

Source: SNL 2007c, Table 6-34.

Table 2.3.4-36. Catalogs for Damaged Area, Maximum Plastic Strain, and Maximum Stiffener Displacement for the 7 Representative Rock Blocks

Block Number (–)	Kinetic Energy (J)	15-mm Thick Plate (0-mm Reduction)	10-mm Thick Plate (5-mm Reduction)	5-mm Thick Plate (10-mm Reduction)
Damaged Area* (m^2):				
1	706914	2.30×10^{-2}	2.72×10^{-2}	NA
2	86559	1.59×10^{-2}	8.27×10^{-3}	3.61×10^{-2}
3	18846	1.15×10^{-3}	3.32×10^{-3}	3.27×10^{-3}
4	3412	2.79×10^{-4}	6.17×10^{-4}	4.80×10^{-4}
5	949	0	0	8.08×10^{-5}
6	228	0	0	0
7	84	0	0	0
Maximum Plastic Strain in Plates (–):				
1	706914	0.655	0.753	NA
2	86559	0.114	0.212	0.256
3	18846	0.041	0.068	0.164
4	3412	0.005	0.024	0.096
5	949	1.14×10^{-4}	0.005	0.039
6	228	0	0	8.16×10^{-4}
7	84	0	0	0
Maximum Plastic Strain in Axial Stiffeners (–):				
1	706914	0.247	0.274	NA
2	86559	0.044	0.067	0.084
3	18846	≤ 0.01	≤ 0.01	0.005
4	3412	≤ 0.01	≤ 0.01	≤ 0.01
5	949	≤ 0.01	≤ 0.01	≤ 0.01
6	228	≤ 0.01	≤ 0.01	≤ 0.01
7	84	≤ 0.01	≤ 0.01	≤ 0.01
Maximum Stiffener Displacement (m)				
1	706914	0.171	0.204	NA
2	86559	0.015	0.025	0.042
3	18846	≤ 0.01	≤ 0.01	8.15×10^{-3}

Table 2.3.4-36. Catalogs for Damaged Area, Maximum Plastic Strain, and Maximum Stiffener Displacement for the 7 Representative Rock Blocks (Continued)

Block Number (–)	Kinetic Energy (J)	15-mm Thick Plate (0-mm Reduction)	10-mm Thick Plate (5-mm Reduction)	5-mm Thick Plate (10-mm Reduction)
4	3412	≤ 0.01	≤ 0.01	≤ 0.01
5	949	≤ 0.01	≤ 0.01	≤ 0.01
6	228	≤ 0.01	≤ 0.01	≤ 0.01
7	84	≤ 0.01	≤ 0.01	≤ 0.01

NOTE: *Damaged area represents damage on one-quarter of the drip shield because the structural response model uses quarter symmetry. Damaged area per drip shield is four times greater.
NA = Not available because calculation stopped with illegal geometry in an element. It was not continued because the plates and stiffeners are expected to fail by tearing based on the results for the 10-mm thick plates.

Source: SNL 2007c, Table 6-51.

Table 2.3.4-37. Damaged Plate Areas as a Function of Total Dynamic Load

5 mm Plate Thickness		10 mm Plate Thickness		15 mm Plate Thickness	
Dynamic Load (Pa)	**Damaged Plate Area (m^2)**	**Dynamic Load (Pa)**	**Damaged Plate Area (m^2)**	**Dynamic Load (Pa)**	**Damaged Plate Area (m^2)**
1.00×10^5	0	2.00×10^5	0	4.00×10^5	0
2.00×10^5	0	4.00×10^5	0	8.00×10^5	0
3.00×10^5	0	6.00×10^5	0	1.20×10^6	1.24×10^{-3}
4.00×10^5	0	8.00×10^5	1.33×10^{-3}	1.60×10^6	9.43×10^{-3}
5.00×10^5	2.79×10^{-3}	1.00×10^6	7.39×10^{-3}	2.00×10^6	1.38×10^{-2}
6.00×10^5	5.34×10^{-3}	1.20×10^6	1.29×10^{-2}	2.40×10^6	2.09×10^{-2}
7.00×10^5	7.01×10^{-3}	1.40×10^6	1.71×10^{-2}	2.42×10^6	2.14×10^{-2}
8.00×10^5	8.03×10^{-3}	1.60×10^6	1.94×10^{-2}	2.44×10^6	2.22×10^{-2}
8.20×10^5	8.21×10^{-3}	1.62×10^6	1.97×10^{-2}	2.46×10^6	2.24×10^{-2}
8.40×10^5	8.38×10^{-3}	1.64×10^6	2.02×10^{-2}	2.48×10^6	2.29×10^{-2}
8.60×10^5	9.64×10^{-3}	1.66×10^6	2.04×10^{-2}	2.50×10^6	2.31×10^{-2}
8.80×10^5	1.11×10^{-2}	1.68×10^6	2.06×10^{-2}	2.52×10^6	2.39×10^{-2}
9.00×10^5	1.38×10^{-2}	1.70×10^6	2.07×10^{-2}	2.54×10^6	2.52×10^{-2}
9.20×10^5	1.78×10^{-2}	1.72×10^6	2.14×10^{-2}	2.56×10^6	2.55×10^{-2}
9.40×10^5	2.19×10^{-2}	1.74×10^6	2.27×10^{-2}	2.58×10^6	2.61×10^{-2}
9.60×10^5	2.80×10^{-2}	1.76×10^6	2.53×10^{-2}	2.60×10^6	2.64×10^{-2}
9.80×10^5	3.86×10^{-2}	1.78×10^6	3.44×10^{-2}	2.62×10^6	2.67×10^{-2}
1.00×10^6	1.64×10^{-1}	1.80×10^6	2.53×10^{-1}	2.64×10^6	2.70×10^{-2}
1.02×10^6	1.74×10^{-1}	1.82×10^6	2.71×10^{-1}	2.66×10^6	2.72×10^{-2}
1.04×10^6	1.96×10^{-1}	1.84×10^6	2.73×10^{-1}	2.68×10^6	2.83×10^{-2}
1.06×10^6	2.11×10^{-1}	1.86×10^6	2.79×10^{-1}	2.70×10^6	2.90×10^{-2}
1.08×10^6	2.23×10^{-1}	1.88×10^6	2.89×10^{-1}	2.72×10^6	3.11×10^{-2}
1.10×10^6	2.24×10^{-1}	1.90×10^6	2.91×10^{-1}	2.74×10^6	3.47×10^{-2}
—	—	1.92×10^6	2.95×10^{-1}	2.76×10^6	3.71×10^{-2}
—	—	1.94×10^6	3.04×10^{-1}	2.78×10^6	4.24×10^{-2}
—	—	—	—	2.80×10^6	4.71×10^{-2}

Table 2.3.4-37. Damaged Plate Areas as a Function of Total Dynamic Load (Continued)

5 mm Plate Thickness		10 mm Plate Thickness		15 mm Plate Thickness	
Dynamic Load (Pa)	**Damaged Plate Area (m^2)**	**Dynamic Load (Pa)**	**Damaged Plate Area (m^2)**	**Dynamic Load (Pa)**	**Damaged Plate Area (m^2)**
—	—	—	—	2.82×10^{6}	3.36×10^{-1}

Source: SNL 2007c, Table 6-49.

Table 2.3.4-38. Probability of Nonzero Damage/Plate Failures from Rock Block Impacts

PGV Level (m/s)	Probability of Damage/Failure			
	Plate Thickness (mm)			
	15	10	5	0
0.40	0.5	0.5	0.56	1
1.05	0.78	0.78	0.88	1
2.44	0.96	0.96	0.98	1

NOTE: Probability of damage/failure for the 0-mm plate thickness has been set to 1.

Source: SNL 2007c, Table 6-53.

Table 2.3.4-39. Conditional Probabilities of Damage States 1 through 5

PGV Level (m/s)	15-mm Thick Plate (0-mm Reduction)	10-mm Thick Plate (5-mm Reduction)	5-mm Thick Plate (10-mm Reduction)
State 1: Damaged Area with No Drip Shield Failures:			
0.4	1	1	0.56
1.05	0.95	0.87	0.34
2.44	0.94	0.73	0.18
5.35	0.81	0.33	0.05
State 2: Damaged Area with 1 Drip Shield Failure:			
0.4	0	0	0.28
1.05	0.05	0.13	0.36
2.44	0.06	0.23	0.31
5.35	0.16	0.42	0.16
State 3: Damaged Area with 2 Drip Shield Failures:			
0.4	0	0	0.11
1.05	0	0	0.20
2.44	0	0.02	0.22
5.35	0.02	0.21	0.23
State 4: Damaged Area with 3 Drip Shield Failures:			
0.4	0	0	0
1.05	0	0	0.05
2.44	0	0.02	0.20
5.35	0	0.05	0.28
State 5: 4 Drip Shield Failures:			
0.4	0	0	0.06
1.05	0	0	0.05
2.44	0	0	0.08
5.35	0	0	0.28

Source: SNL 2007c, Table 6-54.

Table 2.3.4-40. Mean and Standard Deviations of the Conditional Damaged Areas for Realizations of Rock Block Impacts on the Drip Shield

PGV Level (m/s)	Plate Thickness (mm)					
	15		10		5	
	Mean (m^2)	Standard Deviation (m^2)	Mean (m^2)	Standard Deviation (m^2)	Mean (m^2)	Standard Deviation (m^2)
0.4	0.0052	0.0064	0.013	0.016	0.0029	0.0025
1.05	0.018	0.031	0.031	0.046	0.0079	0.010
2.44	0.037	0.054	0.056	0.072	0.013	0.012
5.35	0.093	0.088	0.105	0.085	0.020	0.018

Source: SNL 2007c, Table 6-55.

Table 2.3.4-41. List of Realizations for Dynamic Analysis of Drip Shield Failure Mechanism

Trial #	Rock Structure Realization (Case)	Ground Motion Realization	PGV (m/s)	Plate Thickness (mm)
1	4	3	2.44	5
2	11	7	2.44	5
3	13	13	2.44	5
4	17	9	2.44	5
5	4	3	2.44	10
6	11	7	2.44	10
7	13	13	2.44	10
8	17	9	2.44	10
9	4	3	2.44	15
10	11	7	2.44	15
11	13	13	2.44	15
12	17	9	2.44	15
13	4	3	4.07	5
14	11	7	4.07	5
15	13	13	4.07	5
16	17	9	4.07	5
17	4	3	4.07	10
18	11	7	4.07	10
19	13	13	4.07	10
20	17	9	4.07	10
21	4	3	4.07	15
22	11	7	4.07	15
23	13	13	4.07	15
24	17	9	4.07	15

Source: SNL 2007b, Table 6-145.

Table 2.3.4-42. Comparison of the Drip-Shield Stability Assessment Based on Two-Dimensional Dynamic and Three-Dimensional Quasi-Static (Fragility) Analyses

Case	PGV Level (m/s)	Vertical PGA (g)	Ultimate Load p_{ul} (kPa)[a]	Initial Configuration 15mm Plate Thickness		5-mm-Thinned Configuration 10 mm Plate Thickness		10-mm-Thinned Configuration 5mm Plate Thickness	
				Fragility Analysis (Load Limit 1698 kPa[b])	Dynamic Analysis	Fragility Analysis (Load Limit 1094 kPa[b])	Dynamic Analysis	Fragility Analysis (Load Limit 500.8 kPa[b])	Dynamic Analysis
4	2.44	6.53	963	stable	stable	stable	stable	fails	stable
11	2.44	7.81	1126	stable	stable	fails	stable	fails	fails
13	2.44	3.14	529	stable	stable	stable	stable	fails	stable
17	2.44	12.87	1773	fails	stable	fails	stable	fails	stable
4	4.07	13.31	1830	fails	stable	fails	stable	fails	fails
11	4.07	15.93	2165	fails	fails	fails	fails	fails	fails
13	4.07	6.41	947	stable	fails	stable	fails	fails	fails
17	4.07	26.26	3485	fails	fails	fails	stable	fails	fails

NOTE: [a]Computed as $p_{ult} = p(1 + \text{PGA})$, where p is static rubble pressure, taken from Table 2.3.4.5-41 average top (vertical) pressure.
[b]Quasi-static limit loads taken from *Mechanical Assessment of Degraded Waste Packages and Drip Shields Subject to Vibratory Ground Motion* (SNL 2007b, Table 6-137 and Figure 6-57) for average rubble load distribution.
PGA = peak ground acceleration.

Source: SNL 2007b, Table 6-146.

Table 2.3.4-43. Probability of the Failure of Drip Shield Plates as a Function of Rockfall Load and Plate Thickness

PGV Level (m/s)	Plate Thickness				
	0-mm	2-mm	5-mm	10-mm	15-mm
Probability of Failure with 0% Rockfall Load:					
All	1	0	0	0	0
Probability of Failure with 10% Rockfall Load:					
0.2	1	0	0	0	0
0.4	1	0	0	0	0
1.05	1	0	0	0	0
2.44	1	0.006	0	0	0
4.07	1	0.036	0	0	0
Probability of Failure with 50% Rockfall Load:					
0.2	1	0	0	0	0
0.4	1	0.005	0	0	0
1.05	1	0.083	0.002	0	0
2.44	1	0.377	0.047	0.004	0
4.07	1	0.637	0.182	0.028	0.007
Probability of Failure with 100% Rockfall Load:					
0.2	1	0.027	0	0	0
0.4	1	0.093	0	0	0
1.05	1	0.390	0.030	0.001	0
2.44	1	0.765	0.268	0.047	0.013
4.07	1	0.912	0.557	0.186	0.073

NOTE: Probabilities below 0.001 have been rounded down to 0.

Source: SNL 2007c, Table 6-36.

Table 2.3.4-44. Probability of Failure for the Drip Shield Framework

PGV Level (m/s)	Thicknesses of Drip Shield Components				
	Frame: Reduced by 15-mm	**Frame: Reduced by 13-mm**	**Frame: Reduced by 10-mm**	**Frame: Reduced by 5-mm**	**Frame: Intact**
Probability of Failure with 0% Rockfall Load:					
All	1	0	0	0	0
Probability of Failure with 10% Rockfall Load:					
0.2	1	0	0	0	0
0.4	1	0	0	0	0
1.05	1	0.007	0	0	0
2.44	1	0.107	0.001	0	0
4.07	1	0.311	0.011	0	0
Probability of Failure with 50% Rockfall Load:					
0.2	1	0.048	0	0	0
0.4	1	0.192	0	0	0
1.05	1	0.635	0.025	0	0
2.44	1	0.929	0.230	0.029	0.006
4.07	1	0.985	0.502	0.127	0.039
Probability of Failure with 100% Rockfall Load:					
0.2	1	0.716	0.001	0	0
0.4	1	0.867	0.016	0	0
1.05	1	0.981	0.210	0.018	0.003
2.44	1	0.999	0.649	0.191	0.063
4.07	1	1.000	0.867	0.449	0.219

NOTE: Probabilities below 0.001 have been rounded down to 0.

Source: SNL 2007c, Table 6-40.

Table 2.3.4-45. Simulated Combinations of Ground-Motion Numbers and Random-Number Generator Seed Numbers

Realization (Case) Number	Ground Motion Number	Random-Number-Generator Seed for Rock Block Pattern
1	4	10
2	10	17
3	5	3
4	3	4
5	1	18
6	17	6
7	6	12
8	11	8
9	8	1
10	12	13
11	7	9
12	15	7
13	13	14
14	14	11
15	2	5
16	16	15
17	9	2

Source: SNL 2007b, Table 6-159.

Table 2.3.4-46. Structural Parameters for the TAD-Bearing and Codisposal Waste Packages

Parameter	TAD-Bearing Waste Package	Codisposal Waste Package	Difference
Outer Corrosion Barrier Thickness	25.4-mm	25.4-mm	0%
Outer Diameter of Outer Corrosion Barrier	1881.6-mm (74.08-in)	2044.7-mm (80.50-in)	+8.7%
Fully Loaded Weight	162,055 lbs	127,870 lbs	–21.1%

Source: SNL 2007c, Table 6-48.

Table 2.3.4-47. Mean and Modified Standard Deviations of the Conditional Damaged Areas for the 17-mm-Thick Outer Corrosion Barrier with Degraded Internals

	RST (% of Yield Strength)					
	90%		100%		105%	
PGV Level (m/s)	Mean (% Surf Area)	Standard Deviation (% Surf Area)	Mean (% Surf Area)	Modified Standard Deviation (% Surf Area)	Mean (% Surf Area)	Modified Standard Deviation (% Surf Area)
2.44	1.396	1.003	—	—	—	—
4.07	2.214	2.064	0.409	0.381	0.136	0.127

Source: SNL 2007c, Table 6-46.

Table 2.3.4-48. Probabilities of Puncture for the Waste Package with 17-mm Outer Corrosion Barrier and Degraded Internals Surrounded by Rubble

Realization Number	Probability of Puncture by PGV Level			
	0.4 m/s	1.05 m/s	2.44 m/s	4.07 m/s
1	0	0	0	0.567
2	0	0	0	0
3	0	0	0	0.107
4	0	0.050	0.250	0.171
5	0	0	0	0.432
6	0	0	0	0
7	0	0.128	0	0.128
8	0	0	0	0.065
9	0	0	0	0.175
10	0	0	0	0
11	0	0	0	0.490
12	0	0	0	0
13	0	0	0.820	1.000
14	0	0	0	0
15	0	0	0	0.152
16	0	0	0	0
17	0	0	0	0.194
Average	0	0.010	0.063	0.205

NOTE: Probabilities have been rounded to 3 significant digits.

Source: SNL 2007c, Table 6-42.

Table 2.3.4-49. Probability of Nonzero Damage for the Waste Package Surrounded by Rubble

PGV Level (m/s)	RST (% of Yield Strength)		
	90%	100%	105%
23-mm-Thick Outer Corrosion Barrier with Degraded Internals:			
0.40	0	0	0
1.05	0	0	0
2.44	0	0	0
4.07	0.294	0.118	0.059
17-mm-Thick Outer Corrosion Barrier with Degraded Internals:			
0.40	0	0	0
1.05	0	0	0
2.44	0.118	0	0
4.07	0.412	0.176	0.118

Source: SNL 2007c, Table 6-44.

Table 2.3.4-50. Waste Package Dimensions and Clearance between Drip Shield and Waste Package

Package Type	Outside Diameter of Outer Corrosion Barrier (mm)	Nominal Length (mm)	Clearance without Pallet (mm)	Clearance with Pallet (mm)	Difference in Clearances (mm)
TAD	1881.6	5850.1	836	533	303
Naval Fuel – Long	1881.6	5850.1	836	533	303
Naval Fuel – Short	1881.6	5215.1	836	533	303
5-DHLW/DOE SNF – Short	2044.7	3697.4	673	356	317
5-DHLW/DOE SNF – Long	2044.7	5303.9	673	356	317
2-MCO/2-DHLW	1749.3	5278.6	969	686	283

NOTE: Clearance without pallet is calculated as the interior height of the drip shield (2717.8 mm) minus the outside diameter of the waste package outer corrosion barrier, rounded to 3 significant digits.
Difference in Clearances = Clearance Without Pallet – Clearance With Pallet.
DHLW = defense high-level radioactive waste; MCO = multicanister overpack; SNF = spent nuclear fuel; TAD = transportation, aging, and disposal (canister).

Source: SNL 2007c, Table 6-57.

Table 2.3.4-51. Emplacement Drift Configuration Dimensions that are Independent of the Waste Package

Description	Value	Source
Emplacement Drift Diameter	216-in. (5486.4 mm)	BSC 2007e
Invert Height (maximum)	52-in. (1320.8 mm)	BSC 2007e, Invert Height
Drip Shield Height – Exterior	2886 mm	BSC 2007b, Table 1
Drip Shield Height – Interior	107 in. 2717.8 mm	BSC 2007e, dimensions (D2 + D3) for TAD-bearing package
Clearance from Crown of Drip Shield to Roof of Drift	50 in. 1270 mm	BSC 2007e

Source: SNL 2007c, Table 6-56.

Table 2.3.4-52. Maximum Allowable Displacement with Drift Collapse for an Intact Drip Shield

Package Type	Maximum Allowable Displacement With Drift Collapse (mm)
TAD	836
Naval Fuel – Long	836
Naval Fuel – Short	836
5-DHLW/DOE SNF – Short	673
5-DHLW/DOE SNF – Long	673
2-MCO/2-DHLW	969

NOTE: Maximum allowable displacement with drift collapse for an intact drip shield = clearance without pallet in Table 2.3.4-50.
DHLW = defense high-level radioactive waste; MCO = multicanister overpack; SNF = spent nuclear fuel; TAD = transportation, aging and disposal (canister).

Source: SNL 2007c, Table 6-58.

Table 2.3.4-53. Maximum Allowable Displacement after Drip Shield Failure

Package Type	Maximum Allowable Displacement (mm)
TAD	470
Naval Fuel – Long	470
Naval Fuel – Short	470
5-DHLW/DOE SNF – Short	511
5-DHLW/DOE SNF – Long	511
2-MCO/2-DHLW	437

NOTE: Maximum allowable displacement with drift collapse after drip shield failure = one-quarter of outer diameter of outer corrosion barrier in Table 2.3.4-50 rounded to three significant figures.
DHLW = defense high-level radioactive waste; MCO = multicanister overpack; SNF = spent nuclear fuel; TAD = transportation, aging and disposal (canister).

Source: SNL 2007c, Table 6-59.

Table 2.3.4-54. Intersections of Known Faults with Emplacement Drifts

Fault Designator	Drift Intersections	Number of Intersections
Sundance Fault	1-2, 1-3, 1-4, 1-5, 1-6, and 2-1	6
Drill Hole Wash Fault	4-1, 4-2, 3-4W, 3-5W, 3-6W, 3-7W, 3-8W, 3-9W, 3-9E1, 3-10E1, 3-11E1, 3-12E1, 3-13E1, 3-14E, 3-15E1, 3-16E1, and 3-17E1	17
Pagany Wash Fault	3-1W, 3-1E, 3-2E, 3-3E, 3-4E, 3-5E, 3-6E1, and 3-7E1	8
Sever Wash Fault	3-2 E	1
West Ghost Dance Fault	2-17, 2-18, 2-19, 2-20, 2-21, 2-22, 2-23, 2-24, 2-25, 2-26, and 2-27	11

Source: SNL 2007c, Table 6-60.

Table 2.3.4-55. Fault Displacement from Mean Hazard Curves

Site Number and Fault Name	Mean Annual Exceedance Frequency (1/yr)				
	10^{-4}	10^{-5}	10^{-6}	10^{-7}	10^{-8}
	Displacement (cm)				
2 – Solitario Canyon	<0.1	32	180	490	1300
3 – Drill Hole Wash[a]	<0.1	<0.1	15	75	240
4 – Ghost Dance[b]	<0.1	<0.1	15	69	210
5 – Sundance	<0.1	0.1	6	40	140
7a – small fault with 2-m offset	<0.1	<0.1	2	18	73
7b – shear with 10-cm offset	<0.1	<0.1	1	6	9
7c – fracture with no displacement	<0.1	<0.1	0.1	0.5	0.6
7d – intact rock	<0.1	<0.1	<0.1	<0.1	<0.1
8a – small fault with 2-m offset	<0.1	<0.1	2.0	18	78
8b – shear with 10-cm offset	<0.1	<0.1	0.9	6	9
8c – fracture with no displacement	<0.1	<0.1	0.1	0.5	0.6
8d – intact rock[c]	<0.1	<0.1	<0.1	<0.1	<0.1

NOTE: [a]Also representative of Pagany Wash Fault and Sever Wash Fault.
[b]Representative of West Ghost Dance Fault.
[c]Data for Site 8d are based on the observation that the fault displacements for Sites 7a, 7b, and 7c are essentially identical with the fault displacements for Sites 8a, 8b, and 8c, respectively. In this situation, the fault displacements at Site 8d are anticipated to be very similar to the fault displacements at Site 7d considering that both generic locations involve intact rock within the repository block. This observation is corroborated by information in *Probabilistic Seismic Hazard Analyses for Fault Displacement and Vibratory Ground Motion at Yucca Mountain, Nevada* (CRWMS M&O 1998, Section 8.2.1, first paragraph), which indicates that displacements at Site 8d are below 0.1 cm down to 10^{-8} per year annual exceedance frequency.

Source: SNL 2007c, Table 6-61.

Table 2.3.4-56. Parameters for Simplified Groups of Waste Packages

Waste Package Group	Effective Waste Package Length[c], L_{eff} (mm)	Effective Waste Package Diameter[d], D (mm)	Effective Waste Package Surface Area[a] (m^2)	Nominal Quantity (–)	Total Waste Package Length for Group[b] (mm)	Fraction of Waste Packages (% of Total Length)
TAD	5843	1881.6	40.10	7883	4.606×10^7	74.9
CDSP	4711	2044.7	36.83	3279	1.545×10^7	25.1

NOTE: [a]Effective Surface Area = $(\pi/2)(D)^2 + \pi D L_{eff}$.
[b]Total Waste Package Length for Group= $\Sigma(\text{Length})_i \times (\text{Nominal Quantity})_i$ summed over the package types in each group, based on the lengths and nominal quantities in Table 2.3.4-27.
[c]Effective Waste Package Length = L_{eff} = Total Length / Nominal Quantity.
[d]Outer diameter of the outer corrosion barrier is 1881.6 mm for all waste package types in the TAD group. Outer diameter of the outer corrosion barrier for the codisposal waste group is based on the 5-DHLW/DOE SNF packages because they constitute more than 90% of the inventory in this group.
CDSP = codisposal waste package; TAD = transportation, aging, and disposal (canister); (–) = dimensionless.

Source: SNL 2007c, Table 6-64.

Table 2.3.4-57. Mean Annual Exceedance Frequencies That Cause Waste Package Failure

Fault	TAD Group	CDSP Group
3 – Drill Hole Wash	$< 2.2 \times 10^{-7}$	$< 2.5 \times 10^{-7}$
Pagany Wash	$< 2.2 \times 10^{-7}$	$< 2.5 \times 10^{-7}$
Sever Wash	$< 2.2 \times 10^{-7}$	$< 2.5 \times 10^{-7}$
4 – West Ghost Dance	$< 2.0 \times 10^{-7}$	$< 2.2 \times 10^{-7}$
5 – Sundance	$< 7.8 \times 10^{-8}$	$< 8.6 \times 10^{-8}$
Sites 7a/8a[a]	$< 2.6 \times 10^{-8}$	$< 2.9 \times 10^{-8}$

NOTE: [a]The hazard curves for Sites 7a and 8a are very similar, as shown by the data in Table 2.3.4-56. The maximum exceedance frequency for Sites 7a or 8a is presented here.
CDSP = codisposal waste package; TAD = transportation, aging, and disposal (canister).

Source: SNL 2007c, Table 6-65.

Table 2.3.4-58. Expected Number of Waste Packages Emplaced on Each Fault

Fault	TAD Group	CDSP Group	Total
3 – Drill Hole Wash, etc.	19.5	6.5	26
4 – West Ghost Dance	8.2	2.8	11
5 – Sundance	4.5	1.5	6
Sites 7a/8a	128.1	42.9	171

NOTE: CDSP = codisposal waste package; TAD = transportation, aging, and disposal (canister).

Source: SNL 2007c, Table 6-66.

Table 2.3.4-59. Expected Number of Waste Package Failures Versus Annual Exceedance Frequency

Annual Exceedance Frequency (1/yr)	Expected Number of Failures – TAD Group	Annual Exceedance Frequency (1/yr)	Expected Number of Failures – CDSP Group
$> 2.2 \times 10^{-7}$	0	$> 2.5 \times 10^{-7}$	0
2.0×10^{-7} to 2.2×10^{-7}	19.5	2.2×10^{-7} to 2.5×10^{-7}	6.5
7.8×10^{-8} to 2.0×10^{-7}	27.7	8.6×10^{-8} to 2.2×10^{-7}	9.3
2.6×10^{-8} to 7.8×10^{-8}	32.2	2.9×10^{-8} to 8.6×10^{-8}	10.8
1×10^{-8} to 2.6×10^{-8}	160.3	1×10^{-8} to 2.9×10^{-8}	53.7

NOTE: CDSP = codisposal waste package; TAD = transportation, aging, and disposal (canister).

Source: SNL 2007c, Table 6-67.

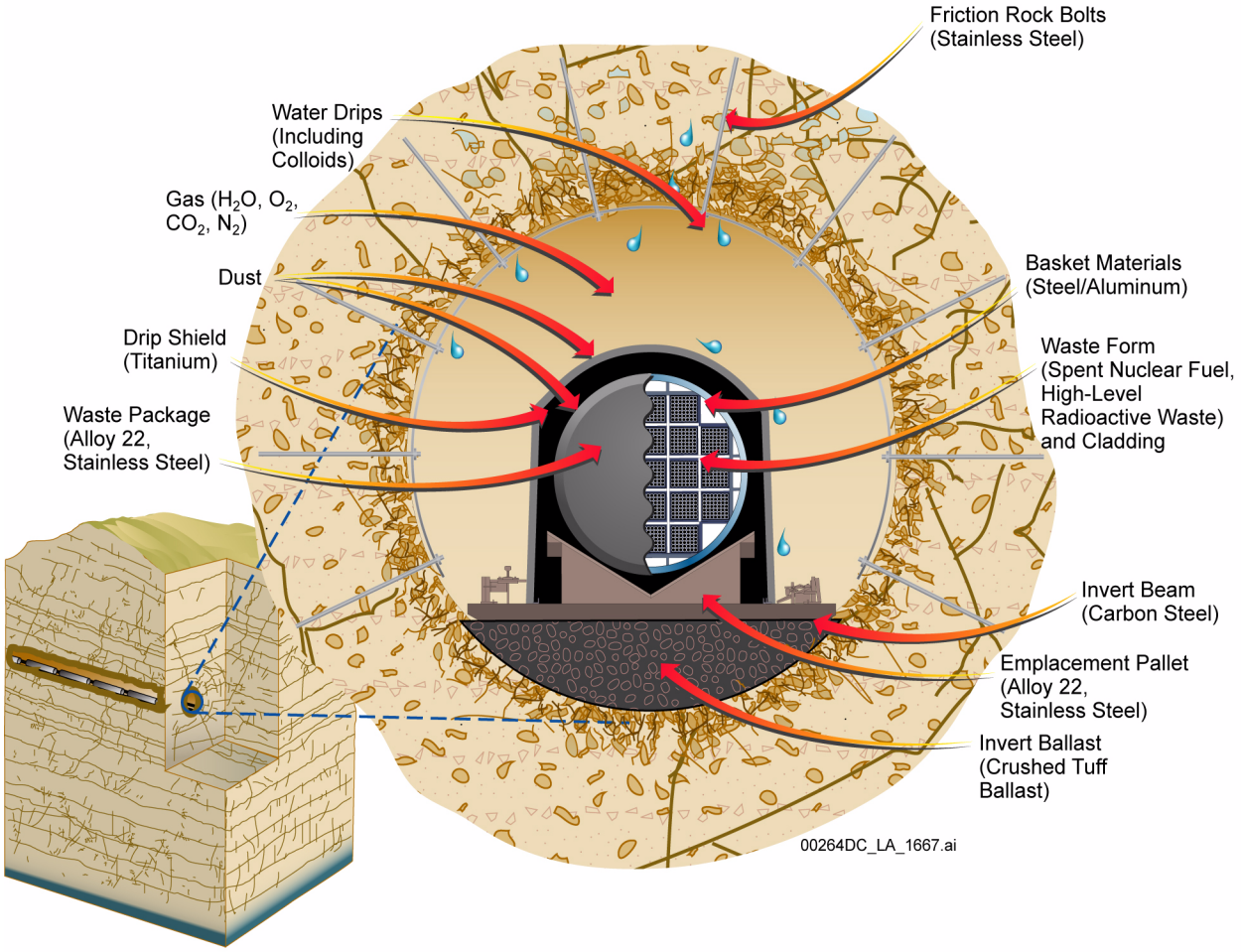

Figure 2.3.4-1. Schematic Diagram of the Engineered Barrier System in a Typical Emplacement Drift

NOTE: The Engineered Barrier System features include emplacement drifts, drip shields, waste packages, cladding, waste forms and waste package internals, waste package pallets, and the ballast in the emplacement drift inverts.

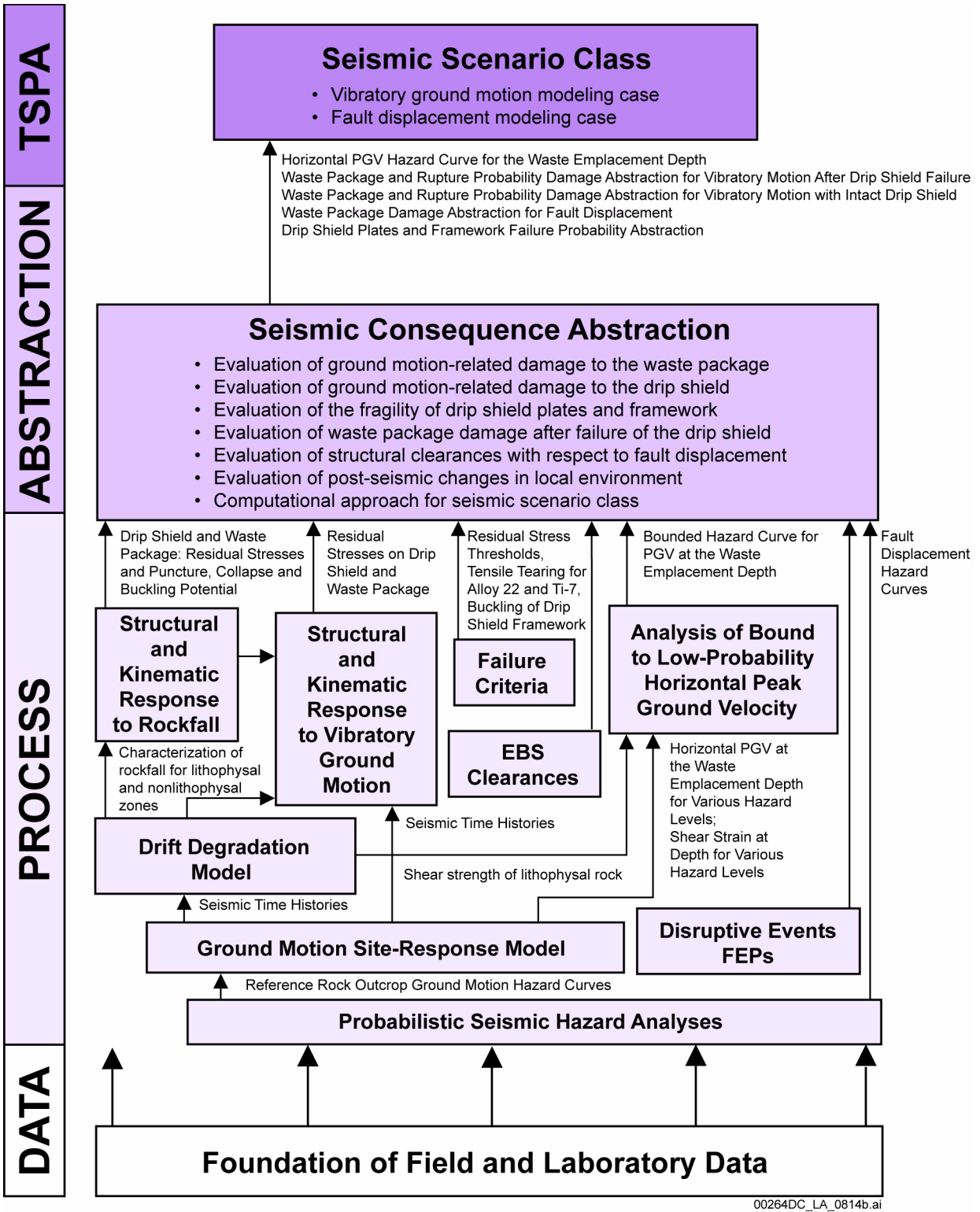

Figure 2.3.4-2. Information Flow Supporting Development of the Models Used to Represent Mechanical Damage of the Engineered Barrier System at the Data, Process, Abstraction, and TSPA Levels

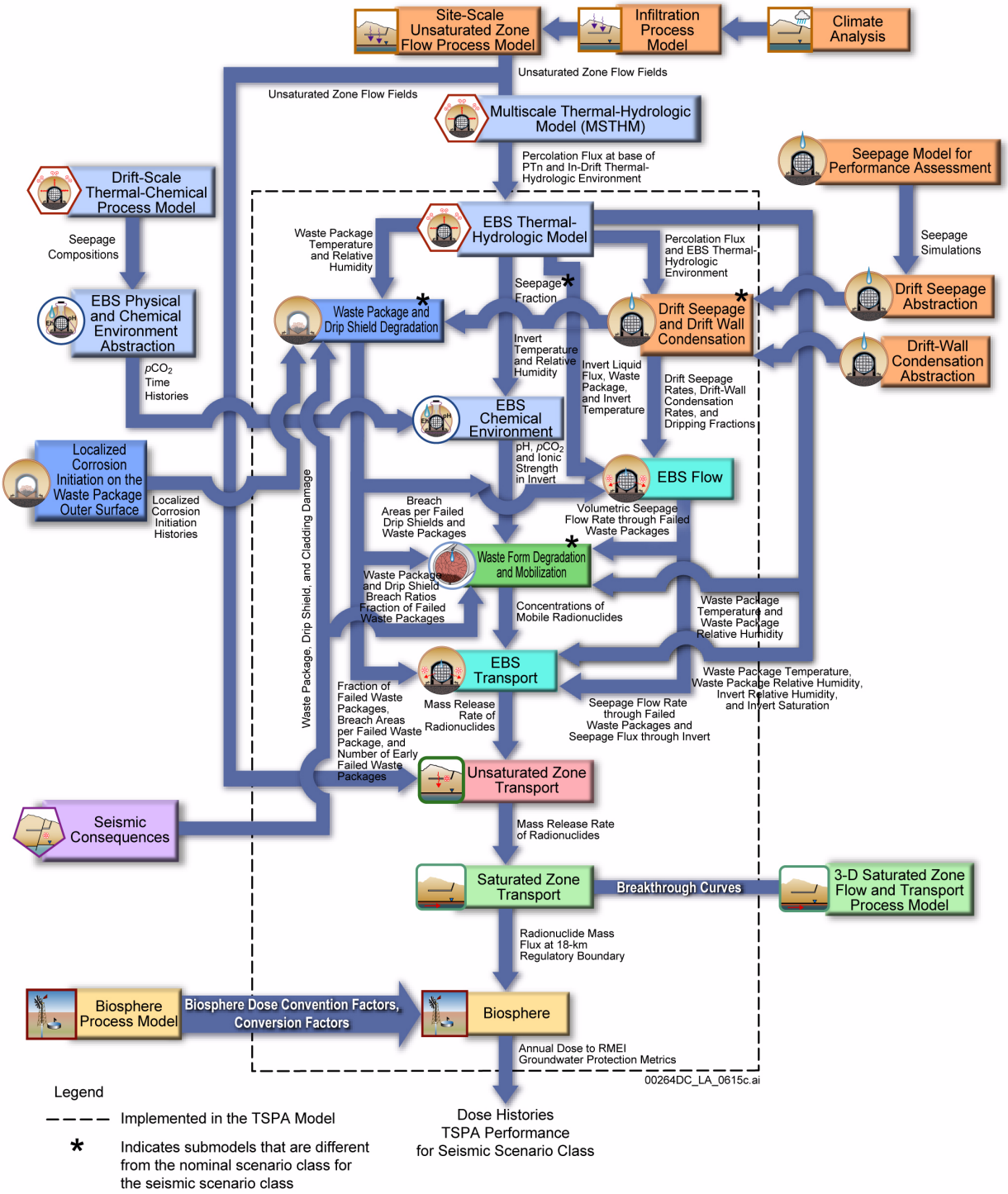

Figure 2.3.4-3. Information Transfer among the Principal Model Components of the TSPA Seismic Scenario Class Model

NOTE: DS = drip shield; LC = localized corrosion; PA = performance assessment; RH = relative humidity; SZ = saturated zone; TH = thermal-hydrologic; THC = thermal-hydrologic-chemical; UZ = unsaturated zone; WF = waste form; WP = waste package.

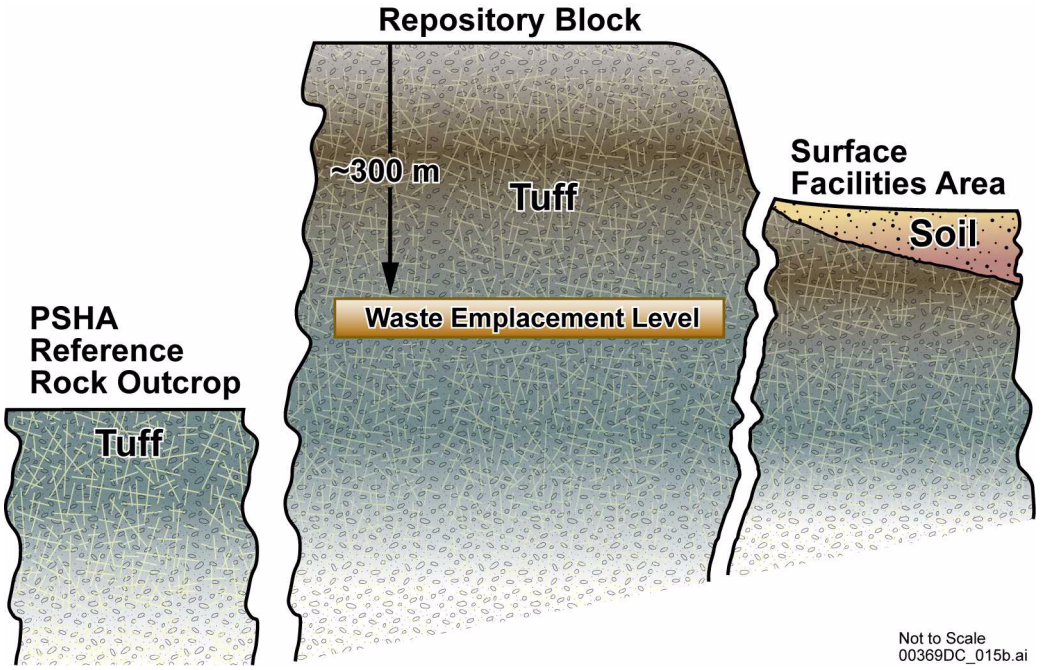

Figure 2.3.4-4. Relation of Reference Rock Outcrop to Sites for Which Seismic Inputs are Developed

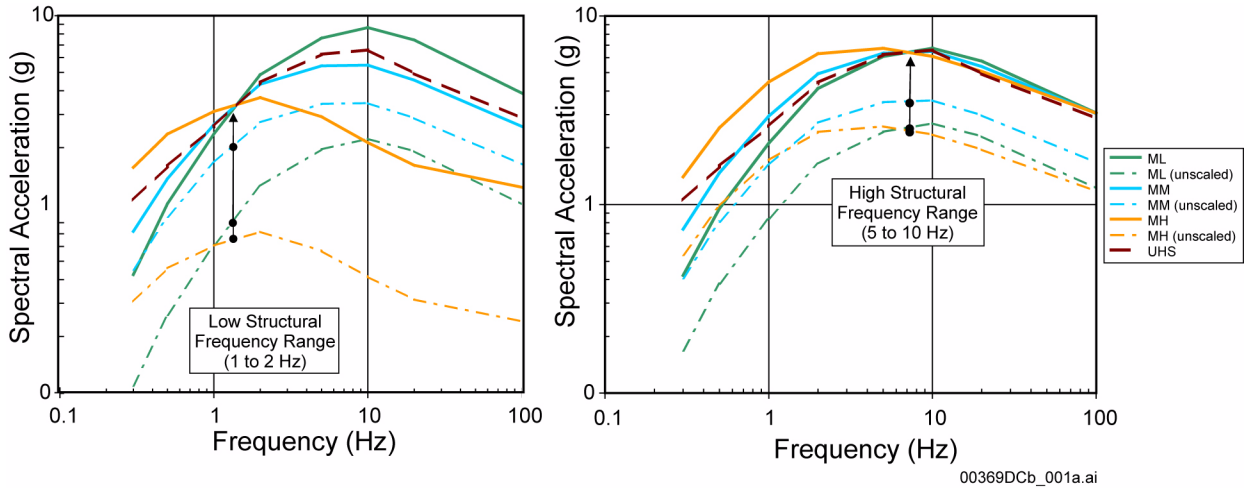

Figure 2.3.4-5. Scaling of Deaggregation Earthquake Response Spectra to the Corresponding Uniform Hazard Spectrum

NOTE: The arrows show how the deaggregation earthquake response spectra are scaled upward to match the uniform hazard spectrum for the particular frequency range (1 to 2 Hz or 5 to 10 Hz). MH = high magnitude deaggregation earthquake; ML = low magnitude deaggregation earthquake; MM = mean magnitude deaggregation earthquake; UHS = uniform hazard spectrum.

Source: BSC 2004b, Section 6.2.2.5, Figures 6.2-9 (uniform hazard spectrum), 6.2-57 (1 to 2 Hz, scaled), and 6.2-58 (5 to 10 Hz, scaled).

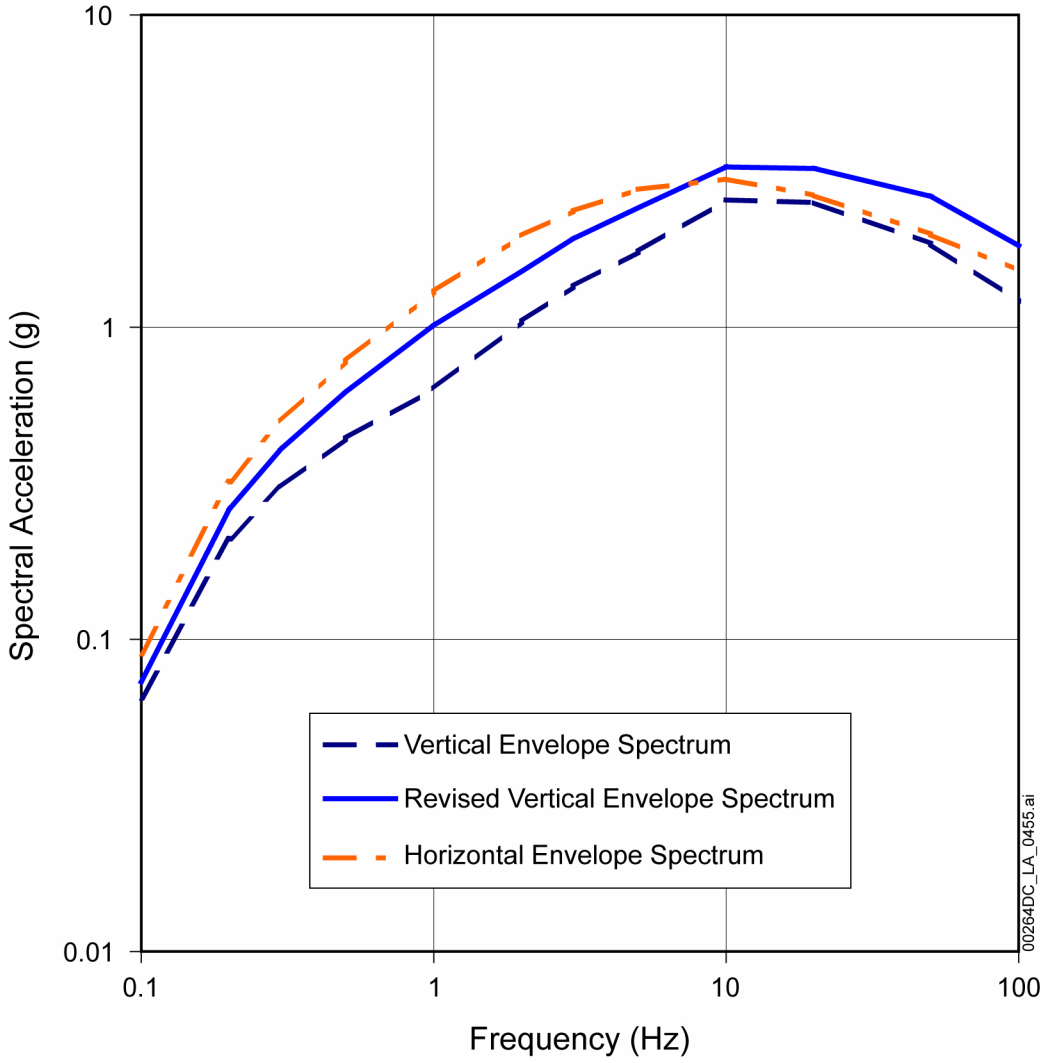

Figure 2.3.4-6. Comparison of the Revised Vertical Envelope Spectrum to the Horizontal and Original Vertical Envelope Spectra

NOTE: The example shown is for an annual frequency of exceedance of 10^{-5}.

Source: BSC 2004b, Figure 6.2-85.

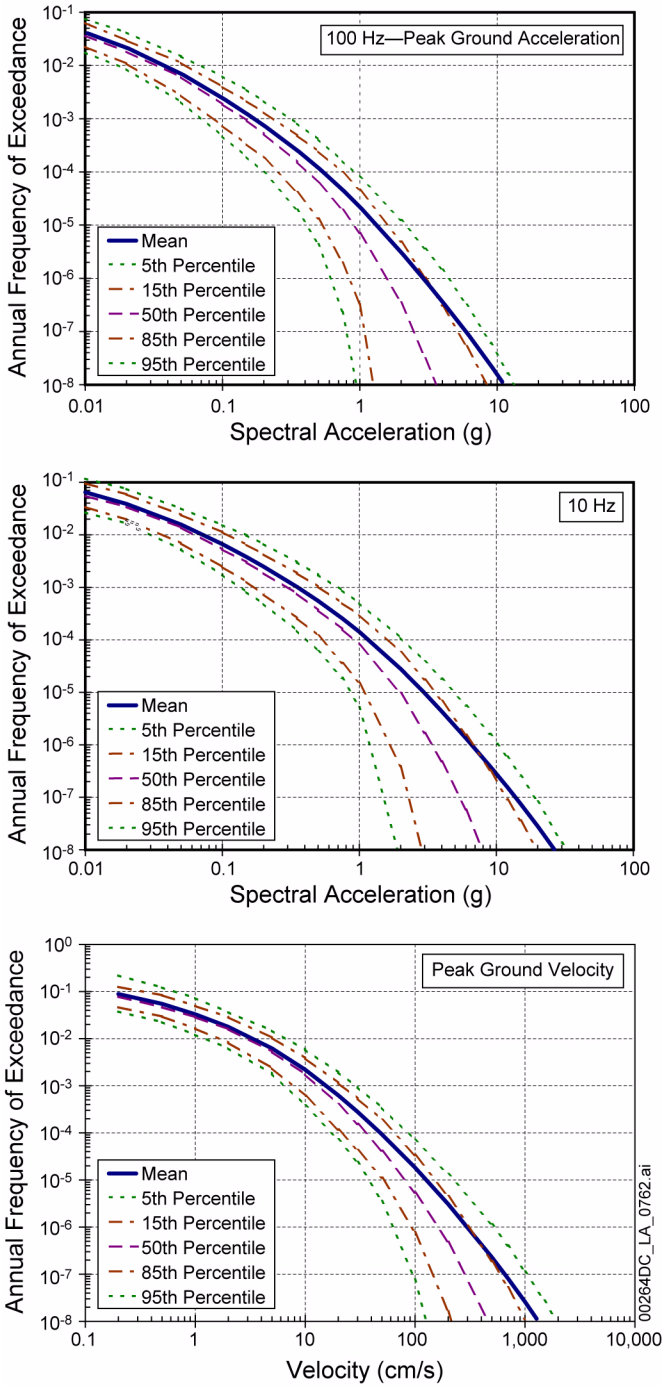

Figure 2.3.4-7. Summary Horizontal Ground Motion Hazard Curves for Yucca Mountain

NOTE: The mean and various percentile hazard curves are shown.
Hazard is for the PSHA reference rock outcrop and does not include the effect of local site materials. These hazard curves also do not reflect information and analyses on limits to extreme ground motion at Yucca Mountain.

Source: BSC 2004b, Figures 6.2-1, 6.2-3, and 6.2-4.

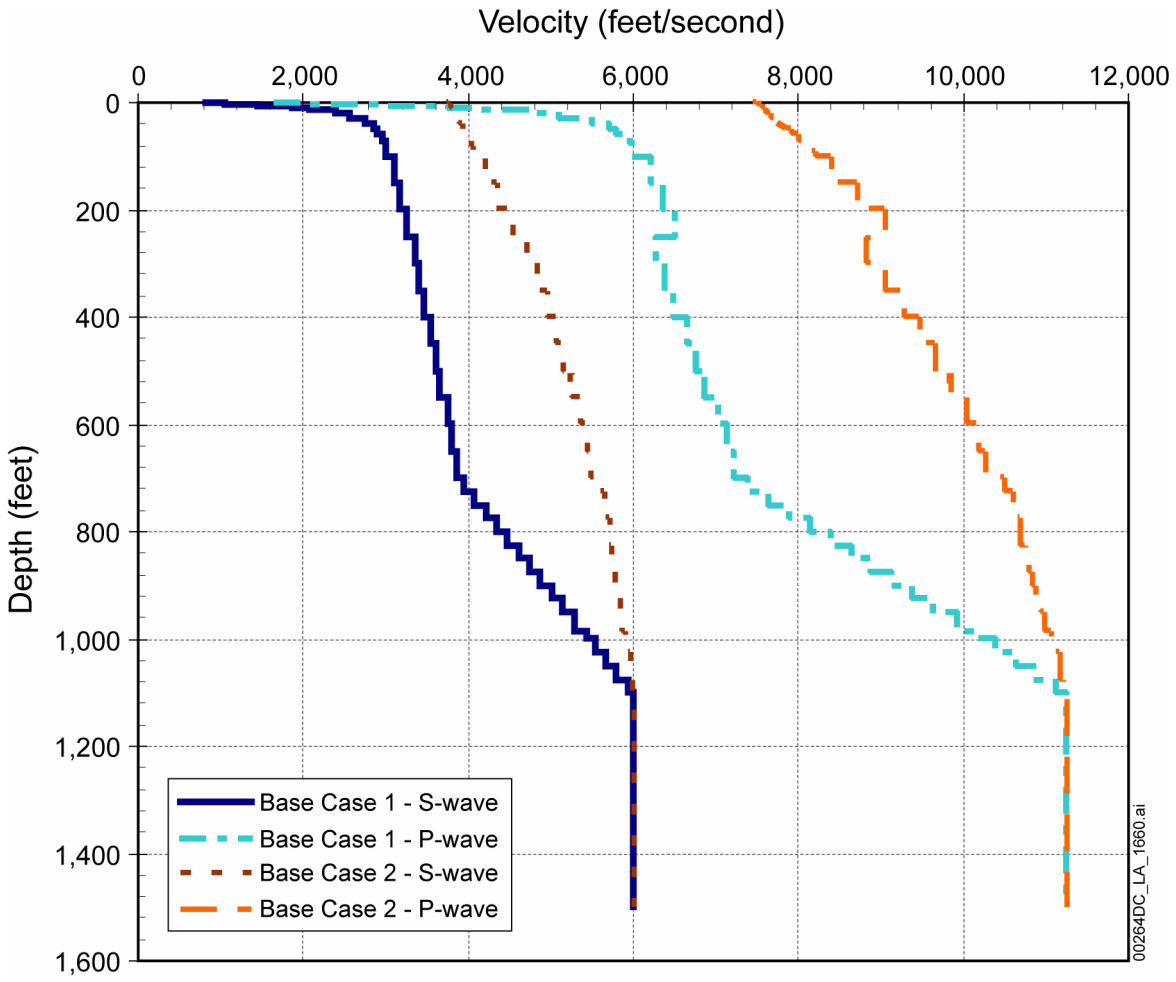

Figure 2.3.4-8. Repository Block Base-Case Velocity Profiles

NOTE: Two sets of base-case velocity profiles are identified to represent the uncertainty in knowledge of seismic velocity for the repository block. P-wave velocity profiles are determined from the corresponding S-wave velocity profiles using observed values of Poisson's ratio as a function of depth.

Source: BSC 2004b, Figure 6.2-118.

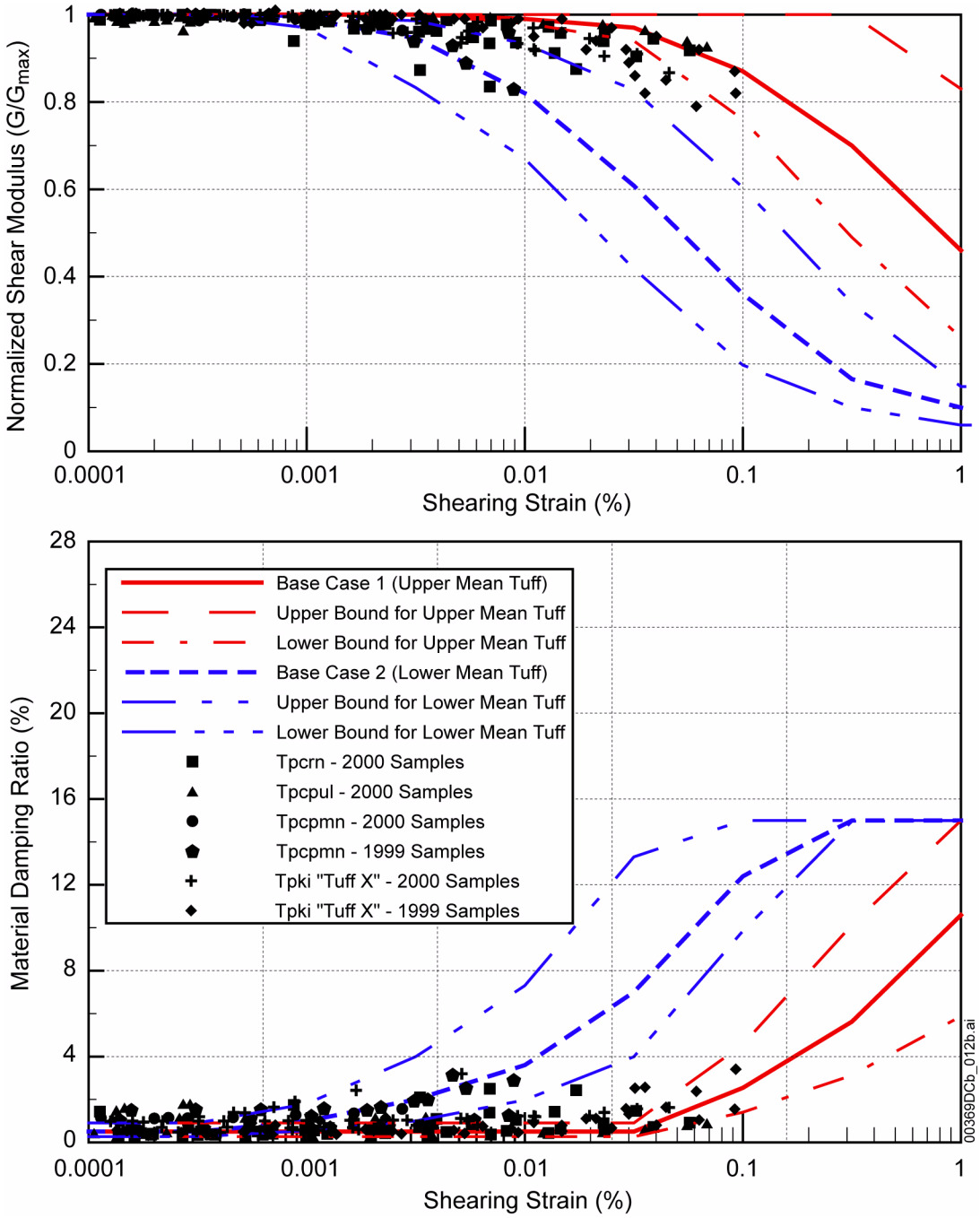

Figure 2.3.4-9. Base-Case Curves for Normalized Shear Modulus and Material Damping as a Function of Shearing Strain for Tuff

NOTE: Two sets of base-case dynamic material property curves are identified to represent the uncertainty in how normalized shear modulus and material damping for tuff vary as a function of shearing strain. The more linear set of curves (Base Case 1) is referred to as the Upper Mean Tuff curves; the less linear set of curves (Base Case 2) is referred to as the Lower Mean Tuff curves.

Source: BSC 2004b, Figure 6.2-139.